Dirac fermion optics and plasmonics in graphene microwave devices

Holger Graef

School of Electrical & Electronic Engineering

A thesis submitted to Sorbonne Universités and to the Nanyang Technological University in partial fulfillment of the requirement for the degree of
Doctor of Philosophy

2019

Statement of Originality

I hereby certify that the work embodied in this thesis is the result of original research, is free of plagiarised materials, and has not been submitted for a higher degree to any other University or Institution.

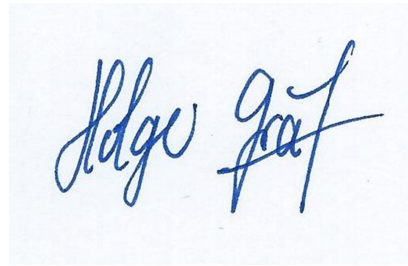

25/07/2019
. . . .
Date

. . . .
Holger Graef

Supervisor Declaration Statement

I have reviewed the content and presentation style of this thesis and declare it is free of plagiarism and of sufficient grammatical clarity to be examined. To the best of my knowledge, the research and writing are those of the candidate except as acknowledged in the Author Attribution Statement. I confirm that the investigations were conducted in accord with the ethics policies and integrity standards of Nanyang Technological University and that the research data are presented honestly and without prejudice.

[Date Here]

July 23 2019

Date

[Supervisor's Signature Here]

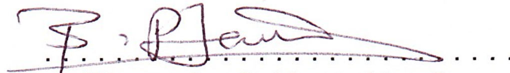

[Supervisor's Name Here]

Bernard Plagain

Supervisor Declaration Statement

I have reviewed the content and presentation style of this thesis and declare it is free of plagiarism and of sufficient grammatical clarity to be examined. To the best of my knowledge, the research and writing are those of the candidate except as acknowledged in the Author Attribution Statement. I confirm that the investigations were conducted in accord with the ethics policies and integrity standards of Nanyang Technological University and that the research data are presented honestly and without prejudice.

23/07/2019

. . . .

Date

. . . .

Teo Hang Tong Edwin

Authorship Attribution Statement

This thesis contains material from 3 paper(s) published in the following peer-reviewed journal(s):

Chapter 3 is published as H. Graef, Q. Wilmart, M. Rosticher, D. Mele, L. Banszerus, C. Stampfer, T. Taniguchi, K. Watanabe, J.-M. Berroir, E. Bocquillon, G. Fève, E.H.T. Teo, and B. Plaçais. A corner reflector of graphene Dirac fermions as a phonon-scattering sensor. *Nature Communications* **10**, 2428 (2019). DOI: 10.1038/s41467-019-10326-6.

The contributions of the co-authors are as follows:

- H.G., Q.W., and B.P. conceived the experiment.
- Q.W. developed the bottom gate fabrication process.
- L.B., C.S., T.T., K.W., H.G., and M.R. participated to sample fabrication at RWTH University in Aachen, Germany, NIMS in Tsukuba, Japan, and École Normale Supérieure in Paris, France.
- H.G. conducted the measurements at École Normale Supérieure in Paris, France.
- H.G., D.M., J.-M.B., G.F., E.B., E.H.T.T., and B.P. participated to the data analysis.
- Q.W. and H.G. developed the ray-tracing simulations.
- H.G. and B.P. worked out the analytic model.
- H.G. and B.P. wrote the manuscript with contributions from the coauthors.

Chapter 4 is published as H. Graef, D. Mele, M. Rosticher, L. Banszerus, C. Stampfer, T. Taniguchi, K. Watanabe, E. Bocquillon, G. Fève, J.-M. Berroir, E.H.T. Teo, and B. Plaçais. Ultra-long wavelength Dirac plasmons in graphene capacitors. *Journal of Physics Materials* **1**, 01LT02 (2018). DOI: 10.1088/2515-7639/aadd8c.

The contributions of the co-authors are as follows:

- H.G. and B.P. conceived the experiment.
- L.B., C.S., T.T., K.W., H.G., D.M. and M.R. participated to sample fabrication at RWTH University in Aachen, Germany, NIMS in Tsukuba, Japan, and École Normale Supérieure in Paris, France.

- H.G. and D.M. conducted the measurements at École Normale Supérieure in Paris, France.
- H.G., D.M., J.-M.B., G.F., E.B., E.H.T.T., and B.P. participated to the data analysis.
- H.G., D.M. and B.P. wrote the manuscript with contributions from the coauthors.

Chapter 5 is published as W. Yang, H. Graef, X. Lu, G. Zhang, T. Taniguchi, K. Watanabe, A. Bachthold, E.H.T. Teo, E. Baudin, E. Bocquillon, G. Fève, J.-M. Berroir, D. Carpentier, M.O. Goerbig, B. Plaçais. Landau velocity for collective quantum Hall breakdown in bilayer graphene. *Physical Review Letters* **121**, 136804 (2018). DOI: 10.1103/PhysRevLett.121.136804.

The contributions of the co-authors are as follows:

- W.Y. and B.P. conceived the experiment.
- X.L., G.Z., T.T., K.W., and W.Y. participated to sample fabrication at Beijing National Laboratory for Condensed Matter Physics and Institute of Physics in Beijing, China, NIMS in Tsukuba, Japan, and École Normale Supérieure in Paris, France.
- W.Y. conducted the measurements at École Normale Supérieure in Paris, France.
- W.Y., H.G., A.B., J.-M.B., G.F., E. Baudin, E. Bocquillon., E.H.T.T., and B.P. participated to the data analysis.
- H.G., D.C., and M.O.G. participated to the theory part.
- B.P. wrote the manuscript with contributions from the coauthors.

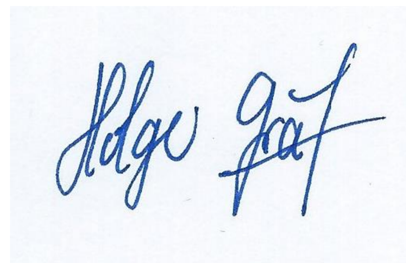

25/07/2019

. . . .
Date

. . . .
Holger Graef

Abstract

This thesis addresses the physics of non-interacting and interacting Dirac fermions in ballistic graphene. Three main phenomena are investigated: Dirac fermion optics in electronic prisms defined by p-n junctions, GHz plasmonics in plasma resonance capacitors, and the breakdown of the integer quantum Hall effect (QHBD) by a magnetoexciton instability. Our technology relies on h-BN encapsulated graphene devices characterized by DC to GHz electronic transport and noise.

We first study the total internal reflection of electrons in a gate-defined corner reflector. Both geometric and coherent electron optics effects are demonstrated and the device is shown to be sensitive to minute phonon scattering rates. It is then used as a proof-of-concept for GHz electron optics experiments in graphene.

We introduce top-gated graphene field-effect capacitors as a platform to study ultra-long wavelength plasmons characterized with a vector network analyzer. We simultaneously measure resistivity, capacitance and kinetic inductance. We observe a resonance at 40 GHz with a quality factor of two, corresponding to a plasmon of 100 μm wavelength. This result sets a milestone for the realization of resonant plasmonic devices.

We finally move our attention to the QHBD in a bilayer graphene sample. DC transport and GHz noise measurements show that the elusive intrinsic breakdown field can be reached in graphene. Its signature is an abrupt increase of noise, with a super-Poissonian Fano factor. We propose a magnetoexciton instability scenario as the origin of breakdown.

These results show how progress in sample fabrication has enabled us to study new classes of ballistic devices, to explore new fundamental phenomena and to envision more complex experiments like: time-of-flight measurements of acoustic phonons, characterization of plasmon propagation in bipolar superlattices, or breakdown in single layer graphene. In terms of applications, this thesis paves the way for room-temperature electron optics devices, plasma-resonance-based THz detectors, and improvement of quantum Hall resistance standards.

Résumé

Cette thèse porte sur la physique des fermions de Dirac dans le graphène balistique, sans et avec interactions. Trois phénomènes principaux sont étudiés: L'optique des fermions de Dirac dans des prismes électroniques définis par des jonctions p-n, la plasmonique GHz dans des condensateurs à résonance plasmons, et la rupture de l'effect Hall quantique (en anglais QHBD) dû à l'instabilité de magnetoexcitons. Notre technique est basée sur la caractérisation du transport électronique et du bruit dans les dispositifs de graphène encapsulé dans du nitrure de bore, du continu aux hyperfréquences.

En optique électronique, nous étudions la réflexion totale interne des électrons dans un réflecteur coin défini par des électrodes de grille. On démontre des effets d'optique électronique géométrique et cohérente. Le dispositif est sensible à des taux de diffusion minuscules et donc capable de détecter des phonons à basse température. On l'utilise pour démontrer la faisabilité d'expériences d'optique de fermions de Dirac en régime hyperfréquences.

En plasmonique, nous introduisons les condensateurs graphène à effet de champs en tant que plateforme pour étudier les plasmons de longeur d'onde très grande. Les dispositifs sont caractérisés avec un analyseur de réseau. Nous mesurons simultanément la résistivité, la capacitance et l'inductance cinétique et nous observons une résonance à 40 GHz avec un facteur de qualité de deux, qui correspond à un plasmon d'une longueur d'onde de 100 μm. Ce résultat constitue un pas important vers la réalisation de dispositifs plasmoniques résonnants.

Enfin, à champs magnétiques et électriques croisés forts, nous étudions la rupture de l'effet Hall quantique entier dans un échantillon modèle de graphène bicouche. Le transport en courant continu et le bruit à 5 GHz démontrent que le champ de rupture intrinsèque peut être atteint dans le graphène. La signature du QHBD est un décollage brutal du bruit, avec un facteur de Fano largement superpoissonien. Comme mécanisme collectif de rupture, nous proposons l'instabilité de magnetoexcitons.

Ces résultats montrent comment le progrès dans la fabrication des échantillons a permis d'étudier de nouvelles classes de dispositifs balistiques, d'explorer de nouveaux phénomènes fondamentaux et d'envisager des expériences plus complexes, comme : des mesures du temps de vol des phonons acoustiques, la caractérisation de la propagation d'un plasmon dans un super-réseau bipolaire ou le QHBD dans le graphène monocouche. En termes d'applications, cette thèse ouvre la voie pour l'exploitation de l'optique de fermions de Dirac à température ambiante, la conception de détecteurs THz utilisant la résonance de plasmon, et l'amélioration des standards de résistance basé sur l'effet Hall quantique.

Acknowledgements

First of all, I would like to thank Prof. Cory Dean for accepting to review this manuscript. Furthermore, I thank Prof. Jean-Noël Fuchs and Dr. Rebeca Ribeiro-Palau for being part of the defense committee.

During the last four years, I have heard at least one person comparing a PhD to mountaineering. I don't know if the comparison is adequate, but either way I would like to thank my supervisors Bernard Plaçais and Edwin Teo for being very patient and understanding mountain guides. Merci à Bernard d'avoir été particulièrement présent pendant tous ces (presque) quatre ans de thèse. Grâce à lui, j'ai non seulement appris des tas de choses sur le graphène – et parfois sur les vortex dans l'hélium liquide – mais aussi plus de jeux de mots et d'expressions que ma mémoire sera capable de retenir. Il était toujours à l'écoute quand il y avait un problème, que ce soit physique, technique ou organisatoire, et ensemble nous avons toujours trouvé des solutions. I would like to express my gratitude to Edwin for the warm welcome at NTU and CINTRA, for always being available for discussions, for removing various administrative hurdles and doing his best to get me started quickly in the N2FC cleanrooms. Je remercie aussi Juliette Mangeney et Christophe Voisin d'avoir formé mon équipe de suivi de thèse. Ils étaient tous les deux compréhensifs face aux difficultés organisatoires de la cotutelle et nous ont aidé à trouver des solutions.

Mein Dank geht außerdem an Mark Oliver Goerbig, der es immer geschafft hat, uns als Experimentalphysikern auch die etwas komplizierteren theoretischen Konzepte näherzubringen und der sich mehrfach Zeit genommen hat, mir einige Grundlagen der RPA zu erklären und einige Verbesserungen zu meinem Manuskript beizutragen. An dieser Stelle möchte ich auch Peter Rickhaus danken, einerseits für die gute Zeit auf Konferenzen in Basel, Dresden, Montpellier, Boston und Paris und andererseits für das Korrekturlesen meines Kapitels über Elektronenoptik. Ein ganz besonderer Dank geht an Christoph Stampfer, Luca Banszerus und Zach Winter in Aachen für den Kickstart bezüglich der Fabrikation von Graphen-Bornitrid-Heterostrukturen und die kontinuierliche Versorgung mit Proben. Ohne ihre großzügige Hilfe zu Beginn meiner Doktorarbeit hätte ich wohl wesentlich mehr Zeit erfolglos im Reinraum verbracht.

Je remercie toute l'équipe de la P13 pour une super ambiance et pour le soutien mutuel: Gwendal Fève et Erwann Bocquillon qui m'ont donné beaucoup de bons conseils, Quentin Wilmart de qui j'ai hérité le projet d'optique des fermions de Dirac et qui m'a fourni avec les outils expérimentaux et théoriques pour avoir des résultats plutôt rapidement, Wei Yang qui a fait le travail expérimental du chapitre sur le breakdown, Andreas Inhofer, qui m'a aidé avec les premières campagnes de mesures dans le Janis et Arthur Marguerite, qui avait la gentillesse de me donner son feedback pour plusieurs chapîtres de cette thèse. Je tiens à remercier David Mele pour son aide avec le projet plasmonique. Ce n'est pas pour rien que Bernard nous a appelé la dream team et c'était très enrichissant de faire la microfabrication

et la charactérisation à deux. Shukran à Mohamed Boukhicha, qui m'a aidé plusieurs fois en salle blanche et shukran à Badih Assaf, qui m'a donné beaucoup de conseils utiles et qui a organisé des super soirées de jeux de sociétés. Merci à Rémi qui était deux fois mon voisin de bureau et qui l'a survecu et qui sait toujours où on trouve ce qu'on cherche dans le laboratoire. Je voudrais aussi remercier Jean-Marc Berroir d'avoir toujours assuré un bon cadre de travail et qui nous a aidé plusieurs fois à résoudre des problèmes administratifs et organisatoires, d'abord en tant que directeur du Laboratoire Pierre Aigrain et ensuite en tant que directeur du Département de Physique. Many thanks also to Manohar Kumar, who gave me his valuable feedback on the breakdown chapter, and Hiroshi Kamata, who I had the pleasure to meet at the end of my PhD. Merci aussi aux "nouveaus arrivés" en P13: Hugo Bartolomei, Clément Roussel, Aurélien Schmitt, Damien Fruleux et Alexandre Gourmelon. À ceux qui restent en P13 je souhaite une ambiance aussi bonne que j'ai eu le plaisir d'expérimenter.

Je remercie le groupe d'optique: Christophe Voisin, Emmanuel Baudin, Carole Diederichs, Adrien Jeantet, Romaric LeGoff, Christophe Raynaud, Louis Nicolas, ..., le groupe HQC: Takis Kontos, Audrey Cottet, Matthieu Delbecq, Lauriane Contamin, Federico Valmorra, Matthieu Desjardins, Matthieu Dartiailh, ..., le groupe QElec: Zaki Leghtas, François Mallet, Raphaël Lescanne, Daniela Markovic, ... et le groupe THz: Jérôme Tignon, Sukhdeep Dhillon, Juliette Mangeney, Sarah Houver, Elisa Riccardi, Panhui Huang, ... et les "visiteurs" en P13, Alberto Montanaro et Kokoura Mensah, qui ont tous contribué à une ambiance conviviale et sympathique pendant ma thèse.

At CINTRA and the EEE department, I would like to thank the other members of Edwin's group, Roland Tay, Fei Ni Leong, Tony Tsang, Matthieu Pawlik, Manuela Loeblein, Jinjun JJ Lin, Lin Jing, Eric Wang Hong, Minmin Zhu, Hongling Li, the lab manager Hasman Bin Hassan, the secretary Jing Fei and CINTRA's director Philippe Coquet. Merci aussi à la French Crew: Nicolas Monfret, Nicolas Kossowski, Umar Saleem, Étienne Rodriguez, Ange Maurice, Olivier et Mathieu Cometto, Adrien Glise, Denis Le Goff et Théo Levert qui m'ont tous accueilli chaleureusement à Singapour

I would also like to thank Pankaj Sethi, Ramu Maddu and Prof. Lew Wen Siang at SPMS for sharing their electron beam lithography and ion beam milling equipment with me and for helping me with a series of etching tests. At this point I also express my gratitude to Xinxin Yang at Chalmers Univesity, who characterized our samples in the sub-THz range.

En tant que thèse expérimentale, ce travail n'aurait jamais été possible sans l'aide précieuse des différentes équipes techniques. Dans ce contexte j'aimerais particulièrement remercier Michael Rosticher, José Palomo et Aurélie Pierret, notre équipe salle blanche qui m'a formé à l'utilisation des différents instruments qui ont servi à fabriquer et caractériser mes échantillons. Merci également à Pascal Morfin, Philippe Pace, Anne Denis et David Darson, qui m'ont aidé à améliorer notre station de transfert, José Romer et Georges Cornudet d'avoir reparé la fuite de notre station de mesure, Olivier Andrieu et Florent Perrin d'avoir assuré l'alimentation d'hélium liquide, et à Didier Courtiade, Catherine Gripe, Célia Ruschinzik et Theo Charpentier qui savent à peu près tout faire, si c'est une ligne d'hélium à reparer ou une mezzanine à construire. Merci aussi aux informaticiens Yann Colin et Frédéric Desprez pour leur soutien avec des fichiers perdus, des serveurs à installer etc. Merci à Anne Matignon et Olga Hodges pour leur aide avec les nombreux documents à remplir et d'autres soucis administratifs.

I would like to thank Takashi Taniguchi and Kenji Watanabe for their high-quality hBN,

that they have provided us with throughout my time at ENS and without which the fabrication of large encapsulated samples would not have been possible. Furthermore, I acknowledge fruitful discussions in the cleanroom with Rebeca Ribeiro-Palau, who showed us some tricks for the fabrication of heterostructures.

Merci à Sylvain Massabeau, Raphaël Lescanne, Vincent Vinel et Alexandre Gourmelon qui ont participé à l'organisation du Friday Bar et merci infiniment à Andreas Inhofer, Arthur Marguerite, Adrien Jeantet et Badih Assaf de m'avoir hébergé quand je n'avais plus/pas encore de logement. Merci à LD qui m'a accompagné pendant les premiers pas de cette thèse et qui m'a donné beaucoup d'inspiration, d'énergie et de soutien. Außerdem möchte ich selbstverständlich auch meinen Eltern Christine und Michael und meiner Schwester Ute für die langjährige Präsenz und Unterstützung danken.

Finally, I sincerely apologize to all the people I forgot to mention in the above. Four years are a long time and it is not easy to keep track of all the people that have helped during this period. Of course my gratitude goes out to all my friends in Paris and elsewhere.

Abbreviations

2DEG	two-dimensional electron gas
AFM	atomic force microscopy
ALD	atomic layer deposition
AP	acoustic phonon
BLG	bilayer graphene
BSEH	bootstrap electron heating
CNP	charge neutrality point
CR	corner reflector
CPW	coplanar waveguide
CVD	chemical vapor deposition
DFR	Dirac fermion reflector
EBL	electron beam lithography
EM	electromagnetic
EMP	edge magnetoplasmon
FET	field effect transistor
GFET	graphene field effect transistor
hBN	hexagonal boron nitride
HPP	hyperbolic phonon polaritons
ILLT	inter-Landau-level tunneling
KTT	Klein tunneling transistor
LHe	liquid helium
LL	Landau level
MBE	molecular beam epitaxy
ME	magnetoexciton
OP	optical phonon
PRC	plasma resonance capacitor
PRT	plasma resonance transistor
PSD	power spectral density
QHBD	quantum Hall breakdown
QHE	quantum Hall effect
QUILLS	quasi-elastic inter-Landau-level scattering
RF	radio frequency
RIE	reactive ion etching
RPA	random phase approximation
SLG	single layer graphene
TIR	total internal reflection
TL	transmission line
VNA	vector network analyzer
ZKT	Zener-Klein tunneling

Contents

1 Introduction **1**
1.1 Electronic properties of graphene 8
1.1.1 Atomic structure and tight binding Hamiltonian 8
1.1.2 Low energy Hamiltonian 9
1.1.3 Sublattice pseudospin and chirality 10
1.1.4 Density of states and quantum capacitance 10
1.1.5 Bilayer graphene 11
1.1.6 Comparison with semiconductor 2DEGs 12
1.2 Electronic transport in mesoscopic systems 13
1.2.1 Diffusive transport 13
1.2.2 Field effect 14
1.2.3 Scattering mechanism in graphene 14
1.2.4 Ballistic transport 15
1.2.5 Coherent transport 16
1.3 Noise 16
1.3.1 Voltage noise vs. current noise 16
1.3.2 Thermal noise 17
1.3.3 Shot noise 17
1.3.4 Fano factor 17
1.3.5 $1/f$ noise 18
1.4 The integer quantum Hall effect 19
1.4.1 Hamiltonian 20
1.4.2 Transport 20
1.4.3 IQHE in graphene 22
1.5 Linear response theory: towards many-body physics 23
1.5.1 The Lindhard function 24
1.5.2 The particle hole excitation spectrum 25
1.5.3 The random phase approximation 25
1.6 Plasmons in graphene 27
1.6.1 Unscreened SLG plasmons from RPA 28
1.6.2 Screened SLG plasmons from RPA 29
1.6.3 Comparison of screened/unscreened SLG/BLG plasmons 30
1.7 Magnetoexcitons in a massive 2DEG 32

2 Experimental methods **35**
2.1 Nanofabrication of encapsulated graphene devices 35
2.1.1 Base materials: graphene and hexagonal boron nitride 36
2.1.2 Nanostructured local bottom gates 37
2.1.3 Graphene encapsulation 43
2.1.4 Characterization of encapsulated samples 47
2.1.5 Defining structures 50
2.2 Device characterization 52
2.2.1 The Janis cryogenic probe station 52
2.2.2 VNA measurements 55
2.2.3 Noise measurements 59

3 Dirac fermion optics **63**
3.1 Principles of Dirac fermion optics 64
3.1.1 Snell-Descartes law 64
3.1.2 The critical angle 65
3.1.3 Fresnel relation 65
3.1.4 Klein tunneling 66
3.1.5 Summary 68
3.2 Review of relevant DFO theory and experiments 69
3.2.1 Rectangular barriers 69
3.2.2 Angle-resolved studies 70
3.2.3 Tilted junctions and electronic switches 71
3.2.4 Other DFO studies 73
3.2.5 Conclusion 74
3.3 Modeling the corner reflector 75
3.3.1 Analytical model 76
3.3.2 Ray tracing simulations 79
3.4 Experimental results 81
3.4.1 The reflection effect as a hallmark of geometrical DFO 81
3.4.2 Coherent Dirac fermion optics in a corner reflector 86
3.4.3 Diffusive optics due to acoustic phonon scattering 87
3.4.4 A corner reflector operating at GHz frequency 90
3.4.5 Comparison of all fabricated devices 93
3.5 Conclusion and perspectives 94

4 GHz plasmonics **97**
4.1 Motivation 98
4.2 Transmission line model of graphene plasmons 100
4.3 Literature review 102
4.3.1 GHz spectroscopy in capacitors 103
4.3.2 From THz to GHz plasmons in massive 2DEGs 105
4.3.3 GHz plasmonics in graphene 107
4.4 Modeling the plasma resonance capacitor 109
4.4.1 General complex admittance formula 109
4.4.2 Important limiting cases 110

4.4.3 Electric potential distribution . . . 110
4.4.4 Access resistance . . . 110
4.4.5 Tunable plasmon characteristics in the PRC . . . 110
4.4.6 Modeled spectra and field from resonant to diffusive regime . . . 112
4.5 Experimental results . . . 114
4.5.1 Evanescent waves in a diffusive capacitor . . . 115
4.5.2 Resonance in a quasi-ballistic capacitor . . . 117
4.5.3 70 GHz spectrum with K-connectors . . . 120
4.5.4 Comparison of all PRC samples . . . 122
4.6 Conclusion and perspectives . . . 125

5 Quantum Hall breakdown 127
5.1 HPP cooling revealed by GHz noise thermometry . . . 128
5.2 Dimensional analysis of the breakdown . . . 130
5.3 Short review of quantum Hall breakdown . . . 132
5.3.1 Pioneering studies . . . 132
5.3.2 Bootstrap electron heating . . . 133
5.3.3 Quasi-elastic inter-Landau-level scattering . . . 135
5.3.4 Summary of experiments: from 2DEG to graphene . . . 136
5.4 Experimental results in BLG . . . 139
5.4.1 Scaling of the DC current . . . 142
5.4.2 Scaling of the noise . . . 143
5.4.3 Contact heating . . . 143
5.4.4 The Fano factor as a hallmark of a collective breakdown . . . 144
5.5 Magnetoexciton instability . . . 146
5.6 Conclusion and perspectives . . . 148

6 Appendix 151
6.1 Fabrication recipes . . . 151
6.1.1 Corner reflector devices . . . 151
6.1.2 Plasma resonance capacitor devices . . . 154
6.2 Derivation of PRC formulas . . . 158
6.3 Modifying the corner reflector scattering model . . . 160
6.4 Literature review of graphene plasmonics . . . 161
6.5 More on magnetoexcitons . . . 168
6.5.1 Matrix element of the density operator . . . 168
6.5.2 Lindhard function . . . 171
6.5.3 Effect of the electric field . . . 172
6.6 Dielectric characterization of hBN . . . 173
6.6.1 Permittivity measurements . . . 174
6.6.2 Breakdown measurements . . . 175

Bibliography 177

1 Introduction

The experimental isolation of graphene as a truly two-dimensional electron system in 2004 [1] has brought to life a whole new sub-domain of research in condensed matter physics. Andre Geim and Konstantin Novoselov, the discoverers, were awarded the 2010 Nobel Prize in Physics for their work. Graphene is a single layer of carbon atoms arranged in a honeycomb lattice. Such two-dimensional crystals were long doubted to be stable until their first isolation by the well-known scotch-tape method a.k.a. micro-mechanical cleaving [2]. Alternatively, this material can nowadays be synthesized by epitaxial growth on silicon carbide or by chemical vapour deposition on copper.

Graphene's astonishing material properties include its thinness (obviously) and a very high breaking strength, "establish[ing] graphene as the strongest material ever measured" [3]. Even though it is nearly transparent, it still absorbs light at around 2% per layer, regardless of the wavelength, which means it can be used for photo-detection [4]. In particular, pristine graphene has a very high conductivity, with electronic mobilities of 10^5 cm^2/Vs at room-temperature and 10^6 cm^2/Vs at cryogenic temperatures, preserved even at substantial doping unlike in semiconductor 2DEGs [5].

For *fun*damental physics, a particularly important property of graphene is its band structure, which originates from the honeycomb arrangement of the carbon atoms and was already calculated by Wallace in 1947 [6]: The valence and conduction band touch in two non-equivalent points of the first Brillouin zone, classifying graphene as a semi-metal. Around these points, the dispersion is linear and isotropic, forming the notorious Dirac cones. As a consequence of this, the low-energy Hamiltonian corresponds to the Dirac equation for massless, relativistic fermions. The Fermi velocity is constant on these cones and about 300 times slower than the speed of light (which is still pretty fast for electronics).

Again owing to the honeycomb arrangement, which implies the existence of two independent sublattices, Dirac fermions in graphene exhibit chirality due to an additional quantum number coined pseudospin. The conservation of this pseudospin gives rise to a surprising phenomenon called Klein-tunneling: The transmission probability for Dirac fermions impinging on a potential step is unity at normal incidence, regardless of the step height. [7] Not long

after the discovery of graphene, similar Dirac states were found at the surface of two- [8] and three-dimensional [9] topological insulators and in the bulk of Weyl semimetals [10]. Altogether, these materials are commonly referred to as Dirac matter. Very recently, the discovery of correlated phases in twisted bilayer graphene [11–13] has once again shown that these relatively simple systems continue to surprise us with new, *fun*damental phenomena.

Other 2D materials with crystalline structures similar to graphene have attracted the interest of the research community, like semiconducting transition metal dichalcogenides or hexagonal boron nitride (hBN). The latter is particularly important for graphene devices, since it was found to be a nearly lattice-matched, atomically flat and electrically isolating substrate [14]. Due to the strong inter-layer van der Waals force, it can even by used to pick up graphene flakes without contaminating them with water or polymers, unlike other techniques, enabling the fabrication of very clean and stable graphene samples, reaching electronic mobilities at the intrinsic phonon limit. In material science, the astonishing properties of these materials have motivated the development of new growth methods [15, 16] and the fabrication of new graphene-based materials, like three-dimensional carbon foams [17, 18] for heat dissipation.

For more details about graphene, in particular from a mesoscopic physics point of view, the reader is referred to the review articles [5, 7, 19–21]. This is the third PhD thesis about electronic transport in graphene in the Mesoscopic Physics group at École Normale Supérieure. It was carried out under the supervision of Dr. Bernard Plaçais and follows the works of Andreas Betz (2012) [22] and Quentin Wilmart (2015) [23]. Related works are Andreas Inhofer's 2017 thesis about GHz spectroscopy of topological insulators [24] and Simon Berthou's 2017 thesis about opto-electronic studies on graphene [25]. Part of this work was carried out in the CINTRA laboratory at Nanyang Technological University in Singapore, under the supervision of Prof. Edwin Hang Tong Teo.

Since the introduction of the hBN-encapsulation method to our laboratory in 2016, the typical room temperature mobility of our devices has increased by an order of magnitude. In contrast to the previous works, we were therefore able to explore ballistic transport in graphene and investigate truly intrinsic properties, like Dirac fermion optics, ultra-long wavelength plasmonics and the intrinsic breakdown of the quantum Hall effect, all phenomena that require minimal scattering and the absence of impurities or charge inhomogeneities.

——— * * * ———

This thesis is organized as follows: In this introductory chapter, I will briefly recall the most important properties of graphene from a condensed matter physics point of view, i.e. the band structure, the low-energy Hamiltonian, the density of states and some differences between single and bilayer graphene. Then, the basic notions of diffusive and ballistic transport and of different types of electronic noise will be revisited. After recalling the basic notions of the quantum Hall effect, I will rapidly introduce the random phase approximation and use it to derive the dispersions of collective excitations (plasmons and magnetoexcitons). The overall aim of the introduction is to familiarize the reader with the zoology of "beasts" investigated in chapters 3–5 (non-interacting fermions, plasmons and magnetoexcitons) and to provide a basic toolbox of formulas to follow the discussion of the experimental results.

Methods: Chapter 2 will discuss the experimental methods in two parts: the fabrication of hBN-encapsulated graphene devices and their characterization by electronic transport and noise measurements. In the fabrication part, I will provide details about the nano-patterning of tungsten and gold bottom gates for Dirac fermion optics, about two different encapsulation methods and about the characterization of encapsulated graphene by Raman spectroscopy and atomic force microscopy. Finally, I will explain the patterning of the heterostructures and the deposit of one-dimensional edge contacts. In the characterization part, we will discuss direct current (DC), lock-in and 0–40 GHz vector network analyzer measurements in our Janis cryogenic probe station and noise measurements at GHz frequency in a conventional immersion cryostat. The aim of this methods chapter is to collect all relevant information about the experiments, so that they do not need to be revisited in the results chapters 3–5, which focus on physics instead.

The results chapters are loosely linked, because all three of them constitute fundamental physics studies in quasi-intrinsic graphene-hBN heterostructures both in DC and at GHz frequency. While chapter 3 focuses on non-interacting Dirac fermions and discusses electron-electron interactions only peripherally as a possible explanation for deviations of our experimental observations from the single-particle theory, chapters 4 and 5 both take into account collective excitations, first in the form of plasmons at zero magnetic field and then in the form of magnetoexcitons in the quantum Hall regime. Despite these parallels, the results chapters can be read independently and in arbitrary order. Each of these chapters starts with an introduction to the relevant physical concepts, possibly preceded by a brief motivation, and followed by a literature review so as to establish the context of this work. Each has a conclusion summarizing the main findings and providing perspectives, both from a fundamental physics point of view and for possible applications, which is why a dedicated conclusion chapter was omitted.

Dirac fermion optics: In chapter 3, we will focus on Dirac fermion optics in a graphene corner reflector (CR). While there have been numerous theoretical proposals for electron optics in ballistic graphene, exploiting the refractive nature of gate-induced p-n junctions, the experimental realizations are mostly elusive until now and limited to rather simple geometries and trajectories. Here we investigate the non-trivial geometry of a graphene field effect transistor (FET) with a sawtooth-shaped gate electrode as opposed to a conventional rectangular gate (c.f. fig. 1.1a-b). In the ballistic transport regime, the gate-induced p-n junctions act like interfaces between two optical media, giving rise to reflection and refraction of electrons, where the gate-controlled Fermi level acts as a tunable refractive index. When the electronic prism's refractive index is tuned to high values, total internal reflection (TIR) of charge carriers leads to an increase in device resistance. In this regime, the transmission of the device becomes gate-voltage independent, giving rise to resistance plateaus. At low temperature < 40 K, resistance oscillations superimposed on these plateaus reflect constructive and destructive interference of the back-reflected electrons, see fig. 1.1c. The plateau resistance itself counter-intuitively decreases with increasing temperature, which translates to a residual transmission proportional to the temperature, see fig. 1.1d. In fact, in this TIR regime, the charge carriers undergo multiple round-trips inside of the prism, which makes them susceptible even to small phonon scattering rates, where a scattering event helps the

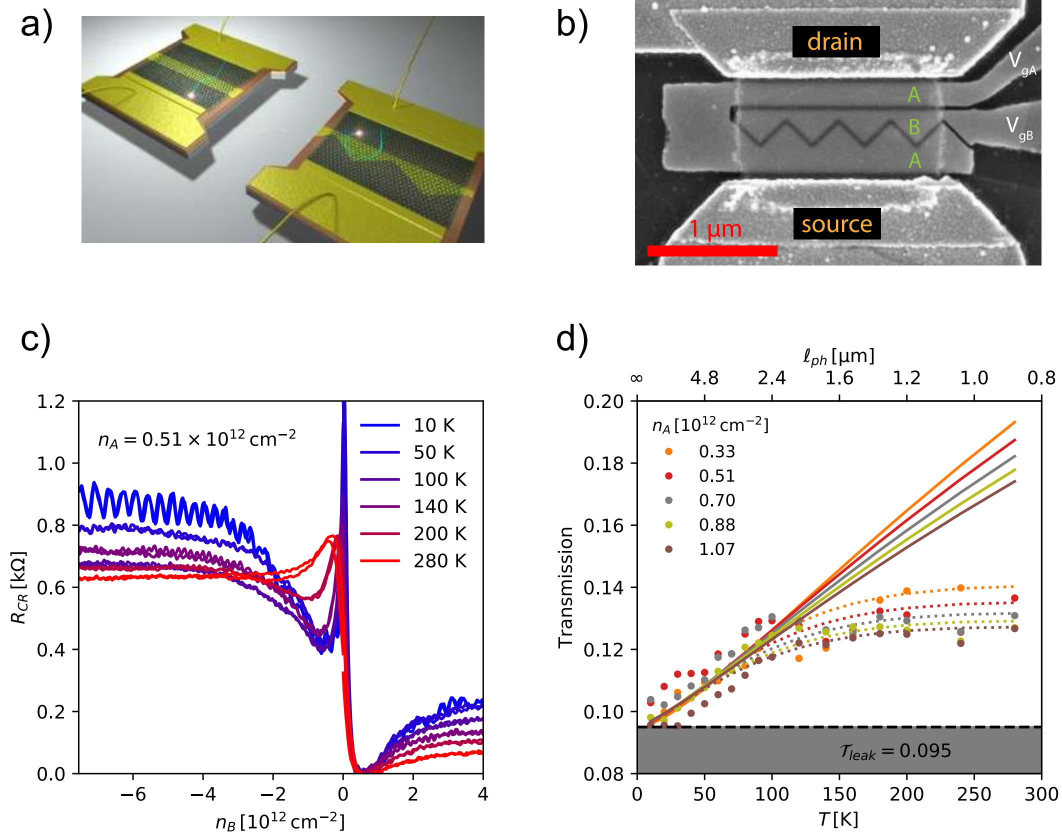

Figure 1.1 – **Dirac fermion optics in a corner reflector.** a) Artist view: rectangular gate vs. prism-shaped gate in a graphene FET. b) Annotated SEM picture of a corner reflector device. hBN-encapsulated graphene appears as a semi-transparent rectangle. Two gate electrodes define the Fermi level in the barrier (B) and in the access (A). c) Device resistance vs. barrier doping for various temperatures. The resistance plateau at $n_B \ll 0$ decreases with increasing temperature. d) Plateau transmission vs. temperature for various access dopings. Solid lines correspond to the analytical model. Dotted lines take into account a temperature-dependent junction length.

electron to be transmitted, as opposed to being back-scattered like in a conventional graphene resistor. For modeling the device transmission, we use both the established ray-tracing approach and a new analytical formula, specific to the 90° apex prism. In the TIR regime, it reads:

$$\langle T_{\mathrm{res}} \rangle = \int_0^{\pi/2} T_1(\theta)[1 - T_1(\theta)]^{\ell_{\mathrm{ph}}/2h} \cos\theta \, d\theta \tag{1.1}$$

where the only inputs are: 1) the angle-dependent transmission of one p-n junction $T_1(\theta)$ and 2) the acoustic phonon mean-free-path ℓ_{ph}. Here h denotes the height of the prism. Making use of our simple theoretical model, we reproduce the experimental data without any adjustable parameters. Finally, I will show that the same type of device can operate at GHz frequency, paving the way for new applications of Dirac fermion optics, for example for the design of fast phonon detectors. In conclusion, chapter 3 demonstrates how geometric,

coherent and weakly diffusive electron optics can be probed in the particular geometry of the corner reflector and how a simple analytical model can be used to quantitatively describe the response of a device with complex trajectories. These results were published in ref. [26].

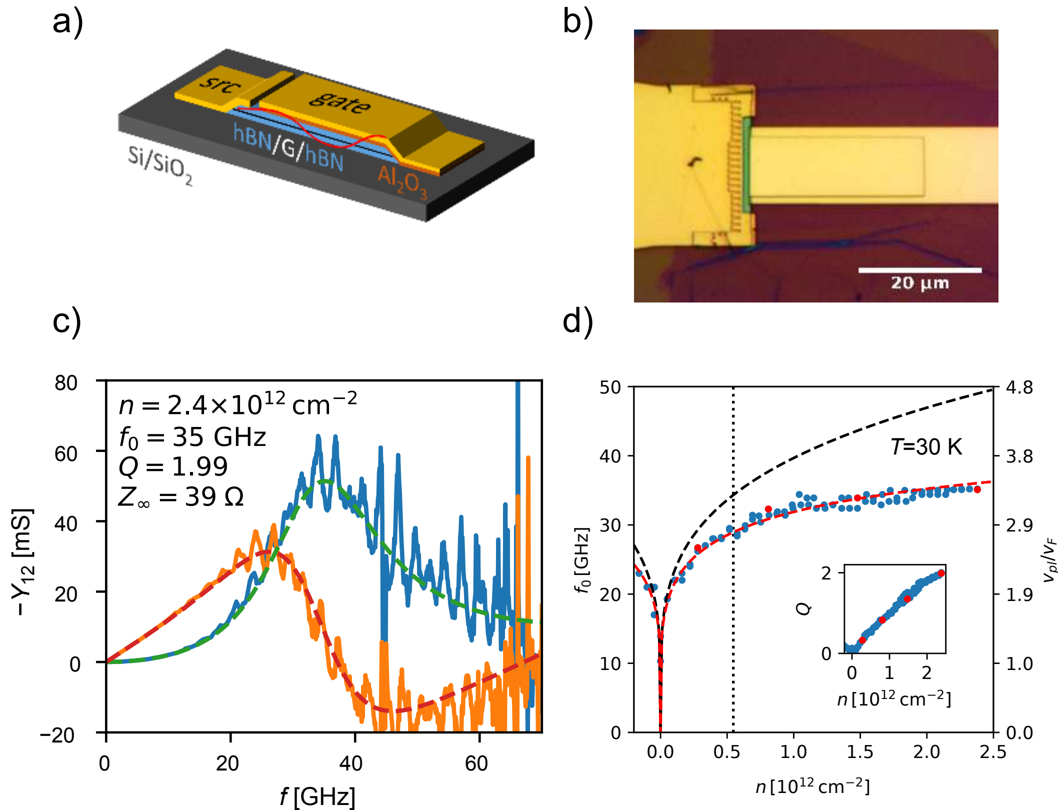

Figure 1.2 – **GHz plasmonics in a plasma resonance capacitor.** a) Artist view and b) microscope image of a PRC ("src" stands for source). The gate electrode is isolated from the graphene edges by an aluminum oxide layer. c) Complex admittance spectrum of a plasma resonance. Blue and orange solid lines are the real and imaginary part of the measured admittance and the green and red dashed lines correspond to a fit. d) Resonance frequency f_0 and quality factor Q from fits vs. carrier density n. Black and red dashed lines correspond to two different theoretical models.

GHz plasmonics: In chapter 4, we will discuss GHz plasmonics in a plasma resonance capacitor (PRC). This work is motivated by the ~ 100 GHz limit of conventional graphene FETs. To move to higher frequencies, a paradigm change is required and plasma resonance devices are suitable candidates, since the plasmon velocity can be much higher than the Fermi velocity. Our sample is a hBN-encapsulated graphene device, contacted on one side by a large, comb-shaped edge contact and covered by a gold electrode, acting simultaneously as a DC gate and as a radio-frequency port (c.f. fig. 1.2a-b). We probe the propagation of microwaves in the PRC by measuring its complex admittance Y with a vector network analyzer. At room temperature, where Ohmic losses are high due to acoustic phonon scattering, the propagation is strongly damped, and admittance spectra typical for evanescent waves are observed in

accordance with previous studies. At cryogenic temperatures, a plasma resonance with a quality factor $Q \sim 2$ can be obtained at $f_0 \sim 40$ GHz by tuning the device to sufficiently large carrier densities, see fig. 1.2c. We fit our experimental data with the following resonator model:

$$Y = jZ_\infty^{-1} \frac{\tan\left(\tilde{f}\sqrt{1-2j/Q\tilde{f}}\right)}{\sqrt{1-2j/Q\tilde{f}}} \tag{1.2}$$

where $\tilde{f} = \pi f/2f_0$ is the reduced frequency and Z_∞ is the characteristic impedance. Measuring and fitting the admittance spectra at different temperatures and carrier densities enables us to map out the parameters f_0, Q and Z_∞ of the resonator (c.f. fig. 1.2d), which can also be represented as parameters of a transmission line model: kinetic inductance, resistance and capacitance. This enables us to measure in one and the same device the most relevant material-specific properties, like the quantum capacitance at low doping or the acoustic-phonon limited mean-free-path, in the simplest device structure one can imagine. While these findings pave the way for smaller device implementations with tunable resonances in the application-relevant THz domain, our device concept also provides a platform for fundamental physics studies, in particular the investigation of the propagation of plasmons in bipolar superlattices. The results of this chapter were published in ref. [27].

Quantum Hall breakdown: In chapter 5, we will move our attention to the breakdown (QHBD) of the integer Quantum Hall effect (IQHE) in a bilayer graphene (BLG) FET. The intrinsic limit of the QHBD is a long-standing issue that has been investigated primarily in semiconductor 2DEGs since the 1980s. However, most of the studies have suffered from sample inhomogeneity, leading to a dramatic reduction of the critical electric field and current density. Our sample is a two-terminal, hBN-supported BLG device with a gold bottom gate electrode, c.f. fig. 1.3a. The breakdown of the IQHE regime is observed as a function of magnetic field at cryogenic temperature. It manifests itself in the DC I-V characteristic as a deviation from the linear Hall regime ($I = G_H V_{ds}$) and in the GHz shot noise measurements – much more dramatically – as an abrupt upsurge from the noiseless ballistic background. Both phenomena are illustrated in fig. 1.3b. The breakdown occurs at extremely high electric fields $\sim 10^6$ V/m, current densities $\sim 10^3$ A/m and drift velocities $\sim 10^5$ m/s, reaching the prediction for the intrinsic Zener breakdown field:

$$E_c = \frac{\hbar\omega_c}{e\ell_B\sqrt{N}} \tag{1.3}$$

where $\hbar\omega_c$ is the cyclotron energy, ℓ_B is the magnetic length and N is the index of the first unoccupied LL. This is in compatibility with the existing quasi-elastic inter-Landau-level scattering theory, but far beyond the predictions of the bootstrap electron heating theory. The combination of transport $I(V)$ and noise $S_I(V)$ measurements allows for the determination of the Fano factor $F = S_I/2eI_{\rm bs}$ (where $I_{\rm bs}$ is the back-scattering current), which provides information about correlations in the breakdown process. A large Fano factor $F \gg 1$ and $F \propto B$ is consistently observed and qualifies the IQHE breakdown as a collective mechanism.

We propose a scenario where breakdown is mediated by the spontaneous proliferation of magnetoexcitons (MEs, see fig. 1.3c), collective inter-LL excitations of the IQHE, in close

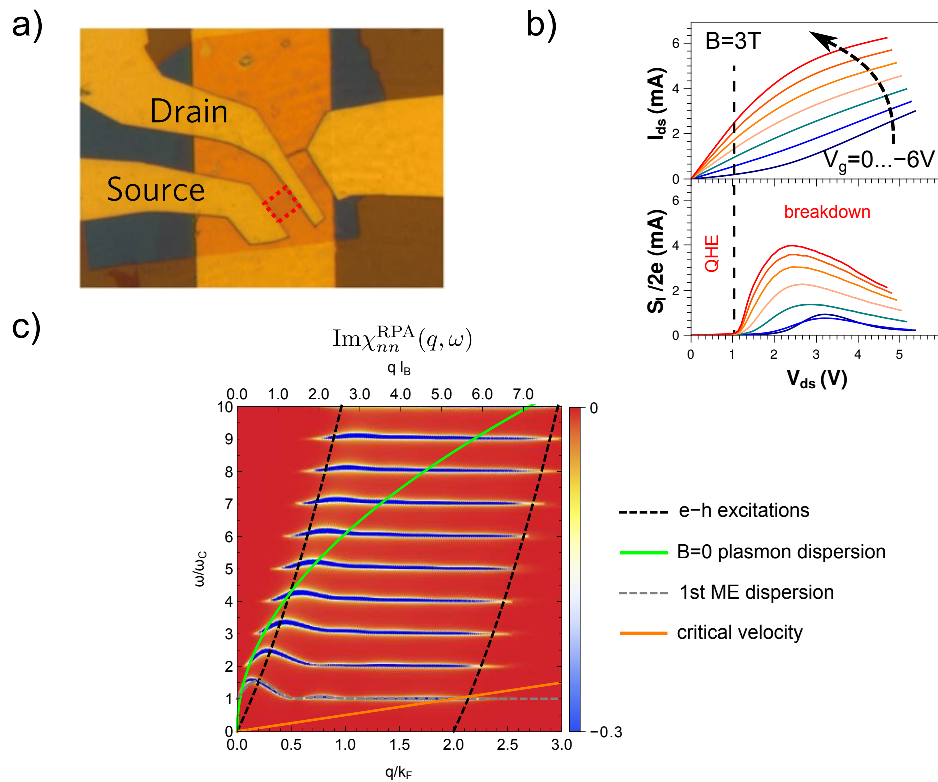

Figure 1.3 – **Quantum Hall breakdown in a bilayer graphene FET.** a) Microscope image of the two-terminal BLG-on-hBN device. The active region ($L \times W = 4 \times 3$ μm) is highlighted by the red, dotted rectangle. b) Top: DC I-V characteristic at fixed B-field for $V_g = 0... - 6$ V. Bottom: Noise (in units of current) vs. bias. The dashed black line marks the onset of the breakdown. c) Imaginary part of the density-density response function in the random phase approximation $\chi_{\mathrm{RPA}}(q,\omega)$, illustrating the existence of collective ME modes at multiples of the cyclotron frequency ω_c. At long wavelengths, these MEs coincide with the $B = 0$ plasmon dispersion (green line). Due to Galilean invariance, they develop an instability when the Landau critical velocity (orange line) is reached.

analogy with the breakdown of the superfluidity of liquid helium by spontaneous emission of rotons. The critical field at which this ME-assisted breakdown occurs is formally identical to the Zener field, but unlike the Zener mechanism, the ME instability naturally explains the strong bunching effect. These experiments introduce pristine graphene devices as a model platform to study the intrinsic QHBD at fields far beyond the typical breakdown values in semiconductor 2DEGs, paving the way for their application as novel resistance standards. From a fundamental physics point of view, it would be interesting to further investigate the QHBD in single-layer graphene, where the energy spectrum of the IQHE is modified due to the massless nature of quasiparticles in this system, and in the fractional quantum Hall regime, where inter-LL magnetoexcitons are replaced by intra-LL magnetorotons. The results presented in this chapter were published in ref. [28].

1.1 Electronic properties of graphene

In the following, I will revisit the most relevant structural and electronic properties of graphene. This section is based on the following review articles and lecture notes, that I recommend for more details: [2, 7, 19]. The aim here is to boil the literature down to the formulas that are essential for chapters 3–5, while keeping in mind the realm of validity of the different approximations.

1.1.1 Atomic structure and tight binding Hamiltonian

Like diamond, graphene is an allotrope of carbon. Others worth mentioning are fullerenes (carbon "footballs", considered 0D) and 1D carbon nanotubes, which are essentially rolled-up sheets of graphene [19]. A very well-known 3D allotrope is graphite, which consists of many stacked graphene layers. In his 1947 paper on the band theory of graphite, Wallace [6] already pointed out that, due to the large separation between the graphite layers (3.37 Å, compared to the in-plane atomic spacing of 1.42 Å), the analysis of a 2D single layer already gives a first approximation to the 3D graphite crystal.

The honeycomb lattice of graphene is illustrated in figure 1.4. This crystalline structure is a result of the sp^2 hybridization of the carbon atoms, leading to the formation of covalent σ bonds between them. The out-of-plane p orbitals, which are not involved in the hybridization, form half-filled π bands [19]. The π electrons can hop from site to site, and therefore conduct electric currents. The band dispersion will be given below.

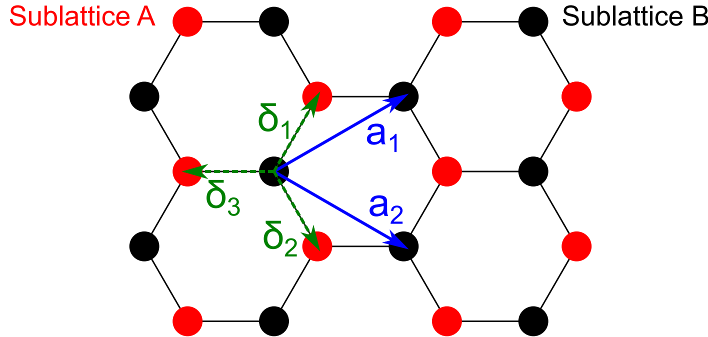

Figure 1.4 – Graphene's honeycomb lattice: A triangular lattice with two carbon atoms per unit cell.

The lattice consists of two non-equivalent, but identical sublattices, denoted A and B in the figure. The distance between two nearest-neighbor carbon atoms (i.e. the length of the vectors $\delta_\mathbf{i}$) is $\delta \approx 1.42$ Å.

In second quantization, the tight binding Hamiltonian is written in terms of creation and annihilation operators as follow:

$$\begin{aligned} H = &- t \sum_{\langle i,j \rangle,\sigma} \left(a^\dagger_{\sigma,i} b_{\sigma,j} + h.c. \right) \\ &- t' \sum_{\langle\langle i,j \rangle\rangle,\sigma} \left(a^\dagger_{\sigma,i} a_{\sigma,j} + b^\dagger_{\sigma,i} b_{\sigma,j} + h.c. \right) \end{aligned} \tag{1.4}$$

where $a^\dagger_{\sigma,i}$ is the creation operator for an electron with spin σ on sublattice A at the site i. Similarly $b_{\sigma,i}$ is the annihilation operator for an electron on sublattice B. The first sum goes over all pairs of nearest neighbors (NNs), where t is the hopping integral, and the second sum goes over all pairs of next-nearest neighbors (NNNs). *h.c.* stands for the Hermitian conjugate. The eigenenergies of this Hamiltonian are given by:

$$\epsilon_\lambda(\mathbf{k}) = \lambda t\sqrt{3+f(\mathbf{k})} - t' f(\mathbf{k})$$
$$\text{with} \quad f(\mathbf{k}) = 2\cos\left(\sqrt{3}k_y\delta\right) + 4\cos\left(\frac{\sqrt{3}}{2}k_y\delta\right)\cos\left(\frac{3}{2}k_x\delta\right) \tag{1.5}$$

where $\lambda = \pm 1$ is the band index. This dispersion is plotted in figure 1.5. In the first Brillouin zone, there are two inequivalent points, denoted $\mathbf{K}$ and $\mathbf{K}'$, where the conduction and valence bands touch.

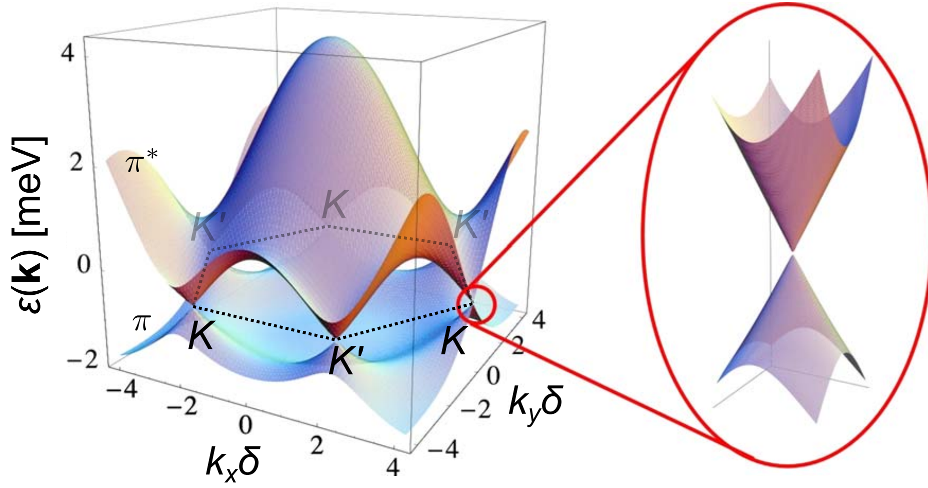

Figure 1.5 – Band diagram of single layer graphene, calculated from the tight binding Hamiltonian. Adapted from [19], where $t = 2.7$ eV and $t' = -0.2\ t$.

1.1.2 Low energy Hamiltonian

As fig. 1.5 suggests, there exists a zone of linear and isotropic dispersion around the points where the two bands touch. Neglecting NNN coupling and linearizing the Hamiltonian around one of these points, one can re-write the effective low energy Hamiltonian in the form of the Dirac equation in two dimensions [19]:

$$-i\frac{3t\delta}{2}\boldsymbol{\sigma}\cdot\nabla\psi(\mathbf{r}) = \epsilon\psi(\mathbf{r}) \tag{1.6}$$

where $\boldsymbol{\sigma}$ is the vector of Pauli matrices σ_x and σ_y and $\psi(\mathbf{r})$ is a spinor wavefunction. To make the linear dispersion directly apparent, this Hamiltonian can be re-written as follows [7]:

$$H_\mathbf{K}(\mathbf{q}) = \hbar v_F \begin{pmatrix} 0 & q_x - iq_y \\ q_x + iq_y & 0 \end{pmatrix} = \hbar v_F \boldsymbol{\sigma}\cdot\mathbf{q} \tag{1.7}$$

where we have introduced the Fermi velocity $v_F = 3t\delta/2\hbar \approx 10^6$ m/s and the new wavevector $\mathbf{q} = \mathbf{k} - \mathbf{K}$. In momentum space, the spinor wavefunctions are given by:

$$\psi_{\lambda,\mathbf{K}}(\mathbf{q}) = \frac{1}{\sqrt{2}} \begin{pmatrix} e^{-i\theta_{\mathbf{q}}/2} \\ \lambda e^{i\theta_{\mathbf{q}}/2} \end{pmatrix} \tag{1.8}$$

where $\theta_{\mathbf{q}} = \arctan(q_y/q_x)$. Taking into account the second order q^2 in the low energy Hamiltonian leads to the so-called trigonal warping of the band structure, reflecting the symmetry of the lattice. It only plays a role at high energies $\epsilon \gtrsim 1$ eV, which are not accessible in transport experiments [2].

1.1.3 Sublattice pseudospin and chirality

The two-component nature of the wavefunction gives rise to a new degree of freedom called (sublattice) pseudospin. It allows for the introduction of the helicity $\hat{h}$, defined as the projection of the momentum $\mathbf{p} = -i\hbar\nabla$ onto the pseudospin direction [19]:

$$\hat{h} = \frac{1}{2}\boldsymbol{\sigma} \cdot \frac{\mathbf{p}}{|\mathbf{p}|} \tag{1.9}$$

The wavefunctions $\psi_{\lambda,\mathbf{K}}$ are eigenfunctions of the helicity operator, and the corresponding eigenvalues are $\lambda/2$ and $-\lambda/2$, respectively. $\hat{h}$ commutes with the Dirac Hamiltonian and the helicity or *chirality* is therefore a conserved quantity close to the Dirac points. A direct consequence of this conservation law is the phenomenon of Klein tunneling: massless Dirac fermions have zero probability of reflection when they are normally incident on a potential barrier, regardless of the barrier height [29, 30].

1.1.4 Density of states and quantum capacitance

In the vicinity of the Dirac point, where the dispersion is linear $\epsilon = \hbar v_F k$, the density of states per unit surface is given by [19]:

$$\rho(\epsilon) = \frac{\partial n}{\partial \epsilon} = \frac{\partial n}{\partial k}\frac{\partial k}{\partial \epsilon} = \frac{2k}{\pi}\frac{1}{\hbar v_F} = \frac{2\epsilon}{\pi(\hbar v_F)^2} \tag{1.10}$$

where we used the fact that a state occupies the volume $(2\pi)^2/L_x L_y$ in two-dimensional k-space and that the states have fourfold degeneracy. A more thorough expression that holds away from the Dirac point can be found in ref. [31].

The density of states is directly linked to the compressibility of the electron fluid. A finite compressibility manifests itself in the capacitance, making it a macroscopically observable quantum effect: Consider a small change of the potential δV across a parallel plate capacitor formed by a graphene sheet and a metallic electrode, separated by a gap d of dielectric constant ϵ_r. On one hand, this causes the "classical" change in *electric* potential $\delta E d$. On the other, it modifies the charge density in graphene, giving rise to a change in *chemical* potential $\frac{\partial \epsilon}{\partial n}\delta n$. The change in number density can be re-expressed in terms of a change in charge density: $\delta n = \delta\sigma/e$. By Gauss' theorem, we can relate the change in electric field and the change in charge density: $\delta E = \delta\sigma/\epsilon_0\epsilon_r$, so that one obtains [32]:

$$\delta V = \frac{\delta\sigma d}{\epsilon_0 \epsilon_r} + \frac{\partial \epsilon}{\partial n}\frac{\delta\sigma}{e^2} \tag{1.11}$$

leading to the following expression for the differential capacitance per unit surface:

$$C = \frac{\delta\sigma}{\delta V} = \left[\left(\frac{\epsilon_0\epsilon_r}{d}\right)^{-1} + \left(e^2\rho(\epsilon)\right)^{-1}\right]^{-1} \tag{1.12}$$

$$= \left[\frac{1}{C_{\text{geo}}} + \frac{1}{C_Q(\epsilon)}\right]^{-1} \tag{1.13}$$

which is a series addition of geometric capacitance C_{geo} and quantum capacitance C_Q. Taking into account the Fermi-Dirac distribution of charge carriers at finite temperature, one obtains [33, 34]:

$$C_Q(\epsilon, T) = \frac{2e^2 k_B T}{\pi(\hbar v_F)^2} \ln\left[2 + 2\cosh\left(\frac{\epsilon}{k_B T}\right)\right] \tag{1.14}$$

At typical doping 10^{12} cm^{-2}, corresponding to a Fermi energy of 117 meV, and temperatures up to ambient conditions where $k_B T \approx 25$ meV, it is reasonable to assume that $\epsilon \gg k_B T$, so that the formula simplifies to the above zero-temperature expression:

$$C_Q(\epsilon \gg k_B T) \approx \frac{2e^2\epsilon}{\pi(\hbar v_F)^2} = e^2\rho(\epsilon) \tag{1.15}$$

At $n = 10^{12}$ cm^{-2}, the value of the quantum capacitance is $C_Q \approx 27$ fF/μm^2. As eq. 1.13 suggests, C_Q only plays a significant role, when it is $\lesssim C_{\text{geo}}$, since in a series addition of admittances, the smallest admittance dominates. This means that quantum capacitance is usually only detected in devices with local gate electrodes, where C_{geo} is sufficiently large (27 fF/μm^2 roughly corresponds to 1 nm equivalent silicon oxide). The energy dependence of the density of states leads to the characteristic dip in the capacitance at the charge neutrality point, which we observe in chapter 4. The measurement of the quantum capacitance can be used to calculate the Fermi level, see e.g. refs. [22, 24].

1.1.5 Bilayer graphene

For bilayer graphene (BLG), one can write a similar Hamiltonian as eq. 1.4, adding additional hopping terms for inter-layer hopping. One finds the following effective Hamiltonian in the vicinity of the **K** point in the first Brillouin zone [19, 35]:

$$H_{\mathbf{K}} = \begin{pmatrix} -V & \hbar v_F q & 0 & 3\gamma_3\delta q^* \\ \hbar v_F q^* & -V & \gamma_1 & 0 \\ 0 & \gamma_1 & V & \hbar v_F q \\ 3\gamma_3\delta q & 0 & \hbar v_F q^* & V \end{pmatrix} \tag{1.16}$$

which is now a 4×4-matrix, acting on wavefunctions that are four-component spinors, for the two sublattices and the two layers, c.f. fig. 1.6a. The potential V accounts for interlayer asymmetry, which can be induced by applying a perpendicular electric field, and the hopping integrals $\gamma_1 \approx 0.4$ eV and $\gamma_3 \approx 0.3$ eV correspond to A–A and B–B interlayer hopping, respectively. A–B (and vice versa) interlayer hopping is neglected here, since the corresponding hopping integral is very small $\gamma_4 \approx 0.04$ eV. The wavevector is a complex quantity, as seen previously for SLG: $q = q_x + iq_y$. When γ_3 is neglected, the resulting energy dispersion for the low energy bands is given by:

$$\epsilon_\lambda(\mathbf{q})^2 = V^2 + \hbar^2 v_F^2 q^2 + \frac{\gamma_1^2}{2} + \lambda\sqrt{(2V\hbar v_F q)^2 + (\gamma_0\hbar v_F q)^2 + \frac{\gamma_1^4}{4}} \tag{1.17}$$

where γ_0 is the in-plane NN hopping integral. In the absence of inter-layer asymmetry, $V = 0$, the dispersion can be re-written as follows [7]:

$$\epsilon_\lambda(\mathbf{q}) = -\lambda m v_F^2 + \lambda m v_F^2 \sqrt{1 + \left(\frac{q}{q_0}\right)^2} \tag{1.18}$$

where $m = \gamma_1/2v_F^2 \approx 0.03 m_e$ is the effective mass and $q_0 = \gamma_1/2\hbar v_F \approx 0.3\ \mathrm{nm}^{-1}$ is the characteristic wavevector, where the dispersion changes from parabolic $\propto q^2$ ($q \ll q_0$) to linear $\propto q$ ($q \gg q_0$). The corresponding threshold energy is $|\epsilon(q_0)| \approx 70$ meV. These hyperbolic bands are shown in fig. 1.6b. Like in single layer graphene, they are electron-hole symmetric and gapless. Two additional bands start at higher energy ($\pm\gamma_1$). If γ_3 is not neglected, the dispersion undergoes trigonal warping. If a finite layer-asymmetry V is taken into account, a gap opens between conduction and valence band, c.f. fig. 1.6c.

In the following, we will use the small q approximation and treat BLG as a gapless, massive 2DEG so that:

$$\epsilon_\lambda(\mathbf{k}) = \lambda \frac{\hbar^2 k^2}{2m} \tag{1.19}$$

which implies for the density of states:

$$\rho(\epsilon) = \frac{\partial n}{\partial k}\frac{\partial k}{\partial \epsilon} = \frac{2k}{\pi}\frac{m}{\hbar^2 k} = \frac{2m}{\pi\hbar^2} \tag{1.20}$$

which is energy independent, like for conventional semiconductor 2DEGs. The quantum capacitance is therefore also energy independent: $C_Q = e^2\rho \approx 40\ \mathrm{fF}/\mu\mathrm{m}^2$.

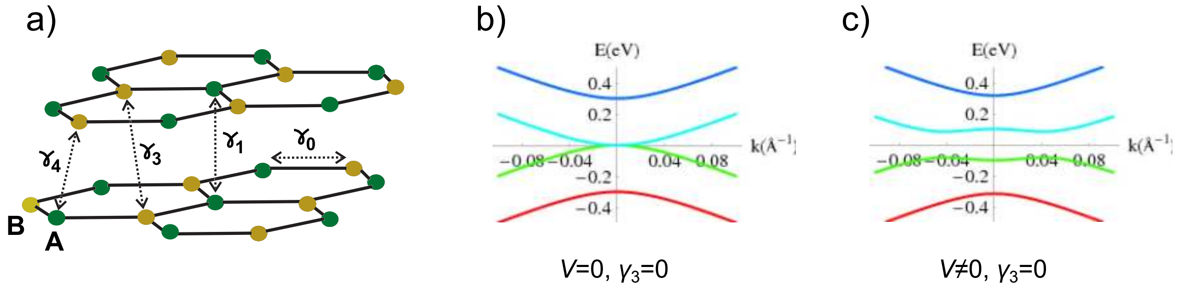

Figure 1.6 – **Bilayer graphene.** a) Crystal structure with hopping integrals $\gamma_1 ... \gamma_4$. From [36]. b) Band structure of BLG at zero and c) finite inter-layer asymmetry. From [19].

1.1.6 Comparison with semiconductor 2DEGs

When comparing graphene to a semiconductor 2DEG like for example GaAs/AlGaAs, there are a couple of significant differences [7]:

- **Confinement.** While the confinement in the third dimension is finite in semiconductor 2DEGs, giving rise to confinement sub-bands, graphene's two-dimensional crystal structure provides a genuine 2D environment for the electrons.
- **Dispersion.** The linear dispersion of SLG (and BLG at sufficiently strong doping) is in strong contrast with the parabolic dispersion of semiconductor 2DEGs. Consequently, the cyclotron mass and the density of states depend on the Fermi level in graphene, while the Fermi velocity is constant.

- **Gap.** Semiconductor 2DEGs have a large band gap $\gtrsim 1$ eV, while graphene is a gapless semimetal (except bilayer graphene in a strong electric field). This means that we can tune continuously from electron to hole doping in graphene, but not achieve a real insulating state.

- **Chirality.** Fermions in graphene exhibit chirality, which leads to interesting phenomena like Klein tunneling, i.e. the absence of back-scattering. The strong impact of this will be nicely visualized and compared to the 2DEG in the susceptibility maps in fig. 1.12.

1.2 Electronic transport in mesoscopic systems

In this section, we will revisit the very basics of diffusive and ballistic transport. The point is mainly to recall the expressions for the conductivity of a diffusive graphene sheet and its gate dependence for chapter 4, to list various known scattering mechanisms and their density-dependence and finally to introduce basic notions of ballistic transport for chapters 3 and 5.

1.2.1 Diffusive transport

The conduction in a disordered conductor can be described by the well-known Drude model: [37] For an electron in a spatially uniform and static electric field $\mathbf{E}$, and in the absence of magnetic field, the rate of change of the *average* momentum is given by:

$$\frac{d\langle \mathbf{p}(t)\rangle}{dt} = e\mathbf{E} - \frac{\langle \mathbf{p}(t)\rangle}{\tau} \tag{1.21}$$

where τ denotes the collision rate and e is the electron charge. In the steady state $d\langle \mathbf{p}(t)\rangle/dt = 0$, one obtains $\langle \mathbf{p}\rangle = e\mathbf{E}\tau$ or equivalently, for the *drift* velocity:

$$\mathbf{v_d} \equiv \langle \mathbf{v}\rangle = \frac{\langle \mathbf{p}\rangle}{m} = \frac{e\tau}{m}\mathbf{E} = \mu\mathbf{E} \tag{1.22}$$

where μ is the mobility of the charge carriers and m their effective mass. By re-expressing this equation in terms of the current density $\mathbf{j} = ne\mathbf{v_d}$, where n is the charge carrier density, we obtain Ohm's law:

$$\mathbf{j} = \frac{ne^2\tau}{m}\mathbf{E} = \sigma\mathbf{E} \tag{1.23}$$

where the proportionality factor between the current density and the electric field is the conductivity σ, which is linked to the mobility by $\sigma = ne\mu$. Whereas charge carriers in massive 2DEGs (with parabolic dispersion) have a constant effective mass, the cyclotron mass in single layer graphene (SLG) depends on the Fermi level [19]: $m^* = \hbar k_F/v_F$. The link between mobility and the scattering time $\mu = e\tau/m$ can therefore be re-written in the case of SLG:

$$\mu = \frac{ev_F\tau}{\hbar k_F} = \frac{e}{\hbar k_F}\ell_{\mathrm{mfp}} \tag{1.24}$$

leading to the following link between conductivity and mean free path:

$$\ell_{\mathrm{mfp}} = \frac{h\sigma}{2e^2 k_F} \tag{1.25}$$

which we will use in chapter 4. A more rigorous approach to transport, taking into account external fields, diffusion and temperature gradients, requires solving the Boltzmann equation. For more details on this, the reader is referred to the book by Ashcroft & Mermin [37]. The specific case of Boltzmann transport in graphene is also covered in the review by Neto *et al.* [19].

Taking into account a non-uniform carrier density $n(\mathbf{x})$, the net current density has an additional diffusive contribution: $\mathbf{j} = \sigma(\epsilon)\mathbf{E} - eD(\epsilon)\nabla n(\mathbf{x})$, where $D(\epsilon)$ is the diffusion constant at the chemical potential ϵ. At equilibrium, we have $\mathbf{j} = 0$ and $\nabla[\epsilon(\mathbf{x}) - eV(\mathbf{x})] = 0$, where V is the electric potential. This leads to the Einstein relation: [37]

$$\sigma(\epsilon) = e^2 D(\epsilon)\frac{\partial n}{\partial \epsilon} = C_Q(\epsilon)D(\epsilon) \tag{1.26}$$

which establishes a link between conductivity, quantum capacitance and the diffusion constant. In GHz-spectroscopy of capacitors (see chapter 4), the former two can be measured in order to calculate the latter. [22, 38]

1.2.2 Field effect

When a gate electrode is brought close to a graphene sheet, so that the gate and the graphene form a parallel plate capacitor with plate separation d, the voltage V_g applied between the two can be used to modulate the carrier density n in the graphene sheet:

$$n = \frac{C(V_g - V_0)}{e} \tag{1.27}$$

where C is the capacitance per unit surface and V_0 is a shift of the charge neutrality point due to chemical doping of the graphene. This shift can be determined by identifying the gate voltage where either the conductivity or the capacitance (see section 1.1.4) is smallest. Note that C is in general a series addition of the geometric capacitance $C_{\text{geo}} = \epsilon_0\epsilon_r/d$ and the quantum capacitance $C_Q(n, T)$ introduced in section 1.1.4. We can thus tune the carrier density and therefore the conductivity $\sigma \propto n$ of our system. By measuring the slope $\partial\sigma/\partial n$, one can determine the *field-effect mobility* $\mu = \partial\sigma/\partial n/e$ in a diffusive system.

1.2.3 Scattering mechanism in graphene

By re-expressing eq. 1.25 we can find the following link between conductivity and the collision time in SLG:

$$\sigma = \frac{k_F e^2 v_F \tau}{\pi\hbar} \propto k_F\tau \tag{1.28}$$

Note that the same result can be obtained using the Einstein relation (eq. 1.26) with $C_Q \propto k_F$ and $D \propto \tau$. This implies that the mobility is $\mu \propto k_F^{-1}\tau$. Taking into account the relation $k_F = \sqrt{\pi n}$ and considering various theoretical calculations of the scattering times induced by the different scattering mechanisms, we list the carrier-density- and Fermi-wavevector-dependence of the mobility and conductivity in table 1.1.

Note that electron-electron scattering (see e.g. [46]) was not included in this list, since it is not directly measurable in a typical (no constrictions) transport experiment, because the overall electron momentum is conserved. Optical phonon (OP) scattering is not listed either, since OPs are gapped with $\omega_{\text{OP}} \approx 200$ meV [7] and only play a role at high bias.

Mechanism	Scattering time	Mobility	Conductivity	Reference
Acoustic phonons (EP)	$\tau \propto k_F^{-1}$	$\mu \propto n^{-1}$	$\sigma \propto$ const.	[39]
Local impurity	$\tau \propto k_F^{-1}$	$\mu \propto n^{-1}$	$\sigma \propto$ const.	[40]
Local impurity	$\tau \propto \ln(k_F) k_F^{-1}$	$\mu \propto \ln(n)/n$	$\sigma \propto \ln(n)$	[41]
Dirac mass disorder	$\tau \propto$ const.	$\mu \propto n^{-1/2}$	$\sigma \propto \sqrt{n}$	[42]
Charged impurity	$\tau \propto k_F$	$\mu \propto$ const.	$\sigma \propto n$	[43]
Resonant scattering	$\tau \propto k_F \ln^2(k_F)$	$\mu \propto \ln^2(n)$	$\sigma \propto n \ln^2(n)$	[44]
Ripples	$\tau \propto k_F^{2H-1}$	$\mu \propto n^{H-1}$	$\sigma \propto n^H$	[45]
Acoustic phonons (BG)	$\tau \propto k_F^2$	$\mu \propto \sqrt{n}$	$\sigma \propto n^{3/2}$	[39]

Table 1.1 – Adapted from [22, 38] and amended with mobility column and acoustic phonons in the equipartition (EP) regime. The "exponent H characterizes the fractal dimension of ripples" [45].

For acoustic phonon (AP) scattering, there are two distinct regimes, roughly separated by the Bloch-Grüneisen (BG) temperature $\Theta_{\mathrm{BG}} = 2\hbar v_s k_F / k_B \approx 54\sqrt{n}$K, where $v_s \approx 2\times10^4$ m/s is the speed of sound in graphene and n is in units of 10^{12} cm^{-2} [39]. Above this temperature, in the equipartition regime, the AP scattering rate is $\propto T$, whereas in the BG regime, it is $\propto T^4$. An experimental study by Efetov & Kim [47] has shown that the linear regime is valid down to about $0.2\Theta_{\mathrm{BG}}$. AP scattering in the equipartition regime is discussed in chapters 3 and 4.

1.2.4 Ballistic transport

If the sample size L is comparable to or smaller than the mean free path ℓ_{mfp} of the electrons, one can no longer model the sample conductance as an average over many scattering events. In this regime of *ballistic* transport, the two-terminal conductance of a device is given by the Landauer formula [48]:

$$G = \frac{ge^2}{h} M \langle T \rangle \tag{1.29}$$

where g is the degeneracy (4 in graphene), e^2/h is the quantum of conductance, M is the number of transverse modes and $\langle T \rangle$ is the transmission probability averaged over these modes. We can count them by considering periodic boundary conditions in the y-direction, so that: $m\lambda_y = W$, where W is the width of the rectangular channel. Taking into account positive and negative k_y, one obtains the total number of modes $M = k_F W/\pi$ [48]. In chapter 3, we refer to the minimum resistance ($\langle T \rangle = 1$) of a two-terminal device as the Landauer resistance R_L.

When we model the corner reflector in chapter 3, we calculate the angle-averaged transmission of the device. Considering a uniform distribution of the incident transverse modes, a factor of $\cos\theta$ needs to be taken into account in the integral:

$$\int_0^{k_F} T(k_y) dk_y = \int_0^{\pi/2} T(\theta) \cos\theta \; d\theta \tag{1.30}$$

For the interpretation of measurements on devices with more than two terminals, one can

rely on the Büttiker formalism [48]:

$$I_p = \sum_q G_{pq} \left[V_p - V_q \right] \tag{1.31}$$

where I_p is the current injected at terminal p and V_p, V_q are the voltages at terminals p and q, respectively. The conductance G_{pq} is given by the Landauer formula $G_{pq} = (ge^2/h)\bar{T}_{p \leftarrow q}$.

1.2.5 Coherent transport

If the electrons maintain their phase coherence during transport, they can undergo interference. If this happens in a disordered conductor, it gives rise to universal conductance fluctuations, i.e. variations of the conductance on the order of e^2/h between samples due to random differences in the disorder. This is the electronic transport equivalent of laser speckle patterns [49].

If transport is phase-coherent in a ballistic conductor, it can give rise to Fabry-Pérot resonances due to p-n junctions or contacts acting as mirrors, see refs. [50–52] and chapter 3 for examples in graphene. If disorder and phonons are excluded as pathways to lose coherence, electron-electron interactions define the phase-relaxation time [48]. A rigorous expression for this time is provided in ref. [53], but for the sake of simplicity, one can derive a very simple formula using dimensional analysis: $\hbar/\tau_\phi \sim k_B T/\pi$.

1.3 Noise

Fluctuations or noise are random deviations of physical quantities from their mean values. In the case of electronic systems, the physical quantities in question are typically the electric current or the voltage. Measuring these fluctuations can provide valuable information about the dynamics of the charge transport or it can be used to measure the temperature of the electronic system. For more details about noise in solids, the reader is referred to the book by Kogan [54] or, more specifically concerning electronic transport in mesoscopic physics, to the review by Blanter & Büttiker [55]. Here I will introduce some basic notions for chapter 5.

1.3.1 Voltage noise vs. current noise

What we measure with a spectrum analyzer or with a digital oscilloscope capable of the fast Fourier transformation (FFT) is the power spectral density (PSD) of the voltage noise [54]:

$$S_{VV} = 2 \int_{-\infty}^{\infty} d(t-t') e^{i\omega(t-t')} \left\langle V(t) V(t') \right\rangle \tag{1.32}$$

which is simply the Fourier transformation of the auto-correlation function. To translate this measured value into current fluctuations within our sample (which we are generally interested in), we have to take into account the impedance of the external circuit R_{ext} in series with our sample so that [55]:

$$S_{VV} = \frac{S_I}{(R_{\text{ext}}^{-1} + R^{-1})^2} \tag{1.33}$$

where R is the sample resistance. This relation is used for the calibration of the noise thermometry setup described in section 2.2.3.

1.3.2 Thermal noise

In a conductor at *equilibrium* and finite temperature, an inevitable fundamental source of fluctuations is the thermal agitation of the charge carriers. This results in so-called Johnson-Nyquist noise, which has the following PSD [54, 56, 57]:

$$S_I(\omega) = 4k_B T \ \mathrm{Re}G(\omega) \approx \frac{4k_B T_0}{R} \tag{1.34}$$

where $G(\omega)$ denotes the complex, frequency-dependent sample admittance and T_0 is the lattice temperature of the sample (in equilibrium with the electron temperature T_e). If we suppose that the sample resistance R does not depend on frequency and that $\omega \ll k_B T/\hbar$ (about 80 GHz at 4 K), the PSD does not depend on frequency and thermal noise can be classified as *white* noise. As an example, the thermal noise PSD generated by a few-mode ballistic conductor ($R \sim 1$ kΩ) at 4 K is $\sim 2\times10^{-25}$ A^2/Hz. At equilibrium, Johnson-Nyquist noise can be used for primary thermometry. We extend the validity of the above formula to out-of-equilibrium situations, where $T_e > T_0$, so that $S_I \gtrsim 4G \ k_B \langle T_e \rangle$, where $\langle T_e \rangle$ is the electron temperature averaged over space. In this context, we define the noise temperature $T_N = S_I/4Gk_B$.

1.3.3 Shot noise

In a *non-equilibrium situation*, another fundamental source of noise is the granularity of the electronic charge. Like rain-drops produce noise when they fall on a tin roof, the electric current contains fluctuations due to this granularity. If the current is mediated by uncorrelated tunneling events with small probability, which obey the *Poisson* distribution, the noise PSD is given by [54, 55, 58]:

$$S_I(\omega) = 2eI \tag{1.35}$$

Like the thermal noise, shot noise is frequency independent (white noise) in the limit $\omega < eV/\hbar$ (about 200 THz at a bias voltage of $V = 1$ V). As an example, the full shot noise generated at a current of 1 mA is 3×10^{-22} A^2/Hz.

1.3.4 Fano factor

The Fano [59] factor $F = S_I/2eI$ is the ratio between the actually observed noise and the Poissonian noise. For example, for an n-channel ballistic conductor, it is given by [55]:

$$F = \frac{\sum_n T_n(1 - T_n)}{\sum_n T_n} \tag{1.36}$$

In a phase-coherent, but strongly disordered mesoscopic conductor, it can be shown that the Fano factor is 1/3 [60]. This is illustrated in fig. 1.7 for samples that are smaller than the inelastic electron-electron scattering length $L_{\mathrm{e-e}}$.

If $L_{\mathrm{e-e}}$ is short enough, electrons can thermalize with each other faster than they thermalize with the lattice through the emission of phonons. This leads to a hot electron population

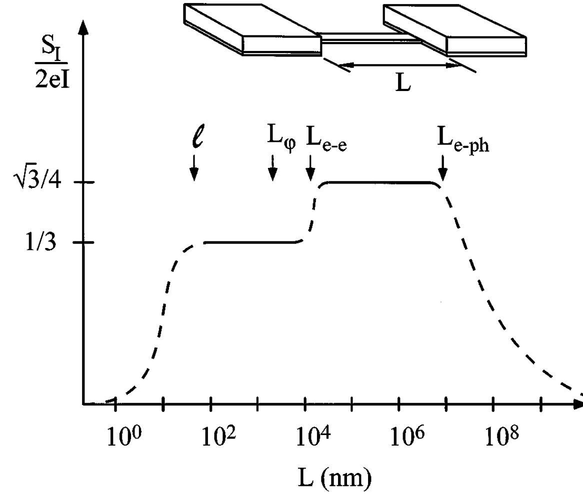

Figure 1.7 – **Fano factor in diffusive mesoscopic systems.** ℓ denotes the elastic mean free path, L_ϕ is the phase coherence length, $L_{\mathrm{e-e}}$ the inelastic electron-electron scattering length, $L_{\mathrm{e-ph}}$ the electron-phonon scattering length and L is the sample size. Figure from ref. [61].

whose main heat drain are the leads, so that one has to define a position-dependent electron temperature $T_e(x)$, where $T_e(0) = T_e(L) = T_0$ is the cold reservoir temperature of the leads. In this case, it can be shown that the noise is proportional to the current with a Fano factor of $\sqrt{3}/4$ [61, 62]. This is also illustrated in fig. 1.7. These Fano factors < 1 lead to sub-Poissonian shot noise. However, there are situations where the Fano factor can be > 1 (super-Poissonian), if there are correlations in the tunneling of the charge carriers [55, 63]. This is what will be discussed in chapter 5.

1.3.5 $1/f$ noise

In practically all studies of the current noise in semiconductors or metals, an excess noise is observed at low frequency. Up to now, the origins of this noise are not fully understood [54]. However, by analyzing a large number of experimental studies on semiconductors and metals, Hooge [64] found the following empirical formula, relating the noise PSD to the total number of charges N carrying the electric current [54]:

$$\frac{S_I}{I^2} = \frac{\alpha_H}{Nf} \tag{1.37}$$

where $\alpha_H = 2\times10^{-3}$ is a constant that Hooge suspected to be universal. Studies in graphene have yielded values for α_H between 2×10^{-4} and 2×10^{-3} [22,65–67] at typical carrier densities $n \sim 10^{12}$ cm^{-2}. The empirical Hooge relation can be used to estimate the "crossover" frequency f_c for shot noise measurements as a function of the current I:

$$\frac{\alpha_H}{Nf_c} I^2 = 2eI \tag{1.38}$$

For graphene samples of typical size 1 μm^2 and carrier density 10^{12} cm^{-2}, one obtains:

$$f_c = 10^{-7} \times \frac{I}{e} \tag{1.39}$$

which means that for the high currents $\sim$ 1 mA considered in chapter 5, the crossover frequency is on the order of 1 GHz, which explains why the noise was measured in this high frequency range. In a previous study [65], the currents were about 10 times smaller at comparable sample sizes and carrier densities, which justifies the smaller measurement bandwidth used in those experiments.

1.4 The integer quantum Hall effect

The classical Hall effect, described by Edwin Hall in 1879 [68], consists in the build-up of a transverse voltage V_H across a conductor carrying a longitudinal current I and exposed to a perpendicular magnetic field $\mathbf{B}$. This voltage builds up due to the Lorentz force $e\mathbf{v_d} \times \mathbf{B}$ felt by the charges carrying the current, where $\mathbf{v_d}$ is their drift velocity. The Hall resistance is defined as the ratio $R_H = V_H/I = B/ne$, where n denotes the charge carrier density. By measuring the slope of $R_H(B)$, one can therefore measure the carrier density and distinguish electron- from hole-conduction.

At strong magnetic fields $B \gtrsim 1/\mu$ (where μ is the carrier mobility), the density of states of the two-dimensional electron gas develops peaks corresponding to highly degenerate Landau levels. These give rise to Shubnikov-de-Haas oscillations in the longitudinal resistivity ρ_{xx} at moderate magnetic fields. Depending on the electronic mobility of the sample, ρ_{xx} is completely suppressed once we reach the quantum Hall regime for $B \gtrsim 2\pi/\mu$. Discovered experimentally in 1980 by von Klitzing *et al.* [69], the quantum Hall effect's characteristics are a not only ballistic longitudinal transport, but also a very accurate quantization (typically within $\sim 10^{-9}$) of the transverse conductivity as multiples of the quantum of conductance ge^2/h, where g takes into account degeneracy. This accuracy is the reason why quantum Hall measurements are used as a resistance standard $R_K = h/e^2 \approx 25.8$ kΩ since 1990 [68] and constitutes today (2019) one of the pillars of the new International System of units [70, 71].

Not long after the discovery of the quantum Hall effect (QHE), the observation of a transverse conductivity with non-integer quantization was reported for the first time in 1982 [72]. While the integer quantum Hall effect is a result of the quantization of the kinetic energy of single electrons, the fractional quantum Hall effect (FQHE) arises from strong Coulomb interactions between electrons [73]. The fractional states require a lot more effort from the theoretical point of view: Depending on the numerator p and denominator q of the fraction $n = p/q$, various theories have been proposed to describe the nature of the corresponding electron liquid [68].

In the following, I will recall the basic notions of the integer quantum Hall effect, from the Hamiltonian to the transverse conductivity, based on the textbooks refs. [32, 48, 74]. The discussion of the FQHE goes beyond the scope of this thesis. In this section, as well as in the introduction of magnetoexcitons in section 1.7, we will ignore the effect of the electric field, which will be discussed in chapter 5.5.

1.4.1 Hamiltonian

The time-independent Schrödinger equation for free electrons (here in two dimensions) of effective mass m_b in the presence of a magnetic field reads as follows:

$$\frac{1}{2m_b}\left[\hat{\mathbf{p}} - e\mathbf{A}(\mathbf{r})\right]^2 \psi(\mathbf{r}) = \epsilon\psi(\mathbf{r}) \tag{1.40}$$

where $\hat{\mathbf{p}} = -i\hbar\nabla$ is the momentum operator and $\mathbf{A}$ is a vector potential, so that $\nabla \times \mathbf{A} = \mathbf{B}$. By choosing an appropriate gauge, e.g. the Landau gauge $\mathbf{A}(\mathbf{r}) = Bx\mathbf{e_y}$, one obtains:

$$\left[-\frac{\hbar^2}{2m_b}\frac{\partial^2}{\partial x^2} + \frac{1}{2m_b}\left(-i\hbar\frac{\partial}{\partial y} - eBx\right)^2\right]\psi(x,y) = \epsilon\psi(x,y) \tag{1.41}$$

By taking into account the independence of the Hamiltonian of y, one can reduce this equation to a one-dimensional problem in the x-direction – corresponding to the Schrödinger equation for a one-dimensional harmonic oscillator – yielding the following eigenstates $\psi_n(x,y)$:

$$\psi_N(x,y) = \frac{1}{\sqrt{L_y}}e^{ik_y y}\chi_{N,k_y}(x) \tag{1.42}$$

$$\chi_{N,k_y}(x) = \frac{\pi^{-1/4}}{\sqrt{2^n n!\ell_B}}e^{-\frac{(x-k_y\ell_B^2)^2}{2\ell_B^2}} H_N\left(\frac{x-k_y\ell_B^2}{\ell_B}\right) \tag{1.43}$$

where L_y is the sample length. This solution describes a plane wave in the y-direction with wavevector k_y and exponential localization in the x-direction, where the localization length is $\ell_B = \sqrt{\hbar/|e|B}$. Here $H_N(x)$ denotes the Hermite polynomial of the N-th order. The typical width of the wave function is then given by the cyclotron radius $R_c = \sqrt{2N+1}\ell_B \approx \sqrt{2N}\ell_B$ (the first expression corresponds to the maximum of the probability density whereas the second expression corresponds to the square root of the expectation value of r^2) [74]. The eigenstates are defined by the quantum numbers N and k_y and the eigenenergies are:

$$\epsilon_N = \hbar\omega_c\left(N + \frac{1}{2}\right) \tag{1.44}$$

where $\omega_c = |e|B/m_b$ is the cyclotron frequency. These discrete energy levels are called Landau levels (LLs). Their degeneracy can be expressed in terms of the magnetic length ℓ_B or the flux quantum $\phi_0 = h/e$:

$$N_L = \frac{L_x L_y}{2\pi\ell_B^2} = \frac{L_x L_y B}{\phi_0} \tag{1.45}$$

1.4.2 Transport

Let us suppose we have filled one or several of the aforementioned LLs with electrons. How can conduction take place if the Fermi level is situated between filled bands? For six- or two-terminal samples like those depicted in figure 1.8a-b, we can explain this in terms of the confinement potential due to the finite sample width: at the sample edges this confinement potential diverges so that all LLs lying below the Fermi level in the bulk cross the latter. If a bias $eV = \mu_L - \mu_R$ is applied across the sample, all states with energy between μ_L and

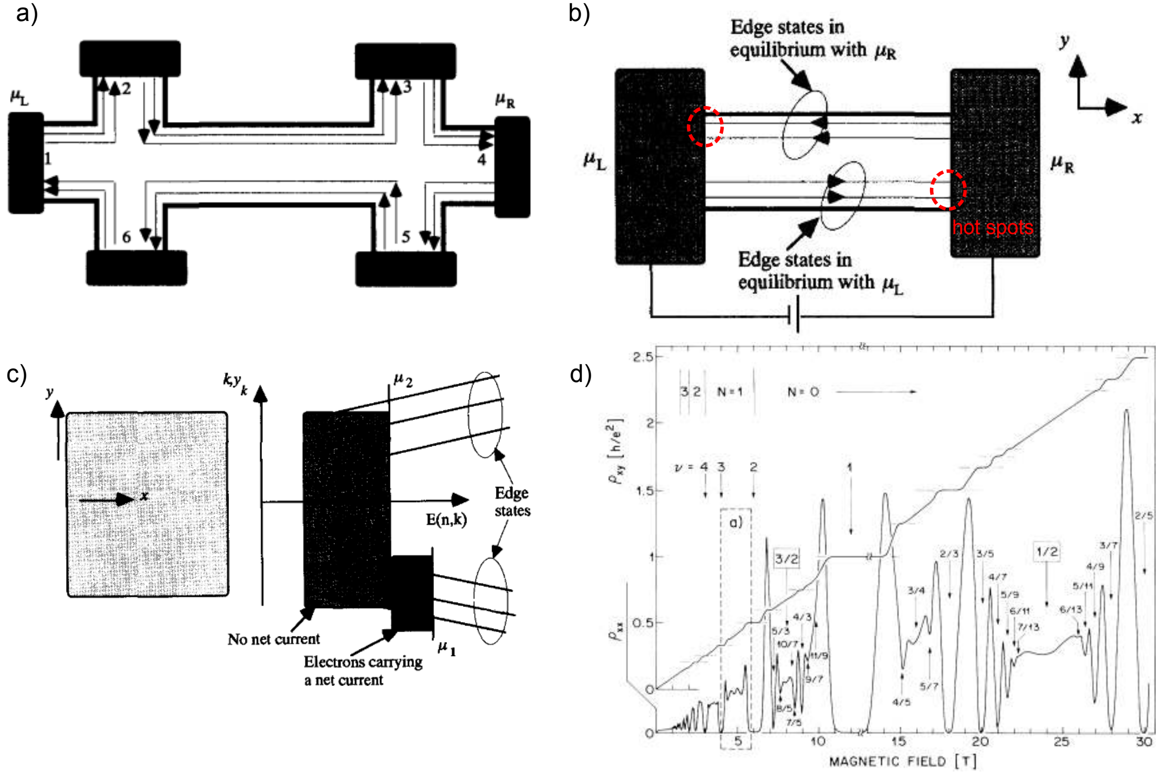

Figure 1.8 – Transport measurements of the QHE. a) Typical Hall bar geometry with six terminals. Current is injected (drained) at terminals 1 (4) and the other terminals serve as voltage probes. b) Two-terminal device with hot spots at the corners. c) Illustration of the current carrying states crossing the Fermi levels due to the confinement caused by the finite sample size. a-c) adapted from [48] d) Typical measurement of longitudinal and transverse resistivity, exhibiting a large number of plateaus corresponding to integer and fractional filling factors. Adapted from [75].

μ_R contribute to the conduction, c.f. fig. 1.8c [48]. This situation is similar to what we have discussed in section 1.2.4 concerning the conductance of a two-terminal device with M transverse ballistic modes, each of which contributing ge^2/h to the overall conductance. In a six-terminal geometry like in fig. 1.8a, one can rely on the Büttiker formula eq. 1.31 to calculate the non-local voltages. The conductance matrix for the device in fig. 1.8a is then

$$G_{pq} = \begin{pmatrix} 0 & 0 & 0 & 0 & 0 & G \\ G & 0 & 0 & 0 & 0 & 0 \\ 0 & G & 0 & 0 & 0 & 0 \\ 0 & 0 & G & 0 & 0 & 0 \\ 0 & 0 & 0 & G & 0 & 0 \\ 0 & 0 & 0 & 0 & G & 0 \end{pmatrix} \tag{1.46}$$

where $G = Mge^2/h$, assuming unity transmission (absence of backscattering). Taking into account that current is only injected and drained at the left and right terminal (1 and 4), so that $I_p = 0 \ \forall p \notin \{1, 4\}$, and that we can arbitrarily choose one of the voltages, so that

$V_4 = 0$, one finds $V_2 = V_3 = V_1$ and $V_5 = V_6 = V_4 = 0$, which means that the longitudinal resistance is:

$$R_{xx} = \frac{V_2 - V_3}{I_1} = \frac{V_6 - V_5}{I_1} = 0 \tag{1.47}$$

whereas the transverse resistance is given by:

$$R_{xy} = \frac{V_2 - V_6}{I_1} = \frac{V_3 - V_5}{I_1} = G^{-1} = R_{2t} \tag{1.48}$$

which is, maybe counter-intuitively, also the resistance R_{2t} measured across a two terminal device like the one illustrated in fig. 1.8. Note that, at low bias, the electric field is parallel to the vertical axis and the top (bottom) of the sample is at equilibrium with the right (left) contact. Since the field is perpendicular to the current flow, there is no dissipation in the sample. However, as the red circles illustrate in the figure, the carriers undergo a potential drop $\mu_L - \mu_R$ when they reach the other side of the device. This is where dissipation can take place, as discussed in section 5.4.3.

Figure 1.8d shows a typical measurement of longitudinal and transverse resistance vs. magnetic field of a GaAs/AlGaAs Hall bar with a mobility $\sim 10^6$ cm^2/Vs [75]. As the magnetic field is swept, the LLs spacing ($\propto B$) is adjusted so that the effective number of LLs below the Fermi level varies. In accordance with the above expressions, at integer filling of the LLs, the longitudinal resistance drops to zero and the transverse resistance forms quantum Hall *plateaus* at $R_{xy} = h/\nu e^2$, where $\nu = N_{\mathrm{el}}/N_L$ is called the filling factor and N_{el} is the total number of electrons. At low B-fields the transverse resistance is linear (corresponding to the classical Hall resistance) and the longitudinal resistance exhibits Shubnikov-de-Haas oscillations. The figure also illustrates a large number of fractional states, thanks to the high electronic quality of this system.

1.4.3 IQHE in graphene

Without writing down the Hamiltonian for relativistic Dirac electrons in a magnetic field, let us only point out the main phenomenological differences to be expected for a magneto-transport experiment in graphene. Due to the exotic band structure of single layer graphene, the Landau level energies are not equidistant like in a massive 2DEG. Instead they are given by [76, 77]:

$$\epsilon_N = \pm\sqrt{2e\hbar v_F^2 N B} \tag{1.49}$$

where positive and negative values are possible due to the gapless nature of the system. Interestingly, this spectrum contains an $N = 0$ state with zero energy, which means that even at low electron or hole doping and strong magnetic fields, the lowest LL is populated. This is sketched in fig. 1.9c, which shows a change of sign of the transverse conductivity σ_{xy} as a function of the density n, here expressed in units of the density of states per LL gB/ϕ_0 (c.f. eq. 1.45), where g is the degeneracy and $\phi_0 = h/e$ is the flux quantum. For a bilayer, the QHE energy spectrum is given by [35, 78]:

$$\epsilon_N = \pm\hbar\omega_c\sqrt{N(N-1)} \tag{1.50}$$

This spectrum has two zero energy states ϵ_0 and ϵ_1 for electron- and hole-doping, respectively. In the conventional massive 2DEG, the lowest LLs have finite energy, so that the lowest LL

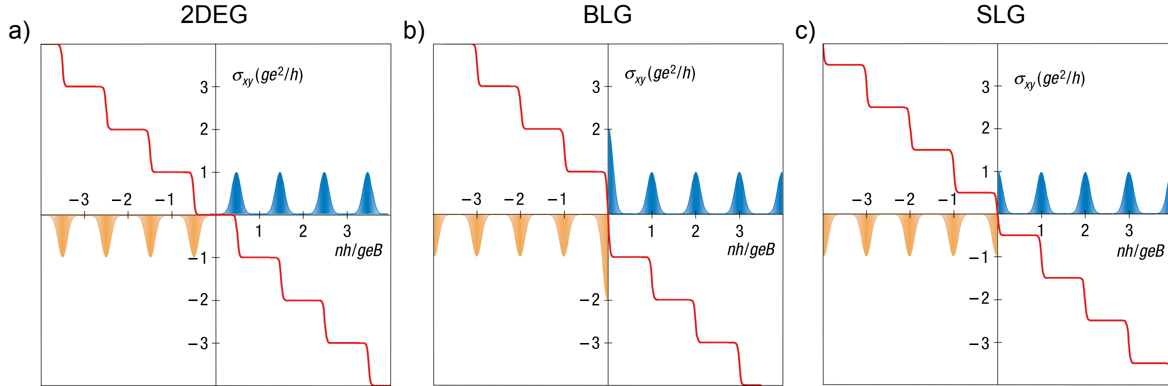

Figure 1.9 – Filling Landau levels in different 2D systems leads to differences in the sequence of transverse conductivity steps. a) In a conventional 2DEG, $g = 2$ and $\sigma_{xy} = 0$ at the origin. b) In BLG, $g = 4$ and there is a $\Delta\sigma_{xy} = 8e^2/h$ jump at the origin. c) In SLG, $g = 4$ and there is a $\Delta\sigma_{xy} = 4e^2/h$ jump at the origin. Figure from [78].

is unfilled (or only partially filled as shown in fig. 1.8d) around charge neutrality or at very high magnetic fields. This is why $\sigma_{xy} = 0$ around the origin in fig. 1.9a. Interestingly, all these systems exhibit equidistant steps of σ_{xy} vs. carrier density n or inverse magnetic field $1/B$, where the step height is $2e^2/h$ for conventional 2DEGs and $4e^2/h$ for single- and bilayer graphene, due to the additional valley degeneracy. The coincidence in energy of the $N = 0$ and $N = 1$ states in bilayer graphene leads to an effective degeneracy of $g = 8$ for the zero-energy level, leading to a step height of $8e^2/h$ at the origin in fig. 1.9b.

Figure 1.10 shows recent (2019) examples for magnetotransport measurements in high-quality hBN-encapsulated graphene with graphite gates, both in a Corbino- [80] and in a Hall-bar-geometry [79]. The sample design ensures extremely well-defined potential landscapes and a large number of fractional quantum Hall states can be resolved. Note that the large minima of σ_{xx} and plateaus of σ_{xy} at filling factors $\nu = 2$ and $\nu = 6$ in fig. 1.10d are specific to the case of SLG, as was pointed out above (see also fig. 1.9c). The particular geometry of the Corbino-disk, not discussed in the above, implies that there are no edge states linking the source and drain terminals. In comparison to the case of a rectangular channel illustrated in figure 1.8b, this leads to a marked difference in the two-terminal conductance: G_{xx} vanishes at well-defined filling of the LLs, as shown in fig. 1.10b.

In chapter 5, we will investigate the breakdown of the IQHE in BLG over a large range of densities, magnetic fields and filling factors. Here, BLG will act as a model system for massive 2DEGs and we will use the corresponding formalism, keeping in mind that in the large N limit, the spinorial character of the BLG wavefunctions loses its relevance and that the energy spacing of the LLs (relevant for the breakdown) is equivalent between 2DEG and BLG.

1.5 Linear response theory: towards many-body physics

For proper introductions on linear response theory in many-body physics, the random phase approximation and more, the reader is referred to the books by Giuliani & Vignale [32] or Coleman [81]. In the following, I will only provide the most crucial elements required to

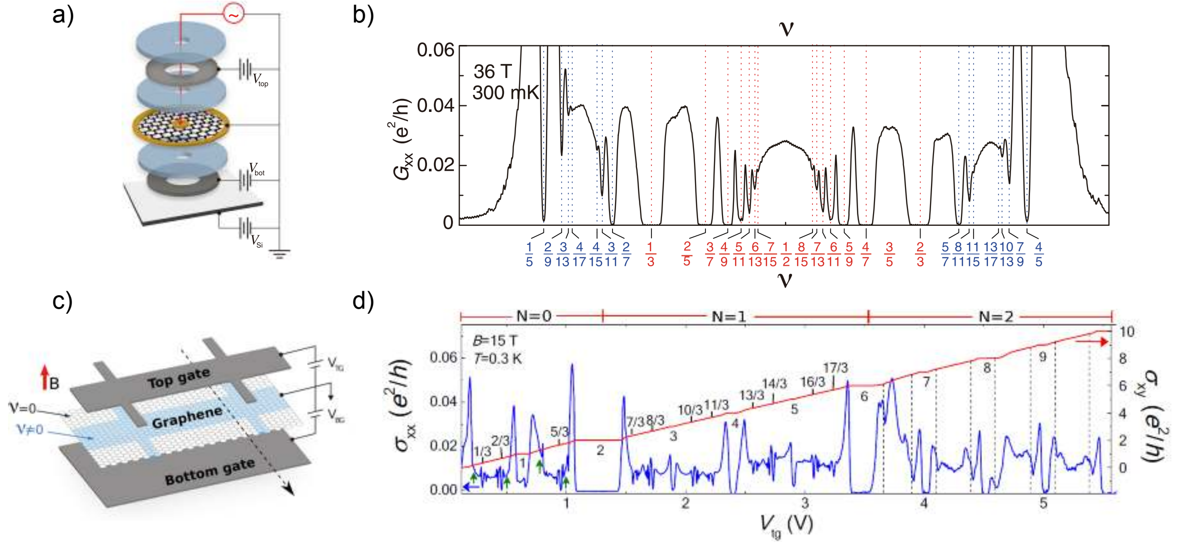

Figure 1.10 – **FQHE in graphite-gated graphene.** a+c) Artist view of a Corbino disk and a Hall bar with top and bottom graphite gate. b+d) Corresponding magnetotransport charts of the longitudinal conductance, demonstrating that a large number of fractional filling factors can be resolved in these samples. From refs. [79, 80].

understand how the graphene plasmon dispersion can be calculated using RPA and how the calculation of the RPA-susceptibility of the 2DEG in a strong magnetic field gives rise to magnetoexcitons.

1.5.1 The Lindhard function

Within linear response theory, the causal response of an observable $\hat{A}$ of a system to a time dependent field that couples linearly to another observable $\hat{B}$ of the system is given by the retarded linear response function χ_{AB}. In the case of a periodic perturbation with frequency ω, the *Lehmann* representation (or *exact eigenstates representation*) of this response function is defined as follows in terms of the eigenstates ψ_n of the system [32]:

$$\chi_{AB}(\omega) = \frac{1}{\hbar} \sum_{m,n} \frac{P_m - P_n}{\omega - \omega_{nm} + i\eta} A_{mn} B_{nm} \tag{1.51}$$

where $\omega_{nm} = \omega_n - \omega_m$ is the energy difference between the two states, $\eta \to 0^+$ (a finite η represents level broadening due to disorder), $A_{mn} \equiv \langle \psi_m | \hat{A} | \psi_n \rangle$ and similarly for B_{nm} and P_n is the equilibrium population of the state ψ_n (for fermions this is simply the Fermi-Dirac distribution, which can be replaced by a Heaviside step function at zero temperature). In order to study the response at a point $\mathbf{r}$ of a charge distribution to a periodic *external* electric potential at a point $\mathbf{r}'$, we need to calculate the *density-density* response function. For a homogeneous, translation-invariant system, this is given by the following expression in Fourier space:

$$\chi_{nn}(\mathbf{q}, \omega) = \frac{1}{\hbar L^d} \sum_{nm} \frac{P_m - P_n}{\omega - \omega_{nm} + i\eta} \left| \langle n | \hat{n}(\mathbf{q}) | m \rangle \right|^2 \tag{1.52}$$

which is also known as the *Lindhard* function [32,82]. Here $\hat{n}(\mathbf{q})$ is the single-particle number-density operator in momentum space:

$$\hat{n}(\mathbf{q}) = e^{-i\mathbf{q}\cdot\hat{\mathbf{r}}} \tag{1.53}$$

At zero temperature, the imaginary part of the response function is directly proportional to the dynamical structure factor $S = -\frac{\hbar}{\pi}\mathrm{Im}\chi_{nn}$, which represents the absorption spectrum for positive frequency and the stimulated emission spectrum for negative frequencies. In the case of our density-density susceptibility the dynamical structure factor corresponds to the particle hole excitation spectrum (PHES) [32].

1.5.2 The particle hole excitation spectrum

Figure 1.11 is an illustration of the possible and forbidden particle-hole excitations in graphene, both at zero doping (panel 1) and at finite electron doping (panels 2 and 3). In the following, we will discuss the dynamical structure factor, i.e. the particle-hole excitation spectrum (PHES), for the doped case.

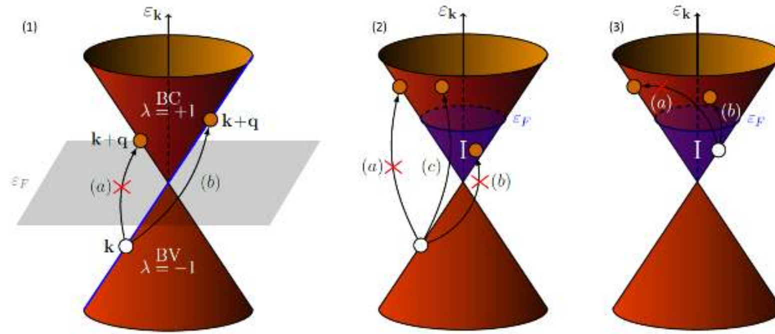

Figure 1.11 – Single particle excitations in undoped (1) and doped (2+3) graphene. BC and BV denote the conduction and valence band, respectively. Taken from [83].

The PHES is plotted in the two top panels of figure 1.12 for SLG and for a standard massive 2DEG, with the Fermi level lying in the conduction band in both cases. A marked difference is that in the 2DEG, the spectral weight is significant within the entire region of authorized intraband transitions ($q^2 - 2k_Fq < \frac{2m\omega}{\hbar} < q^2 + 2k_Fq$), whereas in graphene, it is concentrated on the line $\omega = v_Fq$ (c.f. process b in panel 3 of fig. 1.11). This is a direct consequence of the conservation of pseudospin, which forbids back-scattering (c.f. process a in fig. 1.11).

Due to the Pauli exclusion principle, which forbids the excitation of an electron towards an already occupied state (c.f. process b in the second panel of fig. 1.11), we can define a gap region (**I** in the figure, for $v_Fq < \omega < 2\mu - v_Fq$), where the spectral weight is exactly zero. Region **II** corresponds to interband transitions.

1.5.3 The random phase approximation

In order to take into account interactions *between* particles, i.e. the response to *internal fields*, a first approach would be to write down the Hamiltonian for an independent particle

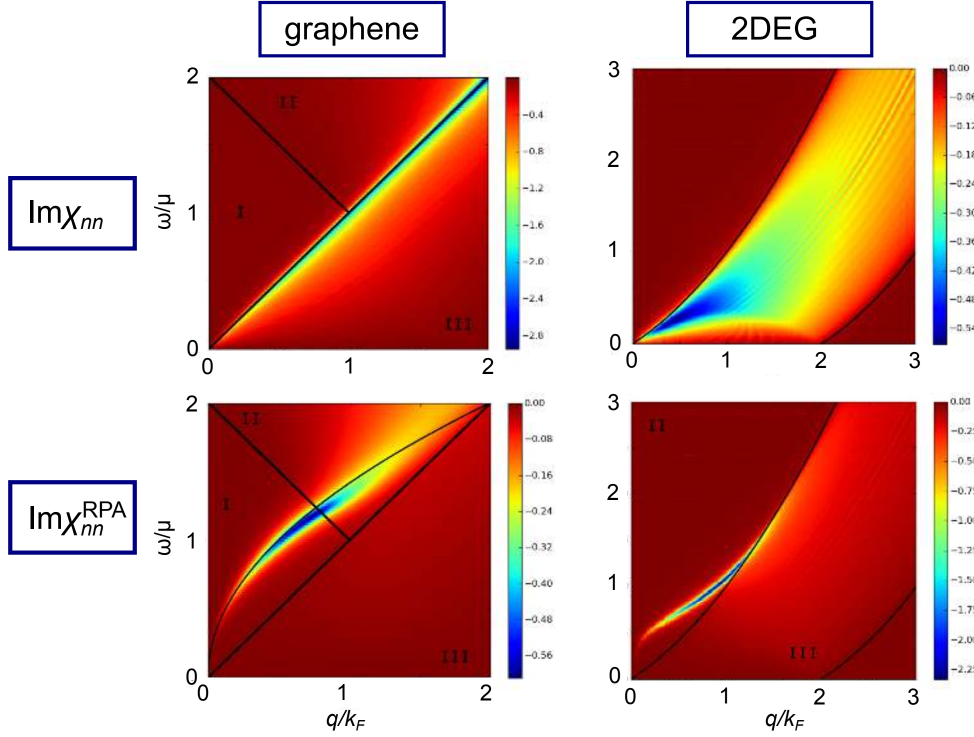

Figure 1.12 – Spectral density for the non-interacting (top row) and the interacting case (bottom row) in graphene (left column) and in a semiconducting massive 2DEG (right column). Adapted from [83].

propagating in a self-consistent field generated by all surrounding particles. This is known as the *Hartree-Fock approximation*. However, as the particle moves, it will itself act on the surrounding distribution of particles, which will in turn provoke a feedback on the motion of the particle. This issue is solved by the time-dependent Hartree approximation, also known as random phase approximation (RPA), within which the particles respond not only to an external field, but also to a time-dependent Hartree potential.

The RPA susceptibility can be calculated using an intuitive linear response argument or using a diagrammatic calculation, for more details see ref. [32]. It is given by the following simple formula:

$$\chi_{nn}^{\text{RPA}}(\mathbf{q},\omega) = \frac{\chi_{nn}(\mathbf{q},\omega)}{\epsilon_{\text{RPA}}(\mathbf{q},\omega)} = \frac{\chi_{nn}(\mathbf{q},\omega)}{1 - v(\mathbf{q})\chi_{nn}(\mathbf{q},\omega)} \tag{1.54}$$

where ϵ_{RPA} is the *dielectric function* and $v(\mathbf{q})$ is the instantaneous interaction potential, e.g. the Coulomb potential, in Fourier space. The poles of χ_{nn}^{RPA} in the lower half of the complex frequency plane correspond to the dispersion of collective modes. They are usually found by looking for the zeros of ϵ_{RPA} [32]. Similarly to what was mentioned for the non-interacting response function above, these poles correspond to peaks in the spectral function $\propto \text{Im}\chi_{nn}^{\text{RPA}}(q,\omega)$, which is plotted in the bottom two panels of figure 1.12, again for graphene and a massive 2DEG. In both cases one observes the apparition of a peak in the spectral weight, which corresponds to the collective modes called *plasmons*. Both in graphene and in the 2DEG, the plasmon disperses with $\omega \propto \sqrt{q}$ at small wavevectors q and is strongly

damped once it approaches the phase space of intraband transitions (**III** in the figure). In the case of graphene, a clear broadening of the plasmon is furthermore observed when it enters region **II**, where it is damped by interband transitions.

1.6 Plasmons in graphene

Surface plasmon polaritons (SPPs, in the following simply plasmons) are modes that generally occur at the interface of a conductor and a dielectric. In the past decades, plasmons have been studied extensively in noble metals and have been exploited for a large range of applications, for example for plasmonic waveguides, high-confinement guiding and focusing, surface enhanced Raman spectroscopy, enhancement of fluorescence, metamaterials and others [84].

Due to the high charge carrier densities $\sim 10^{22}$ cm^{-3} in metals, well-confined SPPs only exist in the visible and near-infrared part of the EM spectrum in these systems. At lower frequencies, the field penetration of the EM field into the metal becomes negligible. Semiconductors, having much lower charge carrier densities can support plasmons in the mid infrared and even in the THz domain [84].

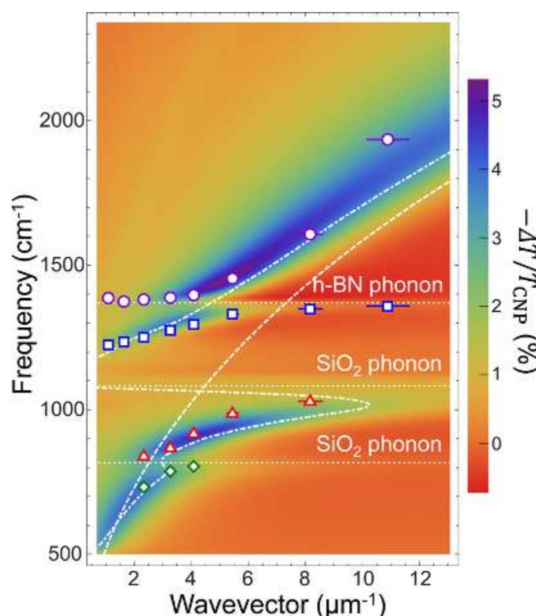

Figure 1.13 – Fourier transform infrared spectroscopy can be used to detect plasmon resonances (data points) in graphene nanoresonators. These plasmons hybridize with the phonons of the SiO_2 and hBN substrate, in accordance with theory (colorplot). Figure from ref. [85]. The frequency range shown here corresponds roughly to 20-80 THz.

Graphene, as a semimetal with a tunable (but low, compared to metals) carrier density and therefore a tunable plasmonic response, is thus a great platform for studies in these low-frequency domains, which might pave the way for the development of novel detectors and emitters in this notoriously elusive part of the EM spectrum between electronics (radio frequency) and optics (visible light). These emitters and detectors are particularly interesting from an application point of view, in telecommunication, homeland security, chemical sensing and many other domains [86].

Detailed reviews of graphene plasmonics in the infrared and THz domains can be found in refs. [86–88]. In this thesis, graphene plasmons are investigated at *even lower* frequency, namely in the GHz domain, as will be discussed in chapter 4. As illustrated in figure 1.13, graphene plasmons hybridize with substrate phonons in the infrared range [85, 89, 90], which means that a shift to lower frequencies is required to study "pure" graphene plasmons. Theoretically, plasmons can be approached from a variety of starting points, for example by solving Maxwell's equations with appropriate boundary conditions [86] or using a hydrodynamical approach [91–93]. The approach I will present here is based on the random phase approximation (see refs. [94–96]). Another approach using a transmission line model (see refs. [97–100]) is explained in section 4.2. In the long-wavelength, low-frequency limit, all the different approaches yield equivalent results, both for the free-standing and for the gated graphene sheet.

For a short literature review about graphene plasmonics from an experimental point of view, the reader is referred to the appendix 6.4, where I describe the evolution of the field from pure material studies (2008-2012) by electron energy loss spectroscopy [101], infrared spectroscopy [102] and near-field optical microscopy [103, 104] over first device implementations (2016) [105] towards functional, resonant devices (2018) in the THz- [106] and in the GHz-domain [27].

1.6.1 Unscreened SLG plasmons from RPA

The approach used in the following to calculate the unscreened and screened plasmon dispersions using the random phase approximation is well-known and can be found e.g. in references [32, 83, 107, 108]. In the long-wavelength limit ($q \to 0$ compared to the Fermi wavevector, with $\omega > v_F q$), the non-interacting response function for single layer graphene is given by [107, 108]:

$$\chi_{nn}(q \to 0, \omega) = \frac{gq^2}{8\pi\hbar\omega}\left[\frac{2E_F}{\hbar\omega} + \frac{1}{2}\ln\left|\frac{2E_F - \hbar\omega}{2E_F + \hbar\omega}\right| - i\frac{\pi}{2}\Theta(\hbar\omega - 2E_F)\right] \tag{1.55}$$

where $g = 4$ takes into account spin and valley degeneracy and E_F is the Fermi energy. At low energy ($\hbar\omega \ll 2E_F$), the Heaviside Θ term disappears and we neglect the logarithmic term ($\propto \hbar\omega/2E_F$ in this limit):

$$\chi_{nn}(q \to 0, \omega \to 0) = \frac{q^2 E_F}{\pi(\hbar\omega)^2} \tag{1.56}$$

We can now find our plasmons by looking for the zeros of the RPA dielectric function ϵ_{RPA}, corresponding to the poles of the RPA susceptibility χ_{nn}^{RPA}:

$$\epsilon_{\mathrm{RPA}}(q, \omega) = 1 - v(q)\chi_{nn}(q, \omega) = 0 \tag{1.57}$$

By inserting the unscreened Coulomb potential $v(q) = e^2/2\epsilon_0\epsilon_r q$ (in two-dimensional Fourier space) and the long-wavelength, low-energy form of χ_{nn} in this equation, we obtain:

$$1 - \frac{e^2 E_F q}{2\pi\epsilon_0\epsilon_r(\hbar\omega)^2} = 0 \tag{1.58}$$

We can simplify this expression by introducing the dimensionless "fine-structure constant" $\alpha_{ee} = e^2/4\pi\hbar v_F \epsilon_0 \epsilon_r \approx 0.7$ (for $\epsilon_r = 3.2$ corresponding to hBN-encapsulation), where v_F denotes the Fermi velocity. This leads to the following expressions for the low-energy dispersion of unscreened plasmons in single layer graphene:

$$\frac{\hbar\omega}{E_F} = \sqrt{2\alpha_{ee}\frac{q}{k_F}} \quad \textbf{or} \quad \omega = v_F\sqrt{2\alpha_{ee}k_F q} \tag{1.59}$$

As pointed out previously regarding the RPA susceptibility map in fig. 1.12, these unscreened plasmons disperse with $\omega \propto \sqrt{q}$. Note that the SLG plasmon's frequency dependence on carrier density is $\omega \propto n^{1/4}$, unlike in semiconductor 2DEGs or in BLG, where it is $\omega \propto n^{1/2}$.

1.6.2 Screened SLG plasmons from RPA

In order to take into account the screening effect of a proximate gate electrode, we use the mirror-charge approach. In figure 1.14, we consider the potential felt by a test charge e at position $\mathbf{r}'$ due to an identical charge at position $\mathbf{r}$. Both charges are located in the graphene sheet which is separated from the gate electrode by a distance d. Assuming that the gate electrode behaves as a perfect metal (electric field lines perpendicular to the surface), we can model its screening effect by introducing a third "mirror charge" of opposite sign $-e$ below the gate electrode.

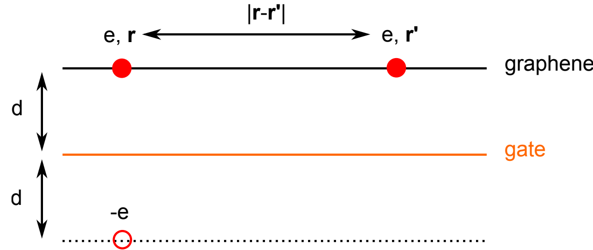

Figure 1.14 – Illustration of the concept of a mirror charge.

The total potential felt by the test charge is now:

$$v_{\text{screened}}(\mathbf{r}, \mathbf{r}') = \frac{e^2}{4\pi\epsilon_0\epsilon_r|\mathbf{r}-\mathbf{r}'|} - \frac{e^2}{4\pi\epsilon_0\epsilon_r\sqrt{(\mathbf{r}-\mathbf{r}')^2 + (2d)^2}} \tag{1.60}$$

which, in Fourier space, corresponds to:

$$v_{\text{screened}}(q) = \frac{e^2}{2\epsilon_0\epsilon_r q}\left(1 - e^{-2qd}\right) \tag{1.61}$$

When the gate electrode is very far away ($d \gg 1/2q$), we recover the unscreened potential used above. When the gate electrode is extremely close ($d \ll 1/2q$) – which is the case for the devices that will be discussed in chapter 4, where the plasmonic wavelength is several orders of magnitude larger than the graphene-gate spacing d – we can Taylor-expand the exponential term of the screened potential and obtain:

$$v^{d\to 0}_{\text{screened}}(q) = \frac{de^2}{\epsilon_0\epsilon_r} \tag{1.62}$$

Inserting this potential in equation 1.57 yields the following dispersion for highly screened plasmons in single layer graphene:

$$\frac{\hbar\omega}{E_F} = 2\sqrt{\alpha_{ee}k_F d}\,\frac{q}{k_F} \qquad \textbf{or} \qquad \omega = 2v_F\sqrt{\alpha_{ee}k_F d}\,q \tag{1.63}$$

which is a linear dispersion. This is why these screened plasmons are also called *acoustic* plasmons, c.f. e.g. refs. [96, 109]. If the gate distance d becomes comparable to the Fermi wavelength λ_F, so that $k_F d \sim 1$, we reach a regime where the plasmon phase velocity is on the order of the Fermi velocity $v_p \gtrsim v_F$, as we will see further below in figure 1.15. Note that it cannot be smaller than the Fermi velocity, because Landau damping inhibits plasmon propagation when the plasmon branch enters the particle-hole continuum, see fig. 1.12.

1.6.3 Comparison of screened/unscreened SLG/BLG plasmons

Figure 1.15 shows a comparison of the calculated dispersion of screened ($d = 10$ nm, $\epsilon_r = 3.2$) and unscreened SLG plasmons, together with the unscreened case for BLG. The calculation is done using the above equations at a typical doping value of $n = 10^{12}$ cm^{-2}, corresponding to a Fermi energy of $E_F = 117$ meV in SLG (plotted as a black dashed line for reference). In the left panel, the curves are plotted on a linear scale. The SLG and BLG plasmons have a very similar dispersion at this doping, however the BLG plasmons are a bit slower than their SLG equivalent. The effect of screening is quite dramatic, in particular for long wavelengths ($q \to 0$). On the one hand, the dispersion becomes linear – as was pointed out above – and on the other, the plasmons are slowed down enormously by the presence of the gate electrode. The three stars on the plots in fig. 1.15 highlight the large frequency difference between previous studies in the infrared and THz domain (e.g. [103, 109]) and this work in the GHz frequency range. This jump is only possible thanks to the use of high mobility hBN-encapsulated graphene at cryogenic temperatures, where $\omega\tau \lesssim 1$ even in the GHz range.

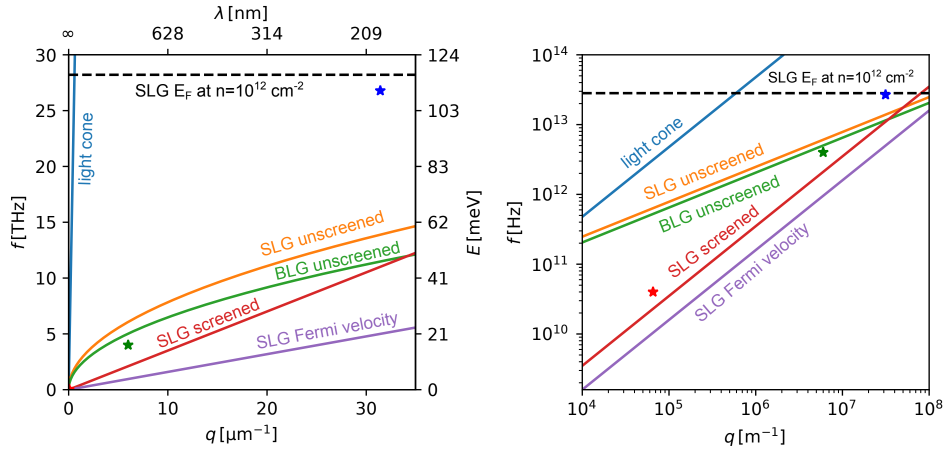

Figure 1.15 – Plasmon dispersions in single- (SLG) and bilayer graphene (BLG) for the unscreened and the screened case on a linear (left) and logarithmic (right) scale. ⋆ Example for an infrared [103] and ⋆ a THz study [109] compared to ⋆ this work.

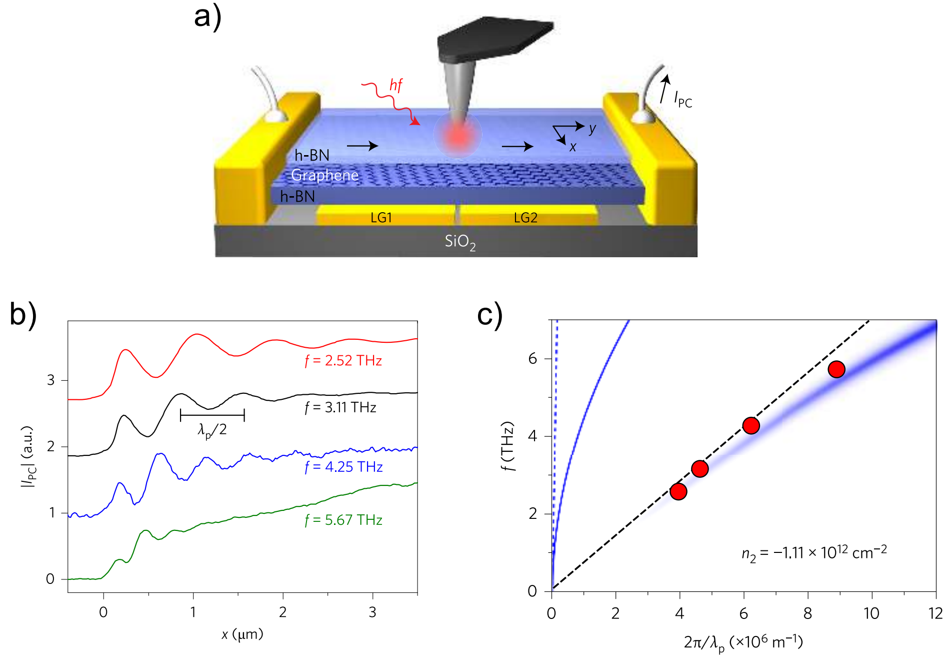

Figure 1.16 – **Photoelectric detection of screened SLG plasmons.** a) Scattering-type scanning near-field optical microscopy combined with gate induced p-n junctions is used to produce photocurrent maps. b) Plasmon interference patterns in the photocurrent, recorded near the sample edges for different excitation frequencies. c) The resulting dispersion is characteristic for screened plasmons. Dashed black line corresponds to linear dispersion, c.f. eq. 1.63. Blue density plot is a finite-temperature local RPA calculation. Solid blue line is the unscreened plasmon dispersion and dotted blue line is the light cone. Figure from ref. [109].

The screening effect is experimentally established in semiconductor 2DEGs [97] and was recently demonstrated in graphene [109]: Figure 1.16 illustrates how a scattering-type near-field optical microscopy setup is used to launch plasmons into a gated graphene sample. By recording the photocurrent as a function of tip position, interference patterns are detected close to the sample edges and the plasmon wavelength is extracted. The dispersion (red dots in fig. 1.16c) deviates strongly from the unscreened plasmon dispersion (solid thin blue line), due to the local gate electrodes. This effect is particularly strong due to the THz frequency range used in this experiment. In the infrared regime, i.e. an order of magnitude higher in frequency and smaller in wavelength, the screening term e^{-2qd} in eq. 1.61 is less dominant. This is particularly interesting for the present work (red star in fig. 1.15), since at the wavelengths that we consider, the screening effect reduces the resonance frequency by more than an order of magnitude. Without this, we could not have obtained the results presented in chapter 4.5.4.

The light cone $\omega = cq$ with $c = 3 \times 10^8$ ms^{-1} is plotted as a solid (dotted) blue line in figure 1.15 (1.16) to highlight the large wavevector mismatch between light propagating in free space and the confined plasmon modes. In optical studies, various wavevector matching techniques (grating coupling, prism coupling, near-field coupling, see appendix 6.4) are used to overcome this mismatch. In this work, the capacitor cavity imposes the wavevector.

1.7 Magnetoexcitons in a massive 2DEG

After discussing collective excitations at zero magnetic field, let us now consider their equivalent in the integer quantum Hall regime: Magnetoexcitons were theoretically introduced in 1984–1985 [110–113]. We can calculate their dispersion using the random phase approximation introduced in section 1.5, similarly to what was done for plasmons at $B = 0$ in section 1.6.1. Here we will use the same approach: Calculate the Lindhard function (the density-density response function) $\chi_{nn}(\mathbf{q}, \omega)$ for a 2DEG in the QHE regime, derive the RPA response function $\chi_{nn}^{\mathrm{RPA}}(\mathbf{q}, \omega) = \chi_{nn}(\mathbf{q}, \omega)/\epsilon_{\mathrm{RPA}}(\mathbf{q}, \omega)$ from this and look for the peaks in its imaginary part, or, look for the zeros of the RPA dielectric function $\epsilon_{\mathrm{RPA}}(\mathbf{q}, \omega) = 1 - v(q)\chi_{nn}(\mathbf{q}, \omega)$, where $v(q) = e^2/2\epsilon_0\epsilon_r q$ is the Coulomb potential in two dimensional Fourier space. Here I will use the results from Giuliani & Vignale's book [32].

In order to calculate the Lindhard function, we first need to evaluate the matrix element $\langle n, k_y|e^{-i\mathbf{q}\cdot\mathbf{r}}|n', k_y'\rangle$ of the single-particle density operator using the wavefunctions $|n, k_y\rangle$ given in equation 1.42. This calculation is demonstrated in appendix 6.5 and yields for $n \geq n'$ (a similar expression is obtained for $n' > n$):

$$\langle n, k_y|e^{-i\mathbf{q}\cdot\mathbf{r}}|n', k_y'\rangle = \delta_{k_y'-k_y,q_y} e^{\frac{-iq_x\ell^2}{2}(k_y+k_y')} e^{-\frac{1}{2}|\alpha|^2} \alpha^{n-n'} \sqrt{\frac{n'!}{n!}} L_{n'}^{n-n'}(|\alpha|^2) \tag{1.64}$$

where $\alpha = \ell_B(q_y - iq_x)/\sqrt{2}$ is the complex wavevector, L_n^m is the associated Laguerre polynomial and $\delta_{k_y'-k_y,q_y}$ is the Kronecker delta function ensuring momentum conservation. Let us insert this into the Lindhard function, eq. 1.52, here re-written in terms of the relevant quantum numbers (we do not worry about spin degeneracy at this point):

$$\chi_{nn}(\mathbf{q}, \omega) = \frac{1}{\hbar L_x L_y} \sum_{n,n'} \sum_{k_y,k_y'} \frac{P_{n'} - P_n}{\omega - \omega_{nn'} + i\eta} \left|\langle n, k_y|\hat{n}(\mathbf{q})|n', k_y'\rangle\right|^2 \tag{1.65}$$

In the zero-temperature limit, where the Fermi Dirac occupation probabilities P_n approach a Heaviside step function centered at the Fermi level, and taking into account the aforementioned momentum conservation which simplifies the sum over k_y and k_y' to a multiplication by the number of possible k_y per LL (eq. 1.45), one obtains (see appendix 6.5 for details):

$$\begin{aligned}\chi_{nn}(\mathbf{q}, \omega) =& \frac{e^{-\frac{q^2\ell_B^2}{2}}}{2\pi\hbar\ell_B^2} \sum_{k=1}^{\infty} \sum_j \frac{j!}{(j+k)!} \left(\frac{q^2\ell_B^2}{2}\right)^k \left[L_j^k\left(\frac{q^2\ell_B^2}{2}\right)\right]^2 \\ &\times \left[\frac{1}{\omega - k\omega_c + i\eta} - \frac{1}{\omega + k\omega_c + i\eta}\right]\end{aligned} \tag{1.66}$$

where we are now summing over all LLs j and the LLs $j \pm k$ whose transitions to j are authorized. The sum over j thus goes over the range $\max(0, N_F - k) < j \leq N_F$, where N_F is the highest occupied LL. As mentioned before, the imaginary part of this function describes the particle-hole excitation spectrum (PHES) and is plotted in fig. 1.17a. The spectral weight is concentrated in the realm of authorized electron-hole excitations delimited by the two black parabolas, a property that will play a role in section 5.5. The distinct “islands” of high spectral weight in this PHES arise from the various different contributing transitions between LLs [114].

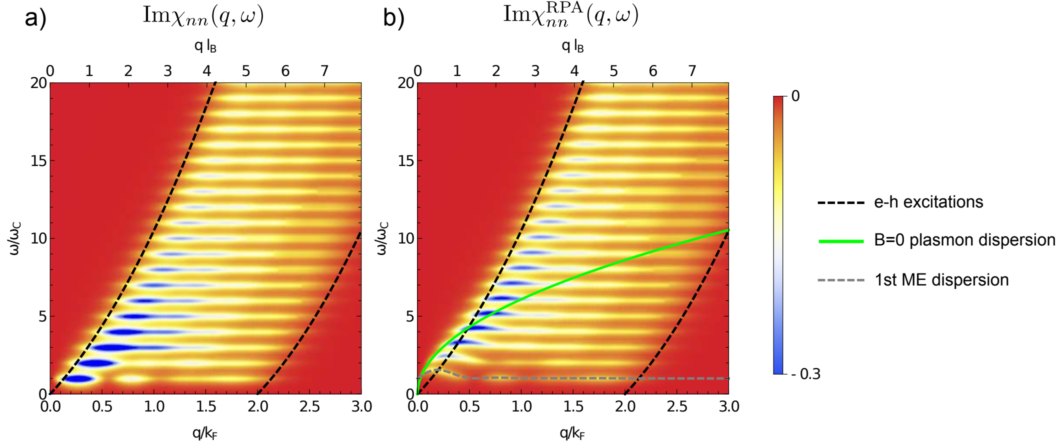

Figure 1.17 – Spectral density of a) the single-particle- and b) the RPA-response function $\chi_{nn}(\mathbf{q}, \omega)$ of a semiconductor 2DEG. The level broadening is $\eta = 0.2\ \omega_c$ and the highest filled LL is $N_F = 3$. Reproduced according to ref. [114].

Let us now focus on $\text{Im}\chi_{nn}^{\text{RPA}}$, which is easily calculated from the non-interacting susceptibility using the above formula. The result is plotted in fig. 1.17b. We still observe horizontal lines of significant spectral weight in the realm of intraband excitations. They are vertically shifted by multiples of the cyclotron frequency ω_c. These are the collective modes called magnetoexcitons (MEs). At small wavevectors q there is a branch of non-zero spectral weight that disperses $\propto \sqrt{q}$ and then merges with the black line delimiting the intraband excitations. This branch corresponds to the $B = 0$ plasmons shown in the susceptibility map in figure 1.12. In order to highlight this, the lowest order plasmon dispersion is plotted as a green line according to eq. 1.59.

By looking for the zeros of the dielectric function $\epsilon_{\text{RPA}}(\text{q}, \omega)$, one obtains the following expression for the ME dispersion [32]:

$$\omega_{\text{ME}}(q) \approx m\omega_c + \frac{e^2}{\hbar\epsilon_b\ell_B} e^{-\frac{q^2\ell_B^2}{2}} \frac{(q\ell_B)^{2m-1}}{2^m} \sum_j \frac{j!}{(j+m)!} \left[L_j^m \left(\frac{q^2\ell_B^2}{2} \right) \right]^2 \tag{1.67}$$

where ϵ_b is the dielectric constant. For the fundamental ME mode ($m = 0$), this dispersion is plotted as a gray dashed line on top of the susceptibility map in fig. 1.17b.

Calculating the ME dispersion within the time-dependent Hartree-Fock approximation (TDHFA) leads to small shifts in the ME energy. These shifts increase with the wavevector, but remain small compared to the cyclotron gap, so they do not play a significant role for the analysis in chapter 5. For more details see refs. [32, 112, 113]. In ref. [115], the ME dispersion is calculated explicitly for bilayer graphene at small filling factors, revealing that the spinorial character of the wavefunctions combined with interaction effects gives rise to significant shifts in the ME energy. In section 5.5, we will consider MEs at large filling factors, where the difference between BLG and a semiconductor 2DEG is less pronounced, as we will point out again in that section. In the fractional quantum Hall effect, inter-LL magnetoexcitons are replaced by intra-LL magnetorotons with longitudinal polarization [32, 116]. The discussion of collective excitations in the FQHE, as well as a more specific analysis of MEs in BLG or TDHFA calculations all go beyond the scope of this thesis.

2
Experimental methods

In this chapter, I will explain the experimental methods used throughout this thesis, from sample fabrication and characterization to DC and high frequency transport and noise measurements. The motivation for accumulating this information in a single chapter is to avoid redundancy in the results chapters 3-5 which will focus on physical insights, rather than experimental details. Whereas the transport and noise measurements were all carried out at ENS in Paris, the nanofabrication was done partly at NTU in Singapore, where two facilities were used: the cleanrooms of the Nanyang NanoFabrication Centre (N2FC) and Prof. Lew Wen Siang's laboratory at the School of Physical & Mathematical Sciences (SPMS).

Three types of high-mobility graphene samples were fabricated throughout this thesis. The corner reflectors for Dirac fermion optics and the plasma resonance capacitors for GHz plasmonics use hBN-encapsulated graphene. The noise-thermometry experiment for the investigation of the breakdown of the quantum Hall effect relies on graphene-on-hBN. Most measurements were performed in a cryogenic microwave probe station. Noise thermometry was carried out at high magnetic field in an immersion cryostat.

2.1 Nanofabrication of encapsulated graphene devices

Since the first isolation of graphene crystals and the fabrication of first graphene devices [1], which already showed electronic mobilities comparable to silicon devices, a huge progress could be observed in terms of sample quality, notably thanks to the identification of hexagonal boron nitride (hBN) as a suitable substrate for graphene [14]. This suitability stems from the fact that it has the same crystalline structure as graphene, without being itself conducting (in fact it has a bandgap of ~ 6 eV [117] and a breakdown voltage of around 0.7 V/nm, which makes it a robust gate dielectric). Furthermore, hBN crystals can be cleaved by exfoliation, much like graphene, which creates atomically flat surfaces and therefore minimizes random strain in graphene. The absence of trapped charges minimized charged impurity scattering and hysteresis. The isolation of both hBN and graphene flakes is described in section 2.1.1.

Eventually, the encapsulation of graphene between two hBN crystals [118] has made it

possible to reach the acoustic phonon limited mobility ($\sim 100\,000$ cm^2/Vs) at room temperature and mean free paths of up to 28 μm at cryogenic temperatures [119].

At the beginning of this thesis project, a considerable amount of work was invested to integrate two encapsulation methods at Ecole Normale Supérieure: the "original" method used by the Columbia group [118] and a CVD-graphene-compatible method developed by Luca Banszerus at RWTH Aachen [120]. Both methods will be described in section 2.1.3. The sample characterization by Raman spectroscopy and atomic force microscopy will be detailed in section 2.1.4.

Similarly to graphene, atomically thin hexagonal boron nitride layers can now also be synthesized by chemical vapour deposition or sputtering on copper [15, 121] and directly on dielectric substrates [16, 122]. These advances might pave the way towards wafer-scale fabrication of graphene-on-hBN or encapsulated graphene devices.

Recent works have shown that despite the encapsulation of graphene in hBN, the underlying substrate (often SiO_2) still has an impact on the maximum mobility that can be reached in the graphene sample, in particular if the bottom hBN layer is too thin [123]. This is why many groups choose to use metallic bottom gates to screen charge inhomogeneities. Graphite flakes are particularly popular for this purpose, due to their compatibility with the hBN-G-hBN heterostructures [79, 124–127]. However, graphite being a microwave absorber, it cannot be used in our high frequency devices. Instead, we have used thin tungsten or gold films, since the technology for nano-structuring these materials was already partly established in our laboratory. This technology, explained in section 2.1.2, is particularly important for the definition of sharp, gate-induced p-n junctions that are used for Dirac fermion optics in chapter 3.

Once a hBN-G-hBN stack has been fabricated – and possibly deposited on top of the above-mentioned gate structures – it has to be shaped into the desired geometry and contacted in order to prepare for electronic transport measurements. This last fabrication process is explained in section 2.1.5. For detailed step-by-step recipes, the reader is referred to the appendix 6.1.

2.1.1 Base materials: graphene and hexagonal boron nitride

All the hexagonal boron nitride used in this thesis was obtained from Takashi Taniguchi and Kenji Watanabe at the National Institute for Materials Science in Japan [117, 128], who are internationally renowned for large, high-quality crystals. In appendix 6.6, we compare this hBN with new samples from Laboratoire des Multimatériaux et Interfaces in Lyon, France, in terms of dielectric properties.

In the early stages of this project, hBN was exfoliated using adhesive tape, but later mostly using thick (~ 5 mm) PDMS wedges, which can be used to transfer thin flakes onto silicon substrates or onto "Aachen"-type stamps (see section 2.1.3). Using this method, thin (~ 20 nm) boron nitride crystals of up to ~ 50 μm in lateral size could be deposited on SiO_2 (and up to ~ 100 μm on stamps).

Graphene was obtained by exfoliation (a.k.a. "micromechanical cleavage") from large ($10 - 20$ mm) graphite crystals bought from NGS Naturgraphit GmbH. A thin, clean and homogeneous layer of graphite was isolated on a large piece of adhesive tape (Blue Low Tack tape from Semiconductor Equipment Corp.). The tape was repeatedly folded to thin down the graphite until large, homogeneous (on the scale of $\gtrsim 1$ mm) and slightly transparent

domains were observed. The tape was then stuck to the destination substrate, which was usually silicon with 280 nm of SiO_2 and a grid of numbered alignment crosses, exposed to oxygen plasma for 5 minutes in the plasma cleaner prior to exfoliation. The tape was carefully flattened with a piece of hard plastic, e.g. the head of a screwdriver or of a pair of scissors. The substrate – with the adhesive tape – was then placed on a hot plate at 100°C for 2 minutes, following ref. [123]. Finally, the adhesive tape was slowly and carefully removed. Atomically thin flakes were found among thicker graphite crystals after some searching under the optical microscope. Single-, bi- and few-layer graphene could be distinguished by the increasing contrast they made with the SiO_2 substrate. Using this method, single layer graphene crystals of up to 70 μm in lateral size could be obtained (about one or two large > 30 μm flakes per cm^2 of SiO_2).

Even though monocrystalline CVD graphene is now available in-house at ENS (grown by Aurélie Pierret), all the CVD graphene used in this thesis was fabricated at RWTH Aachen by Luca Banszerus and more recently by Zachary Winter. Their growth process is described in ref. [120].

2.1.2 Nanostructured local bottom gates

The development of the nano-patterning process for tungsten constituted a major part of the work of Quentin Wilmart during his PhD (2012−2015). The motivation for this work was the design of gate-induced p-n junctions for Dirac fermion optics and the technology was eventually used for the fabrication of high frequency graphene transistors with gated contacts [23, 129].

For Dirac fermion optics, it is also possible to work with dual (top and bottom) gates, like in ref. [130], but this has the drawback of coupling one region of the device to two gates. Besides, top gates make the illumination of the channel difficult and are therefore not suitable for opto-electronic characterization. Finally, the potential profile obtained using dual gates is usually rather smooth, but – as will be explained in chapter 3 – we prefer sharp p-n junctions in our devices, which means that the gap between the gate electrodes should be on the order of the Fermi wavelength, which is 35 nm in graphene at typical doping 10^{12} cm^{-2}.

In order to define such nanometric gaps, conventional lift-off techniques are not feasible, since it is difficult for the developer to "wash out" the material from these tiny gaps. This is why all techniques described in the following are based on the etching of thin metallic films. The thickness of these films is chosen to be on the order of the required resolution, i.e. ~ 20 nm.

During his PhD, Quentin has carried out nanostructuring experiments on a wide range of materials [23]: focused ion beam (FIB) on gold, electron beam lithography (EBL) combined with reactive ion etching (RIE) on palladium, niobium, graphite, silicon-on-insulator and tungsten. In many cases (gold, palladium, niobium) the limiting factor was the annealing step (300° in Ar/H_2 atmosphere) required for the graphene-on-boron-nitride (GoBN) technology. Some materials seemed to become hydrogenated and the thin gold films simply melted. Eventually, tungsten was identified as the best candidate for the nano-patterned bottom gates, due to its refractory nature, its thermal stability, its acceptable resistivity and the good compatibility with reactive ion etching.

In the following, we will revisit the fabrication of tungsten gate electrodes according to the recipe developed by Quentin. I will then show how this recipe was adapted for the

fabrication of gold gates and point out some difficulties that were encountered.

Tungsten gates

The substrate is prepared by sputtering a thin 20−30 nm film of tungsten on a high resistivity (> 3000 Ωcm) silicon substrate with a 280 nm SiO_2 dielectric layer. This is done by Loïc Becerra at Institut des Nanosciences de Paris (INSP). The substrates are then spin coated with a 50 nm PMMA layer at 4000 rpm for 30 seconds and annealed at 160°C.

The PMMA solution is prepared by mixing MicroChem PMMA 950K A6 with anisole 1:2-1:3, corresponding to a total dilution of 1-2% PMMA in anisole. The required dilution ratio is not always the same depending on the substrate, and the effective thickness depends on the age of the solution. It is good practice to carry out spin coating tests from time to time and to check the real thickness with a Dektak profilometer.

The fine structures (i.e. the 20 nm lines) are defined with a Raith EBL at 20 kV acceleration voltage, 7.5 μm aperture (the smallest available) with a step size of 2 nm. I always use the normal "area exposure" even though the Raith EBL also supports a mode for single pixel line exposure. After development, the sample is etched in a Corial 200R RIE with an SF_6 plasma at a pressure of 6 mTorr, a flowrate of 25 sccm and RF power of 10 W. The system is equipped with a laser endpoint detection (EPD), which enables us to detect a minimum in the laser reflection once the tungsten film is completely etched. This is the case after about 40 seconds and we typically overetch by another 40 seconds in order to minimize the risk of short circuits. In order to remove the remaining PMMA layer, we perform a short O_2 stripping step (100 mTorr, 100 sccm, 30 W), again using the EPD to track the etching progress. A second lithography and etching step is carried out to define the rough structures. Then a third EBL step is carried out on a thicker PMMA layer (∼ 500 nm) to define the contact pads (Cr/Au) which are subsequently deposited by Joule evaporation. The whole process is illustrated in figure 2.1.

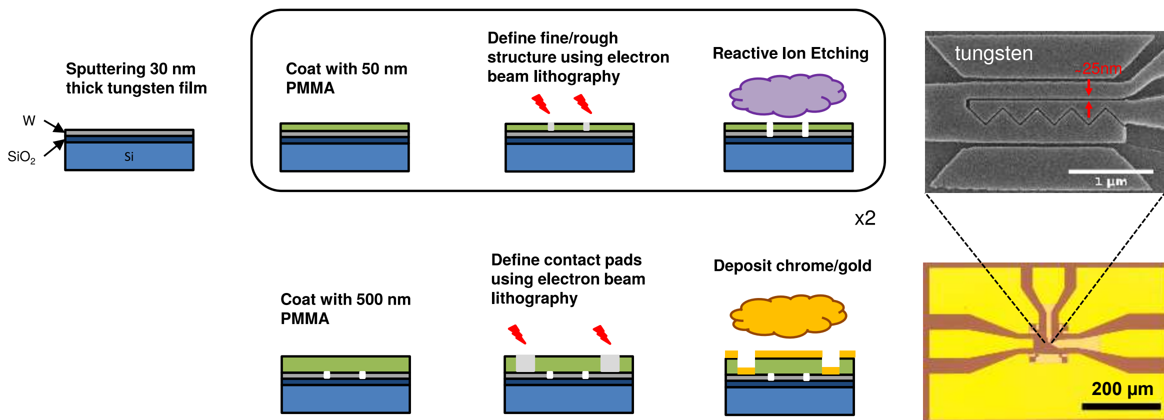

Figure 2.1 – Illustration of the fabrication process for nanostructured bottom gates.

Gold gates

Thanks to the use of encapsulated graphene, the annealing step that was used to remove polymer residues from graphene-on-hBN devices was no longer required for the devices fabri-

cated in the course of this thesis, which means that gold was no longer excluded as a possible gate material. Due to its lower resistivity, it is more suitable for the design of high frequency transistors.

Series of tests were carried out both at NTU and at ENS in order to adapt the tungsten etching process to thin gold films. These films were prepared by Joule or e-beam evaporation of Cr/Au (1/30 nm) on high resistivity silicon with a 280 nm oxide layer (as previously). The lithography to define nanostructures was carried out on a 50 nm PMMA layer with three more or less equivalent Raith eLine electron beam lithography systems, depending on their (geographic) availability:

- at the Nanyang NanoFabrication Centre (N2FC), cleanroom 2 (NTU)
- in Prof. Lew Wen Siang's spintronics laboratory at the School of Physical and Mathematical Sciences (SPMS, NTU)
- in the ENS cleanroom

In order to identify a suitable etching process, I have tried various dry etching systems, listed in table 2.1 with the approximate etch rates for Au and PMMA. For the lithography to be feasible, the etching process should have a decent selectivity, i.e. the Au etch rate should be higher than or similar to the PMMA etch rate. As the table shows, this was only the case for the ion beam milling system at SPMS and for the RIE in the ENS cleanroom. These two systems also have the advantage that they are equipped with end point detection: In the RIE, this is the aforementioned laser, whereas in the ion beam milling system, it is a secondary ion mass spectrometry (SIMS).

Equipment (Location)	Process	Au etch rate [nm/min]	PMMA etch rate [nm/min]
PlasmaTherm PTi790 PECVD (N2FC cleanroom 1)	Ar 42 sccm, CF_4 9 sccm, 32 mTorr, 150 W	10	190
PlasmaTherm PTi790 PECVD (N2FC cleanroom 1)	Ar 40 sccm, 50 mTorr, 120 W	10	180
Cello Nascal-20L RIE (N2FC cleanroom 2)	Cl_2 50 sccm, 50 mTorr, 200 W [131]	<10	90
AJA International IBM (SPMS)	Ion beam milling	30	10
Corial 200R RIE (ENS)	Ar 40 sccm, 50 mTorr, 85 W	20	~ 10

Table 2.1 – **Dry etching processes for gold.** Suitable candidates with sufficient selectivity are highlighted bold.

Most of these processes are using only physical etching, i.e. the ions do not chemically react with the gold film (gold being a noble metal, a chemical reaction is not easy to achieve).

Interestingly, the argon recipe that worked in the Corial 200R RIE at ENS did not work as well in the PlasmaTherm PTi790 PECVD. In particular, the PMMA etch rate was much higher, which was probably due to residues (oxygen...) in the etching chamber.

Removing the PMMA residues after the etching procedure turned out to be quite difficult, since the PMMA got hardened (cross-linked). It could not be removed with acetone. One also had to be careful with plasma cleaners and with piranha (H_2SO_4+H_2O_2) solution since both can damage the nanostructures. The best results were obtained using the stripping program (O_2 plasma, 30 W) combined with laser end point detection in the Corial 200R RIE. Unfortunately, the ion beam milling system cannot create an oxygen plasma for the stripping of resist residues.

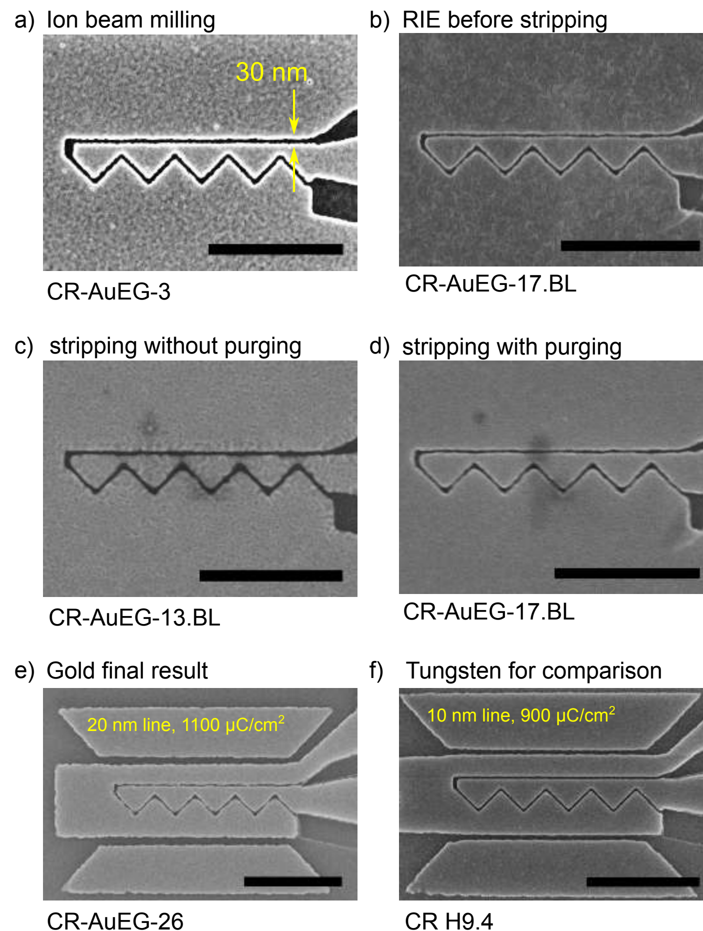

Figure 2.2 – SEM pictures of gold (a-e) and tungsten (f) gates. Scale bars are 1 μm.

Figure 2.2 shows SEM pictures of a couple of examples out of the 27 sets of gold gates that have been fabricated. Panel (a) demonstrates that a nice 30 nm gap could be achieved with the ion beam milling system. However the surface of the metal still looks rough, which might be due to the roughness of the Au film, but more likely due to polymer residues. Panel (b) shows a sample fabricated with the RIE at ENS before oxygen stripping and panel (d) shows the same sample after oxygen stripping. It turned out to be important to purge the etching chamber with oxygen (for $\sim$ 5 minutes; or to simply vent it and load the sample again)

before stripping, otherwise the gold film got damaged (see panel c). Even after many tests, the results of the gold etching were still less satisfying than those obtained with tungsten, see panels (e-f). The main difference is that the argon etching process is much more physical than the SF_6 process, therefore:

- It therefore etches more anisotropically.
- The PMMA is etched much slower.
- A thin PMMA layer (≤ 50 nm) is therefore particularly important.
- The nominal EBL line width has to be increased from 10 to 20 nm.
- Purging of the RIE chamber is crucial (5 min Ar before etching and 5 min O_2 before stripping).

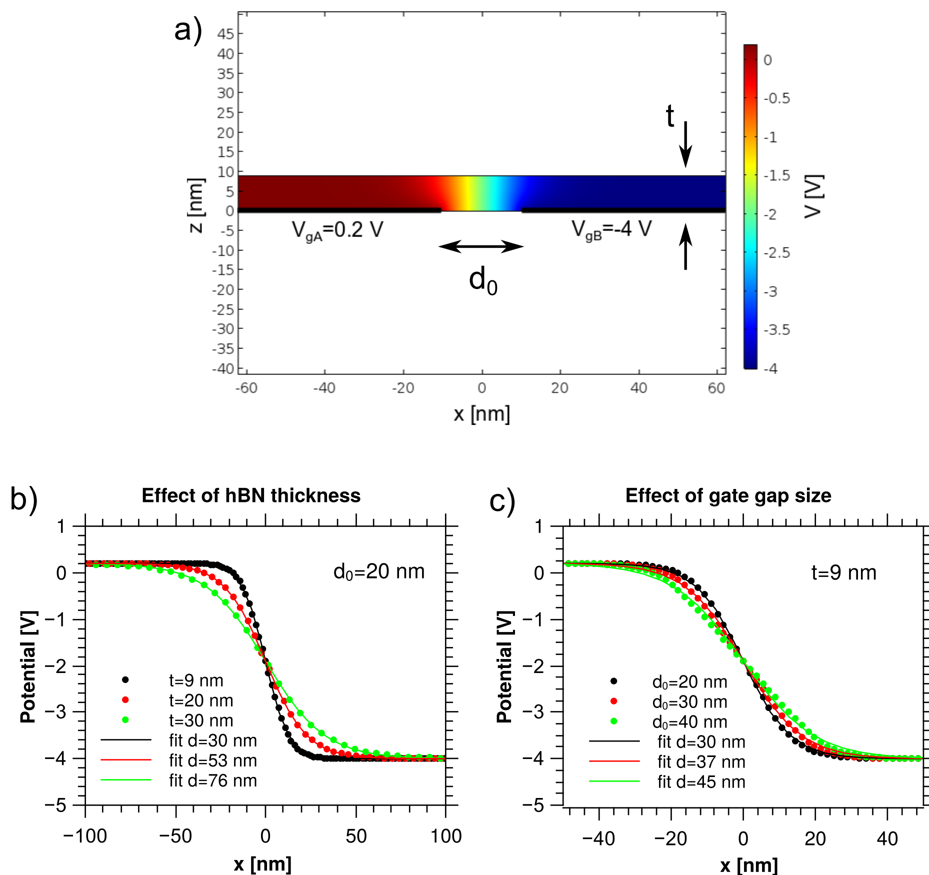

Figure 2.3 – **p-n junction profile.** a) Geometry of the COMSOL simulation. The color plot corresponds to the distribution of the electric potential in the hBN slab. b) [c)] Potential on the surface of the hBN slab for constant d_0 [t] and varying t [d_0].

Remarks on the p-n potential profile

In order to estimate the real potential profile of our gate-induced p-n junctions, we have carried out COMSOL finite element simulations. Figure 2.3a shows the simulated geometry: A slab of hBN with a thickness of t and a relative permittivity of $\epsilon_r = 3.2$ is lying on the two gate electrodes – assumed to be perfect conductors and separated by a gap of width d_0 – with potentials V_{gA} and V_{gB}.

In panels (b) and (c) we show the potential distribution at the top surface of the hBN-slab. In panel (b) we keep the gap size d_0 constant and vary the thickness of the hBN slab and in panel (c) we keep t constant and vary d_0. The data from the COMSOL-simulation is well fitted with a Fermi-type function, similar to Cayssol *et al.*'s model for the p-n junction profile in graphene [132], which will be used in chapter 3:

$$V(x) = V_{gA} + \frac{V_{gB} - V_{gA}}{1 + e^{-2\ln(10)x/d}} \tag{2.1}$$

where the pre-factor $2\ln(10) \approx 4.6$ in the exponential serves as a scaling factor for the junction length, so that d is the distance over which $V(x)$ reaches 90% of its final value.

These simulations show that a thin gate dielectric is crucial for a sharp p-n junction profile. They further demonstrate that a Fermi-type function is indeed adequate for the description of realistic p-n potential profiles. Due to the finite charge carrier density in graphene (which was ignored in our simulations), a realistic calculation should take into account non-linear screening effects [133]. Qualitatively, screening should reduce the effective junction length, which means that we stay in the sharp junction limit required for Dirac fermion optics. A more involved analysis of screening goes beyond the scope of this thesis. In conclusion, the desired sharp p-n junctions can be obtained with our tungsten and gold electrodes, as long as the gate dielectric is kept thinner than the junction length.

Remarks on the junction roughness

A recent experimental work by Zhou *et al.* [127] points out the importance of minimizing the junction roughness in order to obtain well-defined interfaces for Dirac fermion optics experiments. They study the effective junction roughness of gate-induced p-n junctions using scanning tunneling microscopy. This technique enables them to spatially map the Fermi level in an encapsulated graphene sample while a p-n junction is induced using local gate electrodes.

They compare two types of devices, illustrated in figure 2.4b and c, respectively: On the one hand, they look at poly Si gates, defined by photolithography with a 100 nm spacing, buried underneath a layer of SiO_2 of 100 nm thickness. On the other hand, they consider a single graphite gate, created by micromechanical cleaving, whereas the other side of the p-n junction is still gated using the silicon substrate.

The authors claim that for the creation of sharp p-n junctions, cleaved edge graphite gates are required, based on the analysis of the STM topography (fig. 2.4g-h) and dI/dV-maps (fig. 2.4i-j). However they also mention the important influence of inhomogeneities in their SiO_2 dielectric, which had to be taken into account for both types of devices.

While an STM study of our tungsten/gold-gate induced p-n junctions goes beyond the scope of this thesis, I would like to point out two arguments as to why our p-n junctions should be comparable in quality to the graphite-gate-induced junctions studied in ref. [127]: Firstly,

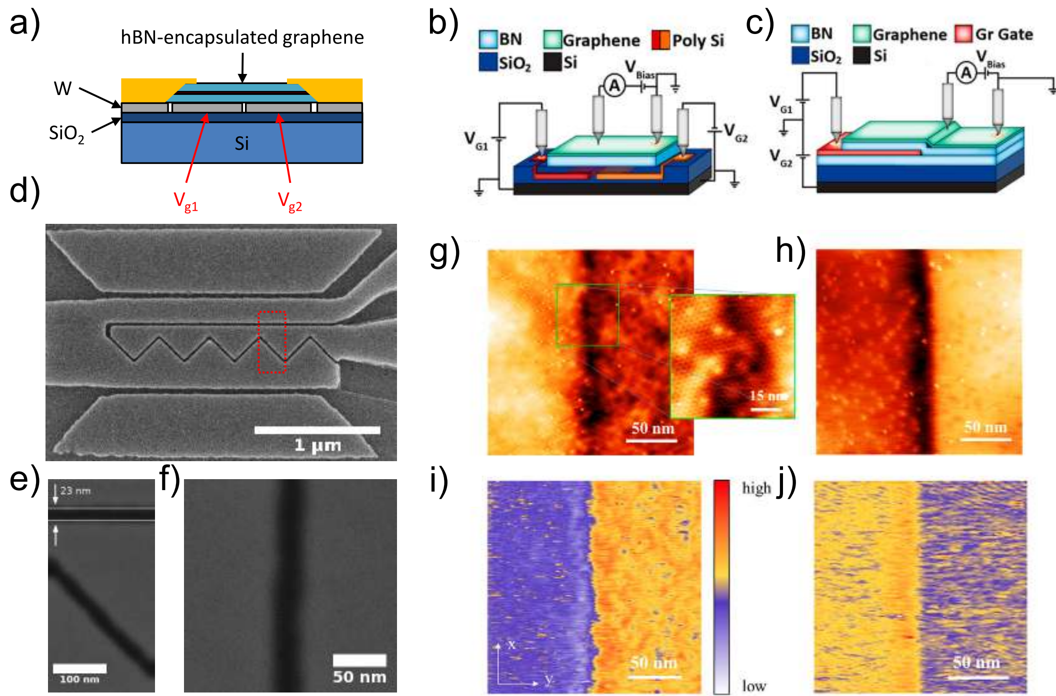

Figure 2.4 – **Junction roughness.** a) Sketch of the device structure for DFO devices. b) Sketch of poly Si- and c) graphite-gated devices studied in ref. [127]. d-f) SEM pictures of a tungsten gate with increasing zoom. g-h) STM topography images and i-j) STM dI/dV-maps of the junctions illustrated in b and c, respectively. Panels b-c) and g-j) taken from ref. [127].

we use high-resolution electron beam lithography to define our gate electrodes, creating gaps on the order of 20 nm (see fig. 2.4d-f with increasing zoom), i.e. one order of magnitude smaller than the ones discussed in ref. [127]. Fig. 2.4f shows that these gate electrodes are smooth on a scale $\ll$10 nm. Secondly, there is no SiO_2 layer between either of the two gate electrodes and the hBN-encapsulated graphene sample, which means that inhomogeneities in the SiO_2 are not an issue in our case.

2.1.3 Graphene encapsulation

Throughout this thesis, two methods have been used to perform the encapsulation of graphene and the transfer of hBN-G-hBN stacks onto gate electrodes or SiO_2 substrates: The "Columbia" method, which was used for the first reported fabrication of a graphene edge contact [118] and the "Aachen" method, which was developed by Luca Banszerus at RWTH Aachen for the pick-up of CVD graphene from copper [120].

The principle of both methods is to exploit the van-der-Waals force between hBN and graphene, which is stronger than the adhesion between these materials and the substrate (SiO_2 or copper). A transparent polymer stamp is used for the transfer of the crystals. The polymer can be melted by heating it beyond its glass temperature and re-solidified by cooling it back down. Its transparency enables us to see through the stamp and align crystals underneath a microscope. Initially, one exfoliates or picks up a hBN flake on the stamp. This

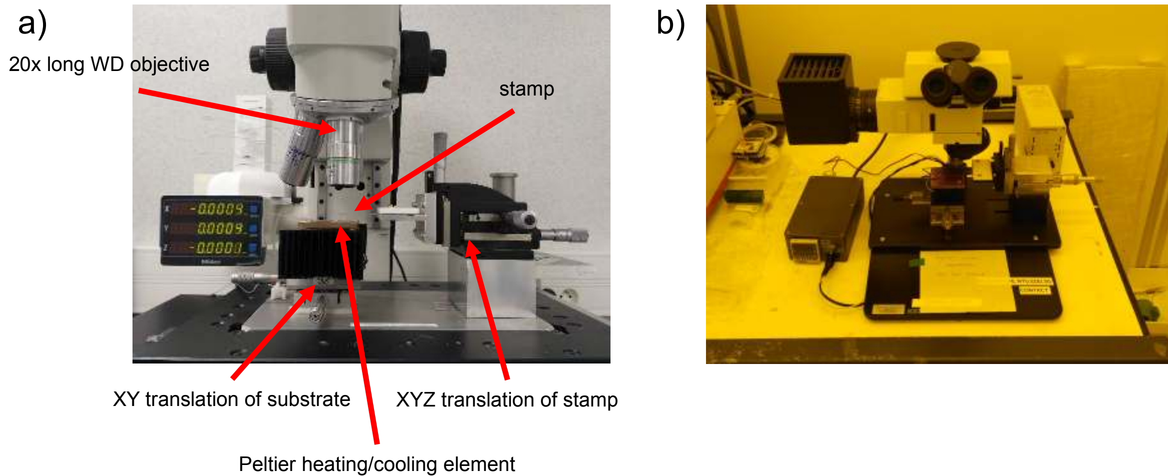

Figure 2.5 – The custom made transfer stations in the ENS cleanroom (a) and in the Nanyang NanoFabrication Centre cleanroom 2 (b).

top hBN is then brought in firm contact with a monocrystal of exfoliated or CVD graphene, which adheres to the hBN thanks to the strong van-der-Waals bonds between the two almost lattice matched materials. Finally, the stack is deposited on a bottom hBN flake. The stacks can then either be transferred onto local bottom gate electrodes or be patterned directly on the bottom hBN substrate. The entire process is illustrated in figure 2.6.

For both methods, we use a custom-made transfer station, consisting of a Mitutoyo microscope with long working distance lens, an XYZ-stage for the positioning of the stamp and an XY-stage carrying a heating plate (20-130°C). A photograph of the setup is shown in figure 2.5a. During the course of this thesis, the setup was upgraded significantly by myself and Romaric LeGoff; it was particularly helpful to upgrade the heater from a simple heating resistance to a Peltier element, which allows for active (faster) cooling. Another, simpler setup was built from scratch during my time at NTU in collaboration with PhotoniTech (Asia) Pte Ltd. It is shown in figure 2.5b. I built the temperature controller and provided the company with the translation stages and the design plan of the setup. The company provided the microscope and the assembly.

Other groups have put considerable efforts into the fabrication of particularly clean van der Waals heterostructures, e.g. using a hot pick-up technique [134], layer by layer stacking in vaccum [135] or "squeezing out" impurities [123]. Furthermore, it has recently become possible to assemble heterostructures in an automated manner [136], which might be a first step in the direction of scalable fabrication of 2D material based devices. These improvements go beyond the scope of this thesis. In the following, I will provide details about the two methods that I have used.

"Columbia" method

The stamps are fabricated by placing a PDMS cube ($\sim$ 2 mm) on a microscope slide. Scotch tape (Duck HD Clear) is placed on top of the PDMS cube, forming a "bubble" around the cube. Polypropylene carbonate (PPC) is spin coated on a silicon chip ($\sim 1 \times 1$ cm^2) and subsequently picked up using a piece of scotch tape with a $\sim 5 \times 5$ mm^2 hole. In this way,

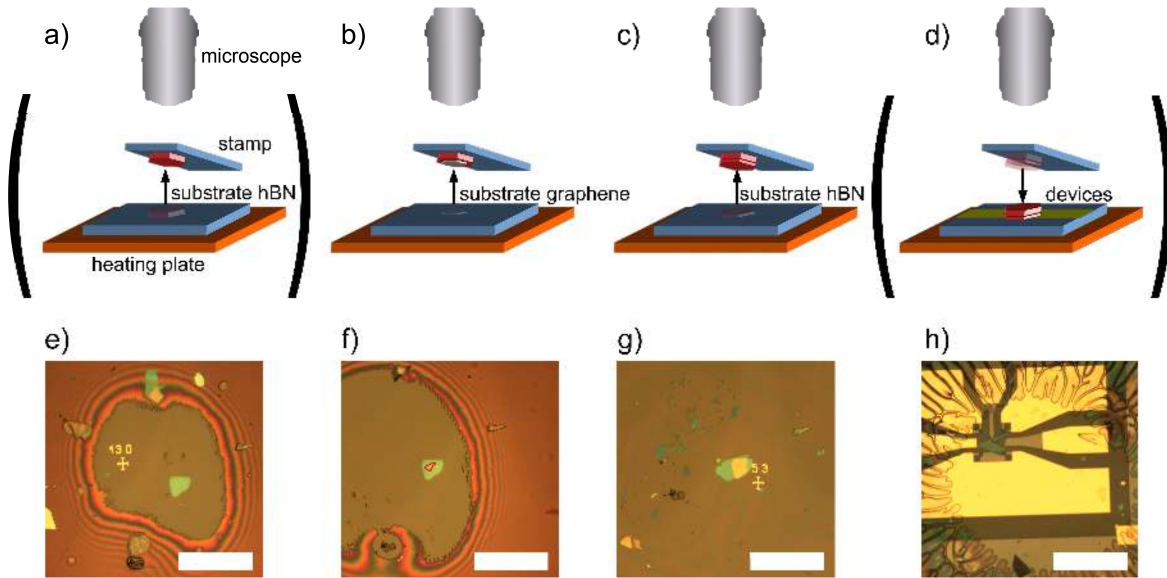

Figure 2.6 – Fabrication of van der Waals heterostructures: a-d) Illustrations of the three pick-up processes (hBN, graphene, hBN, first pick-up is optional) followed by the (optional) deposit of the finished stack on gate electrodes. e) The contact zone during the pick-up of a top hBN flake (while heating). The nearly circular shape of this zone and the surrounding interference pattern are due to the "bubble" shape of the "Columbia" stamp. f) Similar picture for the graphene flake (highlighted by the red contour). g) Similar picture for the bottom hBN flake. The contour of the contact zone is not visible here, because this picture corresponds to a deposit. h) Micrograph of a hBN-G-hBN stack after its deposit onto gate electrodes. The "channel-like" transparent features surrounding the center show where the PPC detached from the stamp. Scale bars are 200 μm.

the PPC film can be fixed on top of the "bubble", aligning the hole with the PDMS cube.

The glass slide is now mounted in the transfer station and aligned over a flake of hBN that was previously exfoliated on a chip of Si/SiO_2. The PPC film is carefully brought into contact with the wafer, such that the contact zone is close to – but not touching – the hBN flake of interest. The temperature of the heating plate is then gradually increased (to about 50-60°C), so that the PPC starts melting and enclosing the flake (c.f. figure 2.6e). In order to pick it up, the substrate is cooled down to 40°C and the stamp is detached. This sequence is repeated for the pick-up of the graphene and the bottom hBN flake (c.f. figure 2.6f-g). For the deposit, the substrate is heated to $\sim$ 100°C and the stamp is detached, leaving the sandwich and a PPC layer on the destination substrate (c.f. figure 2.6h).

For the deposit of large stacks $\gtrsim 30 \times 30\ \mu\text{m}^2$, this method had to be modified, because these stacks tended to stay on the stamp even though the surrounding PPC was transferred to the destination substrate. The trick is to heat to 105°C for 10 minutes, detach the stamp as far as possible, leaving only the center (where the heterostructure is located) in contact, then cool down to about 35°C and detach completely. Finally, the PPC stamp is removed from the substrate in an acetone bath and the sample is rinsed with IPA.

“Aachen” method

For this method, the stamps are fabricated on top of a (half) microscope slide covered with scotch tape: First, a thin layer of polyvinyl alcohol (PVA, 13% in H_2O) is spread with a pipette and annealed at 95°C for around 10 minutes. A layer of PMMA (chain length 50k, 4% in ethyl lactate, AR-P 639.04 from Allresist) is then spin coated at 1000 rpm for 60 s and annealed at 110°C for another 10 min.

The actual stamp only consist of the PVA+PMMA layers, the glass slide just serves as a support for the stamp fabrication and the scotch tape serves as a buffer layer, so that the stamp can easily be cut into small squares ($\lesssim 1 \times 1$ cm^2) and detached.

The major advantages of these stamps over the “Columbia” stamps are:

- **stability:** The rigid PVA+PMMA stamps can be manipulated with tweezers. Even if they stay stuck on a substrate, they can quite “violently” be pulled off without damaging the crystals they hold.
- **direct exfoliation:** Since the stamps are relatively flat and rigid, the top hBN can be exfoliated directly onto the PMMA surface. By identifying a suitable hBN crystal underneath the optical microscope, the stamp can be cut out around the crystal.
- **mass production:** The “Aachen” stamps are quickly fabricated and one half microscope slide can provide at least a handful of top hBN stamps.
- **CVD compatibility:** The high pressure required to pick up CVD graphene from its copper substrate cannot be applied on “Columbia” stamps.

The disadvantage is that due to the flat nature of the “Aachen” stamps, the contact area is much larger, which results in picking up and depositing a large number of crystals and leads to the pollution of the substrate.

For the actual stacking process, the stamp (with or without top hBN) is placed on a small PDMS square ($\lesssim 1 \times 1$ cm^2) of around 2 mm thickness sitting on a microscope slide. No glue is required, neither for the stamp/PDMS nor for the substrate. The glass slide is mounted in the transfer station and aligned over the (exfoliated or CVD) graphene. The stamp is brought into contact with the substrate and heated to around 130°C. After a couple of minutes, when all interference fringes have disappeared from the microscope image, the substrate is cooled down to below 50°C and the stamp is detached. Sometimes, in particular when picking up CVD graphene (see fig. 2.7), the stamp will stay attached to the substrate and has to be carefully peeled off using tweezers. The process is repeated for the bottom hBN. I have found that it helps to expose the bottom hBN substrate to an oxygen plasma (plasma cleaner for 5 minutes, before exfoliating the hBN) in order to promote the adhesion of the polymer stamp. The PVA is then removed from the destination substrate using a 95°C water bath with intermediate IPA rinsing steps. Finally, the PMMA residues are removed with acetone and a last IPA rinse.

Since the hot water bath damaged our thin tungsten films, graphene stacks could not be transferred to the nanostructured tungsten gates using the “Aachen” method. They were assembled using PVA+PMMA stamps and subsequently characterized by Raman spectroscopy and AFM, but the last transfer step was carried out using the “Columbia” PPC stamps described above.

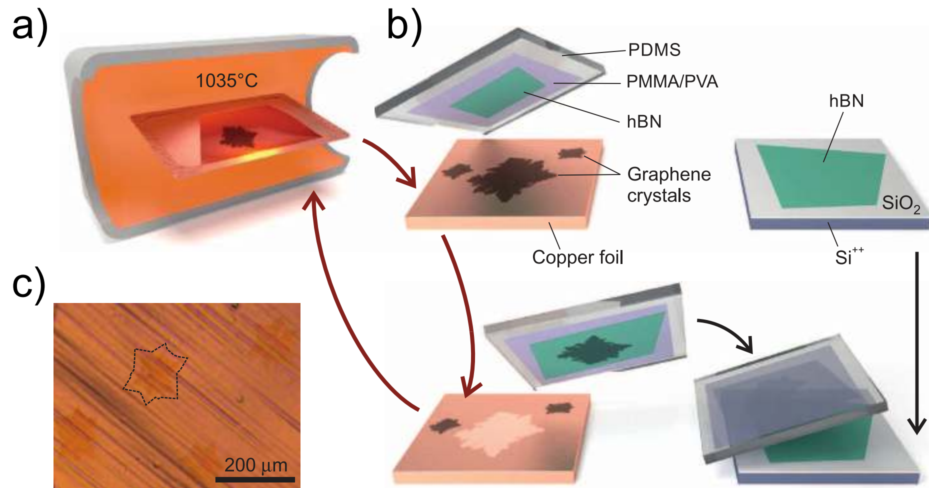

Figure 2.7 – **Encapsulation of CVD graphene.** a) Illustration of the growth and b) encapsulation of CVD graphene, highlighting the re-usability of the copper substrate. c) Microscope image of a typical ∼ 100 μm graphene flake grown in Aachen. Reproduced from [120].

2.1.4 Characterization of encapsulated samples

Raman spectroscopy

Raman spectra (and maps) were obtained with a Renishaw inVia Raman microscope and an excitation wavelength of 532 nm. Figure 2.8 shows typical spectra for encapsulated single- and bilayer graphene. The most prominent features are the graphene G-peak at ~ 1580 cm^{-1}, the 2D-peak at ~ 2700 cm^{-1} [137, 138] and the hBN-peak at ~ 1365 cm^{-1} [139, 140]. The D-peak at ~ 1345 cm^{-1} is either absent or too weak to be distinguished from the hBN-peak, which is an indication for a small density of defects in our samples [137]. A strong difference between the spectra of single- and bilayer graphene lies in the shape of the 2D band, which has four components in bilayer graphene [137], three of which can clearly be distinguished in the spectrum shown here.

A systematic study by Banszerus *et al.* [141] has shown that Raman spectroscopy can be used to study strain variations and substrate-induced doping in graphene, where the positions of the G and 2D peak, as well as the width of the latter were identified as relevant quantities. However, variations in the width of the 2D peak can also be a consequence of misalignment between the hBN and the graphene lattices, resulting in a so-called moiré superlattice. A study by Cheng *et al.* [142] establishes a link between the moiré wavelength (i.e. the twist angle) and the 2D peak width. In a more recent work by Ribeiro-Palau *et al.* [143], the 2D peak width could be tuned *in situ* by rotating a hBN flake with respect to the graphene sample using an AFM tip. This means that a narrow width of the 2D peak alone cannot be a discriminating criterion for a good encapsulated graphene sample (with high electronic mobility). Instead we used the Raman microscope to confirm the successful pick-up of (mostly single-layer) graphene and to identify *homogeneous* regions for subsequent device fabrication.

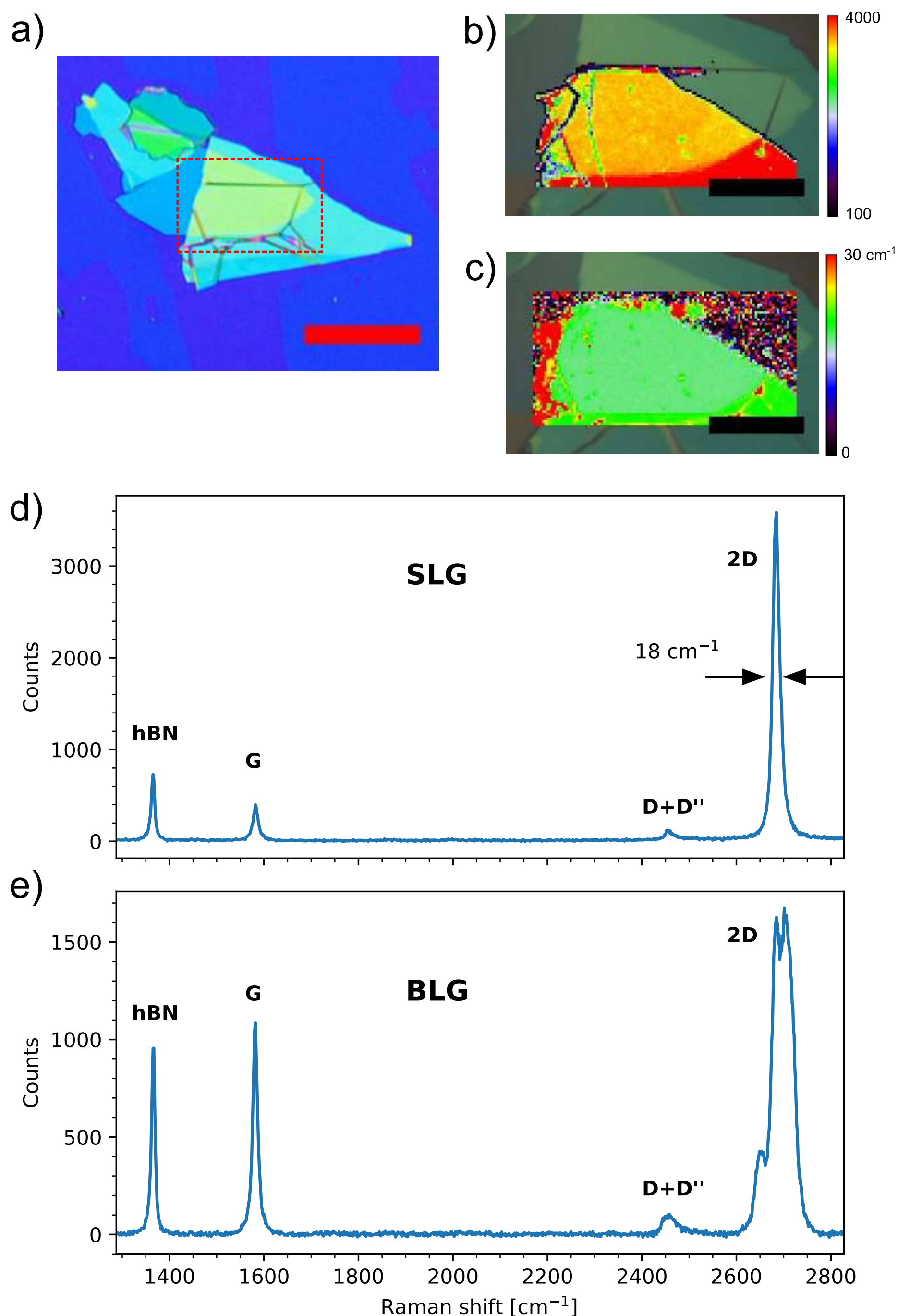

Figure 2.8 – **Characterization by Raman spectroscopy.** a) A white light micrograph of the stack TR-2018-04-19, which was used to fabricate PRC-D7. The red scale bar corresponds to 50 μm and the red dotted box denotes the area of the Raman maps in panels b and c. b) A map of the intensity of the 2D peak. The black scale bar corresponds to 20 μm. c) A map of the width of the 2D peak, consistently around 18 cm^{-1} in this sample. d) A sample spectrum from these maps. e) A sample spectrum from a bilayer graphene sample (TR-2018-08-31.1), which was used to fabricate PRC-D9.

Atomic force microscopy

Even though atomic force microscopy (AFM) does not necessarily give us new information about the quality of the hBN-G-hBN stack, it can be helpful to check for residual surface contamination due to the transfer polymer, and – more importantly – it is used to measure the bottom and top hBN thickness. This information can then be used to calculate the geometric gate capacitance $C_{\mathrm{geo}} = \epsilon_0\epsilon_r/t_{\mathrm{hBN}}$ (however, the gate capacitance can also be measured using the VNA, c.f. chapter 4 or using the quantum Hall effect [144]).

Figure 2.9 shows an example of a complete characterization cycle: After the fabrication of the hBN-G-hBN stack, the graphene layer can in some cases already be seen as a very weak contrast in the optical micrograph (panel a). Raman spectroscopy validates this first impression (panel b). An AFM image is then acquired with a Bruker Dimension Edge AFM (panel c) and used to measure the step height corresponding to the bottom hBN (23 nm here) and the top hBN (15 nm here), c.f. panel d.

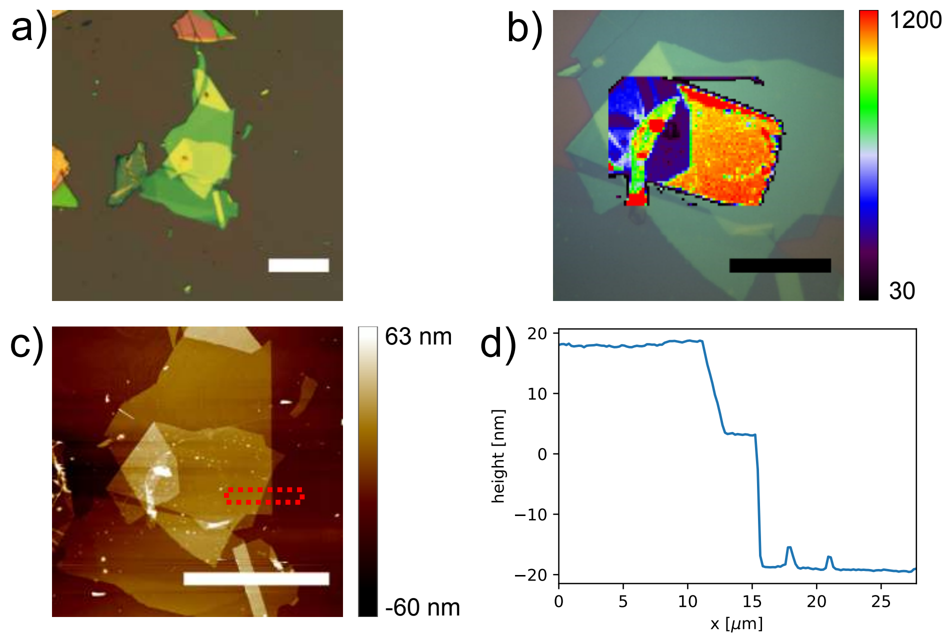

Figure 2.9 – **Full characterization chain: Raman spectroscopy and atomic force microscopy (AFM).** a) A white light micrograph of the stack TR-2018-08-31.1, which was used to fabricate PRC-D9. b) A Raman map of the G-peak intensity, showing clearly the location of the encapsulated graphene. c) AFM image of the sample. d) Height profile along the x-direction in the red dotted box in c). White scale bars 50 μm, black scale bar 20 μm.

2.1.5 Defining structures

Etching the heterostructures

The encapsulated graphene samples are etched into the desired shape using reactive ion etching (RIE). This is a dry etching process where a plasma attacks the material both chemically and physically. The chemical reaction removes the material in a much more isotropic manner than the physical one, because the latter is controlled by the direction of the electric field applied in the etching chamber (c.f. gold gate fabrication in section 2.1.2).

For the fabrication of corner reflector devices (chapter 3), PMMA was used as an etching mask: The sample was coated in PMMA, EBL was used to expose it where the heterostructure should be *removed*, i.e. everywhere around the active region, RIE was carried out and eventually the sample was cleaned in acetone (see also top row of fig. 2.10). The disadvantage of this method is that etching tends to cross-link the resist, which makes it very difficult to remove with acetone and leads to PMMA residues on the entire device.

This is why, for the fabrication of plasma resonance capacitors (chapter 4), we used an aluminum hard mask: the first step is again to coat the sample with PMMA and to use EBL, this time to define the region where the heterostructure should *stay*. A thin layer (~ 50 nm) of aluminum is then deposited. After the lift-off in acetone, the aluminum film only stays where we want to protect the stack. RIE is carried out and, finally, the aluminum mask is removed using a KOH solution. In both cases, RIE was done in a Corial 200R with a CHF_3/O_2 plasma at flow rates of 40 and 4 sccm respectively, a pressure of 6 mTorr and a RF power of 60 W. This etch recipe corresponds to the one used in ref. [118].

Alternatively, a hydrogen-silsesquioxane (HSQ) hard mask could be patterned directly by EBL [118] and the etching could be carried out using SF_6 and Ar plasma [120]. It is also possible to stop the etching process precisely on top of the graphene sheet, see e.g. ref. [145]. The edge profile resulting from these etch processes is typically tilted enough to deposit a metal layer on the side: the edge contact.

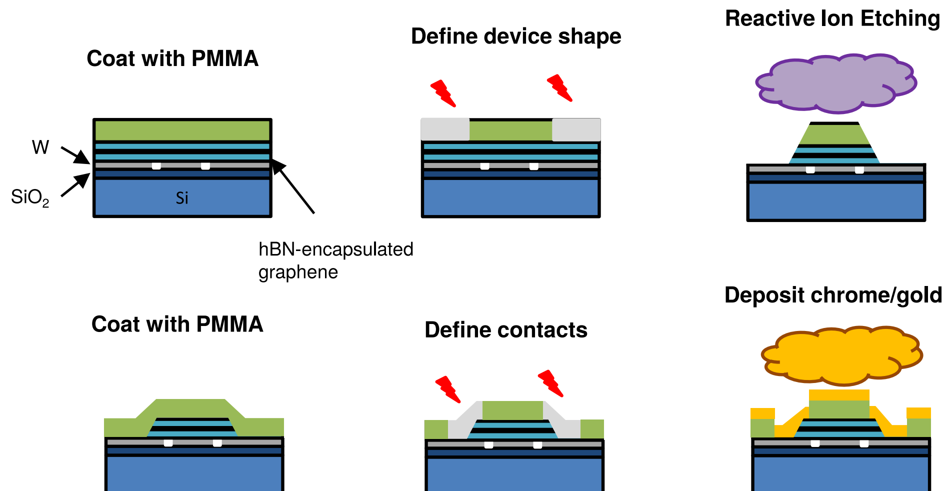

Figure 2.10 – **Defining structures.** Top: Illustration of the etching of heterostructures. Bottom: Illustration of the fabrication of edge contacts.

Depositing contacts

Already in the first reported fabrication of a one-dimensional edge contact [118], a study of different contact metals is given in the supplementary material. Cr/Au and Cr/Pd/Au were identified as particularly suitable. Another group has reported working Ti/Al contacts, see e.g. the supplementary material of [146], but the only time I tried it did not work. All working samples fabricated throughout this thesis project have Cr/Au contacts. The thickness was typically 5 nm Cr and 100−200 nm Au.

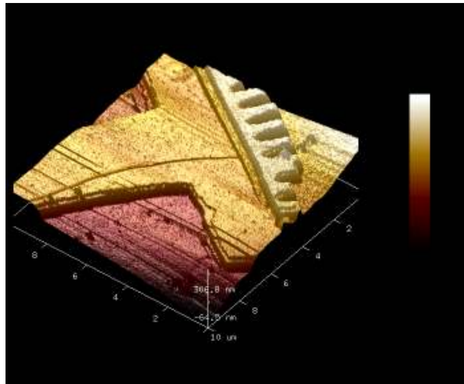

Figure 2.11 – Atomic force microscopy image of the edge contact on PRC-D3.

Contacts were defined using EBL on a PMMA resist and the contact metal was deposited using a resistive (Joule) evaporation process in an Edwards E306A evaporator (see also bottom row of fig. 2.10). In order to reduce the contact resistance of the plasma resonance capacitors (chapter 4), the 1D contact "surface" was enhanced by cutting it into a comb-shape. An AFM picture of such a contact is shown in fig. 2.11.

Passivation of edges

If the graphene edge is exposed around the entire sample, depositing a top gate electrode is difficult without creating a gate-graphene short circuit *via* the edge. For the bottom gated corner reflector devices (chapter 3), this was not an issue, but for the top gated plasma resonance capacitors (chapter 4), the edges of the hBN-G-hBN heterostructure had to be passivated by depositing a layer of aluminum oxide.

This was done in two steps: first, two thin layers of aluminum (1 nm) were deposited by Joule-evaporation and then, each time, left to oxidize for about 15 minutes at 200 mbar O_2. Then, about 10 nm of Al_2O_3 were deposited using an Anric AT400 atomic layer deposition (ALD) at 175°C performing 100 cycles.

It turned out that this layer had pretty catastrophic adhesive properties: if we deposited contact pads directly on top of the aluminum oxide, the probe tips would simply rip them off. The lift-off of aluminum oxide proved to be nearly impossible, so a wet-etch approach was employed: EBL on PMMA defined the regions where the Al_2O_3 film would be removed subsequently by submerging the sample in a KOH bath for a couple of minutes.

Depositing top gates

Top gates are patterned using EBL on PMMA and deposited using a Joule-evaporation process of Cr/Au in an Edwards E306A evaporator, exactly like the edge contacts mentioned above. The thickness was typically 5 nm Cr and 200 nm Au. This was usually done simultaneously with the definition of coplanar waveguides, see below.

Defining coplanar waveguides

In order to make the devices compatible with high frequency characterization in our Janis cryogenic probe station, they have to be embedded in a coplanar waveguide (CPW). This CPW has to fit the 100 μm pitch (tip separation) of the probe tips and to be 50 Ω impedance matched.

For the design of these CPWs, we use Broadcom (formerly Avago) AppCAD. The software predicts a characteristic impedance of 49.2 Ω for a CPW with a center conductor width of 70 μm surrounded by gaps of 40 μm. This tip access is tapered towards the actual device width. If the device width is e.g. 25 μm, we can use AppCAD to calculate the corresponding gap size 16 μm to keep a $\sim$ 50 Ω characteristic impedance. Between the access and the sample, we interpolate with straight lines, c.f. figure 2.17 for an example. The phase velocity predicted for these geometries is 0.40 c, where c is the speed of light in vacuum.

The CPWs are defined by EBL, followed by the deposit of Cr/Au (5/200 nm), in the same manner as the contacts and the top gates were fabricated.

2.2 Device characterization

2.2.1 The Janis cryogenic probe station

The electronic transport measurements presented in chapters 3 and 4 were all carried out in a Janis cryogenic probe station which operates between $T \approx 6$ K and 450 K. Figure 2.12 show pictures of the probe station itself (open), of the instrument rack and of the screen showing the G-S-G probe tips in contact with a sample.

Samples are fixed on the chuck using silver paint, which ensures an electrical contact between the chuck and the substrate (silicon in our case). Since the chuck is electrically isolated from the rest of the chamber, its voltage can be controlled independently by connecting it to the Yokogawa voltage source. This is used for substrate-gating in chapter 4.

Before cooling down the probe station, a lid is placed on top of the vacuum chamber. A window in the lid enables the user to observe the sample and the probe tips using the camera. A combination of primary pump and turbo pump is then used to reduce the pressure in the vacuum chamber to around 10^{-5} mbar at room temperature.

Liquid helium (LHe) is then inserted into the cooling capillary of the cryostat. Unlike in many other cryostats, where LHe is inserted only once and then a measurement campaign can run for a couple of days without supervision, this probe station requires a constant flow of LHe. This can be done without supervision if the pressure in the LHe dewar stays constant, but that is not always easy to guarantee.

The probe tips are moved using remote micrometer screws, which enables the user to precisely place them on the extremities of the coplanar waveguides leading to our samples.

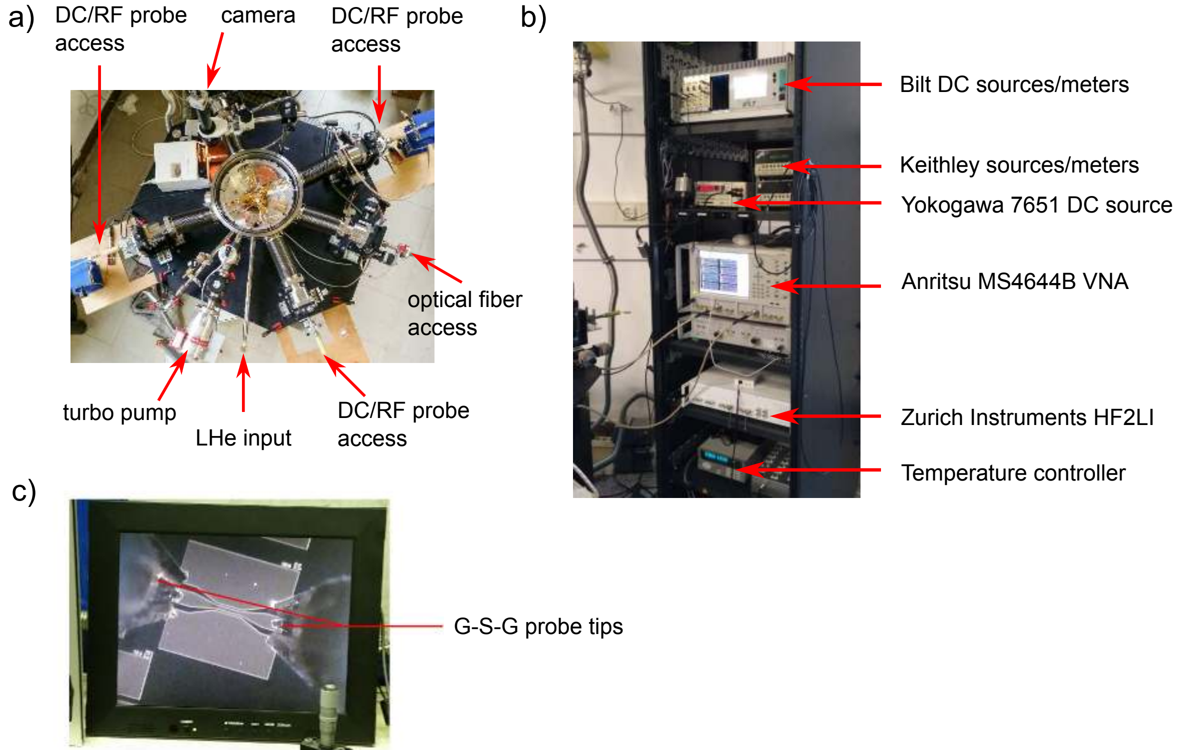

Figure 2.12 – **Janis cryogenic probe station.** a) The cryogenic vacuum chamber with coaxial 40 GHz access lines. b) The instrument rack. c) A screen showing a microscope image of the probe tips. From ref. [24].

On the other hand, instruments are connected to the probe tips *via* the coaxial connectors denoted “DC/RF probe access”.

Lock-in characterization of corner reflector devices

Most of the measurements discussed in chapter 3 were carried out using the Zurich Instruments lock-in amplifier. It was connected to the drain electrode of the sample *via* a 2.2 kΩ voltage divider, c.f. fig. 2.13.

At the lowest temperature (6 K), the thermal excitation corresponds to $k_B T \approx 0.5$ meV. However, since the contact resistance ($\sim$ 5 kΩ) in series with the 2.2 kΩ voltage divider represents a much higher resistance than the typical sample resistance $\lesssim$ 1 kΩ, it seemed safe and reasonable to use an excitation amplitude of 5 mV. A frequency sweep from 10^2 to 10^7 Hz was carried out to identify a frequency range where the device response was flat and the measurement frequency was chosen in the center of this window (10.013 kHz). The time constant (200 μs) was chosen short enough to follow the gate voltage sweep (on the order of 20 ms per data point). Similarly the sampling rate was set to a reasonable value (900 Hz). The device resistance was deduced from the lock-in measurement $R_{\rm ds} = 2.2\ {\rm k}\Omega \times V_{\rm in}^{\rm rms}/(V_{\rm out}^{\rm rms} - V_{\rm in}^{\rm rms})$, where $V_{\rm in/out}^{\rm rms} = V_{\rm in/out}^{\rm peak}/\sqrt{2}$. The 100 kΩ voltage dividers at the gate terminals were used initially to detect potential gate leakage, but were then removed in order to increase the sweep speed.

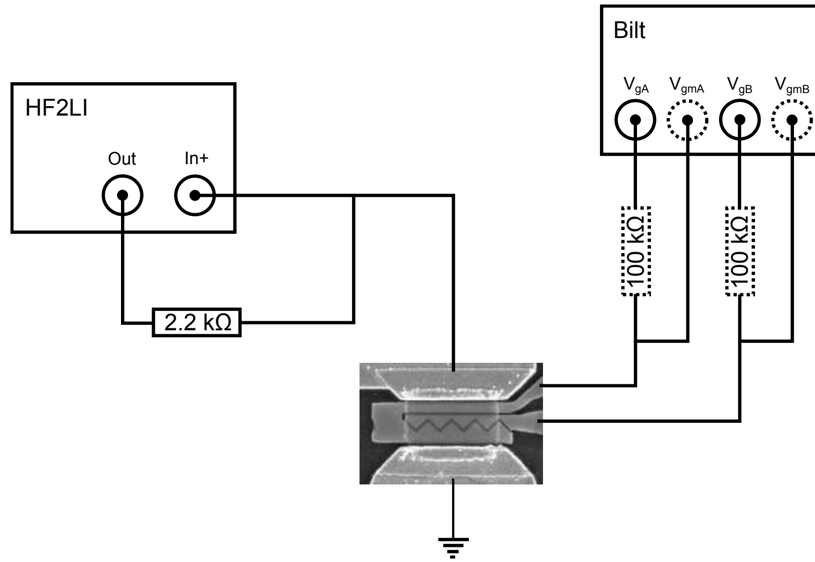

Figure 2.13 – Wiring scheme for the lock-in characterization.

High frequency characterization of corner reflector devices

Figure 2.14 shows the wiring scheme for the VNA characterization of the corner reflector devices. Bias tees (Marki BTN0040 1417, 40 kHz−40 GHz) were used to decouple the DC gate/drain bias from the RF probe signal. A 100 kΩ voltage divider was used at the access gate. Here the voltage is swept very slowly. At the barrier gate terminal, which is swept much quicker – and *via* a bias tee – we omitted this voltage divider in order to avoid delays induced by charging times. The drain voltage was kept constant at 10 mV and the DC device resistance was measured simultaneously with the RF response *via* the 2.2 kΩ voltage divider.

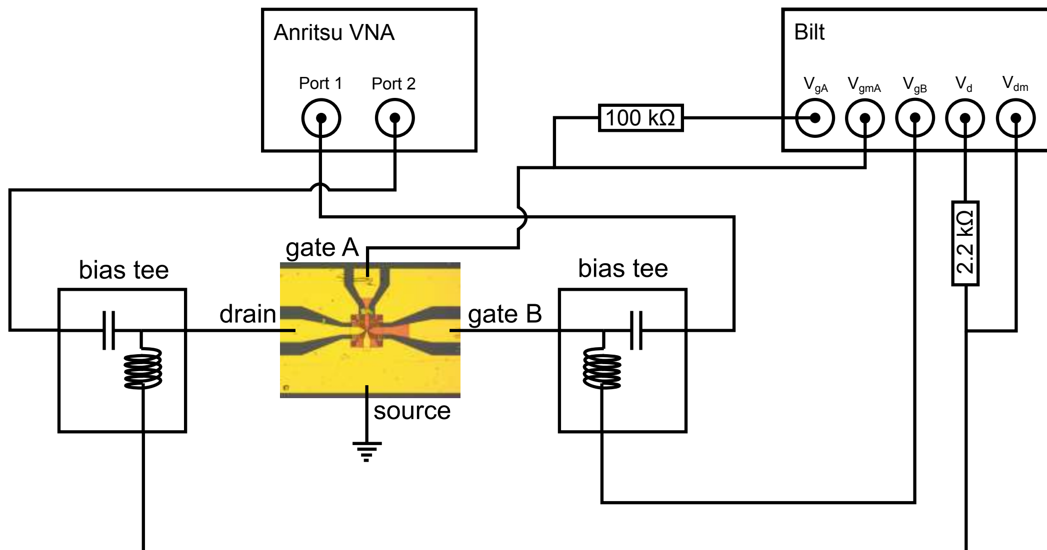

Figure 2.14 – Wiring scheme for the VNA characterization of corner reflector devices.

The RF power was typically set to -27 dBm, which corresponds to an amplitude voltage of 10 mV. At cryogenic temperature, this exceeds the thermal excitation $k_BT \sim 0.9$ meV, but taking into account the losses in the coaxial access lines (frequency dependent, ~ 10 dB) and due to the contact resistance, this power level stays a reasonable choice and provides a decent signal to noise ratio.

High frequency characterization of plasma resonance capacitors

The wiring scheme for the characterization of the plasma resonance capacitors (PRCs) is shown in figure 2.15. As mentioned above, bias tees were used to decouple the gate voltage from the RF signal and again, a 100 kΩ resistor was used as a voltage divider. The chuck of the probe station was connected to a Yokogawa 7651 voltage source, which enabled us to apply an additional gate voltage, since the silicon substrate of the PRCs is glued to the chuck using conductive silver paint. The RF power was typically set to -27 dBm, as explained previously.

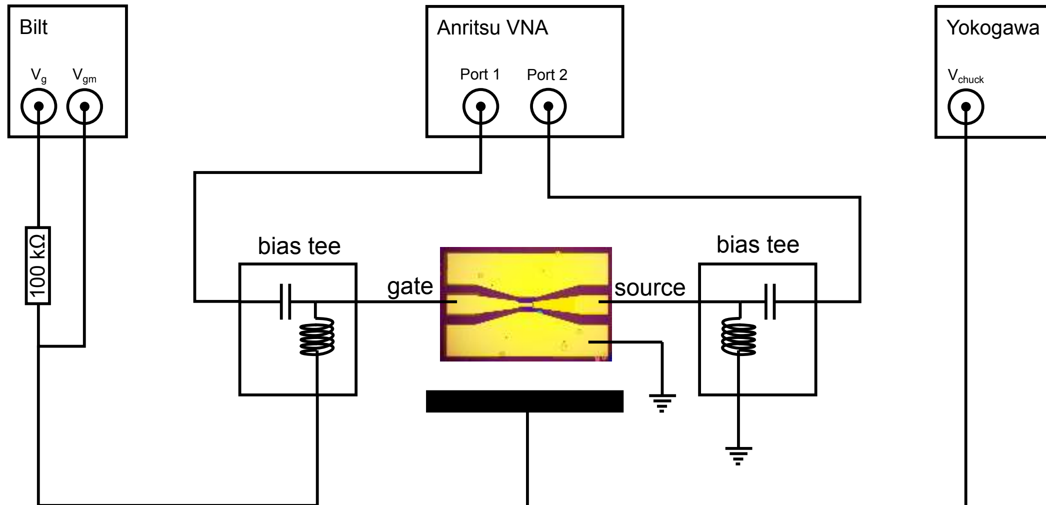

Figure 2.15 – Wiring scheme for the VNA characterization or plasma resonance capacitors.

2.2.2 VNA measurements

The vector network analyzer (VNA) is a powerful characterization tool for high frequency electronics. It enables a broadband measurement of the amplitude and phase of a microwave with respect to a reference signal and can therefore be used to measure the reflection and transmission coefficients of an n-port network [147].

Scattering, admittance and cascade matrices

Throughout this thesis we will concentrate on 2-port networks, such as illustrated in figure 2.16. The VNA measures the *scattering* matrix S_{mn}, defined as follows:

$$S_{ij} = \left.\frac{b_i}{a_j}\right|_{a_k=0 \text{ for } k\neq j} \qquad \text{with} \quad \{i,j\} \in \{1,2\} \tag{2.2}$$

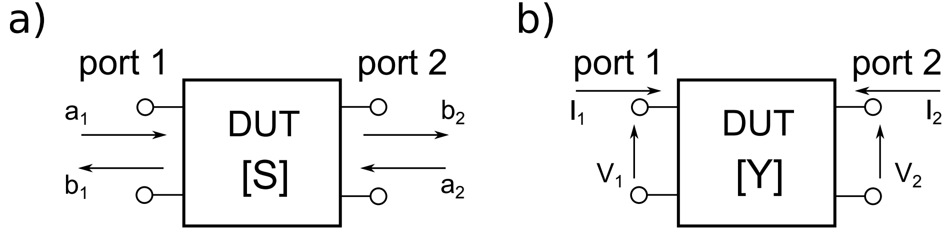

Figure 2.16 – **The two-port network:** scattering (a) and admittance (b).

where a_i and b_i are the complex amplitudes entering and exiting (respectively) the network at port i [148]. Throughout this thesis, we will focus a lot more on the so-called *admittance* matrix Y_{ij}, because it is more closely related to the actual circuit elements. It is defined as follows:

$$Y_{ij} = \left.\frac{I_i}{V_j}\right|_{V_k=0 \text{ for } k\neq j} \tag{2.3}$$

where I_i and V_i are the current entering and the voltage across port i, see fig. 2.16b. It can be calculated from the scattering matrix [148]:

$$Y = \frac{1}{Z_0\Delta}\begin{bmatrix}(1-S_{11})(1+S_{22})+S_{12}S_{21} & -2S_{12} \\ -2S_{21} & (1+S_{11})(1-S_{22})+S_{12}S_{21}\end{bmatrix} \tag{2.4}$$

where $\Delta = (1+S_{11})(1+S_{22})$ and $Z_0 = 50\ \Omega$ in our case. For de-embedding (see below), we will additionally make use of the transmission/cascade matrix ($ABCD$-matrix, denoted $\mathcal{A}$ in the following). Its purpose is to easily calculate the behavior of composite systems by multiplying their cascade matrices and it can be calculated e.g. from the scattering matrix:

$$\mathcal{A} = \frac{1}{2S_{21}}\begin{bmatrix}(1+S_{11})(1-S_{22})+S_{12}S_{21} & Z_0\left[(1+S_{11})(1+S_{22})-S_{12}S_{21}\right] \\ Z_0^{-1}\left[(1-S_{11})(1-S_{22})-S_{12}S_{21}\right] & (1-S_{11})(1+S_{22})+S_{12}S_{21}\end{bmatrix} \tag{2.5}$$

Calibration

In order to account for changes of the physical characteristics of the VNA over time, but also for the frequency response of the cables and probe tips connecting the instrument to our "device under test" (DUT), a calibration has to be carried out prior to the measurement. The calibration enables the instrument to remove the phase propagation and attenuation due to the cables from the measurement. Throughout this thesis, a short-open-load-reciprocal (SOLR) calibration protocol was used. It consists in measuring the frequency response of a short and an open circuit, a 50 Ω impedance match and a thru-line of arbitrary length, all of which are accommodated on a calibration substrate (CS-5 from GGB Industries, Inc.) which is placed inside the Janis cryogenic probe station, next to the substrate containing the DUT.

The calibration moves the so-called "calibration plane" from the macroscopic coaxial VNA ports to the end of the microscopic probe tips. It is carried out after every change of temperature (i.e. after each cool-down), in order to compensate for dilation/compression of the coaxial lines. The possibility of *in situ* calibration of the phase is a major advantage of our probe station compared to "classical" cryostats.

De-embedding

Since our devices are embedded in a co-planar waveguide (CPW), the phase propagation on both sides of the CPW and the parasitic capacitances should be taken into account. In order to de-embed the response of our DUT from these contributions, we fabricate two kinds of reference devices on the same chip: "thru" and "dummy". The thru is a symmetric CPW without any active component in the center, simply connecting the two probes. The dummy has the same geometry as the DUT, but without the active component, i.e. it is an open circuit.

In order to de-embed the phase propagation of the CPW access from the DUT and the dummy, the ABCD matrix of the thru, dummy and DUT ($\mathcal{A}_{\text{thru}}$, $\mathcal{A}_{\text{dummy}}$, $\mathcal{A}_{\text{DUT}}$) are calculated from their scattering parameters. By taking the square root of $\mathcal{A}_{\text{thru}}$, we obtain the half-thru response, which we can then de-embed from the DUT's and dummy's ABCD matrices, simply by multiplying the inverse of the half-thru on both sides [24]:

$$\mathcal{A}'_{\text{DUT}} = \left(\mathcal{A}_{\text{thru}}{}^{1/2}\right)^{-1} \cdot \mathcal{A}_{\text{DUT}} \cdot \left(\mathcal{A}_{\text{thru}}{}^{1/2}\right)^{-1} \tag{2.6}$$

$$\mathcal{A}'_{\text{dummy}} = \left(\mathcal{A}_{\text{thru}}{}^{1/2}\right)^{-1} \cdot \mathcal{A}_{\text{dummy}} \cdot \left(\mathcal{A}_{\text{thru}}{}^{1/2}\right)^{-1} \tag{2.7}$$

The cascade matrices are then converted to admittance parameters (Y'_{dummy}, Y'_{DUT}). Stray capacitances can now be removed from the DUT measurement by subtracting the dummy's admittance:

$$Y''_{\text{DUT}} = Y'_{\text{DUT}} - Y'_{\text{dummy}} \tag{2.8}$$

Figures 2.17a and c show an example picture and spectrum of a thru. The S_{12} and S_{21} spectra of the thru shows that we have a transmission of almost unity (about 3% loss/reflection on average) with a constant dephasing of $\Delta\phi/\Delta f = -60°/40$ GHz. The propagation velocity of the electromagnetic wave can be deduced from this phase shift:

$$v = \frac{2\pi L_{\text{thru}} \Delta f}{\Delta\phi} \tag{2.9}$$

where L_{thru} is the length of the thru. If we take into account a probe overlap of about 30 μm in from both ends of the device, the effective propagation length between the tips is $L_{\text{thru}} = 490$ μm, which results in $v = 0.39\ c$ where c is the speed of light in vacuum. This is in good agreement with the value 0.40 c predicted by AppCAD (see section 2.1.5). This also means that an uncertainty of 10 μm in the tip position corresponds to a $\sim 1°$ phase uncertainty at 40 GHz, which is reasonably small.

Figures 2.17b and d show a picture and a typical admittance matrix Y'_{dummy} of a dummy, which was already de-embedded from the thru. Even though it is difficult to see in the picture, there is a small gap between the "gate" electrode coming from the left and the "contact" electrode on the right. The device has the same shape as the corresponding "device under test" (DUT), which is a plasma resonance capacitor, but does not contain graphene. This enables us to measure the parasitic gate-source capacitance, which appears as a constant slope $j\omega C_{\text{gs}}$ in the imaginary part of the admittance spectrum, where $C_{\text{gs}} \sim 1$ mS/($2\pi \times 40$ GHz) = 4 fF.

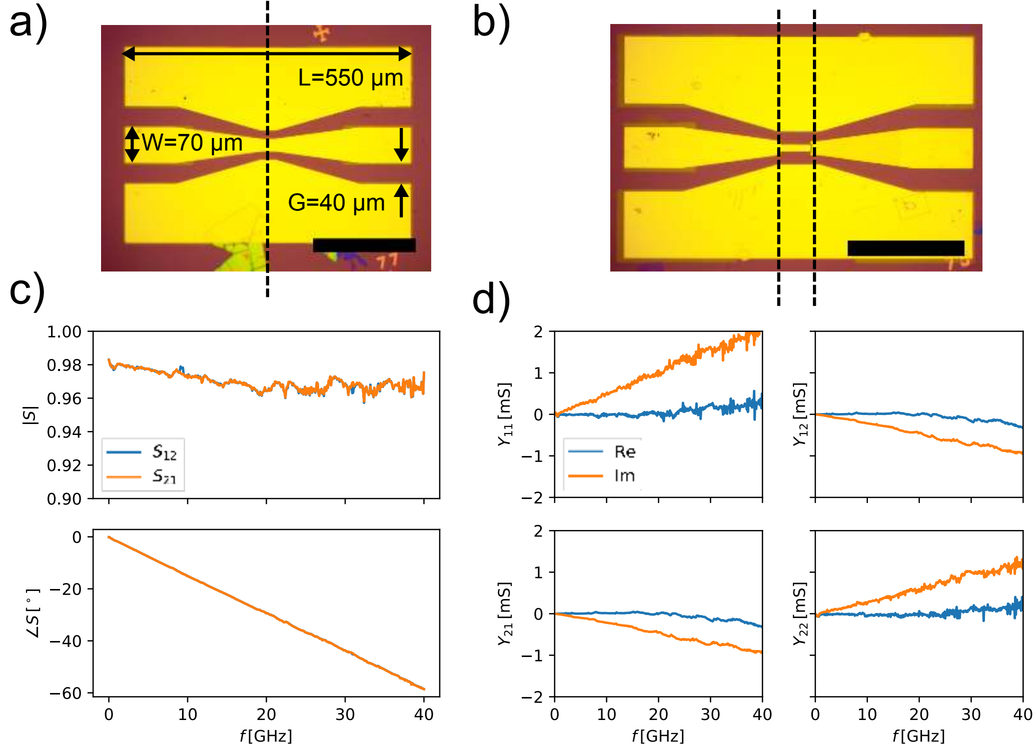

Figure 2.17 – **De-embedding.** a) Microscope image of a thru-line. b) Microscope image of a dummy structure. In both cases the scale bar corresponds to 200 μm. The black dashed lines indicate the calibration plane after de-embedding the propagation in the thru-line. c) Transmission parameters (S_{12} and S_{21}, magnitude and phase) of a thru-line. d) Complex admittance matrix of a dummy structure.

Small signal model of a graphene transistor

Since the design of novel high frequency transistors is not the main aim of this thesis, and the RF measurements presented in chapter 3 are first and foremost a proof of concept of GHz operation of a Dirac fermion optics device rather than a detailed study of the high frequency figures of merit (cut-off frequency etc.), I will only provide the crucial formulas that are used to extract transconductance, source-drain resistance and gate capacitance from the admittance matrix [149]:

$$Y_{11}(\omega) = j(C_{\text{gs}} + C_{\text{gd}})\omega \tag{2.10}$$
$$Y_{12}(\omega) = -j\omega C_{\text{gd}} \tag{2.11}$$
$$Y_{21}(\omega) = g_{\text{m}} - j\omega C_{\text{gd}} \tag{2.12}$$
$$Y_{22}(\omega) = g_{\text{ds}} + j\omega C_{\text{gd}} \tag{2.13}$$

where C_{gs} and C_{gd} are the gate-source and gate-drain capacitances respectively, $g_m = \partial I_d/\partial V_{\text{gs}}|_{V_{\text{ds}}=\text{const.}}$ is the transconductance and $g_{\text{ds}} = R_{\text{ds}}^{-1}$ is the drain-source conductance. The corresponding small-signal equivalent circuit is illustrated in figure 2.18.

Here we are assuming that the charging resistance of the gate and the transit time are

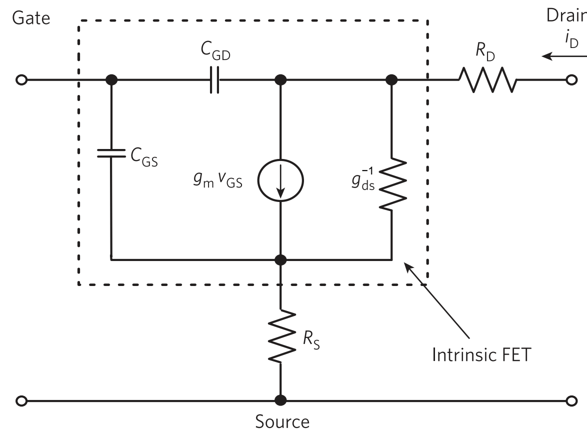

Figure 2.18 – **Small-signal equivalent circuit of a graphene FET.** Parasitic capacitance and gate resistance were omitted in this scheme. Adapted from [150].

negligible. The latter assumption is justified by the fact that the dwell times in our transistor are on the order of the picosecond ($v_F = 10^6$ ms^{-1} and $L \sim 10^{-6}$ m), which leads to $\omega\tau \ll 1$ in the GHz range. For a more detailed analysis, the reader is referred to Quentin Wilmart's thesis [23, p. 117], Frank Schwierz' book [149, pp. 221-231] and article [150] on this topic.

2.2.3 Noise measurements

The DC transport and noise measurements discussed in chapter 5 were carried out by Wei Yang. In this section I will briefly describe the setup used for these measurements.

Whereas all measurements presented in chapters 3 and 4 were carried out in a Janis cryogenic probe station, these noise measurements were done in an Oxford immersion cryostat (see fig. 2.19f) equipped with a superconducting coil to apply strong magnetic fields (up to 9 T). The sample is cooled down to 4.2 K by immersing it in liquid helium. The same setup has been used in the past by Chaste *et al.* [151] for noise measurements in carbon nanotubes and by Betz *et al.* [22, 65, 152] to study cooling pathways in graphene. While these studies were done with a bandwidth of 1 GHz, Wei Yang's measurements cover a frequency range 0-10 GHz [144] which is required to overcome $1/f$-noise at high currents (for an order of magnitude calculation, see section 1.3).

The sample (fig. 2.19c) is wirebonded to the sample holder (designed by Anne Denis, see fig. 2.19d), which is equipped with coaxial "end launch" connectors (K standard, 2.92 mm, Southwest Microwave) that can be used up to 40 GHz. DC voltages are applied using Yokogawa 7651 voltage sources and measured using Keithley 2000 voltmeters. They are decoupled from the RF measurement by a capacitor (C_2 in the wiring scheme in figure 2.19a). The circuit is 50 Ω-impedance matched in order to minimize RF reflection. The noise signal is amplified (32 dB) at cryogenic temperature by a Caltech low noise amplifier with a bandwidth of 12 GHz. The signal is amplified again at room temperature (35 dB) before it enters the oscilloscope. Attenuators (-3 dB) were added to the amplification chain in order to damp standing waves. The noise spectra are obtained by fast Fourier transformation (FFT) of the time domain signal, which was done directly by the oscilloscope (using a Hann window function and averaging 200 times).

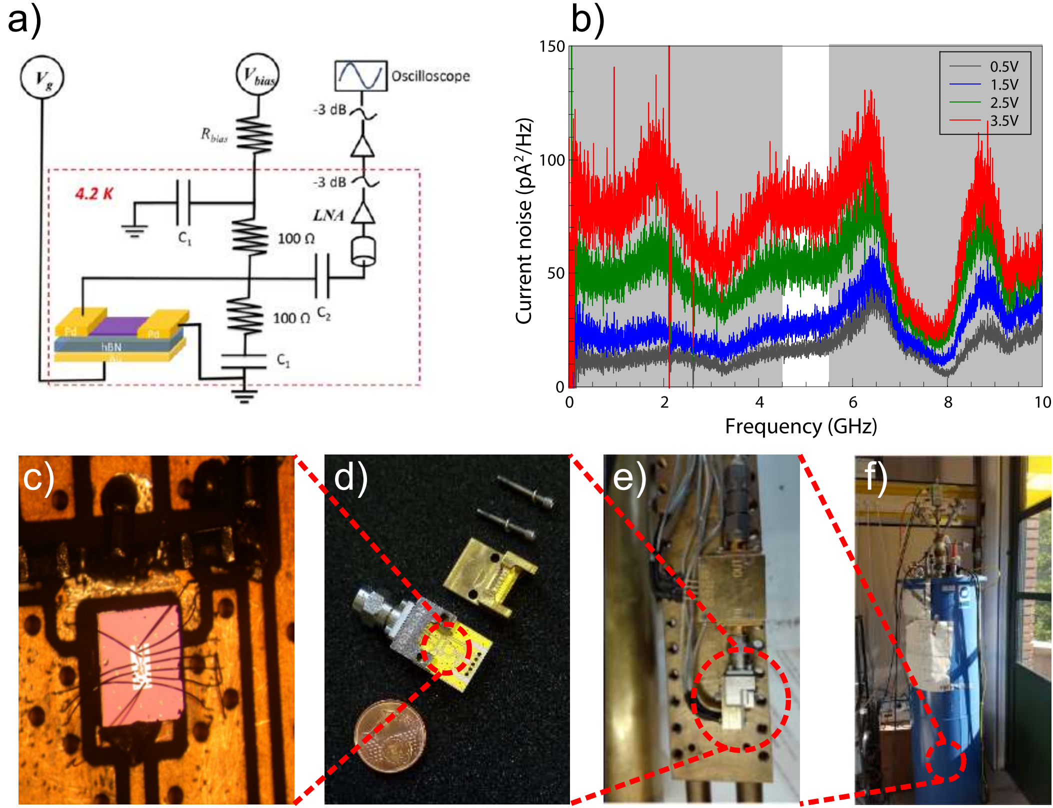

Figure 2.19 – **Noise thermometry setup.** a) Wiring scheme. b) Example spectra, flat around 5 GHz. c) Sample wirebonded to the d) sample holder. e) The sample holder attached to the LNA on the cryostat insert. f) The cryostat. a-b) taken from the supplementary material of ref. [144] c, e and f) taken from ref. [25].

In order to calibrate the power gain of the amplification chain and spurious noise in the setup, the noise of an Al/AlO$_x$/Al tunnel junction is measured. Due to its low transmission, its noise is Poissonian (white noise) with a Fano factor of unity: $S_{VV} \propto 2eI$. By measuring the voltage power spectral density (PSD) $S_{VV}(f, I)$ at a given frequency f as a function of the current I, one therefore obtains a linear relation. Extrapolating this to the current where $S_{VV}(f, I = -I_{\text{noise}}(f)) = 0$, one obtains the current value $I_{\text{noise}}(f)$, which – in combination with the voltage noise at zero current $S_{VV}(f, I = 0)$ – is used to calculate the current noise generated by the sample:

$$S_I^{\text{sample}}(f, I) = \left(\frac{S_{VV}(f, I)}{S_{VV}(f, I = 0)} - 1 \right) 2eI_{\text{noise}}(f) \tag{2.14}$$

For the mathematical details of this calibration method the reader is referred to the PhD theses of Andreas Betz [22] and Simon Berthou [25]. The fitting procedure is illustrated in the fig. 2.20a, with the extracted values for $I_{\text{noise}}(f)$ plotted in panel b.

The value of I_{noise} can also be used to calculate the noise temperature of the overall

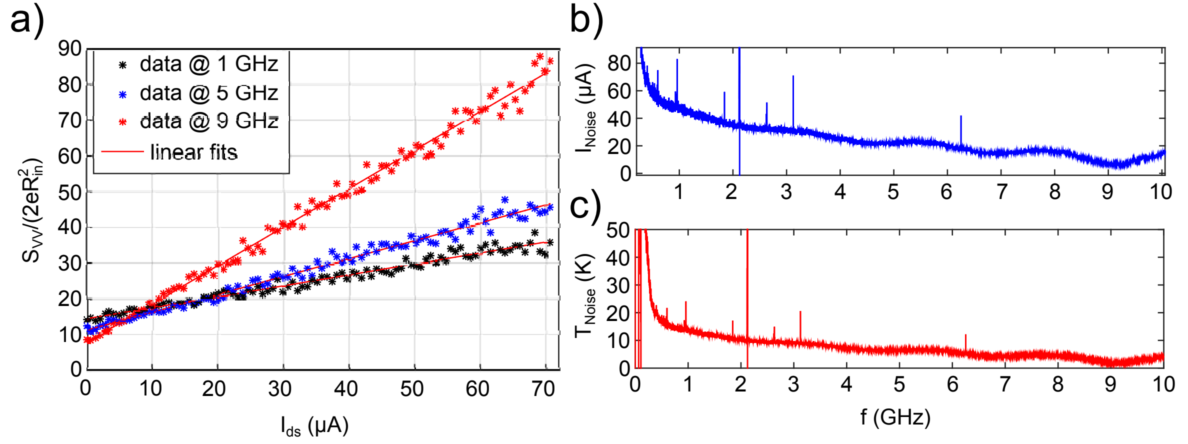

Figure 2.20 – **Noise calibration.** Left panel: Linear fits on noise as a function of current are used to extract I_{noise} and T_{noise}, plotted in the panels on the right for all frequencies.

experimental setup (see also panel c of figure 2.20):

$$T_{\text{setup}} = \frac{2eI_{\text{noise}}(f)R_{\text{in}}}{4k_{\text{B}}} \tag{2.15}$$

where R_{in} is the input impedance of the amplification chain. Subtracting the 4.2 K of the helium bath temperature, one obtains approximately 4 K excess noise (at 5 GHz) due to the amplifiers.

As we can see in the example spectra shown in fig. 2.19, the current noise spectra obtained in this manner still suffer from spurious resonances, caused by imperfections of the calibration process due to the difference between the resistance of the tunnel junction and the graphene channel. The optimization of this circuitry is work in progress and the measurements discussed in chapter 5 are obtained by averaging the PSD between 4.5 and 5.5 GHz, where the spectra are flat.

3
Dirac fermion optics

In this chapter, we will build upon the notions explained in chapter 1 and introduce the concepts of Dirac fermion optics (DFO). Then, a short review of various theoretical proposals and experimental realizations of DFO shall be given. The device we will focus on afterwards is the corner reflector (CR), a graphene transistor with a sawtooth-shaped gate electrode (artist view in fig. 3.1). I will first provide an analytical model for the transmission of this device and explain ray tracing simulations. Then I will show our experimental results and emphasize that it is possible to study geometric, coherent and weakly diffusive electron optics in the same device. It turns out that – besides being a useful platform to study electron optics – our reflector device is extremely sensitive to minute scattering rates, so that it can be used for acoustic phonon sensing. This sensitivity combined with the GHz operation that we demonstrate at the end of the experimental section makes our device a good candidate for high speed phonon sensing. At the end of the chapter, I will provide perspectives for future experiments.

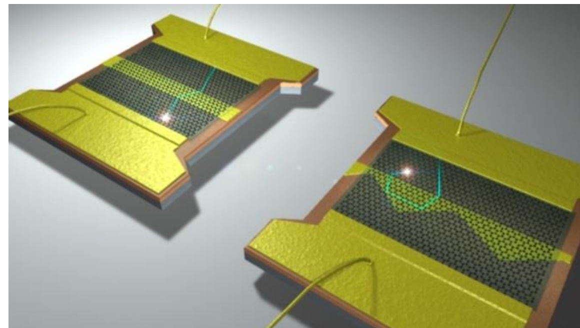

Figure 3.1 – Artist view (credit: David Darson) of ballistic fermion transport in a rectangular barrier (left) and in a sawtooth gate transistor (right).

3.1 Principles of Dirac fermion optics

Already Louis de Broglie's 1924 thesis of the wave-particle duality points out a fundamental analogy between photons and electrons (and all other particles for that matter): They have momentum like a particle, but they can interfere like waves. The idea of doing optics with electrons, for example in a scanning electron microscope [153] is almost as old as de Broglie's thesis. Even though it was carried out at a point of time when the scientific community had little doubt about the electron's wave character, Donati *et al.*'s 1973 double-slit experiment with electrons clearly demonstrated electron interference [154].

Beyond that, Dirac fermions in graphene bear a whole range of analogies with photons: First and foremost their dispersion is also linear in the vicinity of the so-called Dirac points, even though their phase velocity is 300 times smaller than the speed of light. In principle, if we are dealing with a clean graphene sample, these fermions can travel significant lengths (~ 1 μm at room temperature [118] and $\gg 10$ μm at cryogenic temperature) without being scattered, thanks to the weak electron-phonon coupling. On length scales smaller than the scattering length, graphene forms a *transparent* medium for the charge carriers, the electronic transport is *ballistic*.

A more detailed discussion of analogies between classical optics and mesoscopic/quantum physics can be found in references [155] and [156].

3.1.1 Snell-Descartes law

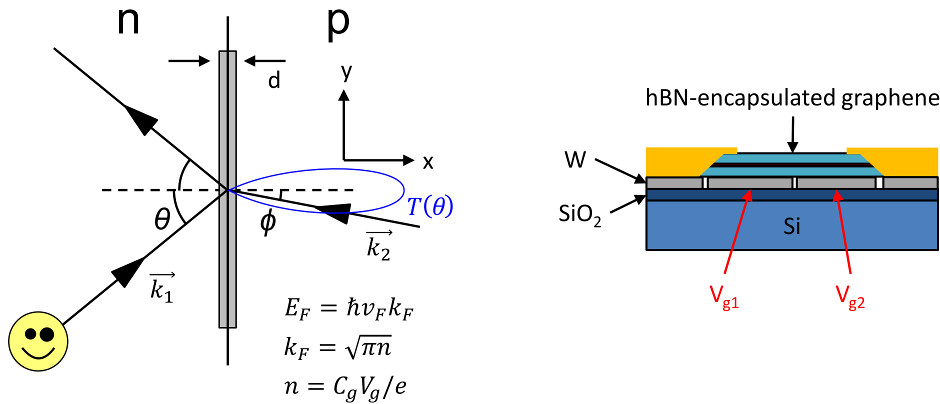

Figure 3.2 – Left: Sketch of a p-n junction in graphene with incident, reflected and transmitted trajectory. Note that due to the opposite sign of the Fermi energy/wavevector on the two sides of the junction, the refraction is *negative*. Right: Illustration of how such a p-n junction can be induced in graphene using gate electrodes.

The analogy that we will be mostly concerned with throughout this chapter occurs at a p-n junction, which can be induced *in situ* by placing two local gate electrodes in the vicinity of the graphene sheet (c.f. figure 3.2). A fermion incident on this junction can either be reflected with opposite angle or it can be transmitted, in which case the link between the incident and the transmitted angle is given by the following law:

$$k_{F1} \sin \theta = k_{F2} \sin \phi \tag{3.1}$$

where θ and ϕ are the incident and transmitted angle and $k_{F1,F2}$ are the Fermi wavevectors on either side of the junction. This law is the electronic equivalent of the Snell-Descartes law in classical optics, where the Fermi wavevector (or the Fermi energy $E_F = \hbar v_F k_F$) acts as the refractive index. Note that this law – like in classical electrodynamics – is a consequence of the conservation of the wavevector component parallel to the junction k_y due to translational invariance. Since the Fermi energy can be easily tuned in 2D materials by applying a gate electrode, it is possible to define "optical" elements of *in situ* tunable refractive index $\eta = k_{F1}/k_{F2} = E_{F1}/E_{F2}$.

First studies of electron refraction in GaAs-AlGaAs 2DEGs were carried out by Spector *et al.* [157, 158] and Sivan *et al.* [159] in 1990. Due to the absence of a bandgap, and unlike in semiconductor 2DEGs, the graphene Fermi level can be continuously tuned from n- to p-doping, which makes negative refraction possible and has therefore led to the proposal of exotic device designs like the electronic Veselago lens [160], which is a lens based on flat interfaces and exploiting a negative refractive index.

3.1.2 The critical angle

Like in conventional optics, the phenomenon of refraction entails the existence of a critical angle when traveling from a more refractive to a less refractive medium:

$$\theta_c = \arcsin\left(\left|\frac{E_{F2}}{E_{F1}}\right|\right) = \arcsin\left(\sqrt{\left|\frac{n_2}{n_1}\right|}\right) \tag{3.2}$$

where $|E_{F2}| < |E_{F1}|$ and $n_{1,2}$ are the charge carrier densities on either side of the junction. The critical angle can thus be tuned by the gate voltage. For example $n_1/n_2 = 10$, corresponding to an effective refractive index $\sqrt{10} = 3.2$ leads to a critical angle $\theta_c = 18°$.

3.1.3 Fresnel relation

The angular dependence of the transmission probability varies strongly with the sharpness of the junction with respect to the Fermi wavelength, i.e. on the product $k_F d$. Consequently, different expressions for different limits have been proposed. The transmission probability for an abrupt barrier ($k_F d \ll 1$) and for a sharp/smooth (symmetric) n-p junction ($k_F d \gg 1$) were derived in 2006 by Katsnelson *et al.* [30] and by Cheianov *et al.* [161] respectively. By matching the wavefunctions on both sides of a sharp junction, one obtains:

$$T_{\text{sharp}}(\theta) = \cos^2\theta \tag{3.3}$$

Cheianov *et al.*'s expression for a smooth junction was modified in 2007 by Huard *et al.* [162] to take into account asymmetric (still bipolar) junctions:

$$\mathcal{T}_{\text{smooth}}(\theta) = e^{-2\pi d \frac{k_{F1}^2}{|k_{F1}|+|k_{F2}|}\sin^2\theta} \tag{3.4}$$

The trajectories of electrons with oblique incidence on the smooth junction are gradually bent away, so that a classically forbidden zone arises. The exponential dependence in eq. 3.4 represents the tunneling probability through this zone. Allain and Fuchs wrote a pedagogical review for the abrupt/smooth junction/barrier case four years later [163]. The essence of

these derivations can also be found in Quentin Wilmart's thesis [23]. Sajjad *et al.* proposed yet another modified version of Cheianov's expression for the case of an asymmetric n-p or n-n' junction in 2012 [164]. In all the above-mentioned works, a linear function was used to model the smooth potential profile. Cayssol *et al.* [132] have proposed an analytical solution for the transmission probability of a possibly more realistic potential landscape defined by a Fermi-type function:

$$E_F(x) = E_{F1} + \frac{E_{F2} - E_{F1}}{e^{-x/w} + 1} \tag{3.5}$$

In order to make the junction length w used in this expression a bit more meaningful, we will rather consider the effective junction length $d = 2w\ln(10)$ in the following, which is the width over which 90% of the potential variation takes place. Cayssol *et al.*'s expression for the junction transparency is:

$$\mathcal{T}(\theta) = 1 - \frac{\sinh(\pi w \kappa^{+-})\sinh(\pi w \kappa^{-+})}{\sinh(\pi w \kappa^{++})\sinh(\pi w \kappa^{--})} \tag{3.6}$$

where $\kappa^{\rho\sigma} = k_{F1}(1 + \rho\cos\theta) - k_{F2}(1 - \sigma\cos\phi)$ and ρ, σ are either $+$ or $-$. This expression can interpolate between the smooth and the sharp limit.

In figure 3.3, we compare some of the expressions for the transmission probability given in the above-mentioned literature. Panel (a) is a color plot of equation 3.4 and panel (b) is a color plot of equation 3.6, which is valid also in the unipolar n-n' regime. In both cases, we plot the results for an experimentally relevant carrier density $n_1 = 10^{12}$ cm^{-2}, which corresponds to a Fermi wavelength of $\lambda_{F1} = 35$ nm. Since equation 3.4 is only valid in the smooth junction limit, we use $d = 100$ nm and observe a good qualitative agreement; both formulas predict a strong collimation effect in the bipolar regime. In the unipolar regime, Cayssol *et al.* (arguably) predict a transmission of almost unity for the entire angular range. The dashed white lines highlight the critical angle (c.f. equation 3.2) as a function of the doping ratio. Above this angle, no transmission can take place.

In panel (c), we plot $T(\theta)$ for a symmetric bipolar junction ($n_2 = -n_1$). The solid lines are calculated using equation 3.6, while the dotted and dashed lines are obtained from equation 3.3 and equation 3.4 for the sharp and the smooth case respectively. We see that there is a good agreement of Cayssol's expression both with the smooth and the sharp limit. Slight deviations can be understood in terms of the difference in the underlying potential shape and our ad-hoc choice of the effective junction length $d = 2w\ln(10)$. Furthermore, the plot emphasizes how the collimation effect of the junction becomes stronger with increasing junction smoothness. However, considering now the angle-averaged transmission of the junction (weighted by a $\cos\theta$ distribution) in panel (d), this increased collimation results in a much lower junction transparency in the bipolar regime. Due to its suitability for modeling smooth *and* sharp junctions, which is required when we vary the refractive indices over a large range and therefore modify the effective junction sharpness $k_F d$, we will use Cayssol *et al.*'s expression for the junction transparency in the following.

3.1.4 Klein tunneling

In figure 3.3, which illustrates the angular dependence of the transmission probability, another peculiarity of Dirac fermions comes into play: At normal incidence on the junction

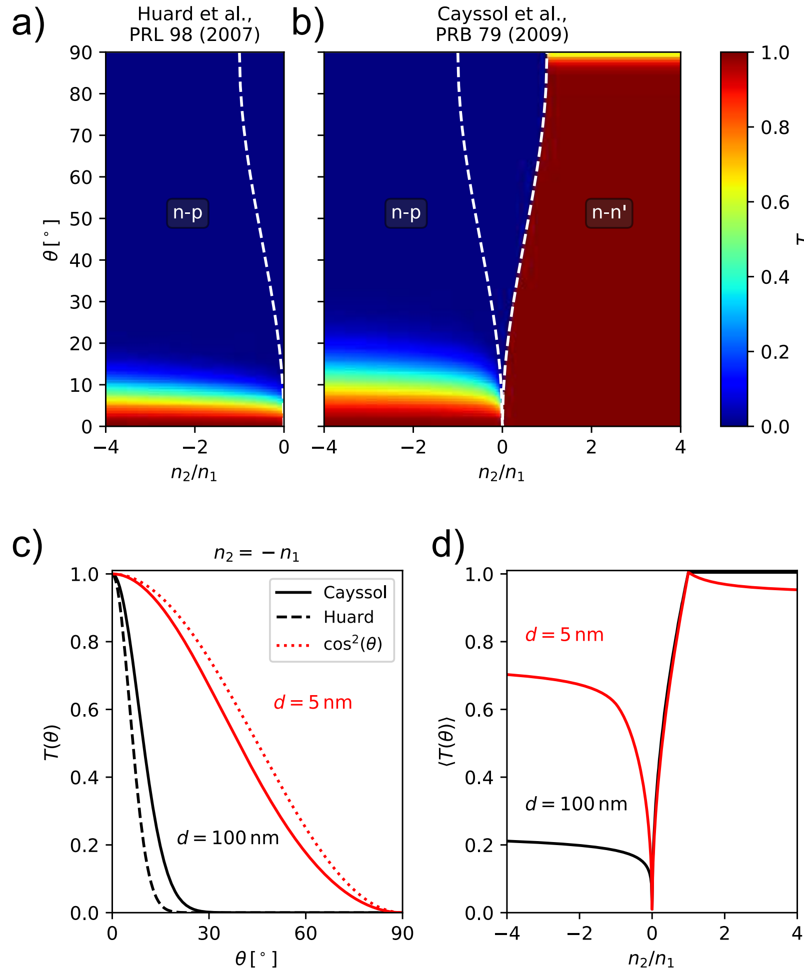

Figure 3.3 – Angular dependence of n-p junction transmission. a) Transmission as a function of doping ratio and incident angle following ref. [162]. b) Same plot following ref. [132]. Dashed white lines correspond to the critical angle $\theta_c = \arcsin(\sqrt{n_2/n_1})$. c) Transmission as a function of incident angle for a symmetric n-p junction in the sharp (red) and smooth (black) case. Solid lines are calculated following ref. [132], dashed lines following ref. [161] and the dotted line corresponds to the sharp junction case, c.f. eq. 3.3. d) Angle-averaged transmission from Cayssol's expression [132] for the smooth (black) and the sharp (red) limit as a function of doping ratio.

$(\theta = 0)$ – no matter what the height of the potential step is – their transmission probability is unity. This behavior is named Klein tunneling after Otto Klein who already described in 1929 for a particle following Dirac's relativistic dynamics [29]. It is however not a real tunneling behavior in the conventional quantum mechanical sense, since it is not mediated by an evanescent wave [163].

3.1.5 Summary

A summarizing list of the principles introduced in this section is given in table 3.1. Following these principles, we can define a set of design criteria for Dirac fermion optics devices. These are listed in table 3.2. Note that in principle, the required junction type depends on the purpose of the device. In a collimator, for example, one might want to exploit the narrow transmission window of a smooth junction, see fig. 3.3c. At the end of section 3.4.1, after familiarizing ourselves with the phenomenology of corner reflectors, we will discuss why sharp junctions are required for these objects.

	Photon optics (3D)	Dirac fermion optics (2D)
Medium	transparent	ballistic
Dispersion	linear	linear
Phase velocity	3×10^8 ms^{-1}	10^6 ms^{-1}
Snell-Descartes	$n_1 \sin\theta_1 = n_2 \sin\theta_2$	$E_{F1} \sin\theta_1 = E_{F2} \sin\theta_2$
Critical angle	$\theta_c = \arcsin\left(\frac{n_2}{n_1}\right)$	$\theta_c = \arcsin\left(\left\lvert\frac{E_{F2}}{E_{F1}}\right\rvert\right)$
Fresnel relation	$\mathcal{T} = 1 - \left\lvert\frac{n_1 \cos\theta_1 - n_2 \cos\theta_2}{n_1 \cos\theta_i + n_2 \cos\theta_2}\right\rvert^2$	$\mathcal{T} = 1 - \frac{\sinh(\pi d\kappa^{+-})\sinh(\pi d\kappa^{-+})}{\sinh(\pi d\kappa^{++})\sinh(\pi d\kappa^{--})}$

Table 3.1 – The analogy between Dirac fermions in graphene and photons. The photon Fresnel relation is valid for light polarized perpendicularly to the plane of incidence. A similar expression exists for the opposite polarization. The “Fresnel relation” for Dirac fermions is from ref. [132] and $\kappa^{\rho\sigma} = k_{F1}(1 + \rho\cos\theta) - k_{F2}(1 - \sigma\cos\phi)$. Alternative expressions are given in refs. [30, 161, 162, 164]

Criterion	Solution
Transparent medium, i.e. the mean free path should exceed the device size: $l_{\mathrm{mfp}} > L$	Use of high-mobility encapsulated graphene and fabrication of small devices. $L \leq 1$ μm for room-temperature compatibility.
Homogeneous medium, i.e. doping variations should be kept minimal in order to avoid mirage effects.	Use of atomically flat hBN as a gate dielectric.
Avoid diffraction for geometrical optics, i.e. the device should be much larger than the Fermi wavelength: $L > \lambda_F$	$L > 0.1$ μm for operation at typical densities $n \sim 10^{12}$ cm^{-2}
Transparent, therefore sharp, junctions (see note in the main text), i.e. $d \lesssim \lambda_F$	Nanostructured bottom gates defined by e-beam lithography, c.f. section 2.1.2.
Flat interfaces (on the length scale of λ_F)	see above

Table 3.2 – Design criteria for Dirac fermion optics devices.

3.2 Review of relevant DFO theory and experiments

Even though the rich phenomenology of the graphene p-n junction was understood quite early after graphene's discovery in 2004 and despite the fact that many device proposals have been made, the experimental demonstration of "actual" DFO devices only became possible recently, due to the advances in sample fabrication (encapsulation), which were crucial to attain ballistic transport.

3.2.1 Rectangular barriers

The rectangular potential barrier is the simplest "composite" DFO device and consists of two straight and parallel p-n junctions. Its optical equivalent is a glass slide, transparent if the graphene is ballistic between the two junctions, "milky" if it's diffusive.

The possible use of such a barrier as a Veselago lens – i.e. a flat lens with negative refractive index – was already identified by Cheianov *et al.* in 2007 [160]. In 2008, Shytov *et al.* [165] theoretically modeled the magneto-transport across such a barrier, also taking into account its nature as a Fabry-Pérot cavity.

In the same year, first experimental results by Gorbachev *et al.* [169] and Young & Kim [50] showed evidence for ballistic transport and signatures of electronic interference (see fig. 3.4b) in such a rectangular barrier, induced using a (top and bottom) dual gate approach (see fig. 3.4a). In both cases, the barrier width was on the order of 100 nm. In 2009, the same device structure was studied by Stander *et al.* [170]. Again, signatures of quasi-ballistic transport could be found, quantum interference was not discussed.

Similarly small devices were fabricated by Williams *et al.* in 2011 [166], who had the original idea to study electronic transport *parallel* instead of perpendicular to the p-n junctions and who showed that the rectangular barrier can be used as a "waveguide" for electrons, much like fiber optics for photons (see fig. 3.4c). This experiment was repeated more thoroughly in suspended graphene by Rickhaus *et al.* in 2015 [171].

Much larger barriers $\sim 1\ \mu$m were realized in 2013 by Rickhaus *et al.* [51] and Grushina *et al.* [172] using suspended graphene in combination with bottom gates. Even over these large distances, coherent transport was observed in the form of Fabry-Pérot oscillations. Also studying a suspended sample, Oksanen *et al.* observed similar oscillations not only in the conductance, but also in the shot noise [173].

In 2015, Rickhaus *et al.* found evidence for so-called "snake states", which are skipping trajectories along a p-n junction occurring due to magnetic focussing (see also next section) along the interface in a moderate magnetic field [174]. While this observation is not directly linked to coherent or geometric electron optics discussed here, the effect they observed is aided by the high Klein tunneling probability at normal incidence and it is a further example for the richness of the physics of the graphene p-n junction. In a unipolar semiconductor heterostructure 2DEG, these states can only be generated by locally inverting the direction of the magnetic field.

Even though the above-mentioned experiments provided no angular resolution for the resistance/transmission measurement, which would be a crucial ingredient to directly observe Klein tunneling, most of the works mentioned here claim to have observed this phenomenon (or evidence for it), since the absence of back-scattering is part of the Fresnel-expression that they use to model their device.

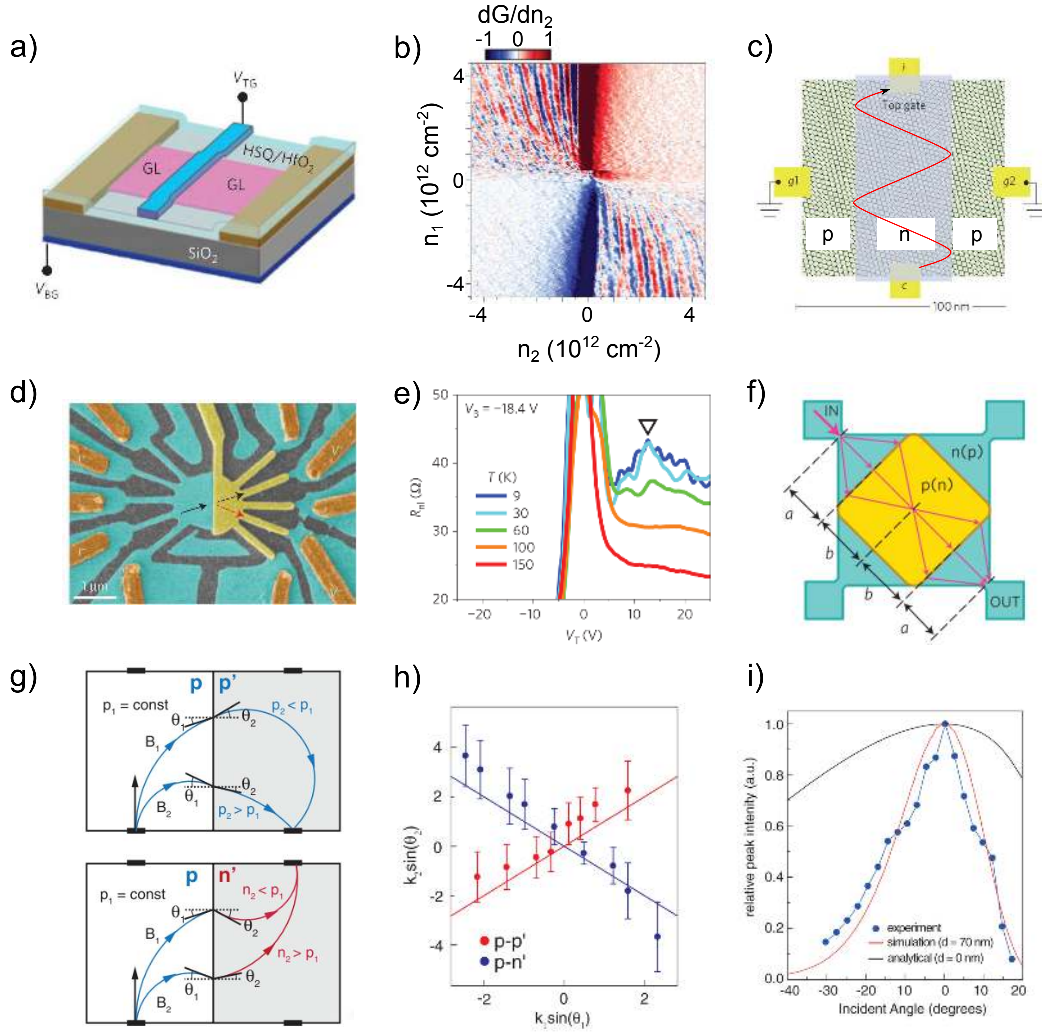

Figure 3.4 – **Rectangular barriers and angle-resolved studies.** a) Illustration of a dual gate graphene device, adapted from [50]. b) Fabry-Pérot oscillations in the differential conductance, adapted from [50]. c) Illustration of p-n-guiding in a rectangular barrier, adapted from [166]. d) Angle-selective contacts and e) non-local resistance peak corresponding to refracted trajectories, taken from [167]. f) Illustration of a Veselago lens device, taken from [167]. g) Illustration of fermion trajectories in a magneto-transport experiment through a gate-induced p-n junction, h) the confirmation of Snell's law and i) of the Fresnel relation, extracted from non-local resistance measurements, adapted from [168].

3.2.2 Angle-resolved studies

In order to directly probe the refraction effect or the angular dependence of transmission, angle-resolved studies require more complex device designs in combination with non-local measurements and ideally some additional control over electron trajectories using a magnetic field:

Lee *et al.* [167] studied the refraction effect in 2015 by measuring the non-local resistance

both in a square-shaped Veselago lens (fig. 3.4f) and in a more complex device with angle-selective contacts (fig. 3.4d). In this work, a peak of the non-local resistance (fig. 3.4e) occurs at the gate voltage ratio that corresponds to the refraction which is required to "bend" the charge carrier trajectory from the source to the detector contact. A similar approach was used by Rahman *et al.* [175], but their results were slightly more ambiguous.

By combining the non-local measurement with a small (non-quantizing) magnetic field, Chen *et al.* removed the necessity of having angle-selective contacts, since the magnetic field could be used to "guide" the electrons across the p-n junction from the source to the destination contact. They carried out an extensive magneto-transport study in 2016 [168], where they managed to map out both the Snell-Descartes and the Fresnel relation (see fig. 3.4g-i) using the established method of transverse magnetic focusing (c.f. e.g. [176–180]).

The same magneto-transport approach was employed by Barnard *et al.* in 2017 [181] to probe the effectiveness of so-called pinhole collimators for Dirac fermions. Again, the resistance peak in a non-local measurement was used to detect the intensity of an electron beam, while the magnetic field was used to control the beam deviation. They demonstrated a significant reduction of the angular spread of the electron beam by evacuating charge carriers with oblique incidence through a grounded contact. Note that this is yet a new way to collimate the electron beam, in addition to the collimation mechanisms provided by refraction and by the Fresnel relation.

3.2.3 Tilted junctions and electronic switches

Due to the absence of a bandgap, graphene is not a great candidate for transistors, in particular for logic applications. In bilayer graphene, such a gap can be induced by applying an out-of-plane electric field [126, 182–186].

Even in monolayer graphene, a gap can be forced by the sample geometry: by reducing the width of the sample towards a quasi-1D channel, quantum confinement leads to an effective energy gap [192, 193]. However, the edge roughness of these thin ribbons is often non-negligible and leads to local resonances rather than a uniform confinement. The quest for the gap in graphene has thus motivated more exotic proposals, building upon the above-mentioned collimation and reflection properties of the graphene p-n junction. Already in 2006, Katsnelson *et al.* [30] pointed out that the comparison of a barrier perpendicular to a graphene channel with a 45° tilted barrier (c.f. fig. 3.5a) should yield a big difference in resistance, since Klein tunneling assists transmission in the perpendicular barrier. However, a detailed analysis of the 45° case and its possible use as a switch was not provided.

A first proposal by Sajjad *et al.* in 2011 [187] suggests the "illumination" of a gate-induced n^+-p junction with a point source of electrons. A barrier is placed at the junction center to suppress all trajectories with normal incidence (see fig. 3.5b). The remaining trajectories undergo total internal reflection when the switch is in the OFF state, whereas they are refracted around the barrier when the switch is in the ON state.

After providing a theoretical analysis [164] of the experimental characterization of a tilted p-n junction by Sutar *et al.* in 2012 [194], Sajjad *et al.* proposed in 2013 [188] the combination of two p-n junctions, tilted with respect to each other (see fig. 3.5c), to induce a *transmission gap* in a graphene device, predicting ON/OFF ratios on the order of up to 10^5. They emphasize the advantage of using a transmission gap, as opposed to the "structural gap": It does not reduce the number of channels available for conduction and

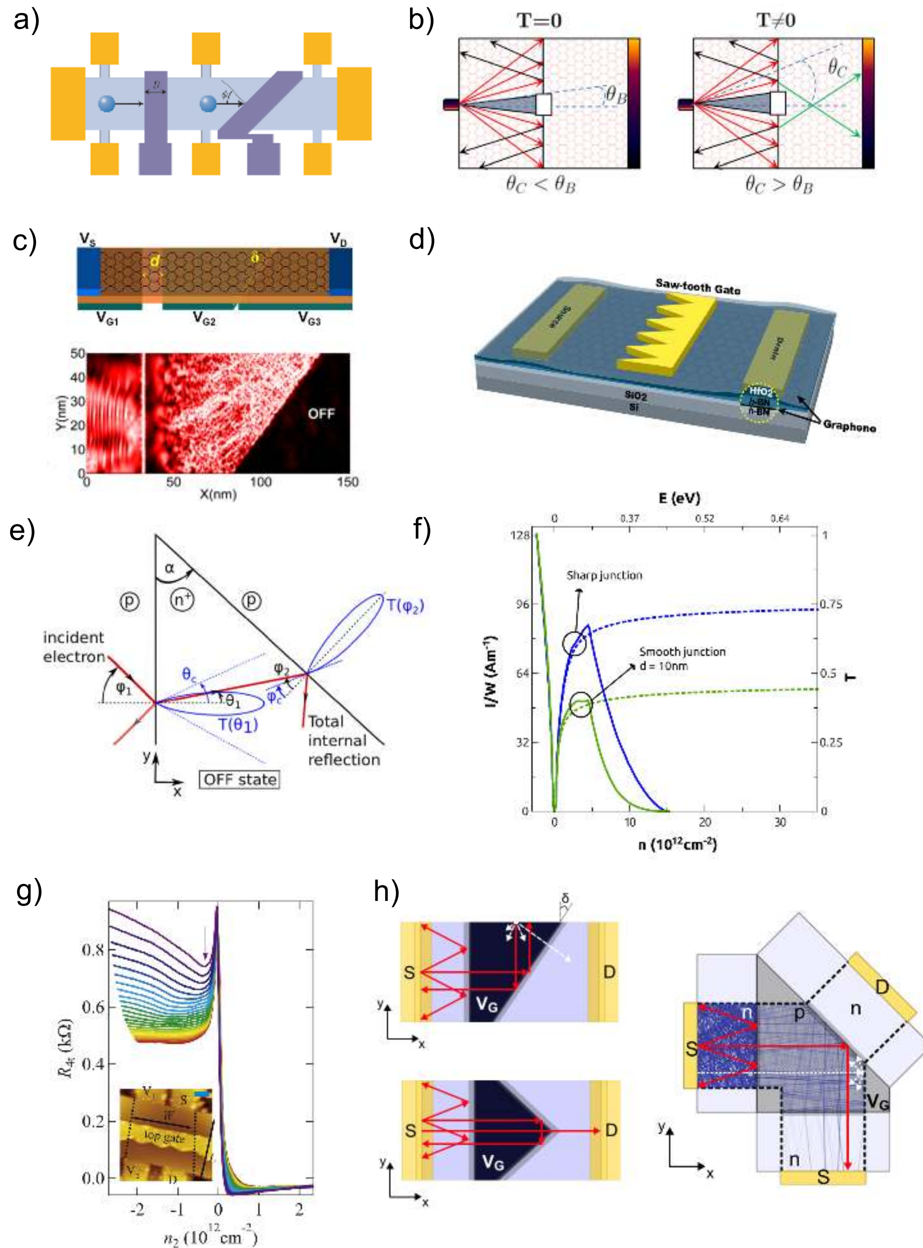

Figure 3.5 – **Tilted junctions and electronic switches.** a) First proposal for a device to probe Klein tunneling, from [30]. b) Sketch of an electronic switch using the DFO critical angle, from [187]. c) Sketch of the polarizer-analyzer approach to achieve an OFF effect, supported by NEGF simulations, from [188]. d) Proposal for a sawtooth gate device, taken from [189]. e) Illustration of the OFF-state of such a device and f) calculated transmission/current density as a function of the barrier charge density, from [190]. g) Experimental resistance of a sawtooth gate device as a function of barrier density, resistance increase on the left corresponds to OFF-state, from [130]. h) Comparison of various switch geometries, including a dual-source design, from [191].

therefore preserves high electronic mobility. Furthermore, they draw yet another analogy with optics by comparing the pair of p-n junctions to polarizer and analyzer in optics, where the transmitted intensity is governed by Malus's law $I \propto \cos^2 \theta$.

While Sajjad *et al.* used an analytical approach combined with non-equilibrium Green's function (NEGF) simulations to model their double-junction, Jang *et al.* studied a similar device geometry [189] consisting of a sawtooth gate electrode (c.f. fig. 3.5d) by means of finite difference time domain simulation (GraFDTD) and predicted more modest ON/OFF ratios on the order of ~ 100. The same geometry was studied using ray tracing simulations by Wilmart *et al.* in 2014 [190], in particular in the light of variations of the sawtooth's opening angle and for finite drain-source bias (the latter again by means of NEGF simulations). They found more conservative predictions for the ON/OFF ratio on the order of 6 and stress the importance of using sharp p-n junctions for achieving high transparency in the ON regime, see fig. 3.5e-f. In yet another theoretical ray tracing study, Tan *et al.* examine the use of so-called Klein tunnel transistors (c.f. fig. 3.5c) for analog high frequency applications and predict a 10-fold increase in the maximum operating frequency $f_{\max}$ compared to a conventional graphene FET [195].

In 2015, Rickhaus *et al.* [196] fabricated tilted p-n junctions in suspended bilayer graphene. They demonstrated that these junctions could be used as beamsplitters and further showed that the effective junction position could be shifted significantly by applying asymmetric gate voltages, which makes the beamsplitter suitable for use in a tunable electronic interferometer. In 2017, Morikawa *et al.* fabricated the first sawtooth-gate device [130], based on the proposal by Wilmart *et al.* and indeed observed a switching effect, in qualitative agreement with theory (c.f. fig. 3.5g), and a small ON/OFF ratio on the order of 1.3. Since the control of the device geometry was limited in this study (rough p-n junctions, non-uniform current injection, tilted channel) and the data analysis was complicated due to the use of dual gates – i.e. there is no independent control of the doping on either side of the junction – a more quantitative understanding of the experimental data was not possible. In this thesis, almost the same geometry is studied, but with a much more precise control of the doping and an overall improved sample quality. Furthermore, our study focuses on understanding different regimes of electron optics.

As far as the electronic switch is concerned, a recent (2019) study by Wang *et al.* [197] re-iterated the initial device design of tilted p-n junction switches [188] in order to overcome edge scattering, "multiple bounce trajectories" and leakage at the sawtooth tips, as discussed by Elahi *et al.* [191]: Using an isosceles right triangle with contacts on all sides of the prism is supposed to lead to direct absorption of charge carriers by one of the source contacts if they are reflected by the hypotenuse junction on the drain side. This is illustrated in fig. 3.5h.

3.2.4 Other DFO studies

Similarly to studies of electron quantum optics in the one dimensional edge channels of semiconductor heterostructures in strong magnetic fields [198], graphene has become a platform for this type of experiment [199–201]. Its advantages compared to semiconductor 2DEGs are the tunability of the charge carrier density and the additional possibility to explore electron-hole symmetry. However, due to its gapless nature, it is much more difficult to create completely isolating regions in graphene and its etched boundaries promote scattering.

As mentioned in section 3.2.3, the absence of a gap can be overcome by applying an electric field to bilayer graphene, making it a potential candidate for this kind of experiment.

Beyond what is discussed here, more complex DFO device structures and experiments have been proposed, like a two-dimensional solid-state electron microscope [202] and chaotic ray dynamics giving rise to a so-called "relativistic quantum chimera" [203]. An example for a more complex *experimentally studied* system is the analogy with Mie scattering by Caridad *et al.* [204].

Dirac fermion optics has also been explored beyond the pure transport approach, e.g. by combining transport with scanning gate microscopy to probe a DFO lens [205] or with scanning tunneling microscopy and spectroscopy to characterize the local doping profile of graphene p-n junctions at the atomic scale [127].

3.2.5 Conclusion

To summarize, there have been many theoretical proposals on how to study and exploit Dirac fermion optics throughout the last 10-15 years, but the systems studied experimentally have been extremely simple so far, which is understandable if we take into account the technological challenges involved in the fabrication of such devices.

The device structure discussed in the following was initially inspired by the tilted-junction proposals mentioned above. It was theorized in 2014 by Wilmart *et al.* [190] as a *Klein tunneling transistor* (KTT), demonstrated experimentally by Morikawa *et al.* [130] as a *Dirac fermion reflector* (DFR) in 2017 and – because we are now looking at the special case of a 90° apex prism – we will call it *corner reflector* (CR) throughout this thesis.

It turns out that progress in terms of device fabrication and the independent control of refractive indices using nanostructured bottom gates enabled us to go further than previous studies and to quantitatively understand electronic transport in this functional device structure.

3.3 Modeling the corner reflector

Before we start discussing the trajectories in our "electronic" prism, let us first have a look at its optical equivalent. Figure 3.6 shows photographs of a 90° glass prism illuminated by a green laser. The prism was placed on a black table in a dark room and the light rays were made visible by blowing smoke on the experimental set up. Both in panel (a) and in panel

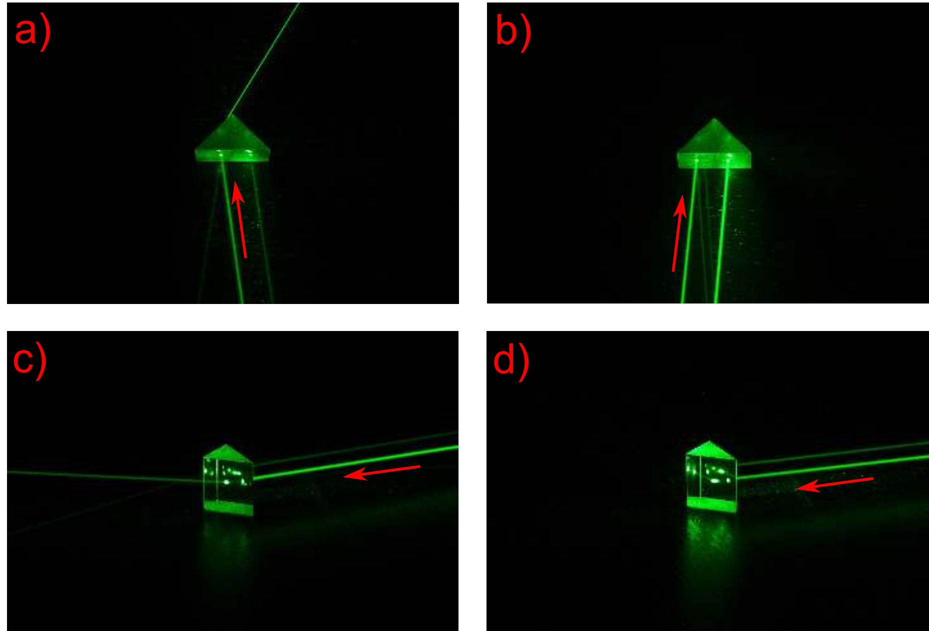

Figure 3.6 – Table-top experiment with a laser pointer and a 90° glass prism. a) and c) Top and side view of sub-critical incidence. b) and d) Top and side view of super-critical incidence. The red arrow illustrates the incident laser beam.

(b) we can see that a small fraction of the laser beam is reflected before it even enters the prism. The beam then undergoes two reflections inside the prism and exits the prism under the original angle. Of course, a small fraction of the beam is reflected back into the prism at the exit point, undergoes two reflections again and reaches a different exit point. Upon close inspection this second exit point can be identified in panel (b). A lot of the physics that we will discuss in the following is already captured in this simple picture. However, there are two substantial differences to the 2D electronic prism:

Firstly, as we can see in panel (a), there are incidence angles for which our optical prism cannot guarantee total internal reflection (TIR) on the tilted sides of the prism and the laser beam can escape to the other side. As we will see in the following, our electronic prism can be tuned to very high refractive indices, which guarantees TIR for all incidence angles.

Secondly, the refractive index of the glass prism is obviously positive. The electronic prism however will be operated in the negative refraction regime, where it turns out to work best.

3.3.1 Analytical model

Let us now analyze in more detail the prism geometry mentioned in the previous section. This analysis is based on references [23, 190] and on the Supplementary Material of ref. [26]. Figure 3.7 shows a typical trajectory of a Dirac fermion inside a $\alpha = 90°$ apex prism. The fermion beam hits the "base" junction (1) with an incidence angle θ and – if it is transmitted – travels inside the prism with angle ϕ. In the following, we will refer to the doping inside (outside) of the prism as n_B (n_A).

Even if some of the following analysis is valid for arbitrary doping ratios, we will mostly focus on the case of bipolar junctions ($n_\mathrm{A} n_\mathrm{B} < 0$) with a higher refractive index inside the prism $|n_\mathrm{B}| > |n_\mathrm{A}|$. This means that the refraction on junction (1) is negative and that the incident fermion beam is collimated to an angular spread of $-\theta_c \leq \phi \leq +\theta_c$.

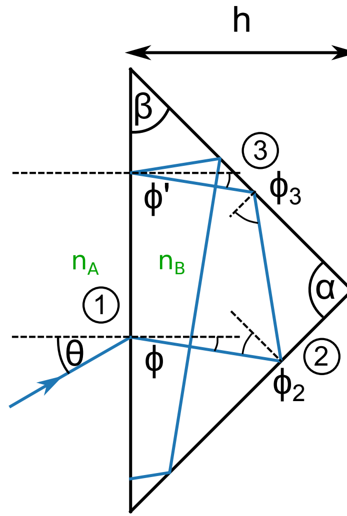

Figure 3.7 – A typical TIR trajectory with two round-trips inside the prism with $\alpha \approx 90°$ apex.

We will first consider the case of arbitrary apex angle (not too far from 90°) and introduce the opening angle $\beta = (180° - \alpha)/2$ of the prism. In this case, the incidence angles on the first (ϕ_2) and the second tilted junction (ϕ_3) and the "return angle" to the baseline (ϕ') are given by:

$$\phi_2 = \beta - \phi \tag{3.7}$$

$$\phi_3 = 180° - 3\beta + \phi \tag{3.8}$$

$$\phi' = 180° - 4\beta + \phi \tag{3.9}$$

If we want to ensure total internal reflection (TIR) – for all incidence angles θ – on both titled junctions (2) and (3) during the first round-trip of the fermion, we require $\phi_2^{\mathrm{min}}, \phi_3^{\mathrm{min}} > \theta_c$. Now $\phi_2^{\mathrm{min}} = \beta - \theta_c$ and $\phi_3^{\mathrm{min}} = 180° - 3\beta - \theta_c$, which yields the conditions:

$$\left|\frac{n_\mathrm{B}}{n_\mathrm{A}}\right| > \arcsin^2\left(\frac{\beta}{2}\right) \tag{3.10}$$

$$\left|\frac{n_\mathrm{B}}{n_\mathrm{A}}\right| > \arcsin^2\left(\frac{180° - 3\beta}{2}\right) \tag{3.11}$$

where we used the definition of the critical angle from equation 3.2. For the 90° apex prism, both conditions are satisfied by [190]:

$$\left|\frac{n_\mathrm{B}}{n_\mathrm{A}}\right| > 6.8 \tag{3.12}$$

which corresponds to an effective refractive index of $\eta = \sqrt{6.8} = 2.6$. It is important to point out that in the context of conventional photon optics, this is a very high refractive index. Window glass has $\eta \approx 1.5$, while diamond reaches $\eta \approx 2.4$. Figure 3.6a and c illustrates this with a glass prism and a green laser: for some incidence angles, the laser can escape the prism. A naturally occuring material that could potentially be compared to our Dirac fermion CRs is moissanite with $\eta \approx 2.7$, but we will see in the following section that our DFO experimental range goes far beyond these values.

It is clear that in the case of the "magic" 90° apex prism – which we call *corner reflector* – equation 3.9 simplifies to $\phi' = \phi$, which means that when the fermion is reflected from the "base" junction (1) back into the prism, it will go through *recurrent* trajectories; the incidence angles on all junctions will stay the same. For the case of the glass prism, this phenomenon can be observed in figure 3.6b, where one can see (i) the initial back-reflection of the laser before entering the prism, (ii) the beam exiting the prism after one round-trip and (iii) the beam exiting after the second round-trip, parallel in direction and similar in intensity to the initial back-reflection (i).

The probability to stay in the prism after one round trip is $\mathcal{P}_\mathrm{stay} = (1-\mathcal{T}_2)(1-\mathcal{T}_3)(1-\mathcal{T}_1)$, where $\mathcal{T}_i$ corresponds to the exit transmission probability at the ith junction. We have dropped the angle dependence for better readability: $\mathcal{T}_i \equiv \mathcal{T}_i(\theta) \equiv \mathcal{T}_{\mathrm{B}\to\mathrm{A}}(\phi_i)$. The probability to be reflected through the "base" junction after one cycle is $\mathcal{R}_\mathrm{cycle} = (1-\mathcal{T}_2)(1-\mathcal{T}_3)\mathcal{T}_1$. The total reflection probability after N cycles can be written in the form of a geometric series:

$$\begin{aligned} \mathcal{R}_\mathrm{CR}^{(N)}(\theta) &= 1 - \mathcal{T}_1(\theta) + \mathcal{T}_1(\theta)\sum_{i=0}^{N-1}\mathcal{P}_\mathrm{stay}^i(\theta)\mathcal{R}_\mathrm{cycle}(\theta) \\ &= 1 - \mathcal{T}_1(\theta)\left[1 - \mathcal{R}_\mathrm{cycle}(\theta)\frac{1-\mathcal{P}_\mathrm{stay}^N(\theta)}{1-\mathcal{P}_\mathrm{stay}(\theta)}\right] \end{aligned} \tag{3.13}$$

where the first term $1-\mathcal{T}_1$ represents the probability of being reflected before entering the prism. We can rewrite this as a transmission probability:

$$\mathcal{T}_\mathrm{CR}^{(N)}(\theta) = \mathcal{T}_1(\theta)\left[1 - \mathcal{R}_\mathrm{cycle}(\theta)\frac{1-\mathcal{P}_\mathrm{stay}^N(\theta)}{1-\mathcal{P}_\mathrm{stay}(\theta)}\right] \tag{3.14}$$

The reason why we initially consider the sum over the cycle reflection $\mathcal{R}_\mathrm{cycle}$ and not the cycle transmission $\mathcal{T}_\mathrm{cycle} = \mathcal{T}_2 + (1-\mathcal{T}_2)\mathcal{T}_3$ is that the latter is zero in the TIR regime $|n_B/n_A| > 6.8$ where $\mathcal{T}_2 = \mathcal{T}_3 = 0$. However, as we will see in the experimental section, a *residual transmission* $\mathcal{T}_\mathrm{res}$ is observed even in the TIR regime. We explain this by taking into account a finite scattering rate within the prism, using the simple hypothesis that a scattering event definitely leads to a transmission. This means that we overestimate the residual transmission, since the scattering event could also lead to a reflection. Within this approximation, the residual transmission is obtained by truncating the sum over the cycle

reflection after $N = \ell_{\rm mfp}/\ell_1$ cycles, where $\ell_{\rm mfp}$ denotes the mean free path and ℓ_1 is the single cycle dwell length. For small ϕ, i.e. for sufficiently collimated beams, this is $\ell_1 \approx 2h$, where h is the height of the prism. In the TIR regime, where $\mathcal{T}_2 = \mathcal{T}_3 = 0$, $\mathcal{R}_{\rm cycle} = \mathcal{T}_1$ and $P_{\rm stay} = 1 - \mathcal{T}_1$, the above expression simplifies to:

$$\mathcal{T}_{\rm res}^{(N)}(\theta) = \mathcal{T}_1(\theta)[1 - \mathcal{T}_1(\theta)]^N \tag{3.15}$$

Including a $\cos\theta$ weight to take into account the distribution of the incident modes and averaging equations 3.14 and 3.15 over all angles yields the following formulas for the transmission of the corner reflector for a given mean free path:

$$\langle \mathcal{T}_{\rm CR} \rangle = \int_0^{\pi/2} \mathcal{T}_1(\theta) \left[1 - \mathcal{R}_{\rm cycle}(\theta) \frac{1 - \mathcal{P}_{\rm stay}^{\ell_{\rm mfp}/\ell_1}(\theta)}{1 - \mathcal{P}_{\rm stay}(\theta)} \right] \cos\theta \, d\theta \tag{3.16}$$

$$\langle \mathcal{T}_{\rm res} \rangle = \int_0^{\pi/2} \mathcal{T}_1(\theta)[1 - \mathcal{T}_1(\theta)]^{\ell_{\rm mfp}/\ell_1} \cos\theta \, d\theta \tag{3.17}$$

where the second formula is specific to the TIR regime. Note that while the Snell-Descartes relation still enters implicitly in equation 3.16 for the calculation of the angles ϕ_2 and ϕ_3, it loses drastically in significance for equation 3.17. In the TIR regime, the Snell-Descartes relation is encoded in $\mathcal{T}_2 = \mathcal{T}_3 = 0$ and the residual device transmission is essentially governed by the Fresnel relation 3.6, which is constant for high refractive indices, c.f. figure 3.3d.

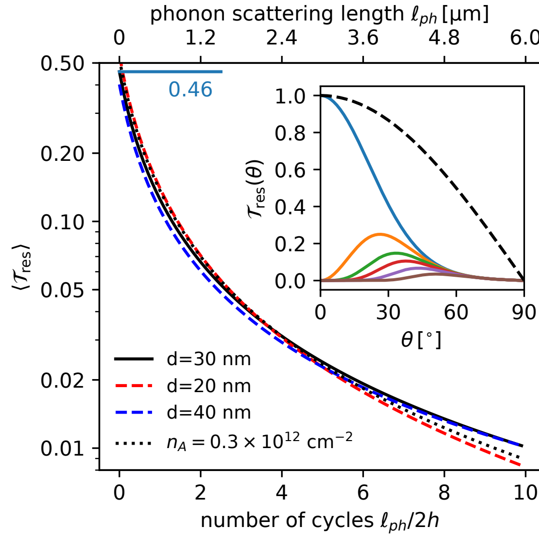

Figure 3.8 – **Residual transmission vs. number of round-trips.** $\langle \mathcal{T}_{\rm KT} \rangle \approx 0.46$ is the transmission of a single straight p-n junction. Inset: Angular dependence of the transmission of increasing number of round-trips: 0 (blue), 1 (orange etc.), 2, 3, 5, 10. The dashed black line is $\cos(\theta)$, by which transmissions are weighted.

In figure 3.8, we consider various junction lengths d around 30 nm, an access density $n_{\rm A} = 0.5 \times 10^{12}$ cm^{-2} (unless indicated otherwise) and a barrier density of $n_{\rm B} = -5 \times 10^{12}$ cm^{-2},

which corresponds to a refractive index of $-\sqrt{10} \approx -3.2$. We plot the residual transmission $\langle \mathcal{T}_{\mathrm{res}} \rangle$ as a function of the number of round-trips in the prism according to eq. 3.17. For zero round-trips, we recover the transmission of a straight $p-n$ junction with the same parameters, $\langle \mathcal{T}_{\mathrm{KT}} \rangle \approx 0.46$. Here we used the Cayssol-Huard formula, c.f. eq. 3.6, for the junction transparency $\mathcal{T}_1(\theta)$. This evaluation shows that the residual transmission is robust and does not significantly vary with the junction length or the doping ratio $n_{\mathrm{B}}/n_{\mathrm{A}}$. The inset illustrates the suppression of the angle-dependent residual transmission for an increasing number of round-trips $N = 0, 1, 2, 3, 5, 10$. At zero round trips, again, we recover the transmission of a $p-n$ junction, which is unity at zero incidence angle, due to Klein tunneling. This maximum is suppressed immediately by the effect of the CR, since normal incidence trajectories are back-reflected with a probability of unity after one round-trip. Trajectories with oblique incidence have a longer dwell-time in the prism, which means that they can still contribute to the residual transmission after a considerable number of round-trips. For a given incidence angle θ, eq. 3.15 enables us to estimate the number of round-trips required to reduce the transmission to a small value ϵ:

$$N_\epsilon(\theta) = \frac{\log(\epsilon) - \log(\mathcal{T}_1(\theta))}{\log(1 - \mathcal{T}_1(\theta))} \tag{3.18}$$

For example, for $\theta = 30°$, we read $T_1(30°) \approx 0.5$ from the inset of fig. 3.8. In order to achieve a 99% reflection ($\epsilon = 0.01$), we thus require $N_\epsilon \approx 6$ round-trips. These considerations demonstrate how useful the analytical approach is for making predictions of the behavior of a complex DFO device.

For smooth junctions with $d \gg 20$ nm, the angle-averaged transmission is smaller than for the sharp junctions considered here, see fig. 3.3c. This means that the zero-round-trip transmission is significantly reduced in this case, and for the same reason, the residual transmission exhibits a weaker dependence on the number of round-trips. This will be discussed again at the end of section 3.4.1.

3.3.2 Ray tracing simulations

In order to numerically model DFO devices, ray tracing simulations – a.k.a. the billiard model – have been used by various groups (including our own) [124, 130, 190, 191, 195, 197]. For this thesis, similar simulations were done using a home-made Python code. The principle is simple: Fermions are considered to be infinitely small, non-interacting particles moving in straight lines unless they are reflected or refracted by a p-n junction. The probability weight of the fermions is initially $\nu = 1$, or weighted by a $\cos(\theta)$ distribution at the injection electrode in order to take into account a uniform distribution of transverse wavevectors. When fermions hit a p-n junction, the new probability weight for the reflected/transmitted fermion is calculated according to the Fresnel relation (eq. 3.6). By integrating the probability weight of the fermions transmitted through the "electronic prism" over all possible trajectories, one obtains the total transmission across the device:

$$\langle \mathcal{T}(n_{\mathrm{A}}, n_{\mathrm{B}}) \rangle_\theta = \frac{1}{2h} \sum_{0}^{h} \Delta y \sum_{-\pi/2}^{\pi/2} \Delta\theta \;\; \mathcal{T}(n_{\mathrm{A}}, n_{\mathrm{B}}, y, \theta) \cos(\theta) \tag{3.19}$$

where Δy and $\Delta\theta$ are the discretizations for the initial position and the incidence angle of the fermion, respectively, and h is the height of the right-angle prism. The sum over y only

goes to half the total length of the prism baseline, due to the symmetry of the problem.

Examples for the calculated trajectories, including the probability weight as a color code, are given in figure 3.9. Panel (a) depicts the situation of a low doping contrast $n_{\mathrm{B}}/n_{\mathrm{A}} = -2$ – corresponding to a refractive index $n_r = -1.4$ and a critical angle of $\phi_c = 45°$ – where total internal reflection is not guaranteed for all incidence angles. The light red arrows on the "drain" (right) side of the prism illustrate this. The other panels (b-e) show that this is no longer the case for a sufficiently high doping ratio $|n_{\mathrm{B}}/n_{\mathrm{A}}| = 10$.

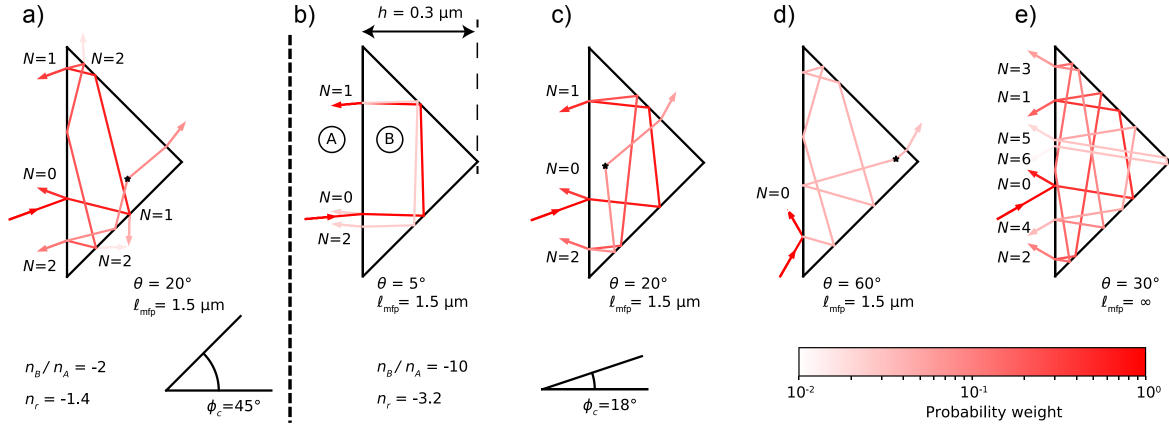

Figure 3.9 – **Ray tracing simulations.** Panels (a-e) show calculated trajectories with color-coded probability weight for different doping ratios, incidence angles and mean free paths.

The panels (b-d) of the figure illustrate trajectories for increasing incidence angles. At small angles ($\theta = 5°$), almost the entire probability weight is reflected after one round trip in the prism. At $\theta = 20°$, multiple round-trips with significant probability weight are possible. At high incidence angle $\theta = 60°$, almost the entire probability weight is reflected before even entering the prism. For the residual transmission this means that intermediate incidence angles contribute the most, as illustrated in the inset of fig. 3.8.

Scattering (impurity, defect, phonon, ...) inside the prism can be taken into account by truncating the total dwell length at the mean free path ℓ_{ph} (that we assume here to be limited by phonons), which is indicated by the little black stars in fig. 3.9. At this point, there are a couple of options from the simulation point of view:

- The fermion can be transmitted to the drain side with 100% probability, in accordance with the assumption used in the analytical model.
- The fermion can be transmitted to the drain side with 50% probability, or be reflected back to the source.
- The trajectory can continue with a new direction of propagation sampled from a uniform distribution.
- The trajectory can continue with a new direction of propagation sampled from a probability distribution that eliminates back-scattering, e.g. $1 - \cos\theta$.

The first option has the advantage of being extremely simple and 100% compatible (at least in the total internal reflection regime) with the analytical model described in the previous section, as we will see in the comparison with the experimental data in section 3.4.1. It has the disadvantage of overestimating the residual transmission.

We have carried out ray tracing simulations with both the first (section 3.4.1) and the third method (appendix 6.3). Both show a linear $\langle \mathcal{T}_{\rm res} \rangle \propto \ell_{\rm mfp}^{-1}$ dependence with prefactors of the same order of magnitude, which suggests that the exact scattering distribution does not play a major role for the leak transmission.

A more detailed analysis of these ray tracing simulations and possible improvements, like e.g. the use of a Monte-Carlo approach to sample the scattering lengths from an exponential distribution, goes beyond the scope of this thesis. As mentioned above, ray tracing is a very common tool to study DFO problems, but it can be very costly in terms of calculation time and programming effort. We will see in this chapter that the simple analytical model from the previous section is sufficient to quantitatively reproduce the experimental data, which is good news, considering the effort that has been invested in complicated simulations of similar geometries [130, 190, 191, 195, 197].

3.4 Experimental results

The challenges inherent to the fabrication of CRs are manifold, c.f. the design criteria in table 3.2. In particular the fabrication of leak-free gate electrodes with ≤30 nm separation, the deposit of hBN-encapsulated graphene on top of the active zone and the precise alignment ≤50 nm of the e-beam lithography for the fabrication of contacts are difficult steps. For more details on the fabrication process, see section 2.1 and appendix 6.1.1. Despite these challenges, which explain the long delay between the proposal by Wilmart *et al.* in 2014 [190] and this experimental work [26], a reasonable number (eight) of samples survived the complete fabrication process. The hBN-graphene-hBN stacks were mostly assembled by Luca Banszerus in Aachen and subsequently transferred onto the bottom gates in Paris. In the following, we will primarily focus on two samples: CR H9.4 with tungsten gates for "DC" and CR AuEG-17.ML with gold gates for high frequency measurements. More details on the other fabricated devices including a comparison of their performances can be found in section 3.4.5.

There are four main results that will be presented and discussed in the following sections. The first three cover the various optical regimes that have been explored in the CR: geometrical, coherent and (weakly) diffusive optics. The last result is the observation of the reflection effect at elevated frequency (10 GHz). These results are published in ref. [26].

The electronic transport measurements were carried out in the Janis cryogenic (0-40 GHz) probe station at temperatures $T = 6 \ldots 300$ K. For the first three results, a lock-in amplifier was used for measuring the device resistance, whereas for the high frequency measurements, it was measured simultaneously with a vector network analyzer and using DC sources in combination with a voltage divider. For more details on the protocol, see chapter 2.

3.4.1 The reflection effect as a hallmark of geometrical DFO

Before discussing the measurements, let us briefly recall the the device design and introduce the relevant variables. To this end, figure 3.10a shows a SEM picture of the device CR-H9.4,

which will be in the focus of our discussion in the following sections (except for the high frequency measurements). The encapsulated graphene sample is visible as a transparent rectangle ($1.6 \times 1.2\ \mu\text{m}^2$) in the center of the picture. It covers the two gate electrodes – separated by a slit of around 20 nm (for a simulation of the resulting electrostatic profile and comments on junction roughness, see section 2.1.2) – and overlaps on the top and bottom side, where the drain and source electrode form 1D edge contacts with the graphene sheet.

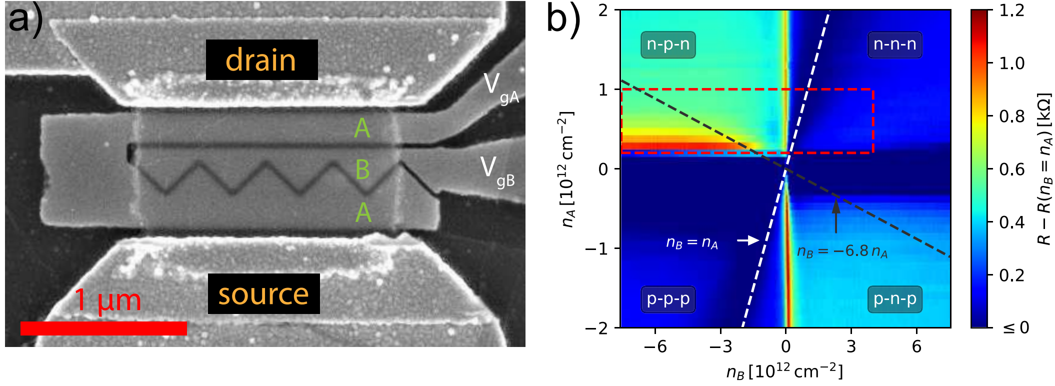

Figure 3.10 – **The corner reflector device.** a) SEM micrograph of sample CR-H9.4. b) Color plot of the reflector resistance at $T = 100$ K as a function of carrier density in the access and barrier regions. The access resistance measured at $n_\text{B} = n_\text{A}$ has been subtracted (dashed white line).

The inner gate electrode V_{gB} defines the doping n_B in the **b**arrier region, consisting of four overlapping right-angle prisms with a base length of 600 nm and a height of 300 nm. An overlap between neighboring prisms has been added to avoid short gate effects and direct source-drain tunneling. The minimum gate length is 100 nm $\gg \lambda_F$ and the total gate width is 1.6 μm. The outer gate electrode V_{gA} controls the doping n_A in the **a**ccess region.

Compared to the combined top- and bottom-gate approach used in ref. [130], the use of bottom gates only ensures an independent control of the refractive indices inside and outside of the prisms, since the capacitive coupling of the A gate to the B region – and vice versa – is kept minimal, illustrated by the orthogonal charge neutrality lines in fig. 3.10b. A similar approach was used in ref. [197].

Let us now look at the device resistance as a function of these two charge carrier concentrations. For a first qualitative impression, this is plotted in figure 3.10b at a temperature of 100 K. Making use of the hypothesis that the device is fully transparent when the access and the barrier are tuned to the same doping, we have subtracted the access resistance: $R_\text{CR}(n_\text{A}, n_\text{B}) = R_\text{raw}(n_\text{A}, n_\text{B}) - R_\text{raw}(n_\text{B} = n_\text{A})$. Note that for an ideal ballistic two-terminal device, one should actually measure the Landauer resistance R_L at full transparency, which is taken into account further below.

At this temperature, the phase coherence length $\ell_\phi = \pi\hbar v_F/k_B T = 240$ nm is sufficiently small compared to the single path dwell length $\ell_1 = 600$ nm, so that interference effects can be ignored. However, the acoustic phonon mean free path $\ell_\text{ph} \approx 0.8\ \mu\text{m} \times 300K/T = 2.4\ \mu\text{m}$ is still much longer than ℓ_1, so that scattering should not majorly disturb the reflection effect (c.f. design criteria in table 3.2).

The resistance peak at zero n_B simply corresponds to the charge carrier depletion at

the charge neutrality point (CNP). For $n_\mathrm{A} = 0$, this resistance peak was overcompensated by subtracting $R(n_\mathrm{B} = n_\mathrm{A})$. The shading of the quadrants (dark blue = low resistance in unipolar and light blue = high resistance in bipolar quadrants) is typical for a n-n'-n (n-p-n) barrier and can be found in refs. [50, 162] for rectangular barriers or in refs. [130, 197] for geometries similar to the one discussed in this section.

However, we can report here for the first time on a very clear resistance resurgence in the bipolar n-p-n regime, typical for a corner reflector. As predicted by theory in section 3.3.1, this resistance resurgence occurs for $|n_\mathrm{B}| > 6.8|n_\mathrm{A}|$, i.e. between the dashed black line and the x-axis ($n_\mathrm{A} = 0$) in fig. 3.10.

A similar, but much weaker resistance increase can be observed in the unipolar and in the p-n-p quadrants. As we will see below, the resistance increase in the unipolar region is actually expected to be much higher according to our theory, but this might be due to an overestimation of the base junction transparency by the Cayssol-Huard model in this regime. Furthermore, since we are typically dealing with n-doped contacts (see chapter 4), we expect spurious p-n junction effects when the access region is p-doped. This justifies our choice of the n-p-n experimental window for the following analysis.

Let us now focus on the data in the red dashed box in fig. 3.10, i.e. on the window $0.2 \times 10^{12}\ \mathrm{cm}^{-2} \le n_\mathrm{A} \le 1 \times 10^{12}\ \mathrm{cm}^{-2}$ and $-8 \times 10^{12}\ \mathrm{cm}^{-2} \le n_\mathrm{B} \le 4 \times 10^{12}\ \mathrm{cm}^{-2}$, which corresponds to Fermi wavelengths of 35 nm $\le \lambda_{FA} \le$ 79 nm and $\lambda_{FB} \ge$ 12 nm. Note that in this window, our effective junction length $d \approx 30$ nm (see COMSOL simulation in section 2.1.2) is neither particularly smooth nor particularly sharp, which justifies the use of the Cayssol-Huard expression for the junction transparency.

In terms of the effective refractive index $\eta = \mathrm{sign}(n_\mathrm{B}/n_\mathrm{A})\sqrt{|n_\mathrm{B}/n_\mathrm{A}|}$, we are exploring a very wide range $-6.3 < \eta < 4.4$, going to much higher values than what can be reached in conventional optical media (e.g. diamond with $\eta = 2.4$).

The data of this experimental window is plotted in figure 3.11a. Here we clearly see the sharp peak at the barrier CNP $n_\mathrm{B} = 0$, the resistance dips on both sides for $|n_\mathrm{B}/n_\mathrm{A}| \sim 1$ followed by a resurgence for $|n_\mathrm{B}/n_\mathrm{A}| \gg 1$. As mentioned before, the resurgence is less dramatic in the n-n'-n regime than in the n-p-n regime. Eventually, the resistance saturates on both sides, forming resistance *plateaus*. On the n-p-n side, the plateau resistance clearly decreases with increasing n_A, which could intuitively be understood by taking into account (a) the increasing ratio of refractive indices, therefore a smaller critical angle and a stronger total internal reflection effect and/or (b) the increasing number of ballistic modes $M = k_{FA}W/\pi$ impinging from the access region.

For the smallest value of n_A, the plateau resistance exceeds the value at the charge neutrality point, highlighting the significance of this reflection effect.

The resistance $R_\mathrm{CR}(n_\mathrm{A}, n_\mathrm{B}) = R(n_\mathrm{A}, n_\mathrm{B}) - R(n_\mathrm{A} = n_\mathrm{B})$ can easily be converted into a transmission: $\mathcal{T}_\mathrm{CR}(n_\mathrm{A}, n_\mathrm{B}) = R_L(n_\mathrm{A})/[R_\mathrm{CR}(n_\mathrm{A}, n_\mathrm{B}) + R_L(n_\mathrm{A})]$, where $R_L(n_\mathrm{A})$ is the two-terminal resistance of a ballistic sample with M modes and a four-fold degeneracy:

$$R_L(n_\mathrm{A}) = \frac{h}{4e^2}\frac{\pi}{k_{FA}W} \tag{3.20}$$

This transmission is shown in figure 3.11c. The plateaus for different n_A coincide when plotted as a transmission, which strongly suggests that the variation of the plateau resistance in fig. 3.11a is primarily due to the variation of M, c.f. hypothesis (b) above.

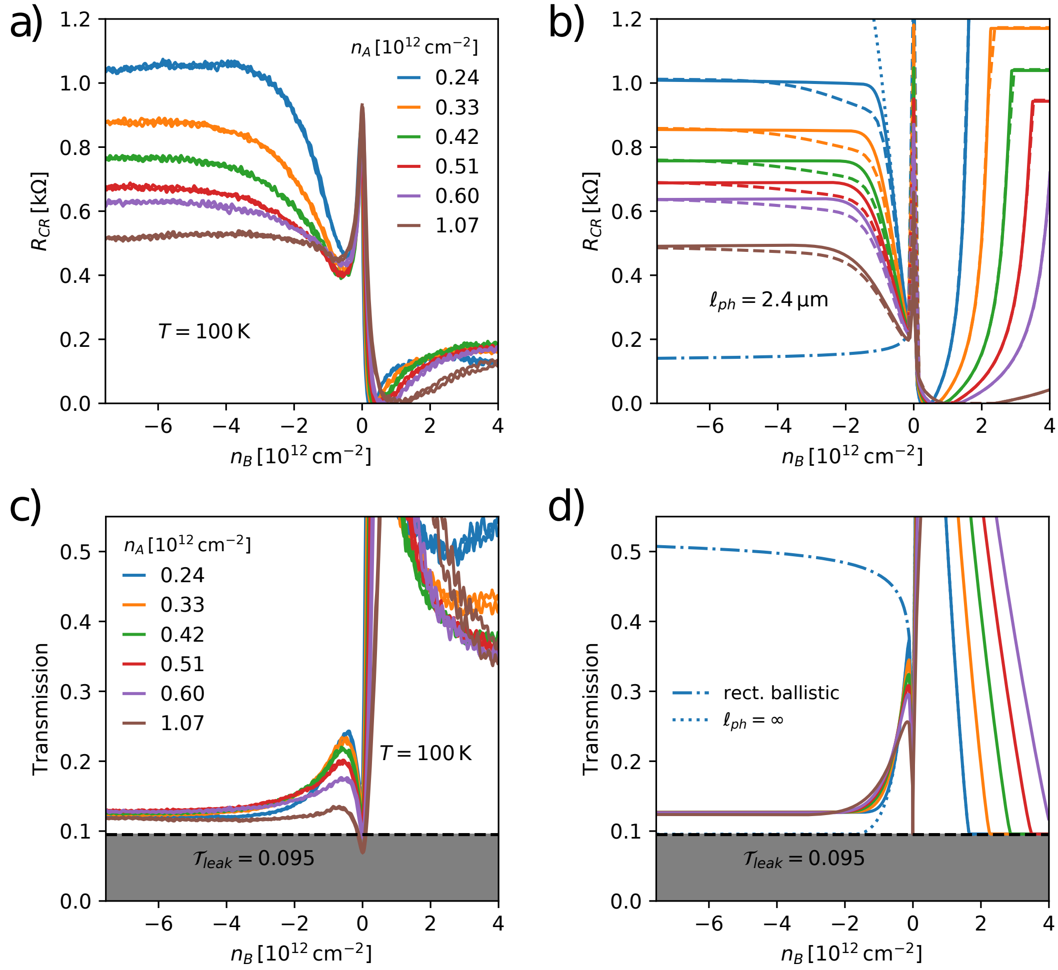

Figure 3.11 – **The reflection effect.** a) Experimental ($T = 100$ K) and b) simulated ($\ell_{\rm ph} = 2.4$ μm) device resistance as a function of barrier doping $n_{\rm B}$ for various access doping values $n_{\rm A}$. c) Experimental and d) simulated device transmission. In the simulation panels, solid lines correspond to analytical calculations according to eq. 3.16, while dashed lines in (b) are from a full ray tracing simulation. The dashed-dotted blue line describes a rectangular barrier, while the dotted blue line corresponds to the CR resistance/transmission in the case of infinite round-trips. Both are calculated for $n_{\rm A} = 0.24 \times 10^{12}$ cm^{-2}.

The fact that the plateau transmission is eventually independent of both $n_{\rm A}$ and $n_{\rm B}$ might initially surprise the reader, since the TIR effect discussed in section 3.3.1 is a direct consequence of the high ratio of refractive indices, but – as we established at the end of that modeling section – the residual device transmission in the TIR regime is no longer governed by the Snell-Descartes relation, but purely by the "base" junction transparency, which is constant for large $|n_{\rm B}/n_{\rm A}|$, see fig. 3.3d.

The panels (b) and (d) of figure 3.11 show the calculated resistance and transmission, respectively. The solid lines are computed using equation 3.16, inserting the phonon mean free path $\ell_{\rm ph} = 2.4$ μm (for $T = 100$ K), the junction length $d = 30$ nm and a leak transmission of $\mathcal{T}_{\rm leak} = 9.5\%$, the origin of which will become clear in section 3.4.3. The plateau values

in resistance and transmission are reproduced by this calculation with remarkable precision, without any adjustable parameters. The dashed lines in panel (b) illustrate the results of a corresponding ray tracing simulation as described in section 3.3.2. Both the resistance dip and the plateau value are in quantitative agreement with the analytical formula. Between the dip and the plateau, there is a slight deviation due to the limited validity of the assumptions underlying eq. 3.16 and due to the discretization of the ray-tracing simulation, but this is irrelevant to the analysis in the following, where we will focus on the resistance plateaus.

For comparison, the dashed-dotted blue line in the simulation figures represents the computed resistance/transmission of a rectangular ballistic barrier. Obviously, in this geometry, there is no resistance resurgence due to total internal reflection. As already shown in ref. [190], the resistance dip ("ON" effect) of the CR on the n-p-n side basically corresponds to the resistance of a rectangular junction and therefore depends on the p-n junction length, c.f. fig. 3.3.

Again for comparison, the dotted blue line illustrates the situation $\ell_{\mathrm{ph}} = \infty$. In this case, the transmission drops to zero (or to 9.5% when taking into account the leak) and resistance rises to infinity in the TIR regime. The strong deviation between this scattering-free picture [190] and our experimental observation highlights the importance of taking into account a finite escape probability for the fermions that undergo multiple internal reflections inside the prism.

The fact that the "Dirac peak" at $n_{\mathrm{B}} = 0$ is much sharper in the simulation than in the experiment can be explained considering that neither thermal smearing nor a residual charge carrier density are taken into account in this calculation.

In Morikawa *et al.* [130], similar resistance resurgences are observed in a device with a prism opening angle $\beta \sim 20°$. However, a resistance plateau could not be observed. This might have several reasons: The doping ratio required to achieve total internal reflection on the first tilted junction in such a device is $|n_{\mathrm{B}}/n_{\mathrm{A}}| > 33$, c.f. equation 3.10, which is larger than the experimental window explored in ref. [130] ($|n_{\mathrm{B}}/n_{\mathrm{A}}| \lesssim 3$). Furthermore, the AFM images shown in the article indicate a non-negligible junction roughness (an uncertainty of $\pm 5°$ is stated), which is another bottleneck for TIR to be effective. Interestingly, Morikawa *et al.* observe a similar discrepancy as we do in the n-n'-n regime, where one would expect a much stronger resistance increase from theoretical predictions. Also interestingly, they observed no TIR resistance increase at all for a prism with $\beta \sim 45°$. One might want to study their specific sample shape – the graphene channel has an almost 45° angle to the horizontal axis and the charge injection is very localized compared to our sample – in order to better understand their observation.

The results published by Wang *et al.* [197] can hardly be compared to this work, since the doping ratios – i.e. the refractive indices – that their article focuses on are on the order of ± 1. In this weakly refractive regime, total internal reflection on the tilted junction cannot be guaranteed at all, which is why no resistance resurgence is observed. Furthermore, the larger gap between the back gate electrodes (possibly convoluted by a high hBN thickness, information not provided in the article) leads to a reduced transparency of the p-n junction, i.e. to a smaller resistance dip.

Why sharp junctions? The corner reflector operates in two experimentally distinguishable regimes. Transmission (resistance dip in fig. 3.11) at small refractive index and reflection, limited by scattering inside the prism, at high refractive index (resistance plateau in fig.

3.11). In this context, smooth junctions have two disadvantages: At small refractive index, the transmission of the device would be reduced due to the narrow angular transmission window (see fig. 3.3c), whereas at high refractive index, fermions would stay trapped in the prism for longer, increasing the possibility of scattering-induced leaks. Overall this would lead to a smaller contrast between the two regimes.

3.4.2 Coherent Dirac fermion optics in a corner reflector

Let us now focus on the low temperature behavior of the CR. Figure 3.12a shows $R_{\mathrm{CR}}(n_{\mathrm{B}})$ at fixed $n_{\mathrm{A}} \approx 0.5 \times 10^{12}$ cm^2 for various temperatures between 10 and 280 K. At the lowest temperature, we can clearly see resistance oscillations superimposed on the TIR plateau. Panel (b) of the same figure is a zoom on the plateau (-8×10^{12} cm^{-2} $< n_{\mathrm{B}} < -3 \times 10^{12}$ cm^{-2}), this time plotted vs. the wavevector within the prism k_{FB}.

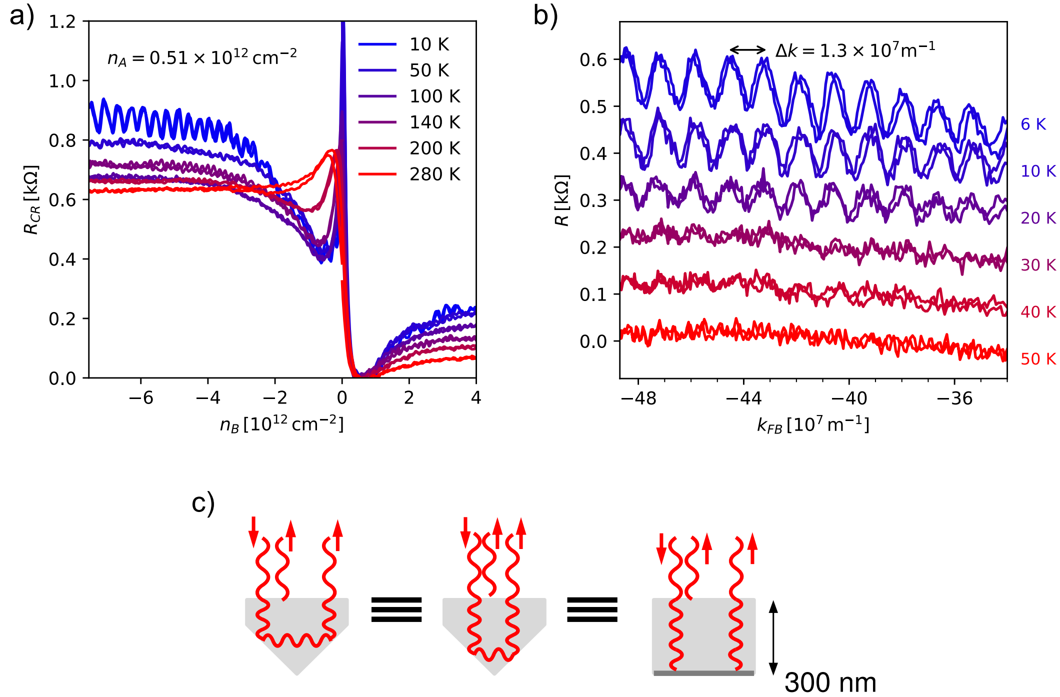

Figure 3.12 – **Coherent DFO.** a) As temperature increases, the CR resistance plateaus decrease. b) Quantum oscillations are superimposed to the resistance plateaus for temperatures lower than 40 K. c) Sketch illustrating the equivalence between the CR and a Fabry Pérot cavity for normal incidence trajectories.

The resistance oscillations are periodic in k_{FB} with a period of $\Delta k = 1.3 \times 10^7$ m^{-1} and their amplitude decreases progressively with increasing temperature. They disappear at around 40 K.

Even though our prism is not a Fabry-Pérot cavity, we have already established in section 3.3.1 that all trajectories with near-normal incidence (or that are simply sufficiently collimated by the Snell-Descartes and the Fresnel effects) have approximately the same length $\ell_1 = 2h = 600$ nm. This means that we can re-interpret our corner reflector's geometry as a Fabry-Pérot interferometer with one semitransparent and one fully reflecting mirror, parallel

to each other and separated by a distance h. This is illustrated in fig. 3.12c. The criterion for constructive interference is then $2h = m\lambda_{FB} = 2\pi m/k_{FB}$, i.e. $k_{FB} = m\pi/h = m\Delta k_{FB}$. This means we can *measure* the size of the electrostatically defined prism using the resistance oscillations:

$$h^{\text{meas}} = \frac{\pi}{\Delta k_{FB}} = 240 \text{ nm} \quad (3.21)$$

which is in fair agreement with the nominal value $h = 300$ nm. Actually, the deviation between the nominal and the measured value is only two junction widths ($d \approx 30$ nm) and therefore within the uncertainty of the gate-defined geometry. The temperature where the oscillations disappear is in accordance with the theoretical smearing temperature $T_{\text{smear}} = \pi\hbar v_F/k_B\ell_1 = 40$ K. A more involved analysis of coherent transport inside the corner reflector could be done by repeating the ray tracing simulations mentioned earlier, taking into account a phase term that depends on the propagation length. For the simpler geometry of a rectangular barrier, such a calculation was done in ref. [50]. However, this goes beyond the scope of this thesis and we will content ourselves with the oscillations as a confirmation of the geometrical reflection effect and as a "calibration" of the cavity size.

Morikawa *et al.* [130] mention the existence of "coherent resistance oscillations" at low temperatures, but they intentionally avoid this regime by characterizing their device at 120 K. Besides, the very clear signature that we show in fig. 3.12b is specific to the 90° apex prism; a different geometry might not ensure a constant round-trip path length.

Wang *et al.* [197] do not mention any signatures of coherent transport, but, as we pointed out in the previous section, they do not achieve high enough doping ratios to ensure TIR and, beyond that, their two-source geometry might affect the possible interference phenomena.

3.4.3 Diffusive optics due to acoustic phonon scattering

Besides the resistance oscillations, another striking feature of fig. 3.12a is the decrease of the resistance plateau with increasing temperature. Compared to the acoustic phonon limited resistivity of $dR/dT \approx 0.14$ Ω/K measured in a "bulk" graphene sample in ref. [47], the sensitivity of our CR thermometer is approximately -2 Ω/K if we look at the dependence of the plateau resistance on temperature, c.f. figure 3.13a and b. Note the unconventional minus sign of the temperature dependence in our experiment. The fact that thermal excitations enhance the electronic transmission, instead of reducing it, is a hallmark of the corner reflector. It violates Matthiessen's rule that resistance is additive in the scattering mechanisms and suggests an alternative rule, that it is the transmission that is additive in the scattering mechanisms. We shall use this property below when we take into account the corner reflector leakage due to imperfections.

This resistance decrease corresponds to a systematic increase of the residual transmission of the corner reflector with temperature, see fig. 3.13c (the transmission value is taken as an average over the plateau -8×10^{12} cm^{-2} $< n_{\text{B}} < -5 \times 10^{12}$ cm^{-2}). Again, we note that the transmission values are very similar for different values of access doping n_{A}. A linear increase of the residual transmission can be observed between 0 and 100 K. From 100 K upwards, the transmission saturates at around 13%.

This linear behavior suggests once more that the residual transmission is assisted by acoustic phonon scattering. The lowest transmission value, i.e. the extrapolation of this slope to $T = 0$ gives us the leak transmission $T_{\text{leak}} = 9.5\%$, that was already used above. We attribute this constant leak to:

- conduction at the rough edges of the graphene sample
- leakage at the tips of our prisms
- residual impurity- or defect-scattering

Let us now compare the experimental evolution of the residual transmission with our analytical model. Since we are strictly in the TIR regime, we can use the simple equation 3.17 and insert the acoustic phonon mean free path $\ell_{\text{ph}} = 0.8\ \mu\text{m} \times 300\ \text{K}/T$ (see also section 4.5.2). We observe a good quantitative agreement between the parameter-free model and the experimentally measured transmission up to $T = 100$ K (solid lines in the figure). Beyond

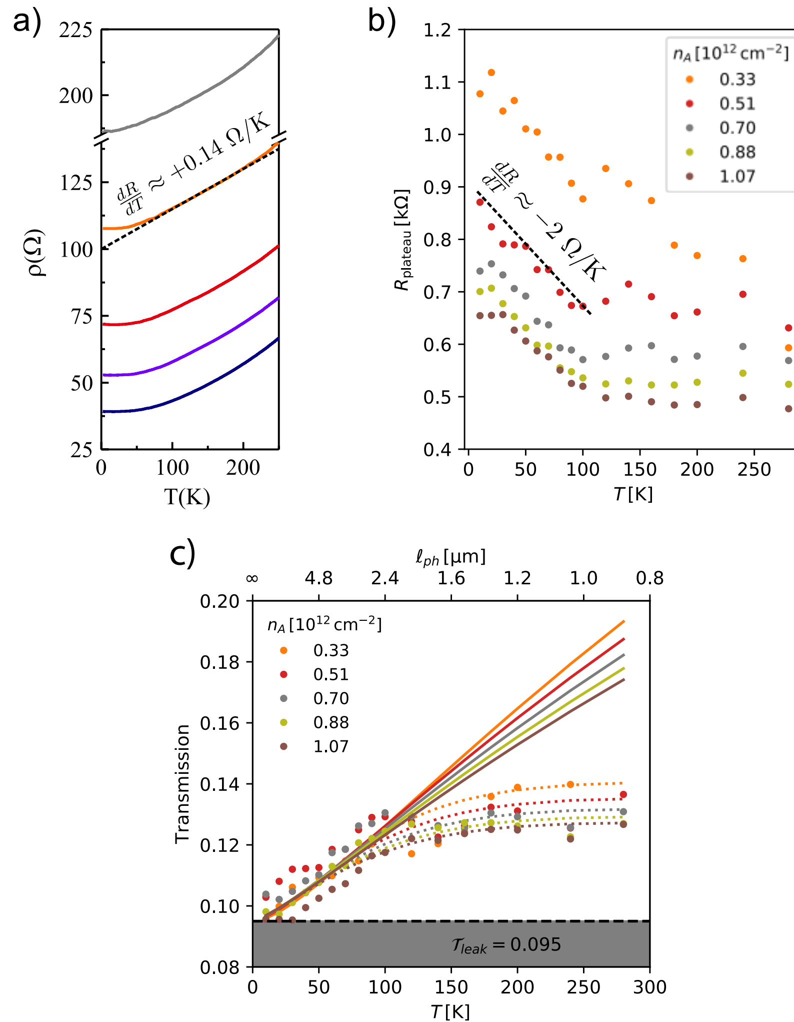

Figure 3.13 – **CR temperature dependence.** a) Temperature dependence of resistivity in a bulk graphene sample, taken from ref. [47]. b) Plateau resistance of the CR as a function of temperature. c) The plateau transmission increases with temperature up to 100 K, where it saturates. Solid lines are calculated using equation 3.17. The dotted lines, too, but with $d = 30\ \text{nm} + 2.25\ \text{pm/K}^2 T^2$.

this temperature, the experimentally observed residual transmission saturates. At the same time, the resistance dip (c.f. fig. 3.12a) starts to be smeared out.

As established in section 3.4.1, the resistance dip measures the single junction transmission which is linked to the junction width. A smaller dip corresponds to a larger junction length (inversely said: a sharper junction is more transparent). By introducing an ad-hoc phenomenological temperature dependence of the junction length $d = 30$ nm $+ \gamma T^2$, we can fit our data very well with $\gamma = 2.25$ pm/K^2 (dotted lines in the figure). However, this implies $d = 200$ nm at room temperature, which means that the junctions would extend almost over the entire prism or at least over the minimal gate length where the prisms overlap. Introducing this temperature dependence in the junction length is only one of many ways of taking into account a decrease of junction transparency with increasing temperature, and should not be taken too "literally". The T^2 dependence in our ad-hoc expression however suggests that electron-electron (e-e) interactions might mediate this effect.

In general, e-e interactions and "viscous effects" [206, 207] are not taken into account in our model, but they could play a non-negligible role in particular at temperatures where the e-e scattering length becomes comparable to or shorter than the acoustic phonon scattering length. For $E_F > k_B T$, which is always the case in the operating regime of our device, the e-e scattering length ℓ_{ee} is on the order of [46]:

$$\ell_{ee} \sim \frac{1}{\alpha_{ee}^2} \frac{(\hbar v_F)^2 \sqrt{\pi n}}{(k_B T)^2} \tag{3.22}$$

Here $\alpha_{ee} \approx 0.7$ is the fine structure constant in hBN-encapsulated graphene (see section 1.6.1), so that $\ell_{ee} \sim 5$ μm at 100 K. In ref. [206] (supplementary material), more sophisticated numerical calculations based on the RPA find $\ell_{ee} \approx 0.3$ μm at 220 K and 3×10^{12} cm^{-2}, which extrapolates to $\ell_{ee} \approx 2$ μm at 100 K and 6×10^{12} cm^{-2}. This value is comparable to the acoustic phonon mean free path at the same temperature, c.f. figure 3.13c.

In the access region, where the doping can be as low as 3×10^{11} cm^{-2}, the e-e mean free path is on the order of $\ell_{ee} \sim 1$ μm at 100 K according to the above formula, which is comparable to the sample width.

There are thus three ways in which e-e interactions could affect the CR transmission at high temperatures $T \gtrsim 100$ K:

- as an additional scattering channel in the barrier, in which case the residual transmission should increase at high temperature, opposite to the experimental observation
- scrambling the flow of electrons in the access region and therefore cause an increased back-flow leading to a lower transmission, in accordance with the experimental observation
- as a renormalization of the junction transmission (Fresnel relations), for which no theory exists to our knowledge

Morikawa *et al.* [130] also characterize the temperature dependence of their device by studying the resistance difference ΔR between two arbitrarily chosen points along the resistance slope for $V_{gB} < 0$. This would correspond to the left side of our resistance dip. They observe a weak increase of this ΔR between 0 and 150 K and then a stronger decrease between 150 and 300 K. This is in accordance with our experiment, c.f. fig. 3.12a: the

resistance dip stays almost the same up to 140 K, and then decreases gradually from 140 to 280 K. This high temperature behavior corroborates the above-mentioned hypothesis that a modification to the junction transparency might be required for $T \gtrsim 100$ K. Since Morikawa *et al.* did not observe the resistance plateaus, the effect of acoustic phonon scattering for $T \lesssim 100$ K could not be studied in their experiment. Their maximum ΔR is on the order of 150 Ω for a channel width of around 2.4 μm, i.e. 360 $\Omega\mu$m, whereas the maximum ΔR in our experiment is $\sim 500\ \Omega$ (c.f. fig. 3.11a) for a channel width of 1.6 μm, i.e. 800 $\Omega\mu$m.

Wang *et al.* [197] report an ON-OFF ratio that is constant with temperature. Their ON-OFF ratio is defined between the extreme values of $R(V_{gB} \ll 0)$ and $R(V_{gB} \gg 0)$. Again, the fact that the effect of acoustic phonon scattering is not observed in Wang *et al.*'s work is simply explained by the fact that they do not explore the high refractive index regime. However, a modified junction transparency should still be detectable in the high temperature limit, provided their device is indeed ballistic.

3.4.4 A corner reflector operating at GHz frequency

Whereas the previously described corner reflector characterization was carried out with a lock-in amplifier in the kHz range, measurements at GHz frequency require a modification of the instrumentation: For this type of acquisition, we use a VNA combined with DC sources and voltmeters, decoupled by bias tees. This was explained in section 2.2, where I also mentioned the origin of the real and imaginary parts of the HF transistor admittance in terms of a small signal circuit model.

Figure 3.14 shows a full set of complex admittance parameters Y_{ij} of the device CR-AuEG-17.ML with both gates set to 0 V and a source drain bias voltage of $V_{ds} = 10$ mV. The data was acquired between 0 and 21 GHz and at $T = 60$ K. This temperature was chosen in order to avoid the coherent CR regime, while observing a strong TIR effect.

For clarity, the small signal circuit quantities – i.e. the drain-source conductance R_{ds}^{-1}, the transconductance $g_m = \partial I_{ds}/\partial V_{gB}$ and the various intrinsic (and parasitic: superscript zero) capacitances, as introduced in section 2.2 – are indicated on the graphs. In the following, we focus in particular on R_{ds}^{-1} and g_m. It is clear from figure 3.14 that both are very small: $R_{ds}^{-1} < 1$ mS and $g_m \sim 1\ \mu$S. Compared to admittances on the order of 10 mS for the plasma resonance capacitors discussed in chapter 4, this small signal is obviously more prone to noise and an increased influence of systematic errors, as we will see in the following.

Even taking into account the small device width of $\sim 1\ \mu$m, these values are disappointingly low compared to state of the art graphene transistors, where drain-source conductances on the order of 8 mS/μm per unit width can be reached [144]. The main issue here is the high contact resistance ~ 5 kΩ of the CR devices. This could be addressed by gating the contact [27, 129] or enhancing the contact length by etching it into a comb shape [27].

The transconductance is in principle proportional to the applied DC bias V_{ds}, but since we want to preserve the ballistic CR effect, we cannot apply biases on the order of 1 V, where the transconductance can go up to $\sim 300\ \mu$S/μm in state of the art devices [144].

Due to the weak response of our device, the de-embedding was kept at a minimum: no thru-line was used, only the dummy parasitic capacitances were subtracted (c.f. section 2.2). Since the reference device did not have exactly the same geometry as the device under test in the center region, the de-embedding is approximative, which might explain certain offsets observed in the following.

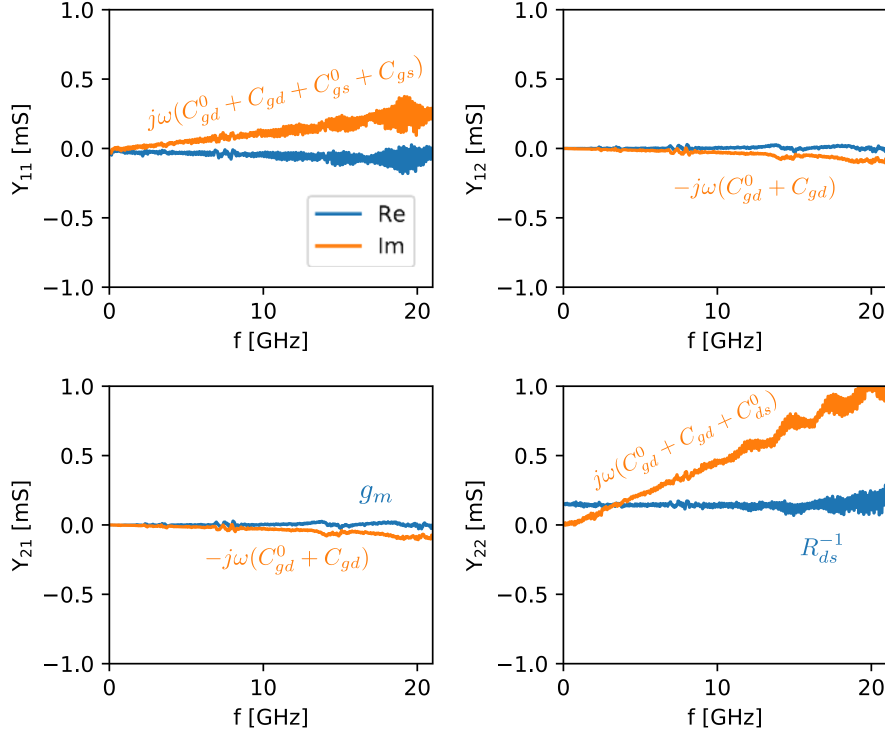

Figure 3.14 – **CR admittance spectra.** Complex admittance parameters of CR-AuEG-17.ML at $T = 60$ K, $V_{gA}, V_{gB} = 0$ and $V_{ds} = 10$ mV.

In order to study the CR behavior at high frequency, we performed gate voltage sweeps in the same manner as in the previous sections: The access gate V_{gA} was kept fixed while the barrier gate V_{gB} was swept. For each point in V_{gB}, only a "narrow bandwidth" spectrum $9.5 \ldots 10.5$ GHz was acquired, because time was a limiting factor (liquid helium consumption, stability of the device behavior, probe tip jumps). This frequency range was chosen because it was still relatively noise-free, compared to the data at 20 GHz, see fig. 3.14.

The data was then averaged over this frequency range and the result is plotted in fig. 3.15. The panels on the left show the DC device resistance and transconductance (calculated by numerical differentiation) and the panels on the right show the corresponding values extracted from the VNA spectra. For clarity, and similarly to section 3.4.1, only a reduced set of (n-doped) V_{gA} is shown.

Even though we observe large offsets between the DC and the 10 GHz data both in R_{ds} and in g_m, the resistance dips and plateaus, which are characteristic for the CR, are clearly visible in both data sets. The transconductance has two sharp peaks close to the charge neutrality point, but remains relatively flat otherwise, in accordance with the weak slope of $R_{ds}(V_{gB})$ in the vicinity of the plateaus. The inset of figure 3.15 shows a plot of the drain-gate capacitance, extracted from the slope of $\mathbb{Im}(Y_{12})$. Here again, the absolute value of ~ 0.5 fF is only in approximate agreement with the predicted value (3 fF$/\mu$m$^2 \times 0.3\ \mu$m$^2 = 0.9$ fF), but we observe the characteristic quantum dip of capacitance around the charge neutrality point. Interestingly, the capacitance seems to depend on the access gate voltage, which might

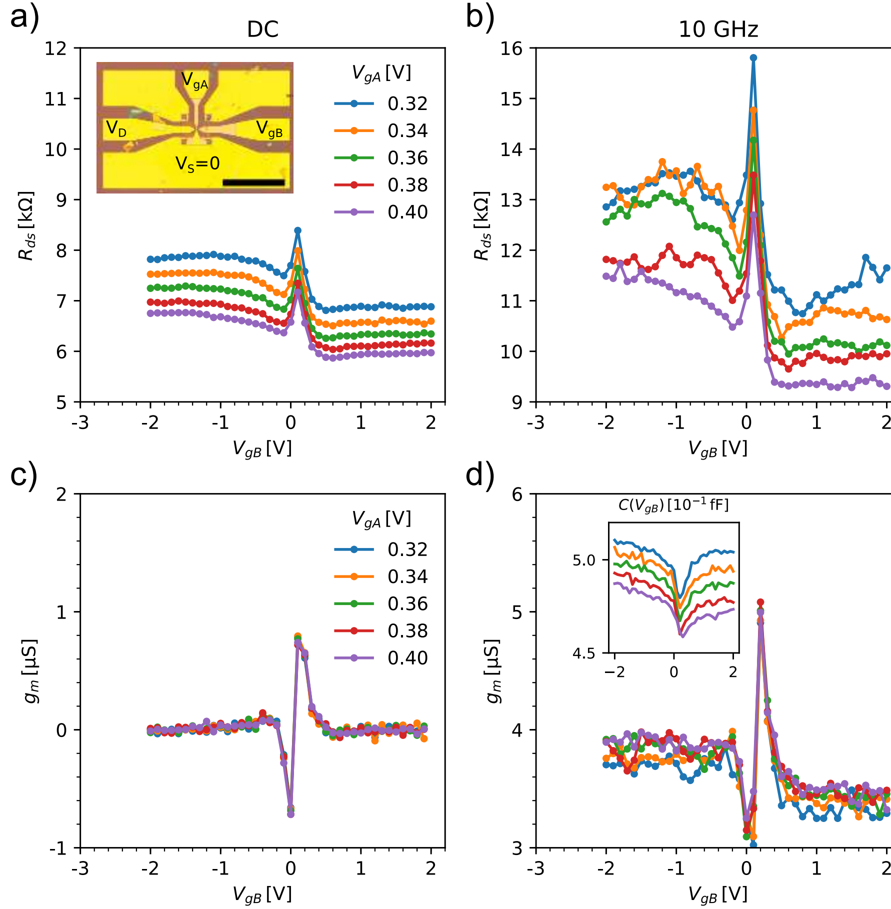

Figure 3.15 – **CR operating at GHz frequency.** a/c) DC device resistance/transconductance as a function of barrier gate voltage for various access gate voltages. Inset a) Micrograph of device CR-AuEG-17.ML with 200 μm scale bar. b/d) Source-drain resistance/transconductance at 10 GHz. Inset d) Gate-drain capacitance.

be due to cross-talk between the access and the barrier region.

Even though these results imply that our device is not a great candidate for high frequency electronics applications, they still constitute – to my knowledge – the first demonstration of Dirac fermion optics in this very high frequency range. From a fundamental point of view, this observation is not surprising since the dwell time of fermions in the device is on the order of picoseconds: compared to this timescale, GHz measurements are still quasi-static and higher frequencies or larger devices are required to actually probe the dynamics (dwell time) of the charge carriers.

Due to the aforementioned issues with contact resistance, a more detailed analysis of cut-off frequency, power gain and other figures of merit of high speed transistors and the comparison with theoretical proposals [195], in particular concerning the dwell time [208], are beyond the scope of this thesis.

3.4.5 Comparison of all fabricated devices

A total of eight corner reflectors was fabricated throughout this thesis. They are listed in table 3.3 and SEM pictures of all devices are shown in 3.16. Out of this series, three devices were defective: CR H8.2 and CR H8.4 had broken contacts, CR-AuEG-11.MC had a leak between the two gate electrodes. The remaining five samples all showed the desired reflection effect (increase in resistance for high doping contrast).

sample	gate material	contact material	apex angle	bottom hBN thickness [nm]	n_A [10^{12}cm^{-2}]	T [K]
CR H4 1x3	W	Cr/Au	90°	6	-0.17	20
CR H5 2x3	W	Cr/Au	90°	25	-0.11	20
CR H8.2	W	Ti/Al	90°	8	defective	
CR H8.4	W	Ti/Al	90°	∼12	defective	
CR H9.4	**W**	**Cr/Au**	90°	**9**	**0.33**	**60**
CR-AuEG-11.MC	Au	Cr/Au	120°	21	defective	
CR-AuEG-17.BL	Au	Cr/Au	90°	19	-0.34	7
CR-AuEG-17.ML	**Au**	**Cr/Au**	90°	**5**	**0.85**	**60**

Table 3.3 – List of fabricated CRs. n_A and T denote the charge carrier density (positive for electron, negative for hole doping) and the working temperatures used in figure 3.17. The two samples that we have mostly focused on are highlighted in bold.

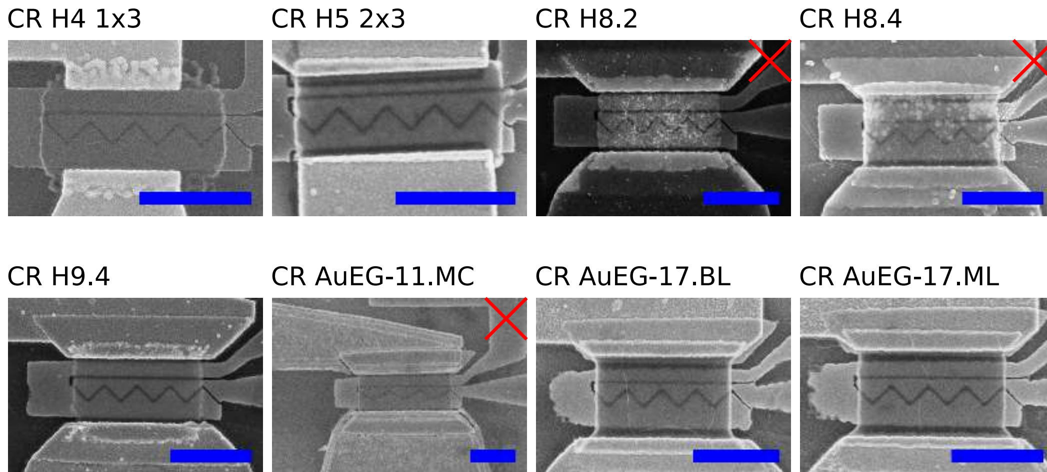

Figure 3.16 – SEM micrographs of the corner reflector samples fabricated throughout this thesis. The blue scale bar in each picture corresponds to 1 μm. Red crosses indicate samples that could not be characterized because they broke early.

This is illustrated in figure 3.17, where the device resistance (minus the minimum resistance, similarly to what was explained previously) at the "working point" is plotted as a function of the doping ratio n_B/n_A. Here I define the "working point" as the combination of access density n_A and temperature T (c.f. table 3.3) where I obtained the best data for a

given device. Since the devices also have different gate capacitances, it makes sense to plot the resistance as a function of the dimensionless density ratio for comparability.

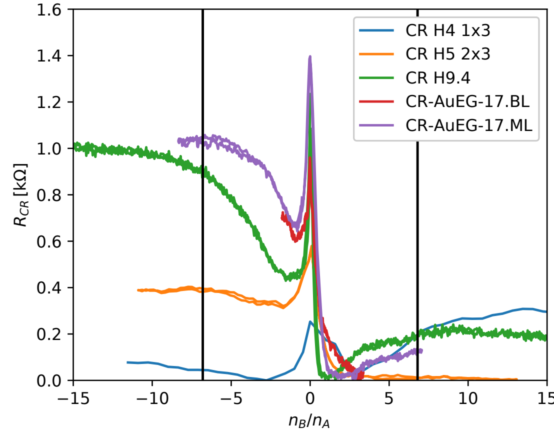

Figure 3.17 – **Scaling of the reflection effect.** Device resistance (minus minimum resistance) for all working CRs as a function of the dimensionless doping ratio $n_\mathrm{B}/n_\mathrm{A}$ at the working point n_A, T given in table 3.3. Vertical black lines correspond to $|n_\mathrm{B}/n_\mathrm{A}| = 6.8$.

While all devices show the characteristic resistance dips on either side of the barrier charge neutrality point, the first two devices CR H4 1x3 and CR H5 2x3 have much broader “Dirac” resistance peaks and only a weak resistance increase due to the reflection effect. This can be understood qualitatively in terms of lower mobility (more impurities) and geometric imperfections, which are clearly visible in fig. 3.16. The other three samples show quantitatively comparable behavior, with resistance dips around 0.5 kΩ and plateaus around 1 kΩ in the bi-polar regime and a much weaker resistance increase for $n_\mathrm{B}/n_\mathrm{A} \gg 1$ in the uni-polar regime.

Overall, this scaling behavior shows that the reflection effect is robust and reproducible, which paves the way for the implementation of DFO principles in real-world applications.

3.5 Conclusion and perspectives

In this chapter, we have investigated gate-tunable corner reflectors for Dirac fermions. Our state-of-the-art nanofabrication technology has enabled us to explore a broad doping range and to observe experimental evidence of the reflection effect in the form of a resistance increase at high doping contrasts. The device transmission eventually saturates, forming well-defined plateaus that are independent of barrier- and access-doping and which represent a new phenomenology for this kind of device. In addition to conventional ray-tracing simulations, we have introduced a simple analytical model to calculate the device transmission in the bipolar regime, in excellent agreement with the experiment. The residual transmission of our device increases linearly with temperature, leading to an anomalous $R(T)$ behavior, which was explained quantitatively by including acoustic phonon scattering as a limit for the number of round-trips in our model. At the lowest temperatures, quantum oscillations are superimposed on the resistance plateaus. To our knowledge, Fabry-Pérot oscillations have

not been reported in this kind of geometry before. Their period corresponds to the round trip length of the TIR trajectories, providing further evidence for a well-defined potential landscape (homogeneous prism with a sharp tip and low interface roughness). Finally, and for the first time to our knowledge, we have performed DFO experiments at GHz frequency. Due to the large Fermi velocity and the ballisticity of the devices, the demonstration of DFO at high frequency is not a fundamental surprise, but still a technological achievement, paving the way for new DFO-based applications. In conclusion, we have studied coherent, geometric and weakly diffusive optics in the CR devices. We have demonstrated their extreme sensitivity to small scattering rates and their high frequency operation. This makes them ideal candidates for high speed phonon sensing.

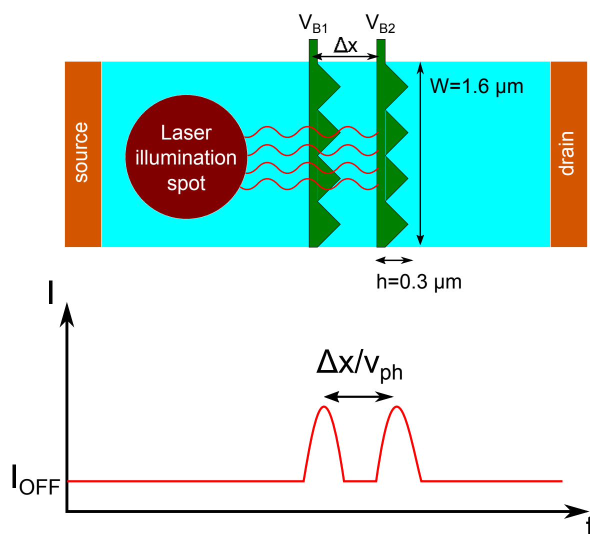

Figure 3.18 – **Phonon time-of-flight measurement.** Two CRs in series could detect the time of flight of (ballistic) phonons as peaks in the source-drain current.

A possible future experiment could therefore be a phonon time-of-flight measurement, using two CRs in series. This is illustrated in fig. 3.18. A picosecond laser pulse illuminates a micrometer-sized spot in the vicinity of the CRs, while the sample is under constant bias. Before the illumination, we would measure the dark current corresponding to a constant phonon population at $T \sim 10$ K. The laser locally heats the sample, creating a phonon pulse of typical width 10 ps, which travels (ideally ballistically, as ref. [209] suggests) through the two CRs, causing leak current boosts, as sketched in the graph in fig. 3.18. With a phonon velocity of approximately 20 km/s, the current peaks should be separated by ~ 50 ps if the CRs are separated by ~ 1 μm distance. The photo-current generated by the laser is not taken into account in this simple sketch, but it should in principle travel much faster than the phonons ($v_F \gg v_{ph}$), leading to an early current peak before the two phonon-induced peaks.

Apart from this application of the CR, a couple of more basic improvements to the device design could be envisaged: The GHz response could be improved significantly by reducing the contact resistance, for example by increasing the contact surface with a comb shape (c.f. plasma resonance capacitors in chapter 4) or by adding contact gates (which might be difficult due to the geometry imposed by the CPWs). In order to benchmark the

quality of our tungsten/gold nanostructured gates, reference devices could be fabricated with graphite gates (c.f. refs. [79, 80, 127]), even though these cannot be used for high frequency characterization. As was pointed out in the results section, our device still suffers from a residual leak transmission of 9.5%, which we attribute to scattering at the sample edges and to possible diffraction effects at the prism tips. The first issue could be solved by eliminating the sample edges altogether, by creating a Corbino-type device with a flat and a sawtooth-shaped p-n junction ring, forming a "sunflower" transistor.

As far as GHz transport measurements are concerned, it would make sense to scale up the devices to a size where the dwell-time enters the high frequency measurement domain. With a 70 GHz VNA we can access dynamics on the order of ~ 10 ps, so scaling the prisms up by a factor of 10 (which should be difficult, but feasible with state of the art encapsulated graphene samples and a lot of patience) and reducing the contact resistance could enable us to measure this dwell-time. The transport dynamics could also be investigated by measuring the shot noise of the corner reflector.

Another interesting experiment would be to submit the CR to a weak magnetic field. This should significantly change the CR transmission, since the recurrent trajectories would be destroyed. By fine-tuning the cyclotron radius to some value close to the prism height h, the TIR effect should be overcome and a transmission close to the rectangular barrier transmission should be restored. The required field is on the order of $B = \hbar k_F / 2eh \sim 0.5$ T.

Beyond these CR-related perspectives, I would find it highly interesting to examine DFO devices with imaging techniques like scanning gate microscopy [205,210,211], a single electron transistor on an AFM tip [212] or NV centers in diamonds [213]. This could lead to a direct observation of the refraction/reflection effects and at the same time remove doubts about the domains of validity of the non-interacting DFO picture. The principles of DFO are obviously not limited to graphene and can be investigated in other Dirac matter, such as 3D topological insulators [214] or in Dirac-Weyl materials [215].

4
GHz plasmonics

Based on the notions of plasmonics introduced in chapter 1, we will focus in this chapter on graphene plasmonics at GHz frequencies. I will first provide a brief motivation of this work in terms of the high frequency limits of the graphene field effect transistors (GFETs). Then, I will introduce the transmission line model for plasmonics and show how it reproduces the plasmon dispersions found from the RPA in chapter 1. A brief bibliography of GHz plasmonics will be provided, illustrating how the spectral gap in the (sub-)THz regime can be addressed when Ohmic losses are minimized. The device we will focus on afterwards is the plasma resonance capacitor (PRC), see fig. 4.1. After providing an analytical model of the PRC's admittance, I will show some simulated spectra for both overdamped and resonant devices. We will then discuss the experimental results, in particular the plasma resonance observed at ~ 40 GHz with a quality factor of ~ 2 at cryogenic temperature. [27] I will emphasize that GHz spectroscopy is a powerful characterization tool, giving access to the inductance, capacitance, conductivity of the sample as a function of carrier density and temperature. Due to the absence of drain-source bias in capacitors, we probe the true equilibrium properties of the electronic system of interest. Finally, possible applications of these results will be pointed out and interesting future experiments will be discussed.

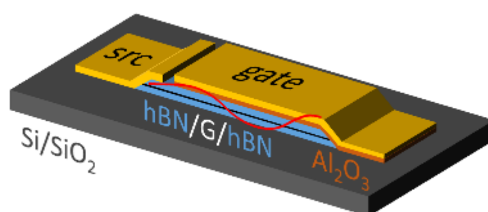

Figure 4.1 – Artist view of a plasma resonance capacitor.

4.1 Motivation

As pointed out in the previous chapter, graphene transistors are not very attractive for logic applications due to the absence of a gap in graphene, leading to poor ON/OFF ratios. However, GFETs stay interesting candidates for high frequency applications [150]. Two important figures of merit of RF transistors are the transit frequency f_T and the maximum oscillation frequency $f_{\max}$. The former is the frequency were the current gain is unity and is relevant for logic applications, whereas the latter is the frequency where the power gain is unity and is relevant for power applications. High mobilities in graphene enable high drift velocities, and current saturation can be obtained *via* substrate phonons [216], see also figure 4.2a [144]. Current saturation is required to obtain a high $f_{\max}$, since it is anti-proportional to the square root of the differential source drain conductance g_{ds}, which vanishes at saturation [149, 217].

To estimate the $f_{\max}$ of an intrinsic device (which is limited by the material properties of pristine graphene rather than by impurities in the channel, access resistance or parasitic capacitances) it is worthwhile considering the BLG transistor from ref. [144], which is also the subject of chapter 5. With a contact resistance $R_c \sim 150\ \Omega\mu\mathrm{m}$, a transconductance $g_m \gtrsim 0.25\ \mathrm{mS}/\mu\mathrm{m}$, a voltage gain $A = g_m/g_{\mathrm{ds}} \sim 8$ (see fig. 4.2c) and a gate capacitance of $C \approx 1.15\ \mathrm{fF}/\mu\mathrm{m}^2$, one predicts a cut-off frequency around $f_T L \approx g_m/2\pi C \approx 34$ GHz μm and a cut-off ratio $f_{\max}/f_T \approx \sqrt{A/4g_m R_c} \approx 7$, so that for a 2 μm long channel, a maximum oscillation frequency on the order of 100 GHz can be envisioned.

As examples of actual realizations of such RF transistors, fig. 4.2d and e show the extraction of f_T and $f_{\max}$ from references [218] (gate length 200 nm) and [219] (gate length 500 nm), respectively. We see that between 2011 and 2019, the extrinsic transit frequency of state-of-the-art devices has increased from $f_T L \approx 2$ GHz μm to 15 GHz μm. Extrapolated cut-off frequencies as high as 100 GHz (gate length 240 nm) have been reported in the literature [220], but $f_{\max}$ remains desperately small. The upper limit of graphene FETs is currently under investigation at ENS: Figure 4.2 shows an example of an encapsulated bilayer graphene FET fabricated by David Mele.

Taking into account the fact that within more than a decade of research, the 100 GHz operation of a GFET has still not been demonstrated and that even for an intrinsic device, this frequency represents the theoretical limit, it is necessary to explore new device operation modes, moving from the broadband "fermionic" devices to the narrowband "plasmonic" devices. Plasma resonance devices could operate in the 0.1−1 THz window, which is particularly interesting for telecommunication ("5G") and high resolution RADAR applications. Intuitively, this can be understood by considering the plasmon velocity, which is several times larger than the Fermi velocity.

An emblematic device for this paradigm change is the plasma resonance transistor (PRT), conceptually invented by Dyakonov and Shur in 1993, which exploits a hydrodynamic instability of the electron fluid to generate or rectify THz radiation [221, 222]. In this chapter, we focus on a similar, but simpler device, the plasma resonance capacitor, which sustains quarter wave resonances at longer wavelengths due to its asymmetric boundary conditions.

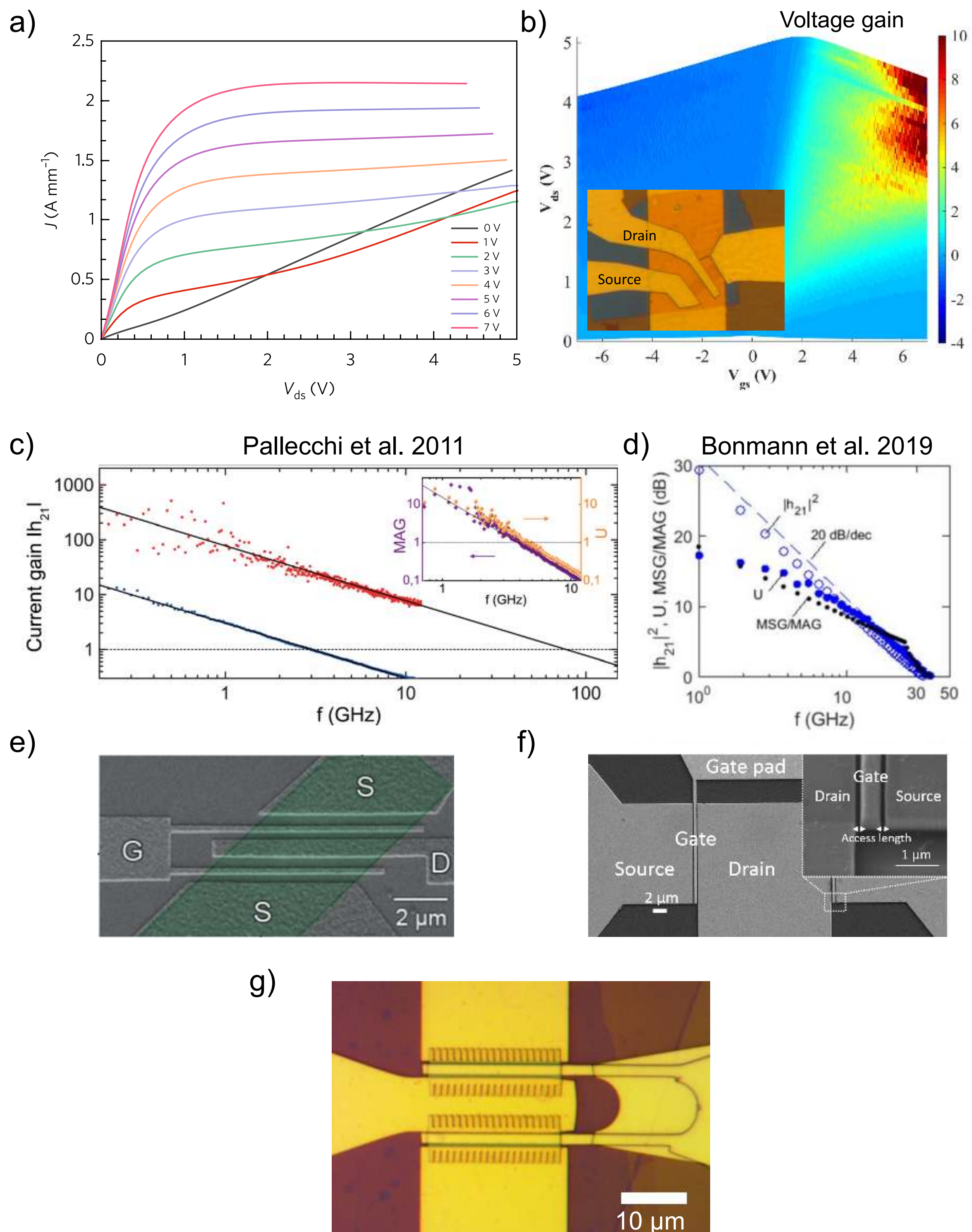

Figure 4.2 – $\mathbf{f_{max}}$ **of GFETs**. a) Current saturation for various gate voltages in a BLG FET, ref. [144] b) Voltage gain of the device as a function of source-drain and gate voltage. Inset: Photo of the device. c) Extrinsic (blue) and de-embedded (red) current gain of a graphene-on-sapphire FET from ref. [218] Inset shows voltage gain U and maximum available gain (MAG). d) Same quantities from ref. [219]. e and f) SEM pictures of the device from refs. [218] and [219], respectively. g) Optical image of an encapsulated-graphene high frequency FET fabricated at ENS.

4.2 Transmission line model of graphene plasmons

Since we characterize our devices in the electronic (hyperfrequency, GHz) domain it is suitable to use an electronic description for plasmons, which is done using circuit models: The graphene sheet is modeled as a transmission line (TL) and the electron interactions are encoded in distributed (lineic) capacitance and inductance. The presence of screening due to a gate electrode can be taken into account by adding a corresponding capacitive element [223]. Ohmic and radiative losses can be taken into account by adding a resistance [224, 225].

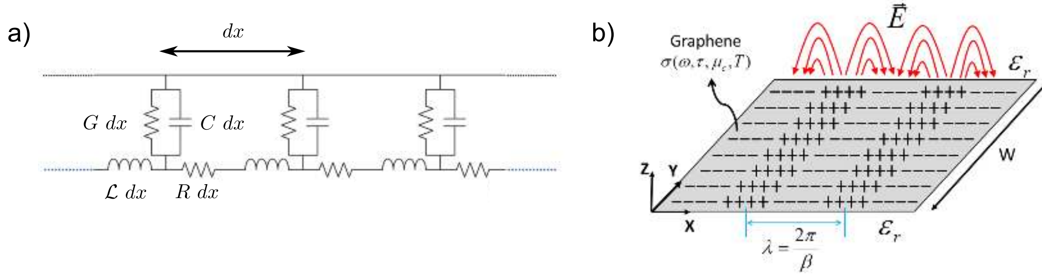

Figure 4.3 – **Transmission line theory.** a) Distributed element circuit model of a two-dimensional electron system. Resistance R, inductance $\mathcal{L}$, capacitance C and "leak" conductance G are defined per unit length. Adapted from ref. [224]. (b) The infinitesimal elements $R, \mathcal{L}, C$ can be calculated by applying Maxwell's equations to a static charge distribution corresponding to a plasmon of wavelength λ. Taken from ref. [225].

Such a transmission line is shown in figure 4.3a. The phase velocity and the characteristic impedance for electromagnetic waves traveling along such a TL are given by:

$$v_p = \sqrt{\frac{1}{\mathcal{L}C}} \tag{4.1}$$

$$Z_\infty = \sqrt{\frac{\mathcal{L}}{C}} \tag{4.2}$$

The expressions for these circuit elements can be derived in various manners, for example by solving Maxwell's equations for a static "plasmonic" charge distribution [223,225] as shown in figure 4.3b or by adequately rewriting the hydrodynamics equations [224]. In the following, we will simply state these expressions and show that they lead to the same dispersion as the RPA calculations described in the introduction. All expressions are given *per unit length* of the graphene channel, where W denotes its width. Typical values will be given for single layer graphene with a doping of $n = 10^{12}$ cm^{-2}, corresponding to a Fermi level of $E_F = 117$ meV, a Fermi wavevector of $k_F = 1.77 \times 10^8$ m^{-1} and an electron wavelength of $\lambda_F = 35$ nm. We will use a plasmon wavelength of $\lambda_{pl} = 2\pi/q = 100$ μm, which is very long compared to infrared and THz studies, but corresponds to the GHz plasmons studied in this chapter. For hBN-encapsulated devices with a thin dielectric layer, a typical gate-channel distance is $d = 20$ nm (with $\epsilon_r = 3.2$).

Kinetic inductance: This term can be derived from the collective kinetic energy of a shifted Fermi disk, as demonstrated e.g. in the supplementary material of ref. [226] or in ref. [100]. One obtains:

$$\mathcal{L}_K = \frac{\pi\hbar^2}{We^2E_F} = 73\ \text{pH}/W \qquad \text{at} \quad n = 10^{12}\ \text{cm}^{-2} \tag{4.3}$$

where E_F denotes the Fermi energy. The kinetic inductance can therefore be tuned by the gate voltage. Another example for tunable kinetic inductance is in Josephson junctions, where this quantity depends on the Josephson phase across the junction. [227]

Faraday inductance: The Faraday inductance can be derived from Maxwell's equations for a plasmon of wavelength $\lambda_{pl} = 2\pi/q$, taking into account a charge distribution as shown in figure 4.3b. For the derivation see refs. [223, 225]:

$$\mathcal{L}_F = \frac{\mu_0}{2qW} = 10\ \text{pH}/W \qquad \text{at} \quad \lambda_{pl} = 100\ \mu\text{m} \tag{4.4}$$

which is significantly smaller than $\mathcal{L}_K$, even at the very long wavelength considered here. In infrared studies, where the wavevector is ~ 1000 times larger, the Faraday inductance is obviously much smaller.

In-plane electrostatic capacitance: Similarly to the Faraday inductance, this term can be derived from Maxwell's equations [223, 225]:

$$C_{ES} = 2\epsilon_0\epsilon_r qW = 3.6 \times 10^{-3}\ \text{fF}/\mu\text{m}^2 \times W \qquad \text{at} \quad \lambda_{pl} = 100\ \mu\text{m} \tag{4.5}$$

where ϵ_r is the relative permittivity of the surrounding dielectric.

Geometric capacitance: This screening term is simply the capacitance of a parallel plate capacitor with a plate-separation d:

$$C_{\text{geo}} = \frac{\epsilon_0\epsilon_r}{d}W = 1.4\ \text{fF}/\mu\text{m}^2 \times W \qquad \text{at} \quad d = 20\ \text{nm} \tag{4.6}$$

Quantum capacitance: At zero temperature, the quantum capacitance of single layer graphene is given by:

$$C_Q = \frac{2e^2E_FW}{\pi(\hbar v_F)^2} = 27\ \text{fF}/\mu\text{m}^2 \times W \qquad \text{at} \quad n = 10^{12}\ \text{cm}^{-2} \tag{4.7}$$

Note that while the competition between C_{ES} and C_{geo} should be seen as "parallel", i.e. the larger capacitance dominates [223], C_{geo} and C_Q are in series (i.e. the smaller dominates) [38]. At the carrier density considered here, we can safely neglect the quantum capacitance since $C_Q \gg C_{ES}, C_{\text{geo}}$. In the following we will also neglect $\mathcal{L}_F$ for simplicity, leaving only $\mathcal{L}_K$, C_{ES} and C_{geo} for further analysis.

Unscreened plasmons: The "free" plasmon dispersion is easily found by neglecting the

presence of the gate electrode, i.e. $d \to \infty$ and $C_{\text{geo}} \to 0$. In this limit the phase velocity along the TL is given by:

$$v_p = \sqrt{\frac{1}{\mathcal{L}_K C_{ES}}} = \left[\frac{\pi\hbar^2}{We^2E_F} 2\epsilon_0\epsilon_r qW\right]^{-\frac{1}{2}} = v_F\sqrt{\frac{2\alpha_{ee}k_F}{q}} \approx 1.2\sqrt{k_F/q}\; v_F \tag{4.8}$$

leading to the same result for $\omega = v_p q$ that was obtained from the random phase approximation, see equation 1.59.

Screened plasmons: For strongly screened plasmons, we simply neglect the in-plane electrostatic capacitance C_{ES} (which is valid in the limit $\lambda_{pl} \gg d$) and find:

$$v_p = \sqrt{\frac{1}{\mathcal{L}_K C_{\text{geo}}}} = \left[\frac{\pi\hbar^2}{We^2E_F} \frac{\epsilon_0\epsilon_r W}{d}\right]^{-\frac{1}{2}} = 2v_F\sqrt{\alpha_{ee}k_F d} \approx 1.7\sqrt{k_F d}\; v_F \tag{4.9}$$

in accordance with the linear dispersion found from the RPA, c.f. equation 1.63.

Bilayer graphene plasmons: We can simply find the plasmon dispersion of BLG using the kinetic inductance of a massive 2DEG, c.f. e.g. ref. [97, 100]:

$$\mathcal{L}_K = \frac{m^*}{ne^2W} \tag{4.10}$$

where $m^* = 0.03m_e$ is the effective electron mass in bilayer graphene. One obtains (see also ref. [7]):

$$v_p = \left[\frac{m^*}{ne^2W} 2\epsilon_0\epsilon_r qW\right]^{-\frac{1}{2}} = \sqrt{\frac{ne^2}{2\epsilon_0\epsilon_r m^* q}} \tag{4.11}$$

which is valid both for BLG and for "conventional" semiconductor 2DEGs. Note that here the plasmon velocity is proportional to $n^{1/2}$ as opposed to $n^{1/4}$ in SLG, which makes the effect of doping modulation – by applying a gate voltage – more dramatic in bilayer graphene. This increased tunability of the plasmon velocity in BLG was recently exploited for resonant THz photodetection in ref. [106]. For screened BLG plasmons, one obtains (see also ref. [97]):

$$v_p = \left[\frac{m^*}{ne^2W} \frac{\epsilon_0\epsilon_r W}{d}\right]^{-\frac{1}{2}} = \sqrt{\frac{ne^2 d}{\epsilon_0\epsilon_r m^*}} \tag{4.12}$$

We have seen that the TL model reliably reproduces the dispersion of two-dimensional plasmons in various limiting cases. Not only is this approach reasonable with respect to the (electronic) spectral range that we will consider, it also enables us to calculate the complex admittance of the plasma resonance capacitor (section 4.4) and to take into account additional circuit elements, like the finite access resistance or p-n junctions in the graphene channel (see conclusion and perspectives).

4.3 Literature review

Graphene plasmons have been probed using a variety of techniques, ranging from electron energy loss spectroscopy [101, 228–230] over angle-resolved photo-emission spectroscopy [231]

and scanning tunneling spectroscopy [232] to a whole series of optical studies, mostly in the far infrared part of the EM spectrum, but also going down to frequencies in the THz range. These optical studies employed grating coupling [102, 233] or near-field coupling [103, 104, 234–237] in scattering-type scanning near-field optical microscopes to probe the plasmons. The latter can be combined with an electrical readout [105,109,238], which paves the way towards plasmonic devices, such as THz photo-detectors [106,239]. A more detailed review of these works is provided in section 6.4.

This section is split into three parts: First I will summarize my research group's previous works on GHz spectroscopy in order to introduce this technique and demonstrate how it can be used for material characterization while simultaneously providing access to fundamental physical properties. Remarkably, the devices under test in all these studies were *capacitors*, i.e. one of the simplest electronic components one can imagine. I will then briefly show how increasing scattering lengths, thanks to improving sample quality, enables the transition from THz to GHz plasmonics in semiconductor 2DEGs. Finally, I will summarize a few recent works, in which graphene plasmons (or signatures of electron-electron interactions) have been detected in the GHz frequency range.

4.3.1 GHz spectroscopy in capacitors

Figure 4.4 shows a summary of the aforementioned GHz spectroscopy studies. Three different 2D systems have been explored, namely graphene, HgTe-based 2D topological insulators (TIs) and Bi_2Se_3 topological surface states (TSS). The top row of the figure shows the respective device sketch and a microscopic image, the middle row shows GHz spectra acquired for different gate voltages – corresponding to different Fermi levels and carrier densities – and the bottom row shows an emblematic result of each individual study.

The journey begins in 2011 with a simple graphene field effect capacitor [38], made from exfoliated graphene, contacted on one side by a drain electrode and covered on the other side by an aluminum-oxide insulation layer which separates the graphene sheet from the gate electrode, see fig. 4.4a. The VNA spectra recorded between 0 and 10 GHz (fig. 4.4b) show variations of the capacitance (slope of the imaginary part of the admittance at low frequency) as a function of applied gate voltage, which are due to the energy-dependence of the density of states. The DOS is directly related to the quantum capacitance and has its minimum at the charge neutrality point. At the same time, the frequency of the crossover between real and imaginary part increases with increasing doping, which can be intuitively understood as a reduced charging time of the capacitor due to the increase of the conductivity with charge carrier density. Since both the quantum capacitance C_Q and the conductivity σ can be extracted from fits to the RF spectra, one can determine the diffusion constant D using the Einstein relation $\sigma(E_F) = C_Q(E_F)D(E_F)$ (where E_F denotes the Fermi energy set by the gate voltage). In the samples studied in ref. [38], this diffusion constant – which is proportional to the scattering rate – was shown to be independent of the Fermi level (fig. 4.4c), a behavior that is not compatible with phonon- or impurity-scattering, but could be explained by Dirac mass disorder.

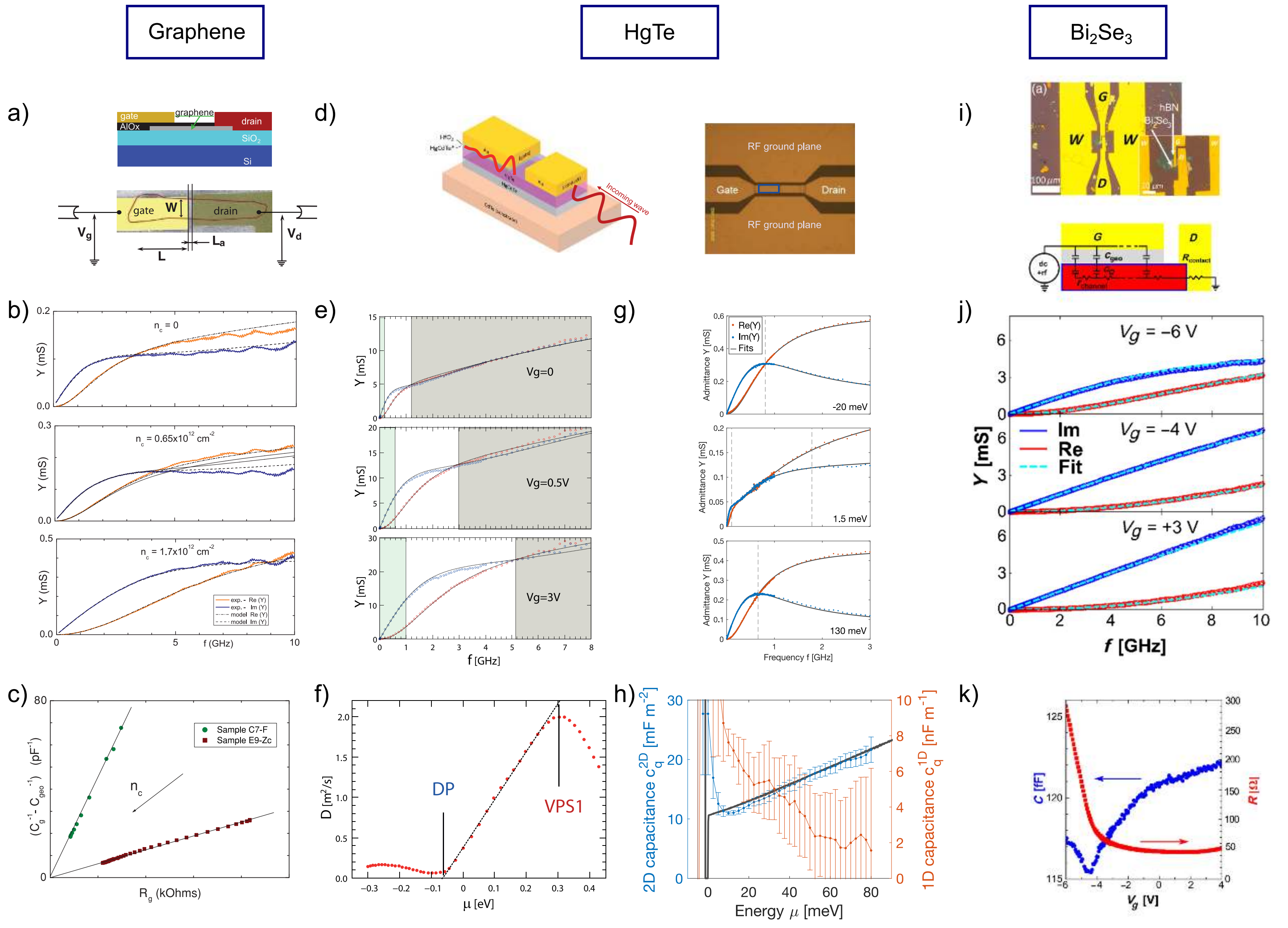

Figure 4.4 – GHz spectroscopy studies carried out at École Normale Supérieure on different materials. Figures from [38, 240–242].

The same approach was used by Inhofer *et al.* in 2017 [240] to study the electron compressibility and scattering in HgTe heterostructures. The spectra shown in fig. 4.4e are similar to those obtained for graphene and were again used to extract the quantum capacitance, the conductivity and thus the diffusion constant. Interestingly, the diffusion constant had a non-monotonous energy-dependence, which indicated the onset of an additional scattering channel (see "VPS1" in figure 4.4f). This behavior – along with other anomalies that occurred at high applied fields – could be explained by the existence of massive surface states (Volkov-Pankratov states) in addition to the expected massless topological surface states. In a more recent work by Dartiailh *et al.* [242], the same material was investigated in the quantum well limit, where topological surface states are substituted by edge states, and two distinct modes were identified in the spectra when the Fermi level was tuned close to the gap (c.f. the middle spectrum in fig. 4.4g). By further analyzing the dependence of these modes on the sample geometry (in particular scaling with length), the modes could be attributed to 2D ("bulk") and 1D (edge) contributions, see fig. 4.4h.

Another three-dimensional TI, namely Bi_2Se_3, grown as a thin layer on a high quality gate dielectric (hBN) using chemical vapor deposition (CVD), was studied using RF spectroscopy [241]. The quantum capacitance of the top surface states was observed in a regime where the bulk was depleted, and capacitive coupling to the bottom surface states could be detected.

Note that in the first study in 2011 the mobility at typical charge carrier densities (10^{12} cm^{-2}) was approximately 4500 cm^2/Vs, whereas the mobility of the TSS studied in ref. [240] (2017) was about 120 000 cm^2/Vs. Still, the spectra observed in all of these studies correspond to *evanescent* waves inside of the capacitor. In the hBN-encapsulated graphene capacitors studied in the present work we reach mobilities of up to 250 000 cm^2/Vs, where the damping effect of impurity- and phonon-scattering becomes weak enough to observe *propagating* waves and therefore a resonance in our capacitor cavity.

4.3.2 From THz to GHz plasmons in massive 2DEGs

In order to detect the effect of electron interactions in the form of kinetic inductance (see chapter 4.2) or of plasmonic resonances, the measurement frequency should be higher than the typical momentum scattering rate: $\omega\tau > 1$. This scattering rate depends both on the material quality (absence of defects and impurities) and on intrinsic parameters (e.g. phonon scattering). High quality two-dimensional electron systems have been available in semiconductors (e.g. Si inversion layers or GaAs/AlGaAs heterostructures) a long time before graphene was even isolated for the first time.

Already in the 1970s, the two-dimensional plasmon could be observed by means of far-infrared transmission spectroscopy in a silicon MOSFET device, equipped with a grating that couples the incident THz field to the plasmons in the inversion layer [243]. Note that this is the semiconductor-2DEG-equivalent to the 2011 experiment with graphene by Ju *et al.* [102] shown in the appendix 6.4. In this study, the maximum mobility was 16 000 cm^2/Vs, corresponding to $\tau = m\mu/e \approx 2$ ps with an effective mass of $m = 0.2\ m_e$. Figure 4.5a shows the relative change in infrared transmission as a function of frequency, where one can identify the Drude tail, oscillations due to inteferences in the silicon substrate, and – more interestingly – a pronounced peak due to the plasmon resonance. Tracking this resonance as a function of charge carrier density leads to the $\sqrt{n}$-law expected for a massive 2DEG and plotted in fig. 4.5b.

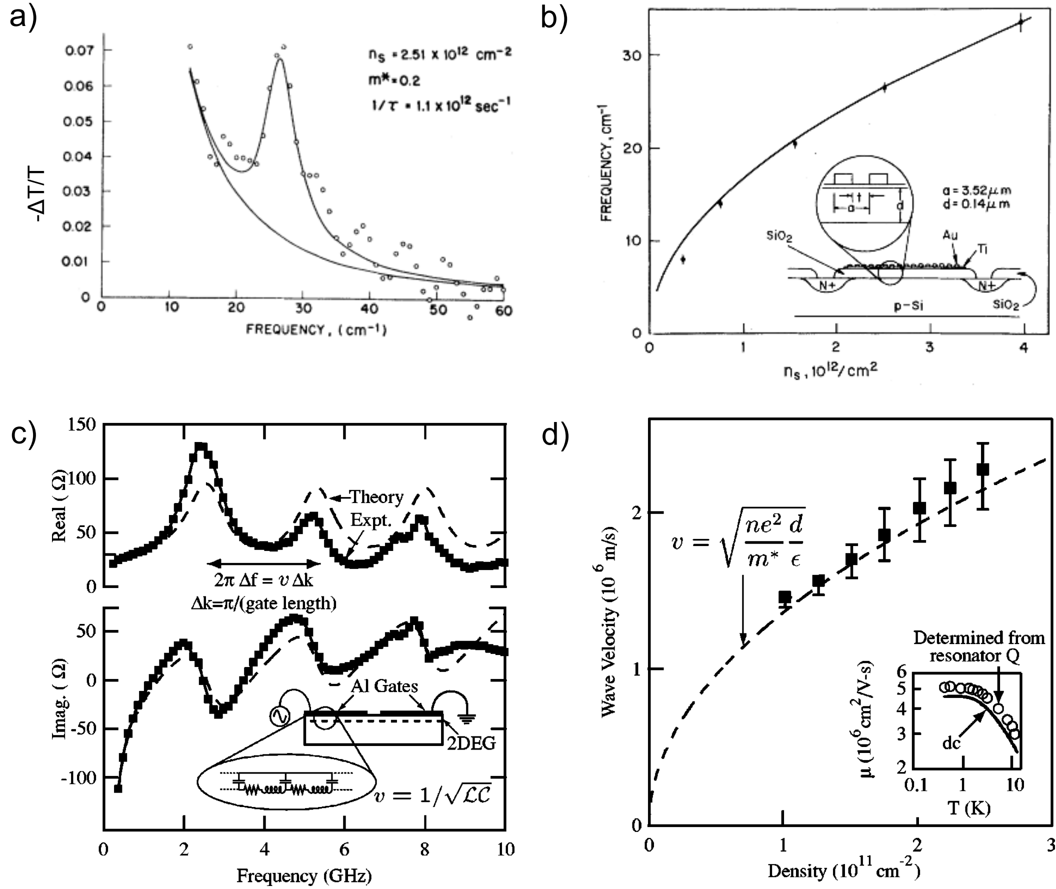

Figure 4.5 – **Plasmon resonances in massive 2DEGs.** a) Far-infrared spectrum of a silicon inversion layer (relative change in transmission). Resonance at $f \approx 30$ cm^{-1} = 0.9 THz. b) Experimental vs. theoretical carrier-density-dependence of the resonance frequency. Inset: Sketch of the device with grating pattern. c) Real and imaginary part of the complex impedance of a GaAs/AlGaAs 2DEG. d) Phase velocity as a function of carrier density. a-b) from [243], c-d) from [97].

The scattering rates are even lower in GaAs/AlGaAs (and similar) heterostructures, where it is possible to achieve electronic mobilities on the order of 10^6 cm^2/Vs corresponding to scattering rates $\sim$ 100 ps. In the year 2000 this enabled Burke *et al.* to observe plamon resonances at extremely low frequencies $\sim$ 1 GHz using vector network analyzer characterization [97]. Figure 4.5c shows the real and imaginary part of the impedance, obtained from the microwave reflection coefficient. Multiple harmonics are observed and – by plotting the phase velocity as a function of carrier density – the familiar $\sqrt{n}$-dependence is recovered, c.f. fig. 4.5d.

As illustrated in the inset of fig. 4.5c, Burke *et al.* have introduced the transmission line (TL) model to calculate the theoretical complex impedance of their 2DEG. The TL model has since been extensively used to describe the high frequency behavior of carbon nanotubes [98, 244–246], but that goes beyond the scope of this thesis. A particular advantage of transmission line theory is the cascade matrix (introduced in section 2.2.2), which facilitates

the calculation of the response of composite TLs, for example in order to describe plasmonic crystals [224, 247]. Within this formalism, ref. [224] predicts the existence of localized states at the boundaries of finite plasmonic crystals. Experimental evidence for the existence of these so-called Tamm states (again in the THz domain) was found in ref. [248].

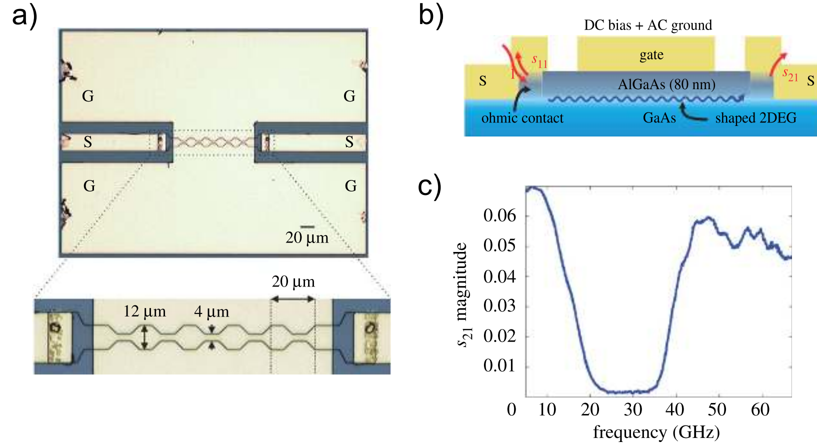

Figure 4.6 – **Plasmonic crystal.** a) Top view of the device, a width-modulated 2DEG with top gate, embedded in a CPW. b) Side view sketch of the device. c) VNA transmission parameter S_{12} plotted vs. frequency. Taken from [100]

Plasmonic crystals have also been studied in the GHz domain. By etching an GaAs/AlGaAs 2DEG into a periodic pattern, thus repeatedly modulating the plasmon impedance (anti-proportional to the width), Andress *et al.* [249] fabricated a GHz plasmonic crystal, embedded in a co-planar waveguide (see fig. 4.6a-b). By measuring the transmission S_{12} of the device, they observed the plasmonic bandgap between 24 and 34 GHz (see fig. 4.6c). In the same study, the authors also demonstrate two-dimensional plasmonic crystals and plasmonic interferometers operating in the GHz range, which shows how versatile these patterned 2DEGs are for controlling coherent plasmon propagation.

An advantage of the aforementioned materials, compared to graphene, is that they can be grown in a very clean manner, at the wafer scale, by molecular beam epitaxy (MBE). This is in contrast to the high-quality state-of-the-art graphene devices studied in this thesis, which are still limited in size by the dimensions of the exfoliated crystals. Still, due to its gapless nature, graphene could become a platform for new and intriguing plasmonics. In particular the investigation of gate-modulated plasmonic crystals (similar to those in ref. [248]) with p-n junctions could become highly interesting. To my knowledge, there is currently no theory for the propagation of plasmons in such a periodic lattice of Klein-tunneling junctions. Similarly to the evolution in semiconductor 2DEGs described above, it is necessary to increase the scattering times in graphene from ~ 1 ps to at least ~ 10 ps in order to move from far infrared to GHz plasmonics.

4.3.3 GHz plasmonics in graphene

In early microwave studies of CVD-grown graphene transmission lines [250, 251], the sample quality was still comparably low, leading to the conclusion that graphene behaves "as a wideband resistor with negligible kinetic inductance".

Kumada *et al.* have carried out time-resolved studies (with nanosecond resolution) of plasmon propagation in graphene grown on SiC, where the “bulk” mobility is on the order of 12 000 cm^2/Vs [252, 253]. Whereas a quantitative agreement with theory was difficult to obtain for “bulk” plasmons [254] (probably due to the high damping rate), exposing the sample to quantizing magnetic fields gives rise to so-called edge magnetoplasmons (EMP), which are less prone to losses and could therefore be probed in accordance with theory both in time-resolved [252, 253] and spectroscopic [253] measurements.

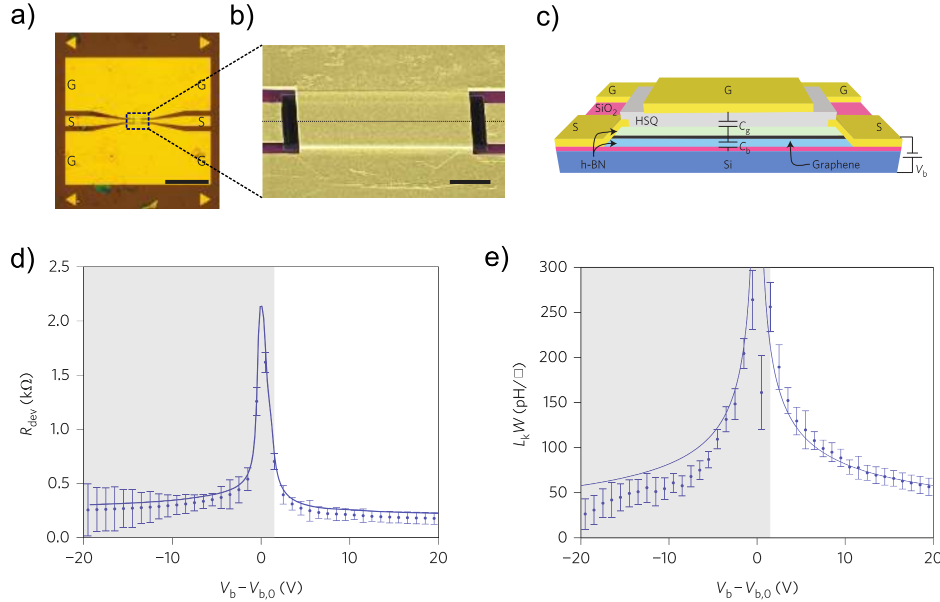

Figure 4.7 – **Kinetic inductance in graphene** a) Graphene transistor with a $\sim 20\ \mu$m long channel, embedded in a b) CPW. c) Sketch of the device design. d) Device resistance and e) inductance with theoretical expectation (solid lines) at $T = 30$ K. Adapted from ref. [226].

Thanks to the progress in device fabrication, in particular the encapsulation of graphene (see section 2.1.3), Yoon *et al.* [226] have fabricated a gated graphene transmission line with a mobility of around 390 000 cm^2/Vs at cryogenic temperatures, which enabled them to extract the kinetic inductance from their VNA spectra. They linked this inductance to the “collective dynamical mass” of the charge carriers, which corresponds to the effective cyclotron mass (*per* carrier) $m^* = \hbar k_F/v_F$ introduced in section 1.2.1.

In their $L \sim 20\ \mu$m long channel they measured an inductance of $\mathcal{L} \sim 100$ pH per square and a gate capacitance of $C \sim 0.15$ fF/μm^2 at typical doping values of $n \sim 10^{12}$ cm^{-2}, which corresponds to plasmon phase velocities of $v_p = 1/\sqrt{\mathcal{L}C} \sim 8 \times 10^6$ ms^{-1}. Since their cavity has symmetric boundary conditions, it supports $\lambda/2$ resonances $f_{res} = mv_p/2L \sim m \times 200$ GHz with $m = 1, 2, 3...$, which are beyond their 0−50 GHz measurement window.

In this chapter I will demonstrate how a resonant cavity can be made using encapsulated graphene of comparable mobility (250 000 cm^2/Vs) and length (24 μm) by making use of the asymmetric boundary conditions of a capacitor (leading to $\lambda/4$ resonances) and by bringing the gate electrode closer to the graphene, hence increasing the geometric capacitance (screening) and reducing the plasmon velocity.

4.4 Modeling the plasma resonance capacitor

In the broad frequency range addressed in the course of this project, a graphene capacitor cannot *per se* be modeled as a discrete electronic component, but one has to take into account wave propagation, which is done by using the transmission line model, introduced in section 4.2, with distributed resistance, inductance and capacitor components (c.f. figure 4.8b). This type of approach is well established for the high-frequency modeling of low-dimensional systems, such as GaAs/AlGaAs 2DEGs [97, 100] and carbon nanotubes [98, 244, 246].

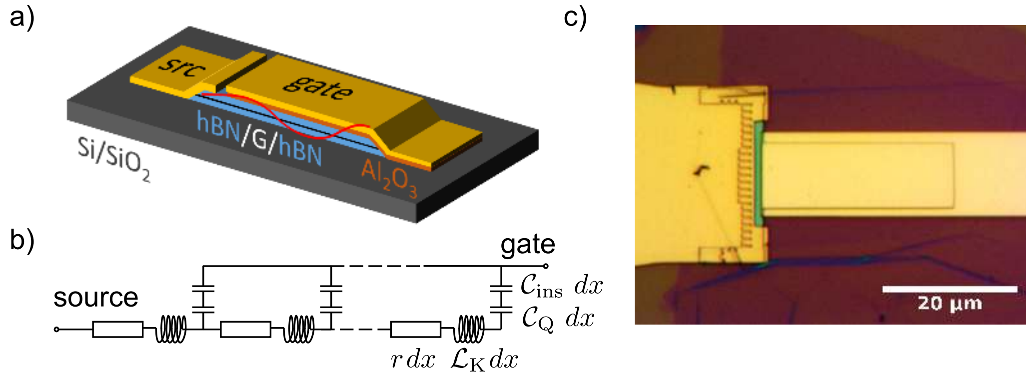

Figure 4.8 – The plasma resonance capacitor (PRC). a) Sketch of the device design. The red curved line illustrates the electric field, with a node at the source contact and an anti-node at the other extremity. b) Transmission line model for this device. c) Optical micrograph of the sample PRC-D7.

4.4.1 General complex admittance formula

The complex admittance of such a capacitor, illustrated in fig. 4.8a (in reality embedded in a co-planar waveguide) can easily be calculated using the TL model introduced in section 4.2. This calculation can be found in appendix 6.2 or in refs. [22, 24] for the diffusive case. If the kinetic inductance is taken into account, one finds the following expression for the PRC's admittance:

$$Y = \frac{\gamma}{r + j\omega\mathcal{L}_K} \tanh(\gamma L) \tag{4.13}$$

where $\gamma = \sqrt{j\omega C\,(r + j\omega\mathcal{L}_K)}$ is the propagation constant, r is the resistance, $\mathcal{L}_K$ the kinetic inductance, C the capacitance per unit length and L is the cavity length. Note that the capacitance has two components: the geometric capacitance $C_{\rm ins}$ and the quantum capacitance C_Q (c.f. figure 4.8b), which are in series so that $C = C_Q C_{\rm ins}/(C_Q + C_{\rm ins})$.

In this simplified model, we are neglecting the in-plane electrostatic capacitance (c.f. Ref. [223]), which amounts to considering plasmons in the screened limit. Furthermore, we are not taking into account the Faraday inductance $\mathcal{L}_F = \mu_0\lambda_{pl}/4\pi W$ which is ~ 1.2 pH/μm at the first resonance for a device with aspect ratio $L/W = 3$.

4.4.2 Important limiting cases

The low frequency admittance is given by the series expansion at $\omega = 0$:

$$Y_{\omega\to 0} = j\omega CL + \frac{1}{3}rL(\omega CL)^2 + \mathcal{O}\left(\omega^3\right) \tag{4.14}$$

which means that the linear imaginary part of the low frequency admittance provides a direct measurement of the total capacitance of the device, whereas the quadratic real part can subsequently be used to calculate the device resistance. Here, "low frequency" obviously also implies that $r \gg j\omega\mathcal{L}_K$. In diffusive capacitors, where this is always the case, the high frequency behavior is given by evanescent wave propagation in the capacitor:

$$Y_{\omega\to\infty}^{\text{diffusive}} = \frac{1+j}{\sqrt{2}}\sqrt{\frac{\omega C}{r}} \tag{4.15}$$

This high frequency admittance has a constant phase $\pi/4$ and is simply proportional to the square root of the frequency.

4.4.3 Electric potential distribution

The potential $V(x)$ within the capacitor is given by the following equation, derived in the appendix 6.2:

$$V(x) = V_0 \frac{\cosh\left(\gamma(x-L)\right)}{\cosh(\gamma L)} \tag{4.16}$$

4.4.4 Access resistance

Since a realistic PRC has a finite access resistance due to the metal-graphene contact and possibly due to ungated regions in the vicinity of the capacitor's "channel", a corresponding lumped element R_a is added to our model, leading to the following expression of the total admittance of our device:

$$Y_{\text{tot}} = \frac{1}{Y^{-1} + R_a} \tag{4.17}$$

Note that this additional real term causes a splitting of the high frequency real and imaginary part of the admittance. In an ideal diffusive capacitor, these are identical if the contact resistance is zero (see above). In order to de-embed spectra from the contact resistance, which will be done in sections 4.5.1 to 4.5.3, we simply solve this equation for Y and insert the experimental admittance data for Y_{tot}.

4.4.5 Tunable plasmon characteristics in the PRC

The phase velocity v_p and the characteristic impedance Z_∞ of our plasmon are given by textbook transmission line formulas [148] (in the lossless approximation):

$$v_p = \frac{1}{\sqrt{\mathcal{L}_K C}} \tag{4.18}$$

$$Z_\infty = \sqrt{\frac{\mathcal{L}_K}{C}} \tag{4.19}$$

Here the reader is also referred to the derivation of the plasmon dispersion for the screened case from the random phase approximation in chapter 1 (eq. 1.63) and from the transmission line model in this chapter (eq. 4.9).

Due to the asymmetric boundary conditions of the PRC (short circuit on the source side, open circuit on the gate side), it forms a quarter-wave resonator with odd harmonics $f_m = (2m+1)f_{\text{res}}$, where the fundamental frequency f_0 is given by:

$$f_0 = f_{\text{res}} = \frac{v_p}{4L} \tag{4.20}$$

We define the quality factor of our cavity as the ratio between the characteristic impedance and the total resistance of the graphene strip:

$$Q = \frac{2Z_\infty}{rL} \tag{4.21}$$

where the factor of 2 ensures compatibility with the common definition $Q = f_{\text{res}}/\Delta f$ (where Δf is the full width at half maximum of the resonance). Since the width Δf of the resonances stays the same for higher harmonics, the quality factor of the m-th harmonic is $Q_m = (2m+1)Q$. In terms of the "resonator" variables f_{res} and Q, the general formula for the admittance of a capacitor, eq. 4.13, can be recast to better reflect the resonating property:

$$Y = jZ_\infty^{-1} \frac{\tan\left(\tilde{f}\sqrt{1 - 2j/Q\tilde{f}}\right)}{\sqrt{1 - 2j/Q\tilde{f}}} \tag{4.22}$$

where $\tilde{f} = \pi f/2f_{\text{res}}$ is the reduced frequency. This formula exhibits resonances with a quality factor Q at the reduced frequencies $\tilde{f}_m = (2m+1)\pi/2$.

Armed with this set of expressions, we can now study the tunability of our PRCs. In table 4.1 we compare how the quality factor, the resonance frequency etc. vary as a function of carrier density, device length, hBN thickness and electronic mobility. A typical value for reasonable device parameters is also provided. We neglect the influence of quantum capacitance, so that $C = C_{\text{ins}} \propto 1/d$, where d is the insulator thickness, and use $\mathcal{L}_K \propto E_F^{-1}$, where E_F is the Fermi energy, which is $\propto n^{1/2}$ in single layer graphene and $\propto n$ in bilayer graphene.

From this evaluation, it becomes clear that – in particular as far as SLG is concerned – the *in situ* tunability of the resonance frequency *via* modulation of the charge carrier density is very limited, which implies that the observation (or not) of a resonance is mostly determined by the fabrication of a device with adequate dimensions. In principle, we were aiming for lateral dimensions as large as possible in order to obtain the lowest possible resonance frequency. However, the exfoliation of crystals bigger than 50×50 μm^2 proved to be difficult and the stacking process often resulted in cracks or bubbles, limiting the usable encapsulated graphene size to about 30×30 μm^2 (hence the conservative choice for $L = 25$ μm in table 4.1). Even with these limitations, we predict a resonance at ~ 30 GHz with a quality factor of ~ 1, compatible with the measurement window $0 - 40$ GHz of our Janis cryogenic probe station.

SLG / BLG	carrier density	length	hBN thickness	mobility	typical value at $n = 2 \times 10^{12}$ cm^{-2}, $\mu = 250\,000$ cm^2/Vs, $L = 25$ μm, $d = 20$ nm
$v_p \propto$	$n^{1/4}$ / $n^{1/2}$		$\sqrt{d}$		3.7×10^6 m/s / 3.6×10^6 m/s
$Z_\infty \propto$	$n^{-1/4}$ / $n^{-1/2}$		$\sqrt{d}$		190 $\Omega\mu$m / 190 $\Omega\mu$m
$f_{\text{res}} \propto$	$n^{1/4}$ / $n^{1/2}$	$\frac{1}{L}$	$\sqrt{d}$		37 GHz / 36 GHz
$Q \propto$	$n^{3/4}$ / $n^{1/2}$	$\frac{1}{L}$	$\sqrt{d}$	μ	1.2 / 1.2
tunability	gate	litho-graphy	stacking	"luck"	

Table 4.1 – PRC tunability and typical values. For the chosen point in parameter space, the SLG and BLG plasmon characteristics almost overlap completely.

4.4.6 Modeled spectra and field from resonant to diffusive regime

Figure 4.9 shows an exemplary set of PRC admittance spectra, calculated using eq. 4.13, and the corresponding potential distribution, calculated using eq. 4.16, in a capacitor of typical length $L = 25$ μm and carrier density $n = 2 \times 10^{12}$ cm^{-2}. The mobility was varied in order to demonstrate the transition from the resonant to the diffusive regime.

Panel (a) illustrates the admittance spectrum of a resonant cavity with a relatively high quality factor $Q \approx 5.0$, which can be obtained with a very clean graphene sample [119]. The first harmonic $f_{\text{res}} \approx 38$ GHz is within our experimental measurement window and the second harmonic is at $f_2 = 3 \times f_{\text{res}} \approx 114$ GHz as expected for a quarter-wave cavity. The amplitude and the phase of the electric potential for these two harmonics are plotted in panels (d) and (e), where we clearly see the node at $x = 0$ and the anti-node at $x = L$, imposed by the boundary conditions of our device.

In panel (b) we consider a more conservative prediction for the device mobility $\mu = 250\,000$ cm^2/Vs, resulting in a quality factor of $Q \approx 1.2$ and, as the figure shows, the first two harmonics can still be clearly distinguished.

Panel (c) shows the case of a diffusive capacitor with a much lower mobility of $\mu = 10\,000$ cm^2/Vs. This type of spectra has been analyzed extensively in order to study scattering processes in graphene [38] and in topological insulators [240], as shown in the literature review in section 4.3.1. The corresponding evanescent potential at $f = 5$ GHz is plotted in panel (f).

In all spectra we can see the low frequency approximation (eq. 4.14) in the form of a linear imaginary and a parabolic real part of the admittance. In the diffusive case, it is easy to recognize the constant $\pi/4$ phase of the admittance at high frequency as predicted by eq. 4.15.

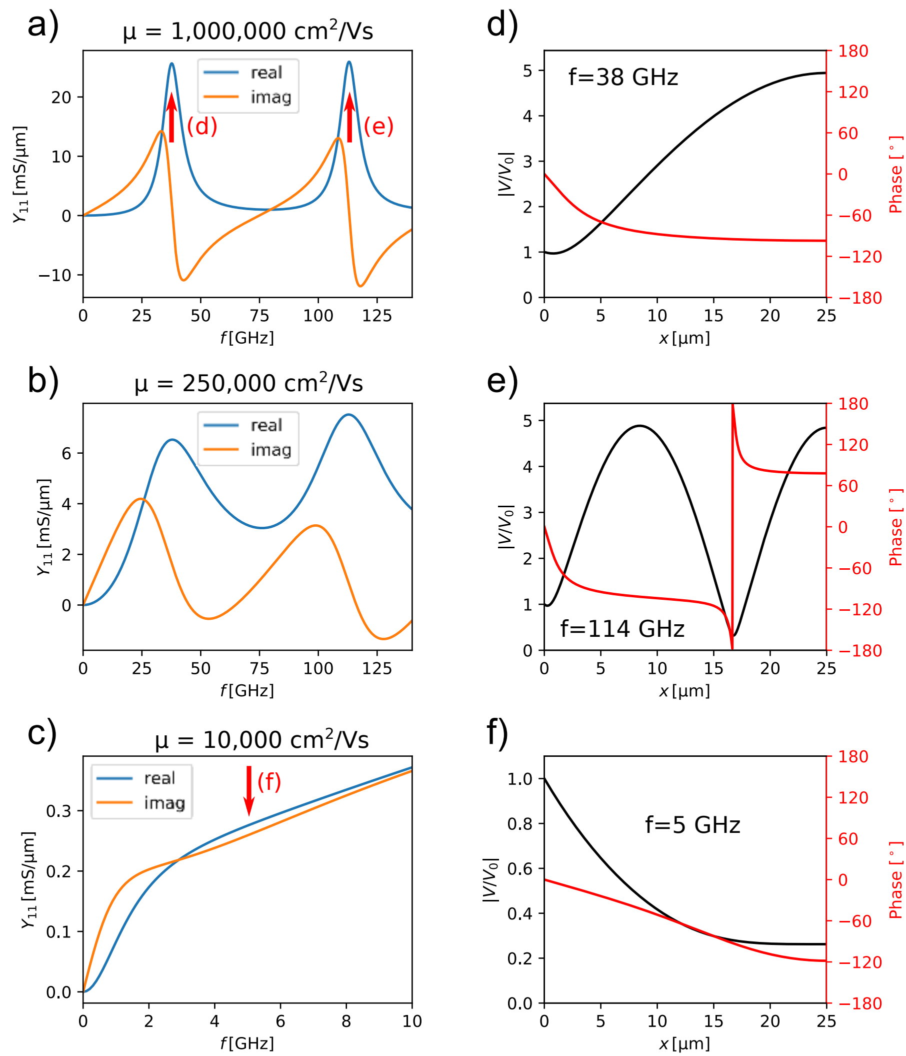

Figure 4.9 – Admittance spectra and electric potential in a PRC for various electronic mobilities.

4.5 Experimental results

Even though the sample fabrication of the PRCs discussed here is less demanding than that of CRs in terms of lithography resolution and alignment, the difficulty here lies in the required lateral sample dimensions. While it was not impossible to exfoliate sufficiently large ($> 20 \times 20\ \mu m^2$) hBN and graphene flakes, it was not easy to stack them in a way as to preserve a sufficiently large crack- and fold-free zone. Due to the risk of damaging or misaligning the active zone during the last transfer process, the idea of using bottom gates like in the previous chapter was quickly abandoned. Using top gates required an additional passivation step in the fabrication recipe, which led to adhesion problems of gate and contact pads. On top of these issues, electronic mobility had to be high enough and contact resistance low enough to observe a resonance. A comparison of all fabricated PRCs is given in section 4.5.4. The fabrication and characterization of these devices was done in close collaboration with David Mele. Some of them were made using CVD graphene grown by Luca Banszerus and Zachary Winter in Aachen.

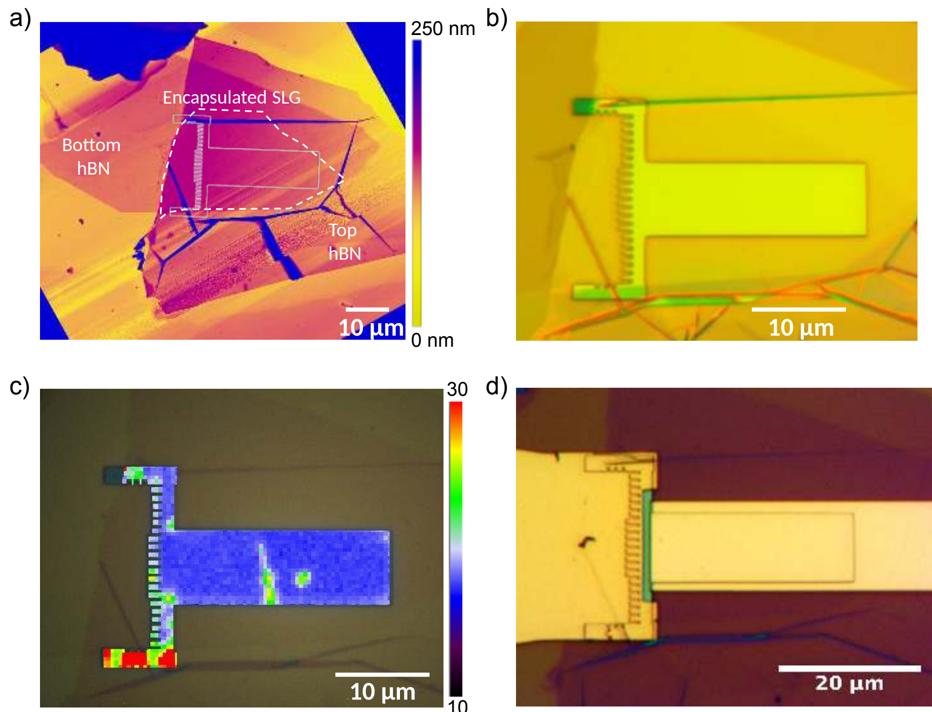

Figure 4.10 – **Fabrication of PRC-D7.** a) AFM image of the hBN-graphene-hBN stack. The dashed line shows the outline of the graphene flake. b) Microscope image of the stack after etching. c) Raman map of the 2D peak width. d) Final device with contact and gate.

The fabrication process is illustrated in fig. 4.10. A hBN-graphene-hBN heterostructure is assembled using the van der Waals pick-up technique and characterized by atomic force microscopy (panel a) and Raman spectroscopy (panel c). It is etched into the PRC shape (panel b) and a contact electrode is deposited on the comb-shaped access region. After depositing an Al_2O_3 passivation layer and subsequently etching away the oxide in the contact-pad regions, the gate electrode and the CPW are deposited (panel d). For more details on

the sample fabrication, see section 2.1.

In this section, we will focus on sample PRC-D6 and discuss the observation of a quarter-wave plasma resonance and the full characterization of all relevant parameters (introduced in the previous section) as a function of both charge carrier density and temperature. These results have been published in ref. [27].

The electronic transport measurements were carried out in a Janis cryogenic probe station. The high frequency measurements were carried out using a vector network analyzer and DC sources in combination with a bias tee. For more details on the GHz characterization, see section 2.2.

4.5.1 Evanescent waves in a diffusive capacitor

Before discussing the resonant behavior, let us first study the simpler case of evanescent waves. Figure 4.11a shows a typical admittance spectrum of a diffusive graphene capacitor (sample PRC-D6 at room temperature). For clarity, only fourth data point is plotted. The phase propagation in the CPW access and parasitic capacitances have already been subtracted using the de-embedding protocol explained in section 2.2.2. Here the silicon substrate is connected to the ground ($V_{\mathrm{chuck}} = 0$).

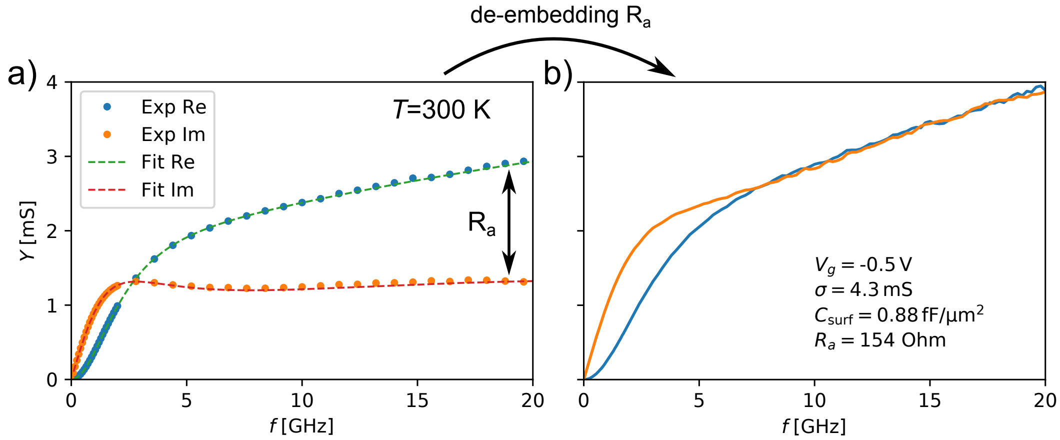

Figure 4.11 – Admittance spectra of a diffusive capacitor. a) Before and b) after de-embedding from the contact resistance. To distinguish the experimental data from the fit in panel a, only every fourth data point is plotted.

The spectra are fitted using equations 4.13, without the inductive term (which can be neglected when $r \gg j\omega\mathcal{L}_K$), but taking into account a finite access resistance, modeled as a discrete series contribution, c.f. equation 4.17. This access resistance contains both the contribution of the contact and the resistance of the graphene in the immediate vicinity of the contact, where it is not covered by the top gate. Figure 4.11b shows the same spectrum, but de-embedded from the access resistance, as explained in section 4.4.4. Here and in the following, the experimental spectrum is plotted as a solid line. As predicted by eq. 4.15 and illustrated in fig. 4.9c, real and imaginary part overlap at high frequency.

The fit results – i.e. resistance, capacitance (re-expressed as conductivity and capacitance per unit surface C_{surf}) and access resistance – are given in fig. 4.11b for $V_g = -0.5$ V, and are plotted for all applied gate voltages in fig. 4.12. We observe a conductivity minimum at

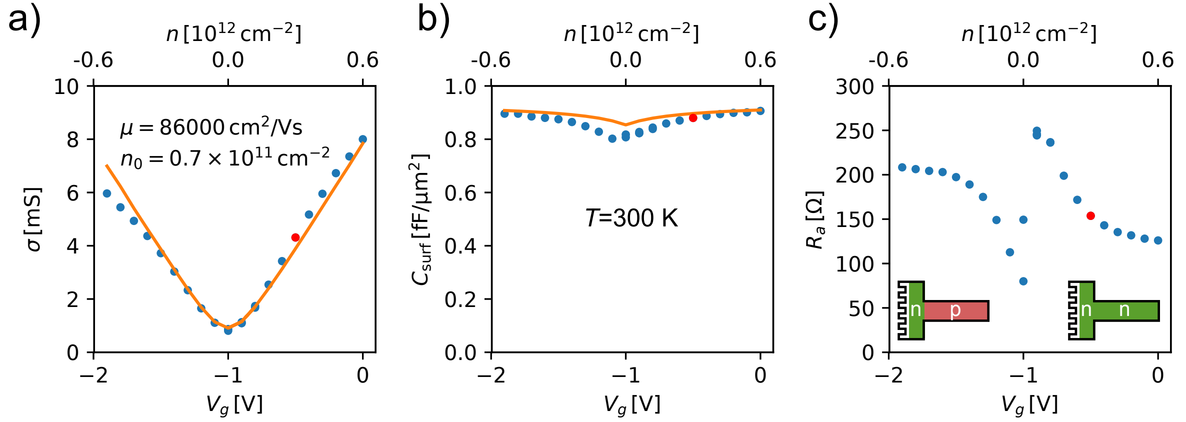

Figure 4.12 – Fit parameters (conductivity, capacitance and contact resistance) as a function of gate voltage / carrier density. The red dots highlight the fit results from fig. 4.11.

$V_g = -1$ V, which defines our charge neutrality point V_0^{top} and enables us to calculate the charge carrier density $n = C_{\mathrm{surf}}(V_g - V_0^{\mathrm{top}})/e$ (since we are actually measuring the capacitance here, we do not have to calculate it from the hBN thickness). The capacitance also has a minimum at the charge neutrality point, which is a manifestation of the reduced density of states.

In the diffusive transport model, we can obtain the mobility directly from the slope of $\sigma(n) = n_{\mathrm{eff}} e\mu$, where $n_{\mathrm{eff}} = \sqrt{n^2 + n_0^2}$ and n_0 is a residual charge carrier density. By fitting the conductivity data with this model, we obtain a room temperature mobility of $\mu = 86\,000$ cm^2/Vs and a residual charge carrier density of $n_0 = 0.7 \times 10^{11}$ cm^{-2}.

The access resistance has a particularly interesting behavior: Around the charge neutrality point of the channel, it exhibits a local minimum followed by a local maximum. The maximum at weak n-doping can be qualitatively understood in terms of a partial depletion of the contact-adjacent region when the channel is at neutrality. The minimum at weak p-doping however is difficult to justify and its analysis goes beyond the scope of this thesis. At large positive or negative channel doping, the access resistance saturates. Assuming that we have a reasonably homogeneous graphene sample, the chemical doping should be the same in the contact-adjacent region as in the capacitor channel. The former should therefore be intrinsically n-doped, which is why we observe a significantly lower access resistance when the channel is also n-doped (120 instead of 210 Ω). This is illustrated by the sketches in fig. 4.12c.

Interestingly this intrinsic n-doping is roughly the same in all of our samples, c.f. table 4.2. The contact resistance can be further reduced by applying a positive gate voltage (typically $V_{\mathrm{chuck}} \sim 10$ V) on the silicon substrate, which increases the charge carrier density in the contact-adjacent region, but also pushes V_0^{top} to a lower value. The leverage of the substrate gate (beneath 280 nm of silicon dioxide) is about 10 times weaker than that of the top gate, $C_{\mathrm{substrate}} \approx 3.9\ \epsilon_0/280$ nm $= 0.12$ fF/μm^2 compared to $C_{\mathrm{surf}} \sim 1$ fF/μm^2. This means that for a shift $\Delta V_{\mathrm{chuck}}$ of the voltage applied to the substrate, the top gate charge neutrality point will move by $\Delta V_0^{\mathrm{top}} \approx -\Delta V_{\mathrm{chuck}}/10$.

With this preliminary understanding of our sample, we can now explore the low temperature, high mobility regime.

4.5.2 Resonance in a quasi-ballistic capacitor

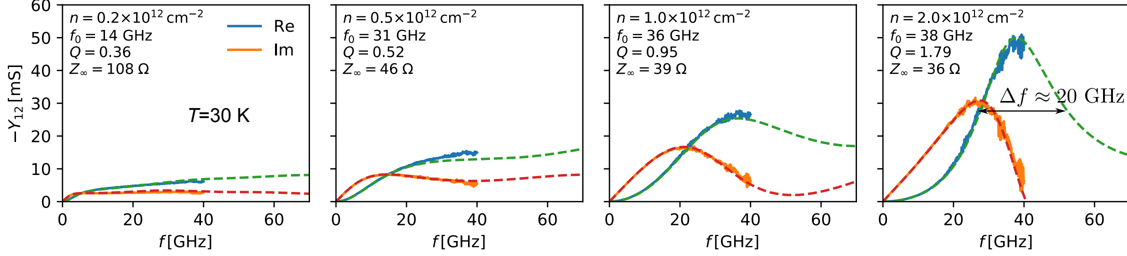

Figure 4.13 – Admittance spectra of a resonant capacitor. As the carrier density is dialed up, the quality factor of the resonance increases up to ~ 2.

Figure 4.13 shows exemplary admittance spectra from the same sample PRC-D6, this time at much lower temperature $T = 30$ K. The spectra are recorded at increasing charge carrier density going from left to right. Here the substrate was gated at $V_{\text{chuck}} = 10$ V, pushing the top gate charge neutrality point to $V_0^{\text{top}} = -2.2$ V. The additional doping in the access region reduced the access resistance to $R_a = 43$ Ω. The spectra shown in the figure have been de-embedded from this access resistance.

For clarity, the fitting model is plotted for a larger frequency range (0−70 GHz), so that the resonant behavior becomes more apparent. Here, the fitting to equation 4.13 or 4.22 was carried out by first adjusting the channel capacitance value to fit the low frequency imaginary part of the admittance and then the values of f_0 and Q to fit the resonance. Note that Z_∞ is implicitly adjusted by this procedure, since it can be expressed in terms of the capacitance C and the resonance frequency f_0: $Z_\infty = (4Lf_0C)^{-1}$. The fitted resonator parameters f_0, Q and Z_∞ are indicated on the plots in fig. 4.13.

At the lowest doping $n = 0.2\times10^{12}$ cm^{-2}, the admittance is reminiscent of the evanescent-wave spectrum presented in fig. 4.11 of the previous section. Here the real and the imaginary part do not overlap at high frequency (as predicted by the high frequency limit in eq. 4.15) because the kinetic inductance is no longer negligible. At this particularly low doping, an increased access resistance might also play a role; this is further discussed in section 4.5.3. As the doping is increased to $n = 1\times10^{12}$ cm^{-2}, the imaginary part of the admittance starts to approach zero, indicating the rise of the resonance, and at $n = 2\times10^{12}$ cm^{-2}, we observe a fully developed resonance at $f_0 \sim 40$ GHz with a quality factor of $Q \sim 2$. These values corresponds reasonably to the predictions in table 4.1.

In plasmonics, a typical figure of merit is the confinement ratio $\lambda_0/\lambda_{pl} = c/v_{pl}$, where λ_0 denotes the free-space wavelength and c is the speed of light in vacuum. In metals this ratio is typically ~ 1, in graphene it can be more than an order of magnitude larger, e.g. $\lambda_0/\lambda_{pl} = 66$ in the infrared range in ref. [237] or $\lambda_0/\lambda_{pl} \approx 75$ in this work. The plasmon lifetime $\tau = 2Q/\omega$ is on the order of tens of femtoseconds in metals, whereas it reaches 1.6 ps in graphene at $T = 60$ K in ref. [237] and similar values at $T = 30$ K in this work.

A more detailed analysis of the fit parameters is shown in figure 4.14. RF spectra were recorded for charge carrier densities in the range $-0.5 < n/(10^{12}\ \text{cm}^{-2}) < 2.5$ and for temperatures between 10 and 300 K and fitted with the resonator model. The fit parameters f_0, Q and $C_{\text{surf}} = C/W$ at $T = 30$ K are plotted in panel (a), its inset and panel (c),

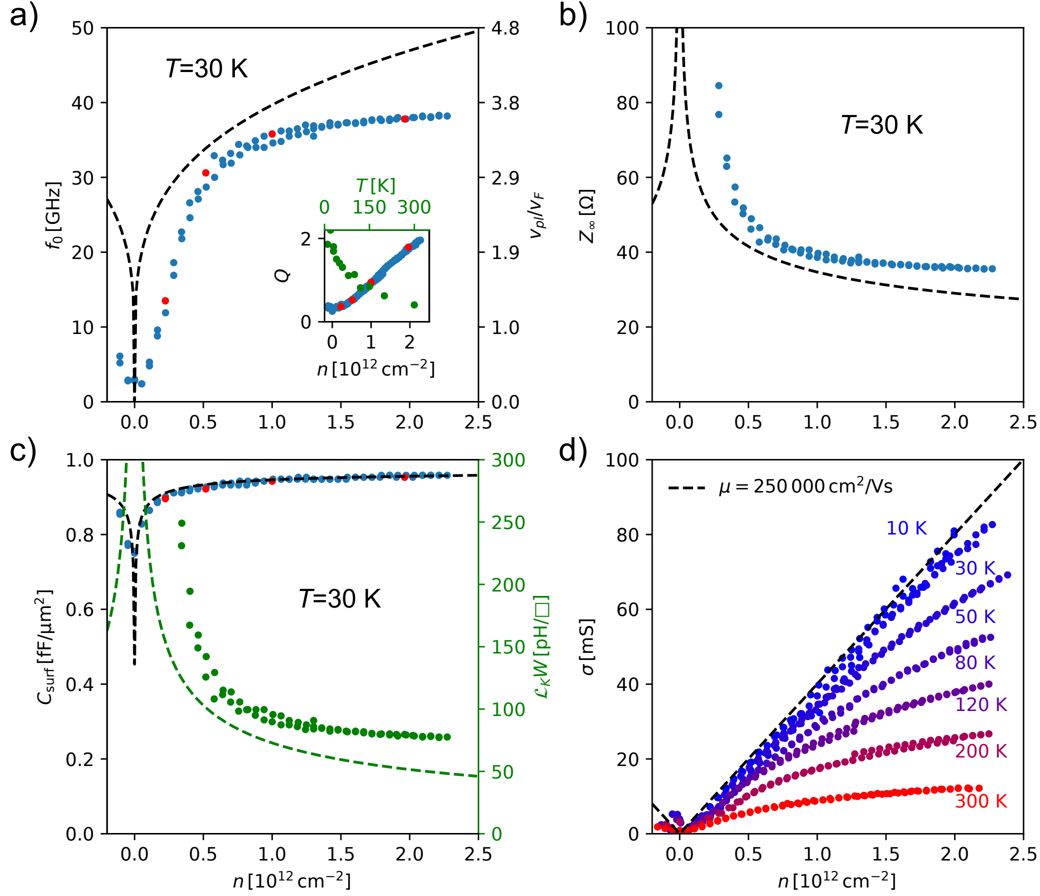

Figure 4.14 – Fit parameters (resonance frequency, quality factor and capacitance) and derived parameters (plasmon velocity, characteristic impedance, kinetic inductance per square □ and conductivity) as a function of carrier density for PRC-D6 at $T = 30$ K unless otherwise indicated. Black and green dashed lines represent the theoretical expectations for capacitance, inductance, impedance, resonance and conductivity (at low T).

respectively. A second y-axis was added to panel (a), in order to compare the plasmon phase velocity $v_{pl} = 4Lf_0$ to the Fermi velocity $v_F \approx 10^6$ m/s.

From these parameters – using equations 4.18 to 4.21 – it is straightforward to calculate the characteristic impedance Z_∞ (formula above, plotted in panel b of fig. 4.14) and the inductance per unit length $\mathcal{L}_K = (16f_0^2L^2C)^{-1}$ (panel c). Similarly, one can calculate the resistance per unit length $r = 2Z_\infty/QL$ and finally the conductivity $\sigma = (rW)^{-1}$ (panel d).

The theoretical expectation for the capacitance is in excellent agreement with the measurements, as shown by the black dashed line in fig. 4.14. Here the only adjustable parameter is the geometric capacitance which was found to be $C_{\text{geo}} = 0.98$ fF/μm^2. Theoretically, for a top hBN thickness of 17 nm we expect 1.7 fF/μm^2. This value is reduced by the series contribution of the ~ 10 nm aluminum oxide dielectric layer.

The theoretical expectation for the resonance frequency and characteristic impedance is plotted as black dashed lines in panels a and b of fig. 4.14. Here we used the expression for

the kinetic inductance from equation 4.3, for the geometric capacitance from equation 4.6 and for the quantum capacitance from equation 1.14. There is a good qualitative agreement of our data with the theory, but we still observe a deviation that exceeds the uncertainty of our fitting procedure. The offset between experiment and theory is also reflected in the plot of the kinetic inductance and reaches up to 30 pH. In the next section, we will discuss this offset in terms of an additional series inductance.

The conductivity as a function of carrier density, plotted for various temperatures in fig. 4.14, exhibits two limiting behaviors: At low temperatures, it is proportional to the carrier density ($\sigma \propto n$), which is characteristic for charged impurity scattering, c.f. section 1.2.3, with a constant mobility of $\mu = 250\,000$ cm^2/Vs. At high temperature, the conductivity saturates at large n ($\sigma \propto$ const.), which is reminiscent of acoustic phonon scattering, c.f. section 1.2.3.

The acoustic phonon mean free path is inversely proportional to k_F and T in the equipartition regime [39]. Figure 4.15a shows the mean free path calculated from the conductivity using $\ell_{\mathrm{mfp}} = \sigma h/(2e^2\sqrt{\pi|n|})$. A quick analysis shows that the room temperature mean free path at a typical doping of 10^{12} cm^{-2} is approximately 0.65 μm. Taking into account the impurity scattering length $\ell_{\mathrm{mfp}}^{\mathrm{imp}} = \hbar\sqrt{\pi 10^{12}\ \mathrm{cm}^{-2}} \times 250\,000\ \mathrm{cm}^2/\mathrm{Vs}/e \approx 3$ μm at this doping, one finds, according to Matthiessen's rule, an acoustic phonon mean free path of $\ell_{\mathrm{AP}}^{300\ \mathrm{K}} = 1/(\ell_{\mathrm{mfp}}^{-1} - \ell_{\mathrm{imp}}^{-1}) \approx 0.8$ μm. This has been used in chapter 3.

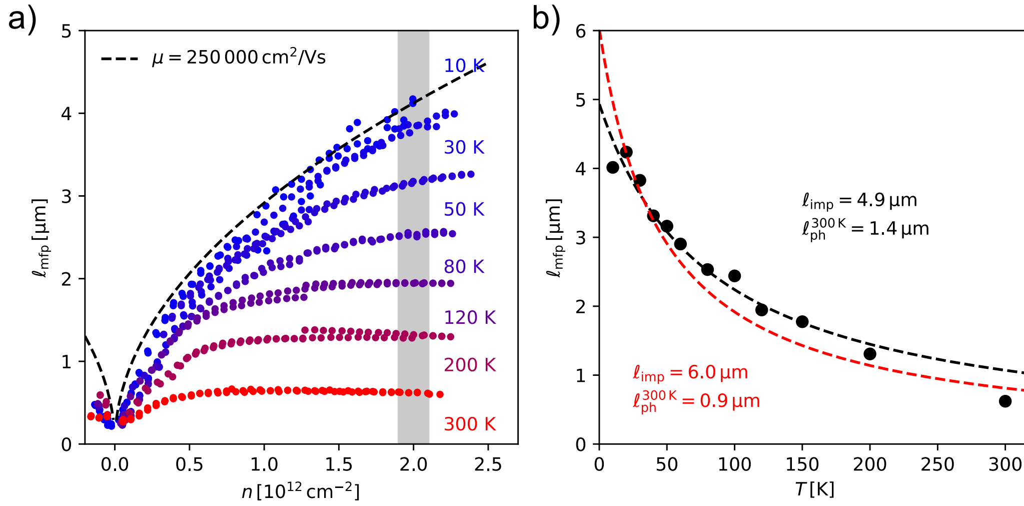

Figure 4.15 – **Temperature dependence of the mean free path.** a) Mean free path as a function of carrier density for various temperatures. b) Fitting of the mean free path at $n = 2 \times 10^{12}$ cm^{-2}. Black dashed line is an unweighted fit, red dashed line is a weighted fit.

A more detailed analysis is shown in panel b of figure 4.15, where the mean free path at $n = 2 \times 10^{12}$ cm^{-2} is plotted vs. temperature and fitted with a normal [weighted] least-squares fit to the formula $\ell = 1/(\ell_{\mathrm{imp}}^{-1} + \ell_{AP}^{-1} T/300\ \mathrm{K})$, visualized by the black [red] line. For the red line fit, the data points are weighted by their spacing so that the high temperature data is better taken into account.

The fits confirm the $1/T$ behavior of the acoustic phonon mean free path and suggest a charged impurity scattering length between 5 and 6 μm, comparable to the device width (8

μm). We can compare the room temperature phonon mean free path $\ell_{\rm ph}$ to literature values for the equipartition regime using the formula from ref. [39]:

$$\ell_{\rm ph} = \frac{4(\hbar v_F)^2}{\sqrt{\pi n}} \frac{\rho_m v_{\rm ph}^2}{D^2} \frac{1}{k_B T} = \ell_{\rm ph}^{300\ \rm K}(n) \times \frac{300\ \rm K}{T} \tag{4.23}$$

where $\rho_m = 7.6 \times 10^{-7}$ kg/m^2 is the mass density, $v_{\rm ph}$ is the sound velocity and D denotes the deformation potential in graphene. Inserting the values $v_{\rm ph} = 2 \times 10^4$ m/s and $D = 19$ eV from ref. [39], one obtains $\ell_{\rm ph}^{300\ \rm K} = 0.79$ μm at $n = 2 \times 10^{12}$ cm^{-2}. Using instead the values from the experimental study by Efetov & Kim [47], $v_{\rm ph} = 2.6 \times 10^4$ m/s and $D = 25$ eV, one finds $\ell_{\rm ph}^{300\ \rm K} = 0.77$ μm. Both values are in good agreement with the result of the weighted fit in figure 4.15.

4.5.3 70 GHz spectrum with K-connectors

Even though our Janis cryogenic probe station is equipped with K-type coaxial lines which are only specified up to 40 GHz, the delivery of a new Rohde & Schwarz ZVA67 vector network analyzer (0–70 GHz) made it tempting to push the experimental setup to the highest possible frequency in order to see the other side of the PRC resonance. Unfortunately, the new Cascade cryogenic 70 GHz probe station did not arrive in time for these measurements to be done with a more suitable system.

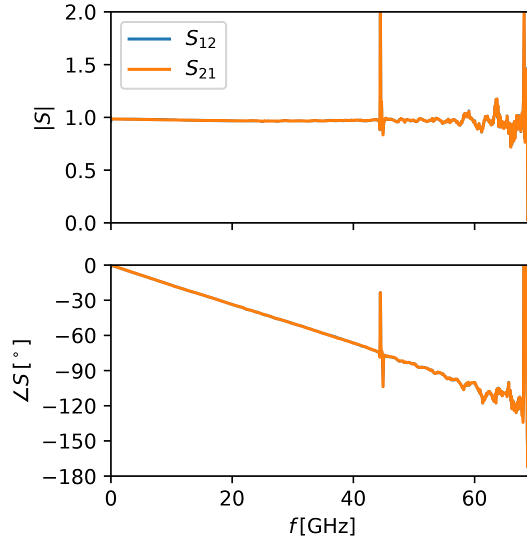

Figure 4.16 – Thru line measured with a 70 GHz VNA on a 40 GHz probe station.

In order to get a first idea of the transmission properties of the coaxial lines inside and outside of the cryostat, a thruline (see section 2.2.2) was characterized, see figure 4.16. The magnitude and the phase behaved as expected up to about 45 GHz, where a strong resonance was observed, and then continued their typical trend with increasing noise up to about 65 GHz. Beyond this frequency, both magnitude and phase were extremely noisy.

After this encouraging first test, the device discussed in the previous section (PRC-D6) was characterized once more at 30 K, with the chuck voltage set to 10 V to obtain a

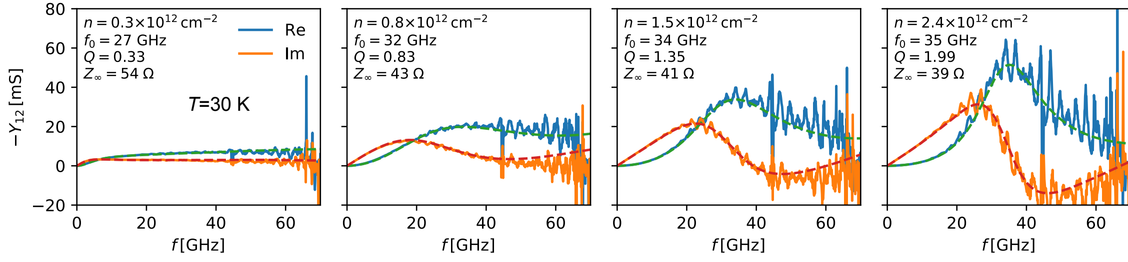

Figure 4.17 – Admittance spectra of a resonant capacitor. The 70 GHz spectral range enables us to see the right hand side of the resonance from fig. 4.13.

low contact resistance. Figure 4.17 shows a set of example spectra from this measurement campaign, de-embedded from the access resistance. Even though the data is a bit more noisy than what was presented in fig. 4.13 – due to a less optimal calibration – the overall behavior of the device is reproducible:

- we observe diffusive behavior ($Q \ll 1$) at low doping
- at $\sim 2 \times 10^{12}$ cm^{-2} doping, we observe a resonance at ~ 40 GHz with $Q \sim 2$
- the access resistance is again 43 Ω

However, thanks to the larger frequency window, we can now also clearly see the decrease of the real part of the admittance at $f > f_{\mathrm{res}}$ and the imaginary part of the admittance crosses over to negative values at the resonance.

Figure 4.18 shows the resonator parameters extracted from the fits to the 70 GHz spectra. In order to push the data analysis a bit further, two things have been modified with respect to the previous characterization in fig. 4.14:

The first modification is the introduction of a constant additional series inductance of 40 pH/□ (the total inductance, like the resistance depends on the number of squares □ in series) in the red dashed lines in panels a and c. Such a series addition excellently reproduces the experimental data, concerning both the inductance and the resonance frequency. This could be due to a Faraday inductance as mentioned in section 4.2, which was estimated to be ~ 10 pH/□ at the resonance and is therefore of the corresponding order of magnitude. However, it cannot be excluded that the additional inductance is due to coupling to the electrons in the charged silicon substrate, as stated in ref. [27]. A more detailed analysis of this could be done by studying the inductance offset as a function of chuck voltage, but that goes beyond the scope of this thesis.

The second modification is the fitting strategy close to the charge neutrality point: On the right side of the vertical dotted lines in fig. 4.18, the spectra were fitted in the habitual manner, with a fixed access resistance of $R_a = 43\ \Omega$. As already pointed out in 4.5.1, the access resistance indeed saturates at high doping, but close to the CNP it usually increases. However, in this regime, the contact resistance, the resonance frequency and the quality factor are not independent fit parameters, which means that we have to fix one of them. Since the additional series inductance reasonably reproduces our data in the high doping regime, we now use the theoretical curve to fix the resonance frequency in the low doping

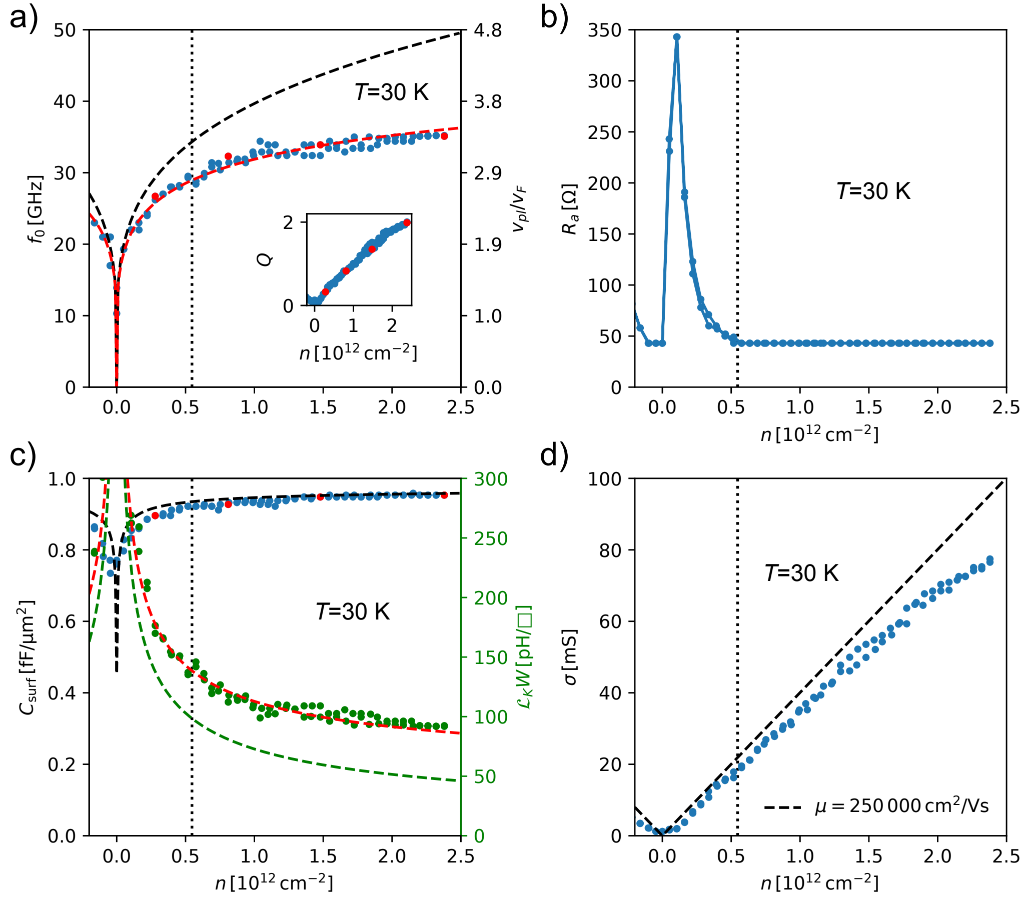

Figure 4.18 – Fit parameters and derived parameters like in fig. 4.14. Red dashed lines correspond to the theoretical expectation (black and green dashed lines), corrected by an additional series inductance. Black dotted line indicates transition from fitting with fixed (right) and adjustable (left) access resistance.

regime (on the left of the vertical dotted lines) and leave the contact resistance as adjustable parameter. This way, we obtain a $R_a(n)$ reminiscent of the one in fig. 4.12, peaking at a similar value $\sim 300\ \Omega$.

4.5.4 Comparison of all PRC samples

In total, 12 PRCs were fabricated throughout this thesis. They are listed in table 4.2 and microscope images of all samples are shown in figure 4.19. Five of them were made using CVD graphene from RWTH Aachen and seven were made using exfoliated graphene. The encapsulation was mostly done at École Normale Supérieure and almost all of the devices are top-gated. Out of the 12 samples, six survived the full fabrication process and three had a sufficiently high mobility (almost phonon-limited at room temperature) to potentially sustain a plasma resonance at cryogenic T. One of these samples (PRC-D3) started to leak and the other one (PRC-D7) did not reach high enough mobility after cooldown. Only PRC-D6 exhibited the required electronic quality to observe the plasma resonance.

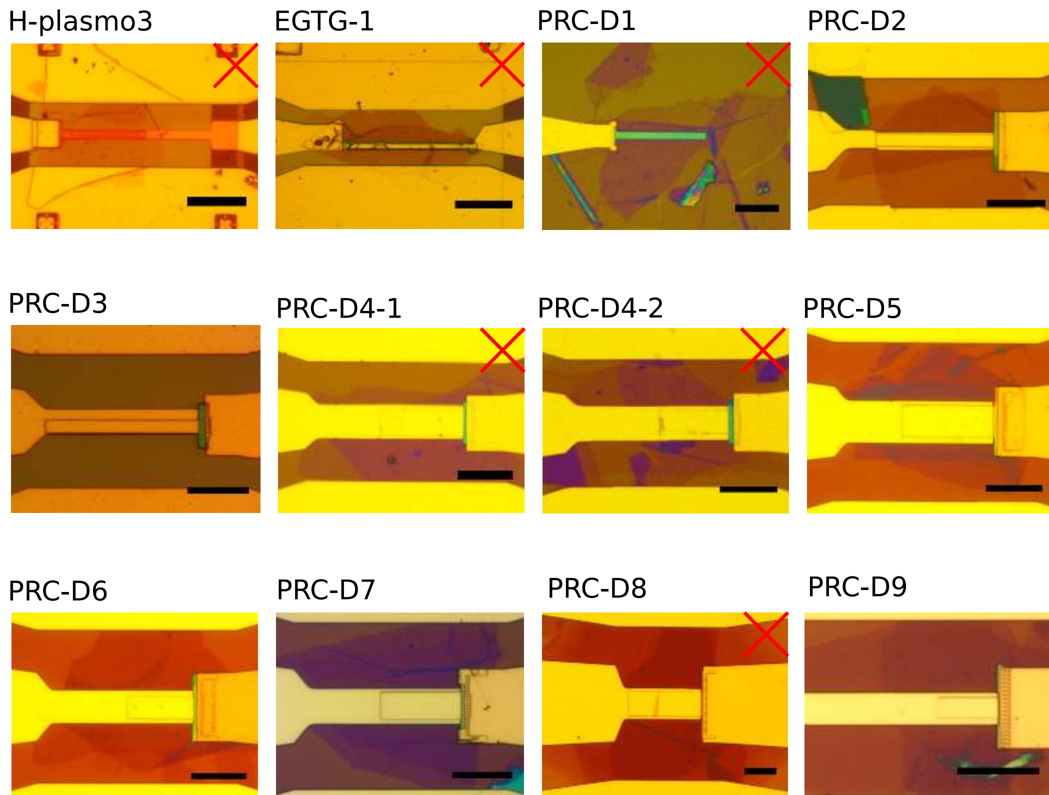

Figure 4.19 – Microscope images of all PRC samples. Red crosses indicate defective samples. The scale bars correspond to 20 μm.

This might seem surprising in comparison with the success rate of the sample fabrication in the previous chapter, where five out of eight devices at least showed a hint of the desired ballistic effect, in particular when one takes into account the relatively simple device design of the PRCs compared to the CRs. In fact, the advantage of the CRs is the small size $\sim 1 \times 1\ \mu\text{m}^2$ of their active zone. It is relatively easy to identify a suitable homogeneous zone in a hBN-G-hBN heterostructure and to align it on top of the device structure. As for the PRCs, even if we fabricate top-gate devices (which removes the necessity of aligning the heterostructures with bottom gates during the deposit), it is difficult to obtain sufficiently large $> 20\ \mu$m zones that are homogeneous. Here it is advisable to improve the sample fabrication, for example by de-bubbling the heterostructures as detailed in ref. [123], in order to obtain larger homogeneous zones, before the fabrication of more complex devices is envisaged, for example incorporating bottom gate arrays.

sample	type *	L [μm]	W [μm]	C_{geo} [fF/μm^2]	V_0^{top} [V]	μ_{RT} [cm^2/Vs]	μ_{10K} [cm^2/Vs]	comment
H-plasmo3	bSC	28	2.5	-	-	-	-	hole in graphene
EGTG-1	tSC	44	2.7	-	-	-	-	bad adhesion of gate
PRC-D1	tSC	40	3	-	-	-	-	died during ALD
PRC-D2	tSC	40	4	1.2	-1.0	-	$<$10 000	first working (but diffusive) PRC
PRC-D3	tSe	48	4	1.1	-1.0	$\sim$80 000	-	sample started leaking
PRC-D4-1	tSe	30	10	-	-	-	-	problem with gate deposit
PRC-D4-2	tSe	25	8	-	-	-	-	problem with gate deposit
PRC-D5	tSe	33	11	0.7	-0.6	20 000		
PRC-D6	tSe	24	8	0.9	-1.0	80 000	250 000	best PRC so far
PRC-D7	tSe	27	9	0.6	-0.9	70 000	$\lesssim$150 000	
PRC-D8	tSC	48	16	-	-	-	-	crack appeared in the stack during fabrication
PRC-D9	tBe	15	5	1.3	-1.1	30 000	60 000	

Table 4.2 – List of fabricated PRCs. (*) The first letter of the “type” corresponds to top (t) or bottom (b) gate, the second letter to single- (S) or bilayer (B) graphene and the third letter denotes CVD (C) or exfoliated (e) graphene.

4.6 Conclusion and perspectives

In this chapter, we have investigated a plasma resonance in a graphene capacitor by GHz spectroscopy. We have discussed the $0-40$ GHz experimental results, first at room temperature (diffusive capacitor), then at cryogenic temperature (resonant capacitor with tunable quality factor) and finally for all intermediate temperatures in order to study mobility limits and the evolution of the acoustic phonon mean free path. The resonance parameters (frequency, characteristic impedance, etc.) were in reasonable agreement with the theoretical prediction. The remaining offset could possibly be justified with coupling to the electron system in the silicon substrate. Finally, we have shown preliminary experimental data for the $0-70$ GHz frequency window, where we now observe the full resonance. Furthermore we have provided better fits to the theory by taking into account a phenomenological additional inductance and by adapting the fit strategy close to the charge neutrality point.

In conclusion, our study constitutes – to our knowledge – the first observation of a GHz plasma resonance in a graphene device (not taking into account edge magnetoplasmon resonances [253]). By scaling down the device size to ~ 1 μm, this resonance can be moved to THz frequencies and room temperature operation can be envisaged. This paves the way to the design of novel, resonant THz detectors [106].

Possible future experiments therefore include the embedding of these devices in bowtie antennas for THz characterization. Even with co-planar waveguides similar to those currently used, a characterization up to 500 GHz (at room temperature) is feasible, e.g. at the THz and mm-wave Laboratory at Chalmers University, Gothenburg, where we have carried out first experiments in collaboration with Xinxin Yang. However, since our waveguides were not compatible with the pitch of the 350−500 GHz probe station and calibration was thus quite difficult, no exploitable data has been obtained so far. In principle, since the absolute FWHM Δf of the resonances is supposed to be independent of the harmonic order, one expects the quality factor of the mth harmonic to be $(2m+1)$ times as high as that of the zeroth harmonic, so that our room-temperature $Q \sim 0.2$ at $f_0 \sim 40$ GHz scales to $Q \sim 2.2$ at $f_5 \sim 440$ GHz.

As far as further GHz experiments are concerned, the fabrication of *in situ* tunable plasmonic crystals [224, 248, 249, 255] should be considered. The combination of top gated capacitors (or transistors) with nano-patterned bottom gates such as used in chapter 3 could be exploited to introduce a sharp p-n junction in the capacitor channel [83, 256]. This device could then be used to study the dynamic properties of graphene p-n junctions, i.e. to see to what extent they exhibit capacitive or inductive behavior, in analogy with a Josephson junction. In the transmission line model, one would have to introduce corresponding discrete (lumped) elements. The next step would be to fabricate periodic p-n junctions in the graphene channel. This is sketched in figure 4.20a.

The channel is split into N unit cells of length a, each comprising two differently doped regions. The resulting dispersion (for an infinite plasmonic crystal) can be calculated using the cascade matrix approach in combination with Bloch's theorem (see ref. [224]) and is sketched in fig. 4.20b. The orange line represents the linear dispersion of the unmodulated channel. The green line represents the resonance frequency of a unit cell. The coupling of these cells in a plasmonic crystals leads to the opening of a gap (here quite dramatically because I chose a large impedance mismatch between the sub-cells). In a transistor, one would probe $\lambda/2$ resonances, indicated by the red vertical line, and observe a decrease of the

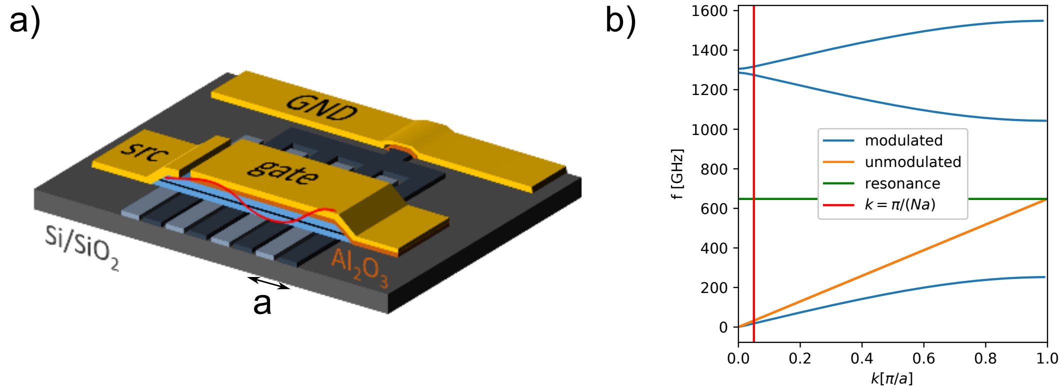

Figure 4.20 – **Gate-tunable plasmonic crystals.** a) Sketch of the proposed device design. b) Calculated dispersion in the first Brillouin zone of a plasmonic crystal (here actually calculated for a width modulation, not a doping modulation).

resonance frequency as the modulation is switched on. In terms of applications, this type of device could be used for resonant THz detection with a highly tunable resonance frequency. For fundamental physics, it would be particularly interesting to study the effect of inducing a bipolar superlattice. To our knowledge, there is no theory for the propagation of plasmons in p-n junction lattices.

Having studied a monolayer graphene device in detail, it would also be interesting to fabricate better bilayer graphene samples (PRC-D9's mobility was not high enough to observe a resonance), since the resonance frequency is more tunable in BLG ($\propto n^{1/2}$) than in SLG ($\propto n^{1/4}$). Finally, exposing the sample to a strong enough magnetic field should activate the quantum Hall effect and one could probe the capacitive and inductive response of the 1D edge channels, and potentially observe edge magnetoplasmon resonances [253].

As recent theoretical proposals suggest, plasmons in graphene and other Dirac matter might still bear a lot of surprises, like for example quantum oscillations in Dirac magneto-plasmons [257] or "tachyon ghost modes" [258] which lead to sharp plasma resonances even though the loss rate is high. Thanks to the high electronic quality and the easy tunability of graphene, it has become the ideal platform to study many-body effects in two dimensions.

5

Quantum Hall breakdown

Having introduced the notions of the integer quantum Hall effect in chapter 1, the present chapter will focus on its breakdown (QHBD) in a bilayer graphene (BLG) sample. I will first revisit the high-bias properties of the sample at zero magnetic field, highlighting the powerful cooling effect of the hyperbolic phonon polaritons (HPPs) of the hBN substrate. Then, I will provide a short overview of the physical quantities relevant for the intrinsic QHBD, followed by a brief literature review, summarizing a couple of experiments and the existing theories for the intrinsic limit of the QHE in semiconductor 2DEGs and graphene, in particular quasi-elastic inter Landau level tunneling and bootstrap electron heating. The former requires impurity scattering, while the latter relies on phonon relaxtion. We will then discuss our own experimental results: The QHBD at very high fields ($\sim 10^6$ V/m), current

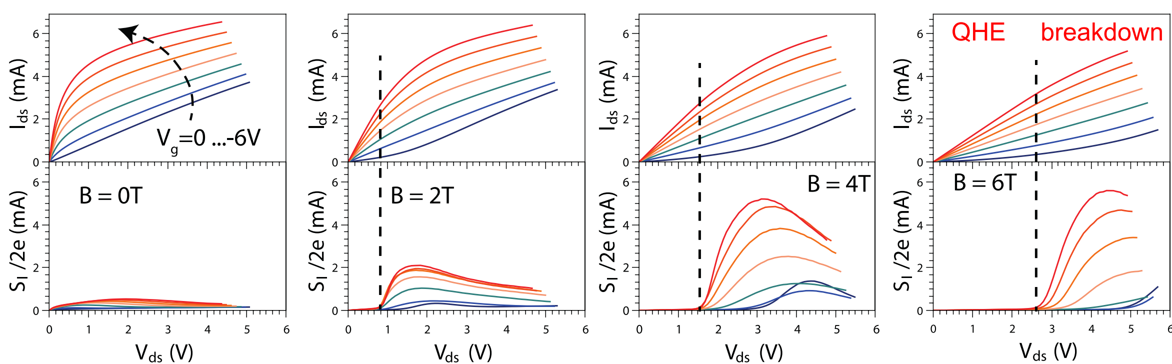

Figure 5.1 – DC current and GHz noise current as a function of source-drain bias for various magnetic fields and carrier densities $|n| = 0...4.3\times10^{12}$ cm^{-2} in a bottom gated BLG sample of dimensions $L\times W = 4\times3$ μm. Below breakdown (black dashed lines) transport is ballistic, I-V behavior is defined by the Hall conductance and noise is suppressed. Breakdown is characterized by a deviation from the Hall conductance and more prominently by an abrupt and strong increase of the noise.

densities ($\sim 10^3$ A/m) and drift velocities ($\sim 10^5$ m/s), characterized both by DC transport and by noise measurements in a 1 GHz-bandwidth window around 5 GHz (see figure 5.1). We provide a new explanation for intrinsic QHBD due to a collective magnetoexciton instability. At the end of the chapter, a short conclusion is followed by a discussion of possible future experiments.

5.1 HPP cooling revealed by GHz noise thermometry

The sample used in this chapter is a two-terminal BLG transistor, see fig. 5.2a (inset). Its high bias properties in the absence of a magnetic field were already studied extensively in a previous work [144]. We will summarize these findings here and use them as an introduction to GHz noise measurements. At the same time, this summary will later illustrate how the zero-B-field cooling mechanism loses its relevance under quantizing magnetic fields where electronic waves are localized into discrete Landau states. The setup used for these measurements is explained in section 2.2.3.

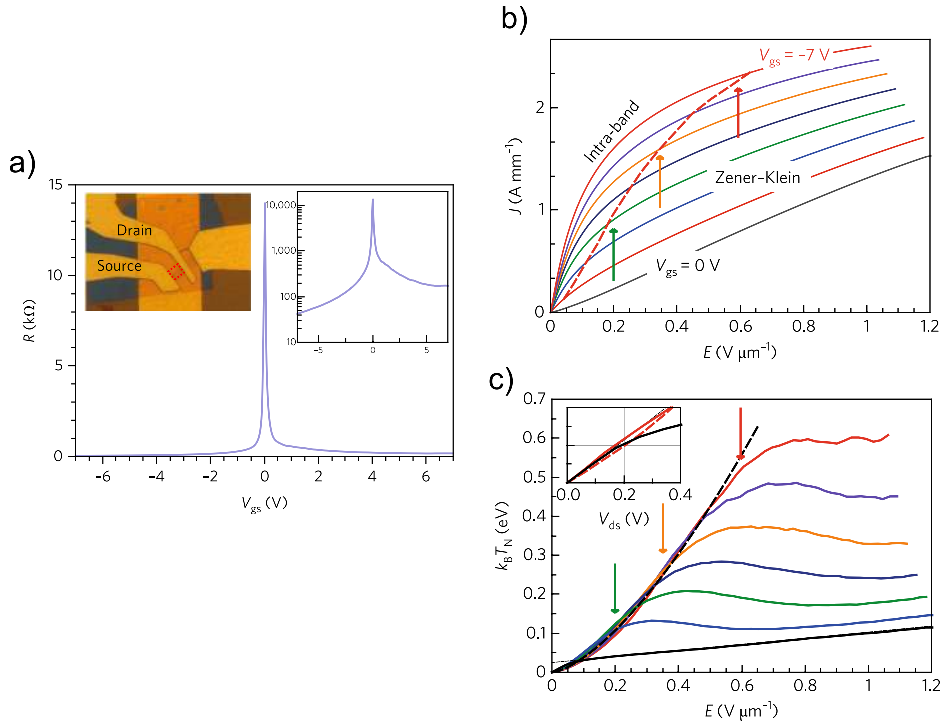

Figure 5.2 – **Zener-Klein transistor cooled by hyperbolic phonon polaritons.** a) Low-bias resistance of the two-terminal device as a function of gate voltage. Left inset: microscope image of the device. The graphene channel is highlighted by the red rectangle. Right inset: $R(V_{gs})$ on a semi-logarithmic scale. b) Current density vs. bias for gate voltages $V_{gs} = 0 \ldots -7$ V (carrier densities $n = 0 \ldots -5 \times 10^{12}$ cm^{-2}). Red dashed line indicates the onset of Zener-Klein tunneling. c) Noise temperature vs. bias for the same gate voltages. Black dashed line corresponds to a model of Wiedemann-Franz cooling. Colored arrows correspond to threshold field from panel b. Figure adapted from [144].

The graphene channel dimensions are $L \times W = 4 \times 3$ μm. The channel is separated from the local bottom gate (gold) by a 23 nm thick exfoliated hBN flake, giving rise to a gate capacitance of $C_{gs} = 1.15$ fF/μm^2. The BLG is as-exfoliated, i.e. it did not have to undergo any etching steps, which minimizes edge disorder.

Its low bias ($V_{ds} = 10$ mV) resistance at LHe temperature (4 K) is plotted in fig. 5.2a. One can extract a mobility of around $\mu = 30\,000$ cm^2/Vs. The second inset of this panel shows the resistance on a semi-logarithmic scale. In the hole-doping regime, the two-terminal resistance reaches values as low as 40 Ω at $V_g = -7$ V. The Sharvin resistance [259] at the corresponding density $|n| = 5 \times 10^{12}$ cm^{-2} is $R_S = \left[4e^2 k_F W/\pi h\right]^{-1} \approx 20$ Ω indicating the high transparency of the contacts. In order to benefit from this, all measurements described in the following were carried out in the hole-doping regime. Furthermore, since the sample was submitted to very high source-drain voltages (comparable to the gate voltage), the drain-gating ($V_s = 0$ here) had to be compensated by shifts in the gate voltage. In order to do this, the charge neutrality point (maximum in the source-drain resistance) was tracked as a function of V_{ds} and V_{gs} to obtain $V_{gs}^{\mathrm{CNP}} = \alpha V_{ds}$, where $\alpha \approx 0.4$. After this "calibration", measurements are taken at the effective gate voltage $V_{gs}^{\mathrm{eff}} = V_{gs} - \alpha V_{ds}$.

Figure 5.2b shows the source-drain current density as a function of applied field for different hole densities ($V_{gs} = 0... - 7$ V). This corresponds to the first top row panel of fig. 5.1, where we plotted current against bias. At low bias, there is a steep current increase limited by intraband velocity saturation, followed by a regime where the differential conductance $\sigma_{ds} = \partial I_{ds}/\partial V_{ds}$ saturates towards a bias- and doping-independent value σ_{zk}. This regime of constant σ_{ds} is reached at lower bias for lower channel doping. The red dashed line indicates the onset field of Zener-Klein tunneling (ZKT) $E_{zk} = 2E_F/e\ell_{zk}$, where E_F denotes the Fermi energy and ℓ_{zk} is a density-dependent tunneling length that can be extracted from the low doping Zener-Klein conductance $\sigma_{zk} \propto k_F \ell_{zk}$.

Figure 5.2c shows the noise temperature as a function of the electric field, for the same hole densities that were shown in panel b. This corresponds to the first bottom row panel of fig. 5.1, but the current noise $S_I/2e$ was re-expressed as a noise temperature $k_B T_N = S_I/4G$, where G is the sample's conductance. The noise temperature follows a steep, weakly super-linear increase at low bias, in accordance with a Wiedemann-Franz cooling mechanism (black dashed line). At the onset of ZKT, illustrated by colored arrows that refer to the corresponding fields in panel b, the noise temperature starts to saturate, indicating the activation of a new cooling pathway. At zero doping, this mechanism is activated at $V_{ds} = 0.2$ V (see inset of panel c), corresponding to the energy of the type-II hyperbolic phonon polaritons $\hbar\Omega_{II} \approx 0.2$ eV.

The fact that this cooling pathway opens only in the ZKT regime can be understood in terms of population inversion: the high bias generates electron-hole pairs which relax through HPP emission, otherwise inhibited due to Pauli blocking. Since the excess Joule power is equilibrated by the HPP cooling power in this sample, the overall noise temperature becomes bias-independent, leading to the plateaus in figure 5.2c. HPP cooling is highly efficient, evacuating heat at rates on the order of ~ 1 GW/m^2.

These experiments have demonstrated how a clean graphene-on-boron-nitride sample, pushed to its intrinsic limits, can be used to study fundamental physics (coupling to HPPs) and at the same time establish new perspectives for industrial applications: efficient cooling pathways for semiconductors. In this chapter, we will study the high-bias current and noise in the same BLG sample, under quantizing magnetic fields, in order to revisit an "old"

fundamental physics question (the breakdown of the QHE) which naturally has a direct application in quantum Hall resistance standards.

5.2 Dimensional analysis of the breakdown

In the following, I will introduce the quantities of interest for an intrinsic breakdown of the quantum Hall effect. In the literature review below, we will see that this corresponds roughly to the 1986 findings of Eaves & Sheard [260].

When exposed to a strong enough magnetic field, the density of states of the two-dimensional electron gas develops periodic peaks, corresponding to the Landau levels (LLs). Their width depends on the homogeneity of the sample. The longitudinal resistivity ρ_{xx} drops to zero and the transverse conductivity σ_{xy} has discrete plateaus at $\nu e^2/h$, where ν is called the filling factor. In semiconductor 2DEGs and BLG, $\nu = g(N+1)$, where g takes into account spin and valley degeneracy and N is the highest filled LL. In SLG, $\nu = g(N+1/2)$.

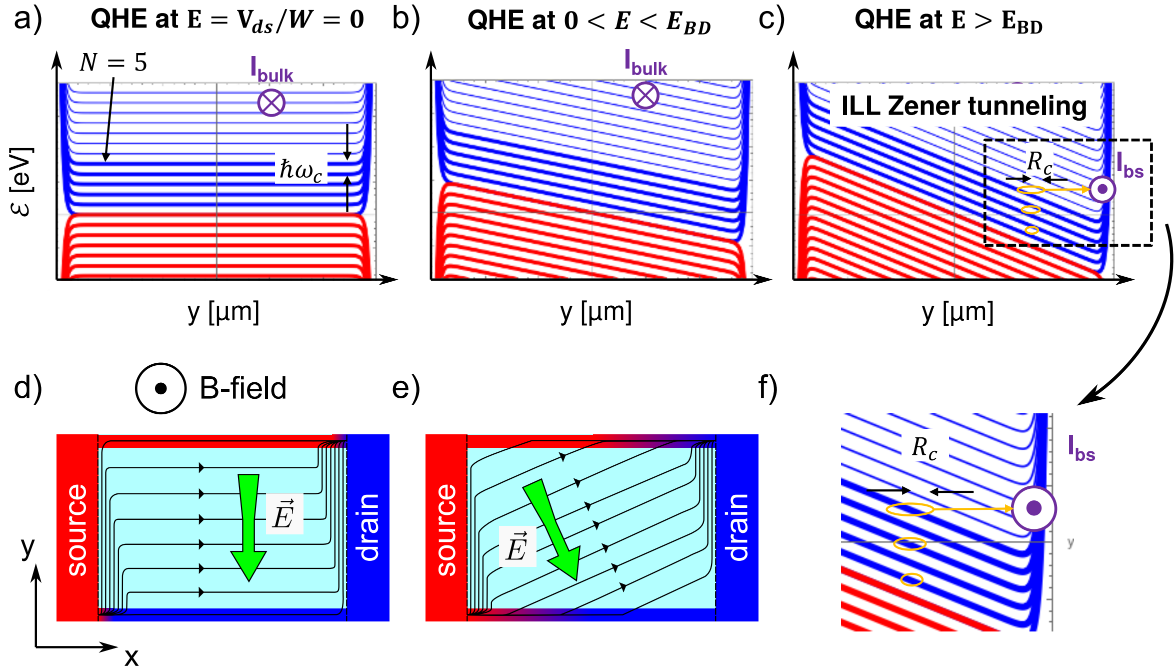

Figure 5.3 – **Landau levels in a high electric field.** a-c) Landau levels (LLs) in massive 2DEGs are evenly split by the cyclotron energy $\hbar\omega_c$. If an electric field is applied, the levels are inclined. Intrinsic breakdown occurs when the wavefunctions of adjacent LLs (spatial extent R_c) overlap, giving rise to the back-scattering current I_{bs}. d-e) Current lines (black arrows) and electric field (green arrow) at negligible (d) and finite (e) source drain bias. f) Zoom on the LLs from panel c.

In a two-terminal device at low bias, the longitudinal voltage measures the transverse resistivity ρ_{xy} since the two transverse channel edges are at equilibrium with the source and drain contact, respectively; see fig. 5.3d and also ref. [261]. Even though we measure a finite resistance, the transport is dissipationless since the electric field is perpendicular to the current. The corresponding "band diagram in real space" is shown in fig. 5.3a, where the

bold lines illustrate full LLs; see also ref. [74, p. 48]. In BLG and semiconductor 2DEGs, the LLs are evenly spaced by the cyclotron gap $\hbar\omega_c$. In a 2DEG:

$$\epsilon_N = \hbar\omega_c\left(N + \frac{1}{2}\right) \tag{5.1}$$

where $N = 0, 1, 2, 3, ...$ is the index of the LLs and the cyclotron frequency ω_c is given by:

$$\omega_c = \frac{eB}{m^*} \tag{5.2}$$

where m^* denotes the effective mass of the charge carriers. This is in contrast with SLG, where the energy spacing of the Landau levels decreases with their index [76, 77]. In BLG, the LLs are actually shifted by $\hbar\omega_c/2$ and their gap depends slightly on the LL index as pointed out in section 1.4.3, but we will ignore this difference in the following. In BLG, $m^* \approx 0.03m_e$, so that $\hbar\omega_c \approx 4$ meV/T $\times B$. As the source-drain bias is dialed up, the LLs become tilted $\epsilon_N^{E\neq 0}(y) = \epsilon_N + eE_y y$ and the electric field rotates towards the horizontal; see fig. 5.3b and e. The longitudinal component of the electric field gives rise to dissipation of power $\mathbf{E}\cdot\mathbf{j}$.

The spatial extent of the wavefunctions of the QHE is determined by the cyclotron radius, defined as follows [32]:

$$R_c = \sqrt{2N}\ell_B \tag{5.3}$$

where ℓ_B is the magnetic length (a.k.a. Larmor radius):

$$\ell_B = \sqrt{\frac{\hbar}{eB}} \tag{5.4}$$

The threshold field for an intrinsic Zener breakdown can therefore be derived from pure dimensional analysis: the wavefunctions of two adjacent LLs will have a maximum overlap when the electric field corresponds to the ratio of the cyclotron gap $\hbar\omega_c$ and the typical spatial extent $\sim \sqrt{N}\ell_B$. This is illustrated in fig. 5.3c and f. We thus obtain the following expression for the critical Zener field:

$$E_c = \rho_{xy} j_c = \frac{\hbar\omega_c}{e\ell_B\sqrt{N}} \propto B^{3/2} \tag{5.5}$$

where $\rho_{xy} = h/\nu e^2$. Using the expression for the Hall conductivity $\sigma_H = ne/B$, the definition of the current density $j = nev_d$ in terms of the drift velocity v_d and Ohm's law $j = \sigma E$, one can easily obtain the relation $v_d = E/B$ (where we call $1/B$ the Hall mobility), so that the critical drift velocity v_c is given by:

$$v_c = \frac{\hbar\omega_c}{e\ell_B\sqrt{N}B} = \frac{\omega_c\ell_B}{\sqrt{N}} \tag{5.6}$$

It is also straightforward to derive an expression linking the critical drift velocity v_c to the critical electric field E_c, which we will use in section 5.4:

$$v_c = \left[\frac{\hbar e}{Nm^{*2}}E_c\right]^{1/3} \tag{5.7}$$

5.3 Short review of quantum Hall breakdown

In this section, I will start by summarizing the first experimental studies of the QHBD from 1983. I will then provide a little more detail about two theories that first came up in 1985 and 1986, respectively: the bootstrap electron heating theory and the quasi-elastic inter-Landau-level scattering theory. I will finally summarize a couple of other experiments in semiconductor 2DEGs and move on to studies in single- and bilayer graphene, where I will also quantitatively confront the two theories with each other and with the experiments, highlighting how the sample under discussion in this chapter sticks out from the bibliography. For a more detailed review of the breakdown, the reader is referred to ref. [262].

5.3.1 Pioneering studies

Only a short time after the integer quantum Hall effect (IQHE) was discovered by von Klitzing *et al.* in 1980 [69], its physical limitations were studied by various groups. The knowledge of the phase space of stable quantization – i.e. the knowledge of critical current, field, carrier density and temperature – is important, because from the moment of its discovery onwards, the IQHE became a candidate for a high-precision resistance standard, which constitutes today (2019) one of the pillars of the new International System of units [70, 71]. Already in 1983, first experimental studies of the critical current were published [263, 264].

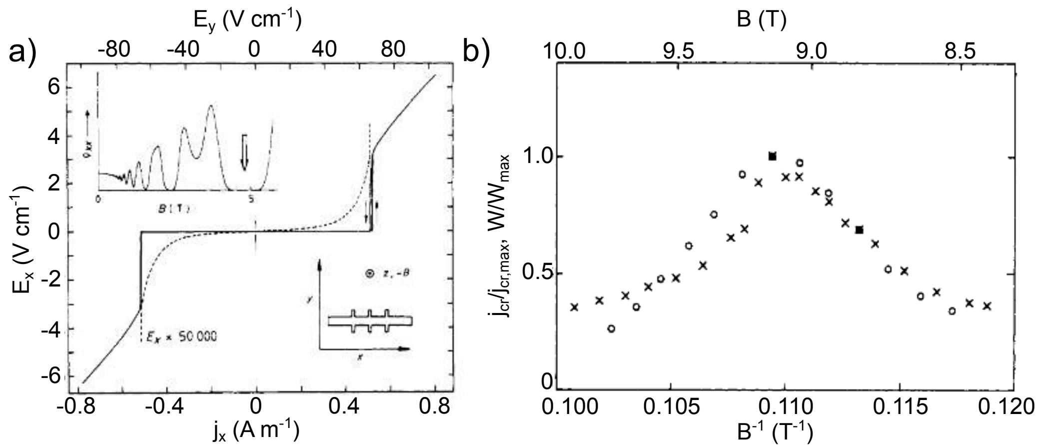

Figure 5.4 – **First studies of breakdown.** a) Longitudinal electric field E_x as a function of the current density j_x in a GaAs/AlGaAs hallbar (bottom inset). The top inset shows Shubnikov-de-Haas oscillations. b) Typical "triangular" shape of the B-field dependence of the breakdown current and the activation energy W. Reproduced from [263].

Figure 5.4a shows Ebert *et al.*'s measurements [263] on a Hall bar fabricated in a GaAs-AlGaAs 2DEG with a mobility of 10^5 cm^2/Vs and a width of 380 μm. They observed an abrupt breakdown of the dissipationless quantum Hall current at a critical current density of $j_{cr} \approx 0.56$ A/m, where the longitudinal electric field E_x increases by a factor of 10 000 for a current variation smaller than 1%. By measuring the longitudinal resistivity as a function of temperature, they extract an activation energy. This energy (circles) and the critical current density (crosses) are plotted as a function of the magnetic field in fig. 5.4, centered around a magnetic field that corresponds to a filling factor of 2, with the Fermi level centered between

two Landau levels (LLs). As the Fermi level moves closer to an adjacent Landau level (upon sweeping the B-field), both the critical current and the activation energy decrease. Ebert *et al.* conclude that the dissipation is mostly due to transitions between Landau levels and they propose a thermal instability as a mechanism of breakdown.

At the same time, Cage *et al.* [264] carried out studies on similar heterostructures and established that the breakdown is highly inhomogeneous in these samples, which means that the notion of a critical current *density* has to be handled with care. The authors also note that the onset of the breakdown is associated with strong broadband noise spanning from 0−5 MHz.

A whole range of experimental works followed these first studies and entailed a certain number of theories for the mechanism of the breakdown: Zener-tunneling between LLs [265], spontaneous emission of phonons when the drift velocity exceeds the sound velocity [266], percolation between the two sample edges across localized bulk states [267], quasi-elastic inter-Landau-level scattering [260,268] and bootstrap electron heating [269]. In the following, I will provide some more details about the last two of these.

5.3.2 Bootstrap electron heating

In order to gain more insight into the heating effects proposed as a cause of the breakdown, Komiyama *et al.* [269] conducted an experimental study in 1985, in which the onset of dissipation was detected in $W = 50$ μm large GaAs/AlGaAs hall bars as a function both of the applied field and of the lattice temperature T_L (see fig. 5.5a). The breakdown occurred at fields on the order of 4×10^3 V/m in the $\nu = 4$ state ($\sigma_{xy} = \nu e^2/h$), corresponding to a critical current density $j_c \sim 0.6$ A/m.

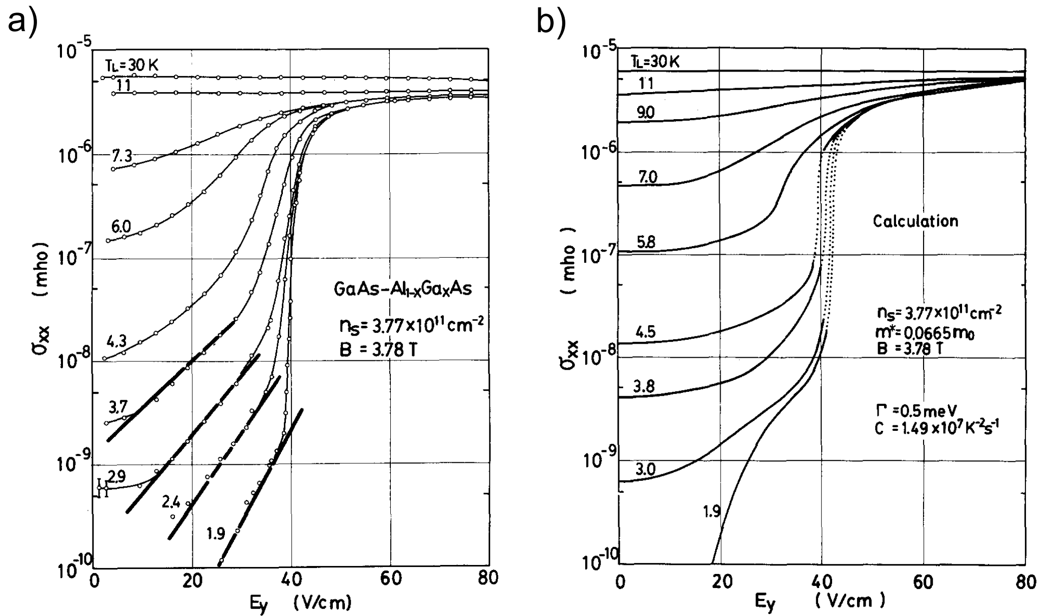

Figure 5.5 – **Bootstrap electron heating.** a) Experimental and b) modeled longitudinal conductivity as a function of the electric field for various lattice temperatures. From [269].

The authors proposed a theory, later coined bootstrap electron heating (BSEH), to ex-

plain their measurements in terms of a thermal instability. A review about this theory can be found in ref. [270]. In the following, I will summarize the derivation of the critical field from that reference:

In order for the electron temperature to be stable, the rate G at which the electrons gain energy should not exceed the rate L at which electrons lose heat to the lattice. The gain and loss rates are given by:

$$G = \sigma_{xx}(T_e)E_y^2 \tag{5.8}$$

$$L = \frac{Z(T_e) - Z(T_L)}{\tau_\epsilon} \tag{5.9}$$

where T_e and T_L denote the temperature of the electron system and of the lattice, respectively, τ_ϵ is the energy relaxation time and $Z(T)$ stands for the internal energy of the electron system:

$$Z(T) = 2\int_{\epsilon_F}^{\infty} (\epsilon - \epsilon_F)D(\epsilon)f(\epsilon, T)\; d\epsilon \tag{5.10}$$

where $f(\epsilon, T)$ is the Fermi-Dirac distribution at temperature T, $D(\epsilon)$ is the density of states of the LLs and ϵ_F denotes the Fermi energy, lying at the middle between two adjacent LLs. Approximating the LL DOS by a delta function, one finds:

$$Z(T_e) = (\pi\ell_B^2)^{-1}\hbar\omega_c \exp\left(-\frac{\hbar\omega_c}{2k_BT_e}\right) \tag{5.11}$$

where $(\pi\ell_B^2)^{-1}$ is the degeneracy of each LL. Under the simple assumption that the lattice temperature is zero, it is easy to show that $Z(T_L) = 0$. The longitudinal component of the conductivity is given by the empirical activation law:

$$\sigma_{xx}(T_e) = \frac{e^2}{h}\exp\left(-\frac{\hbar\omega_c}{2k_BT_e}\right) \tag{5.12}$$

Now, at zero T_e, the energy gain is matched by the dissipation to the lattice for any E_y. However, for this to be a truly stable state, it must also resist against fluctuations of T_e. At the threshold one obtains:

$$\left.\frac{\partial G}{\partial T_e}\right|_{T_e=0^+} = \left.\frac{\partial L}{\partial T_e}\right|_{T_e=0^+} \tag{5.13}$$

Inserting the expressions for $\sigma_{xx}(T_e)$ and $Z(T_e)$ into those for the gain G and the loss L, combining this with the stability criterion in eq. 5.13 and solving for E_y yields the following expression for the critical field:

$$E_b = \sqrt{\frac{2\hbar}{m^*\tau_\epsilon}}B \tag{5.14}$$

As pointed out in ref. [270], the energy loss rate $1/\tau_e$ is expected to be proportional to the magnetic field, so that the BSEH breakdown field $E_b \propto B^{3/2}$, like the Zener field in eq. 5.5. In their original article [269], Komiyama *et al.* used their low-field $\sigma_{xx}(T)$ to determine the activation law, and an electron energy loss rate $1/\tau_\epsilon$ estimated from their measurements to model the high-field behavior of the longitudinal conductivity, in excellent agreement with the experiment, see figure 5.5b.

The formula was adapted for the single layer graphene case in ref. [271]:

$$E_b = \sqrt{\frac{4B\hbar\omega_c}{\eta e\tau_e}} \tag{5.15}$$

where η takes into account spin and valley degeneracy, i.e. $\eta = 4$ in graphene and $\eta = 2$ in standard semiconductor 2DEGs.

The BSEH theory can explain the hysteresis observed in some experiments [269, 272] and the "triangular" shape of $j_c(B)$ illustrated in fig. 5.4 [270]. Furthermore, it explains the dependence of the breakdown on the constriction length observed in refs. [273, 274], since electrons have to travel and gain heat over a certain length until a new (stable) equilibrium temperature is reached, giving rise to an avalanche of inter-LL excitations. Within this picture, Komiyama *et al.* [274] also justify why Bliek *et al.* [275] might have obtained much higher breakdown currents in their short constrictions, see next section. For more details on the BSEH theory, the reader is referred to the review article by Komiyama *et al.* [270].

5.3.3 Quasi-elastic inter-Landau-level scattering

Arguing that previous studies were limited by "spurious inhomogeneities, reducing the effective widths of the samples", Bliek *et al.* [275] investigated the breakdown in narrow constrictions ($W = 1$ μm and 66 μm) of GaAs/AlGaAs 2DEGs in 1986 and indeed, they found much higher critical current densities than the previous works, with values peaking at $j_c = 32$ Am^{-1} for $\nu = 2$. Their results were published simultaneously with a theory by Eaves & Sheard [260], in which they attribute the breakdown to quasi-elastic inter-Landau-level scattering (QUILLS).

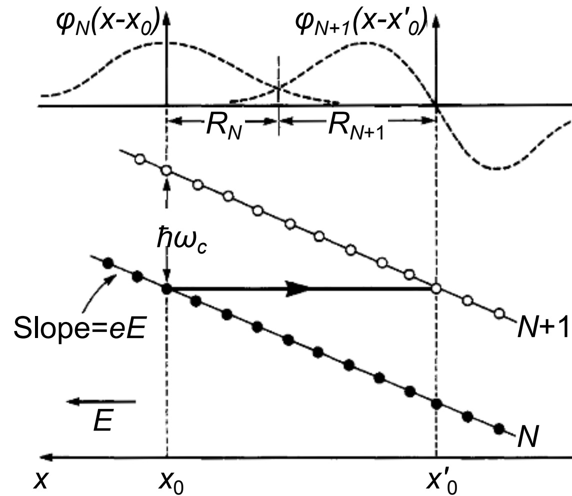

Figure 5.6 – **Quasi-elastic inter-Landau-level scattering.** Illustration of wavefunction overlap between adjacent LLs close to the critical electric field. Taken from ref. [260].

In its essence, this theory is very similar to the Zener analysis in section 5.2: The authors calculate the solutions of the single-electron Schrödinger equation in crossed magnetic and

electric fields and find that a maximum overlap between the wavefunctions of adjacent LLs is obtained at the critical field:

$$E_c = \frac{\hbar\omega_c}{e\ell_B\left[\sqrt{2N+1}+\sqrt{2N+3}\right]} \tag{5.16}$$

which differs from our order-or-magnitude expression in eq. 5.5 only as far as the N-dependent term in the denominator is concerned, because Eaves & Sheard's calculation actually takes into account the sum of the cyclotron radii of the two LLs N and $N+1$. This is illustrated in figure 5.6. In the large N limit, the square-bracket-term reduces to $2\sqrt{2N}$, implying a correction of about $2\sqrt{2} \approx 2.8$ to eq. 5.5.

Since the wavevector mismatch is very large ($\sim 2k_F$) between the LLs, Eaves & Sheard mention various mechanisms that could solve the momentum conversation issue in the inter-LL tunneling process: impurities, charge inhomogeneities, many-body effects or long-wavelength acoustic phonons. The energy of these phonons would be very small compared to the cyclotron gap, which is why the proposed mechanism was coined *quasi-elastic*.

Their theory was in excellent quantitative agreement (10% deviation) with Bliek *et al.*'s experiment, predicting breakdown current densities of 29 and 14 A/m for the $\nu = 2$ and the $\nu = 4$ plateaus, respectively, at $B = 6.3$ T. Note that these values are more than an order of magnitude larger than those reported by Komiyama *et al.* [269].

5.3.4 Summary of experiments: from 2DEG to graphene

A large number of experiments, some of which have already been mentioned, have been carried out to better investigate the mechanism of the QHBD. A particularly important question concerns the homogeneity of the current flow at the breakdown, where the current is generally thought to fill the bulk instead of being localized at the sample edges [262]. In low mobility devices, the breakdown current was observed to be proportional to the device width [276,277], whereas a sublinear dependence was observed in high mobility samples [278]. Nachtwei [262] attributes this to short- and long-range scatterers respectively. In order to further investigate this question, Nachtwei *et al.* [272] have fabricated antidot arrays in GaAs/AlGaAs 2DEGs in order to study how modifications in the homogeneity of the current flow affect the breakdown. They find that aperiodic arrays lead to a lower critical current due to localized peaks in the current density, see fig. 5.7a. Sample homogeneity is particularly questionable when the breakdown occurs in discrete voltage steps. This kind of behavior was observed for example in refs. [263, 279].

In order to locally image the potential profile in the sample when it approaches the breakdown regime, Panos *et al.* [283] have probed Hall bars using scanning force microscopy. Even though this method enables the determination of the homogeneity of the potential landscape, and therefore the distinction between edge- and bulk-dominated breakdown, it cannot distinguish between the proposed breakdown mechanisms.

Apart from the aforementioned Hall bars, constrictions and antidot arrays, another interesting geometry for the investigation of the QHBD is the Corbino disk, where the QHE manifests itself in the absence of edge currents and an isolating bulk, leading to a suppression of the source-drain current, see fig. 5.7b and c. In GaAs/AlGaAs 2DEGs of this geometry, the QHBD was investigated in conjunction with noise measurements in the $0 - 200$ kHz

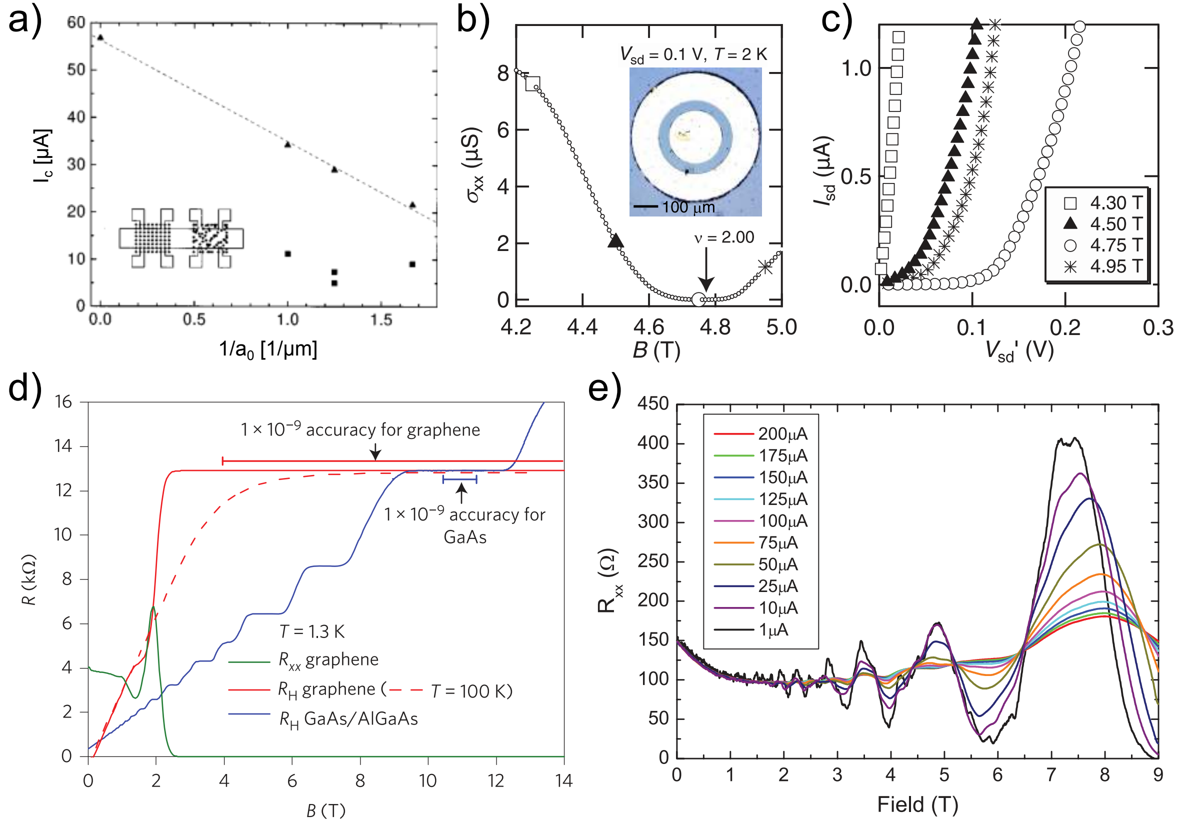

Figure 5.7 – **QHBD experiments.** a) Breakdown currents are higher in periodic (▲) than in aperiodic (■) antidot arrays. From [272]. b) Source-drain conductivity vs. B-field of a Corbino disk (inset) shows minimum at filling factor 2. c) Breakdown I-V characteristics of the Corbino device at (○) and around (□, ▲, ⋆) $\nu = 2$. From [280]. d) Comparison of GaAs and graphene as candidates for quantum Hall resistance standards. 100 K operation can be realized with graphene. From [281] e) The damping of Shubnikov-de Haas oscillations can be used to determine electron energy loss rates and scattering rates as a function of temperature and applied current. From [282].

range [280, 284]. They observe super-Poissonian Fano factors at the breakdown and justify this within the framework of the avalanche mechanism in BSEH.

Due to the large Landau gaps of both single layer and bilayer graphene and their highly tunable carrier density, compared to semiconductor 2DEG systems, they both constitute candidates for novel quantum Hall resistance standards (see fig. 5.7d) that can potentially operate up to room temperature [285]. There have been a few studies of the breakdown both in exfoliated [282, 285, 286], epitaxial (grown on SiC) [271, 281, 287], suspended [288, 289] and hBN-encapsulated [290] single- and bilayer graphene. The chosen geometry was typically a Hall bar, except for refs. [288, 289], where Corbino disks were investigated. The carrier mobilities for most of the devices (except the suspended and encapsulated ones) was on the order of $5000 - 10000$ cm^2/Vs and breakdown current densities were typically on the order of $1 - 5$ A/m at temperatures around $0.3 - 2$ K. In most of these works, the breakdown was characterized around $B = 9 - 10$ T and the filling factor $\nu = 2$.

The 2013 work by Alexander-Webber *et al.* [271] sticks out here: The authors report unprecedented (both in graphene and semiconductor 2DEGs) breakdown current densities of up to 43 A/m at $B = 23$ T, $\nu = 2$ in epitaxial graphene on SiC. Note that this record value is mostly due to the high magnetic field, which results in a large cyclotron gap $\hbar\omega_c \propto B$. At $B = 7$ T, closer to the other works mentioned above, the authors report a breakdown current density of 4 A/m. Still, we can translate the record current density 43 A/m to a record breakdown field $E_c = j_c h/\nu e^2 \approx 5 \times 10^5$ V/m, which – so far – only compares to the breakdown fields $\sim 10^5$ V/m observed for the $\nu = 0$ scenario by Laitinen *et al.* [288] in suspended graphene.

Alexander-Webber *et al.* [271] benchmark their results against the critical current densities predicted for the BSEH theory and compare to previous studies. This comparison is reproduced in table 5.1 and amended by the Zener breakdown current densities $j_c^{\mathrm{Z}} = \sigma_{xy} E_c^{\mathrm{Z}}$, where E_c^{Z} is the Zener breakdown field from equation 5.5, so that:

$$j_c^{\mathrm{Z}} = \frac{\nu e^2}{h} \frac{\hbar\omega_c}{e\ell_B\sqrt{N}} \tag{5.17}$$

where N denotes the first unoccupied Landau level. For example, both in a semiconductor 2DEG and in SLG at $\nu = 2$, it will be $N = 1$. In BLG, $N = 1$ corresponds to $\nu = 4$. Let us also recall the BSEH critical current density (c.f. eq. 5.15):

$$j_c^{\mathrm{BSEH}} = \frac{\nu e^2}{h} \sqrt{\frac{4B\hbar\omega_c}{\eta e \tau_e}} \tag{5.18}$$

Table 5.1 has also been amended with the work by Bliek *et al.* [275], who have attained record current densities in a GaAs system, and the second row (concerning ref. [291]) has been re-calculated, taking into account the correct B-field value and filling factor ν from that reference. The scattering times τ_e can be calculated from electron energy loss measurements using Shubnikov-de Haas oscillations, c.f. refs. [282, 292–295] and fig. 5.7e. The relaxation time is measured at the critical temperature, which is why it decreases with increasing cyclotron gap (increasing critical temperature).

Material (geometry ⋆)	B (T)	ν	$\hbar\omega_c$ (meV)	τ_e (ps)	Experiment j_c (Am^{-1})	BSEH j_c	Zener j_c	width (μm)
GaAs (c)	6	2	10	100 [292]	32	2.6	74	1 [275]
GaAs (H)	5.7	4	10	100 [292]	1.4	5.2	100	35 [291]
InSb (H)	7	2	40	500 [293]	0.3	2.6	320	600 [293]
Graphene (H)	7	2	105	80 [294]	4.3	7.3	840	35 [271]
Graphene (H)	23	2	200	6 [294]	43	71	2900	5 [271]
BLG (c)	7	4	27	100 † [295]	**150**	6.7	430	3 [28]

Table 5.1 – **Material comparison for the QHBD.** Measured critical current densities from various works in comparison with the theoretical breakdown densities predicted by the BSEH theory and the ILLT theory. ⋆c denotes constriction, while H stands for Hall bar. †Order of magnitude, assuming doping on the order of 10^{12} cm^{-2} and critical temperature on the order of 10 K. Table adapted from ref. [271].

Inspection of the order of magnitude of the theoretical values shows immediately that the BSEH theory predicts critical current densities (and critical electric fields) one or two orders of magnitude smaller than the QUILLS/Zener approach. It is obvious that so far, the critical currents observed experimentally have mostly been in the “BSEH range”, with the exception of Bliek *et al.*'s early study [275].

When comparing the current densities in graphene to those in semiconductor 2DEGs, one has to keep in mind that the carrier densities in the latter are typically one order of magnitude smaller ($\sim 10^{11}$ cm^{-2}, see e.g. ref. [280] for GaAs and ref. [293] for InSb systems). Since $j = nev$, this implies higher current densities in graphene at the same drift velocity, unless the graphene is intentionally weakly doped like in ref. [271], where $n \lesssim 10^{12}$ cm^{-2}, see table 5.1. The critical current density listed in that table for our own BLG sample was measured at $n \approx 7 \times 10^{11}$ cm^{-2}, ensuring comparability with the other works.

At comparable magnetic field and filling factor, the critical current density $j_c \approx 150$ A/m in our BLG sample (last line of the table) is five times larger than Bliek *et al.*'s record value and four times larger than Alexander-Webber *et al.*'s value recorded at $B = 23$ T. It is more than twenty times larger than the critical current predicted by the thermal bootstrap theory and reaches the range of the theoretical Zener field.

5.4 Experimental results in BLG

Our sample is an as-exfoliated BLG-on-hBN sample with a local bottom gate electrode as a particularly homogeneous model system for the breakdown of the IQHE, since the bottom gate screens trapped charge potentials from the semiconducting/insulating substrate. The sample was described in section 5.1 and is shown again in fig. 5.8a (inset). It was fabricated by Xiaobo Lu, Guangyu Zhang and Wei Yang. In order to gain insight into the dynamics of the QHBD, we study DC transport *and* noise, measured by Wei Yang. To overcome $1/f$ noise at these high source-drain currents, the noise power spectral density is measured in a 1 GHz bandwidth window around 5 GHz, which requires the sample to be embedded in a two-terminal co-planar waveguide, contrarily to most other studies, where the sample geometry is either a Hall bar or a Corbino disk. In short, we are combining the homogeneous constrictions introduced by Bliek *et al.* [275] with noise measurements similar to those carried out by the Kobayashi group [280,284,296] and an intrinsic BLG sample from Yang *et al.* [144] to shed a new light on the old problem of the quantum Hall breakdown.

Since the contact resistance of the device is more than a factor of two smaller for a p-doped channel ($R_{\text{cont}} \approx 40\ \Omega$), we will focus in the following on the negative gate-voltage range. There are two reasons for this: a) Since we are dealing with a two-terminal device, we cannot directly extract the contact resistance and therefore need to minimize it as much as possible towards the Sharvin limit [259] and b) we send high currents through the device and measure the electronic temperature *via* the noise, so we want to avoid any spurious noise due Joule dissipation in the contacts. The results presented in the following were published in ref. [28].

Let us first look at the low-bias magnetotransport. For a magnetic field of $B = 0 \to 4$ T, the conductance σ of the device is plotted as a function of applied gate voltage in figure 5.8a, where the emblematic quantum Hall plateaus are observed for multiples of the quantum of conductance $4e^2/h$, corresponding to the incremental filling of the quantum Hall states. The

conductance steps are consistently multiples of $4e^2/h$, which is specific to bilayer graphene [78], since in single layer graphene the smallest filling factor is 2 [77]. The steps between the plateaus are strongly smeared, which indicates a very low density of localized states due to impurities or charge inhomogeneities and underlines the high quality of the device.

Figure 5.8b shows the typical Landau fan diagram of the differential conductance $\partial G_{\mathrm{ds}}/\partial V_g$ as a function of gate voltage and magnetic field. The plateaus of panel (a) correspond to the blue triangles emanating from the origin. They are numbered according to the lowest unoccupied LL, denoted N, so that the filling factor is simply $\nu = 4N$. States from $N = 0$ to $N \sim 10$ can be clearly distinguished, where the median value $N = 5$ is highlighted by a yellow dashed line. We observe the splitting of the zero energy states, which is an additional confirmation of the high quality of the sample.

Panels (c-j) of figure 5.8 show the DC current and the shot noise (in units of current: $S_I/2e$) as a function of source-drain voltage for increasing magnetic fields. Each panel shows the measurements taken for gate voltages ranging from 0 to -6 V, corresponding to hole densities between 0 and 4.3×10^{12} cm^{-2}. The applied bias corresponds to extremely high electric fields on the order of 10^6 V/m, leading to extremely high current densities on the order of 10^3 A/m.

At zero magnetic field (panel c), a saturation behavior due to Zener-Klein tunneling is observed. It is limited by the excitation of hyperbolic phonon polaritons of the hBN substrate, which acts as a highly efficient cooling pathway for the hot electrons in the device. This zero-B-field behavior was discussed in section 5.1 and ref. [144]. It is important to point out that at $B = 0$, the noise clearly is non-negligible regardless of source-drain bias, compared to what we are about to see for quantizing magnetic fields:

With increasing B-field, both the current and the noise start to exhibit two distinct regimes: At low source-drain bias, the current increases linearly with the bias (where the slope is simply given by the Hall conductance as we will see in the following) and the noise is completely suppressed (as one would expect for dissipationless transport in the ballistic quantum Hall channels). When a certain threshold – highlighted by the vertical dashed lines in the figure – is reached, the current shows a trend towards saturation, leading to a differential conductance $\partial I_{\mathrm{ds}}/\partial V_{\mathrm{ds}} \approx 0.6$ mS $= G_{\mathrm{sat}}$ that becomes independent of the gate voltage and the magnetic field, and the noise increases abruptly, up to values that by far exceed the zero-B-field noise.

Comparing the abrupt increase of the noise to the gradual saturation of the DC current immediately qualifies the noise as much more clear-cut indicator for the breakdown. As expected, the threshold source-drain bias clearly increases with the applied magnetic field. The fully developed shot noise under quantizing fields furthermore suggests that the cooling mechanism due to the substrate phonons described in section 5.1 and ref. [144] are suppressed at high magnetic fields.

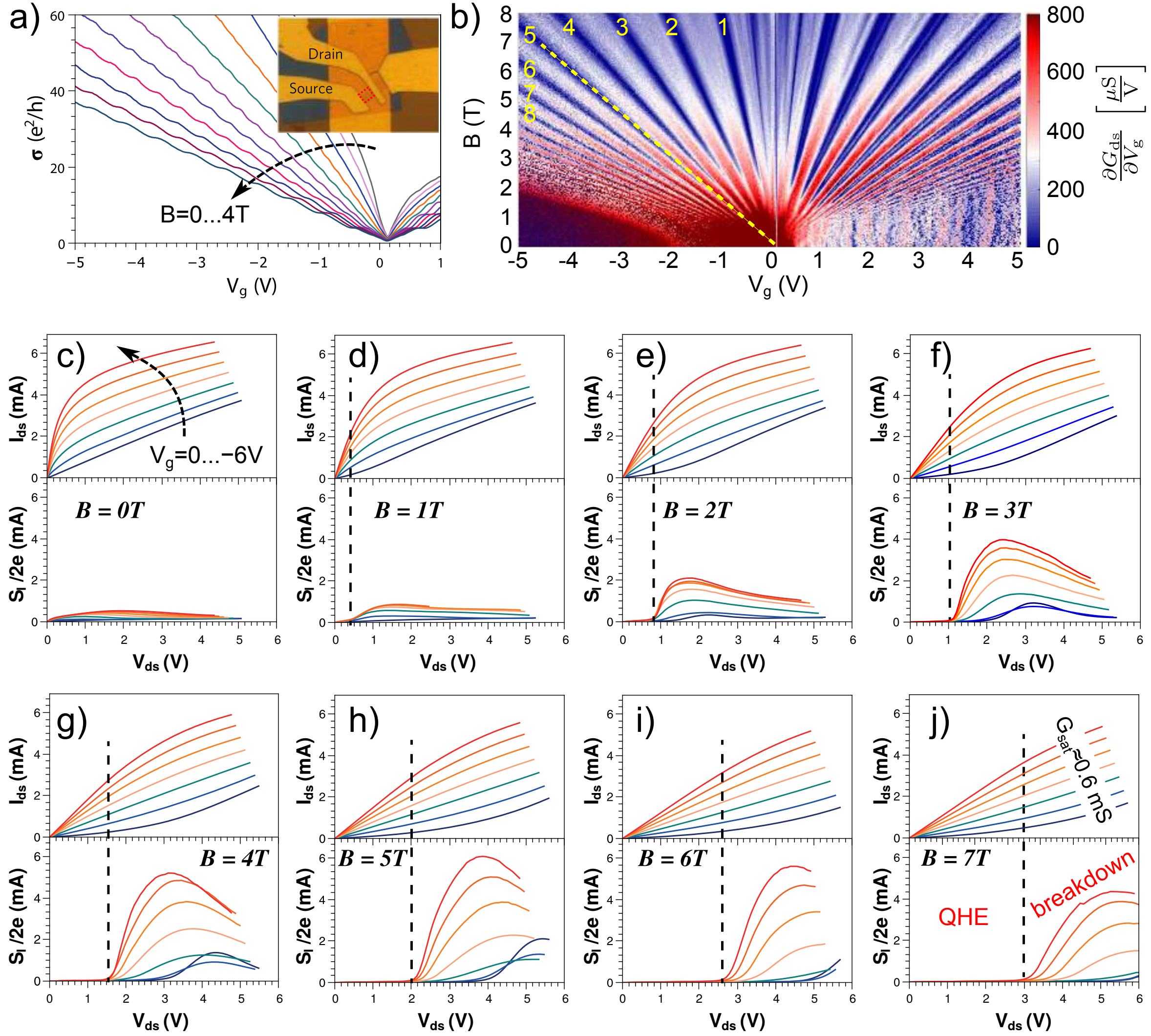

Figure 5.8 – **Raw data.** a) The device conductance vs. gate voltage, plotted for $B = 0 \to 4$ T (step 0.4 T) exhibits smeared steps of $4e^2/h$. Inset is a microscope image of the sample. b) Typical Landau fan diagram of the differential conductance $\partial G_{ds}/\partial V_g$ at fixed $V_{ds} = 5$ mV. The plateaus of panel a correspond to the minima (blue) of the differential conductance. They follow lines $B = CV_g h/4e^2 N$ where $C = 1.15$ fF/μm^2 is the gate capacitance per unit surface and N is the lowest unoccupied LL. The yellow dashed line highlights the experimental median $N = 5$. c-j) DC source-drain current (top) and 5 GHz noise in units of current (bottom) for increasing $B = 0 \to 7$ T. Black dashed lines mark the onset of the noise.

5.4.1 Scaling of the DC current

In order to make the dataset from figure 5.8 easier to analyze, we can scale the measured quantities using intensive units that are relevant to the QHE. By re-expressing all the DC current measurements as drift velocities $v_d = J_{\rm ds}/ne$ where $n = C|V_g|/e$ is the hole density and plotting it as a function of the applied electric field $E = V_{\rm ds}/W$, we obtain individual sets of overlapping lines for each applied magnetic field, c.f. figure 5.9a, the slope of which is given by the Hall mobility $\mu = 1/B$, as shown in the figure's inset.

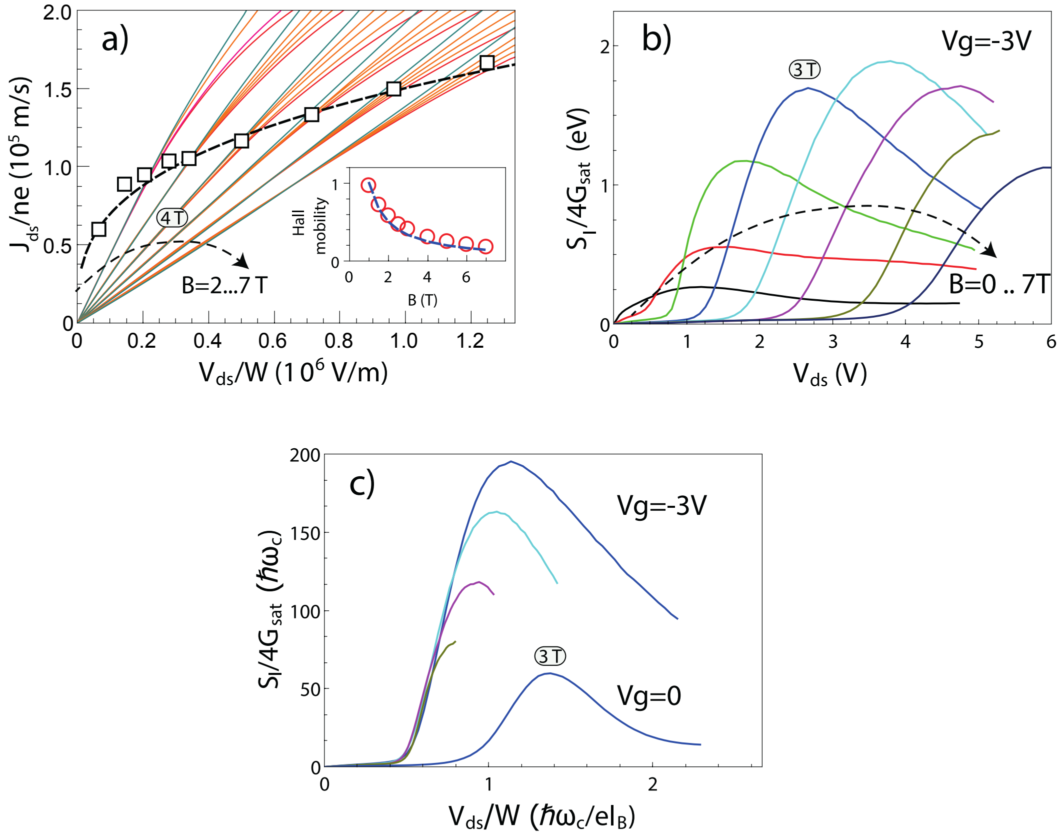

Figure 5.9 – **Scaling of current and noise.** a) Drift velocity $v_d = I_{ds}/Wne$ vs. electric field $E = V_{ds}/W$ for various gate voltages and magnetic fields $B = 2 \rightarrow 7$ T. Below the breakdown, the various density curves collapse on single lines defined by $v_d = \mu E$ where $\mu = 1/B$ is the Hall mobility (inset). The breakdown is characterized by the fanning out of these lines. The black dashed line is the critical drift velocity eq. 5.7 with $N = 5$ corresponding to the experimental median value. Black squares represent the onset of the noise. b) Noise energy vs. bias at fixed density for increasing magnetic field. At $B \geq 2$ T, the low bias noise is fully suppressed, as opposed to $B < 2$ T. c) Noise energy scaled by cyclotron gap vs. electric field scaled by maximum Zener field $\hbar\omega_c/e\ell_B$.

Upon increasing the electric field and therefore the drift velocity, the overlapping lines gradually fan out; this is the breakdown regime. Comparing this point of "fanning-out" to the breakdown field determined from the abrupt rise in the noise measurement (vertical dashed lines in figure 5.8) leads to a good agreement, except at very high E-fields, where the

drain-gating compensation described in section 5.1 is not fully effective anymore.

The black dashed line in figure 5.9 corresponds to the critical Zener velocity v_c defined in equation 5.7, where a constant filling factor of $N = 5$ was used – corresponding to the experimental median value. There is an excellent agreement between this intrinsic theoretical prediction and the experimentally determined breakdown fields, both in the current and – particularly – in the noise measurement.

5.4.2 Scaling of the noise

Figure 5.9b shows the noise measurements from figure 5.8, this time represented as a noise energy $S_I/4G_{\text{sat}}$ and at constant charge carrier density $n = 2.15 \times 10^{12}$ cm^{-2} for the entire magnetic field range $0 \leq B \leq 7$ T. The difference between low and high B-field is striking in this figure: Whereas the noise increases quickly with applied bias at zero magnetic field, due to the creation of a hot carrier population, noise reduction becomes apparent already at a moderate field $B = 1$ T until noise is completely suppressed under fully quantizing fields $B \gtrsim 2$ T ($\mu B \gtrsim 2\pi$).

The noise data can now also be scaled in terms of quantities that are relevant to the QHE: In figure 5.9c, the electric field is scaled by the maximum Zener field $\hbar\omega_c/e\ell_B = \sqrt{N}E_{\text{bd}}$ and the noise energy is scaled by the LL energy spacing $\hbar\omega_c$. At the breakdown field, the noise curves of panel (b) collapse. This scaling of the noise data with the QHE-relevant quantities is strong evidence for the fundamental origin of the noise.

Besides, we notice two interesting features: (a) The onset of the noise occurs at a reduced electric field of $1/\sqrt{5}$, in accordance with the black dashed line from fig. 5.9a and (b) the noise energies reach extremely high values, two orders of magnitudes larger than the LL spacing $\hbar\omega_c$. This suggests that, when breakdown is reached, charge carriers are spread over a very large number of LLs. Conversely, close to the charge neutrality point at $V_g = 0$, the breakdown occurs at a higher reduced electric field $1/\sqrt{1}$, as expected [288].[1]

5.4.3 Contact heating

Since we are applying significant bias voltages, giving rise to significant current densities, even below the breakdown field, one is naturally curious about the noise evolution below the threshold. So far we have simply stated that the noise is suppressed in this regime, due to the ballistic source-drain transport, but let us have a closer look at this low-bias noise. Figure 5.10a recalls the DC current and noise data from fig. 5.8f.

Panel b shows a zoom on the bias range $V_{ds} = 0 \to 1.5$ V of the noise data. We observe a linear increase (with a slope dependent on the gate voltage) of the noise up to $V_{ds} = 0.8$ V (black dashed line), where it starts to increase abruptly. By plotting the Fano factor $F = S_I/2eI$ in panel c, we see that it is bias independent, that it depends only weakly on the gate voltage and, most importantly, that it is *small*: $0.02 \leq F \leq 0.04$. It is small compared to the Fano factor 1/3 of a disordered phase-coherent conductor [60] or to the Fano factor $\sqrt{3}/4$ of hot-electron shot noise [61, 62], which is why we attribute it to a residual proximity heating as the electrons relax in the contacts.

[1] A detailed experimental investigation of the $N = 1$ state is difficult due to the doping inhomogeneity associated with drain gating.

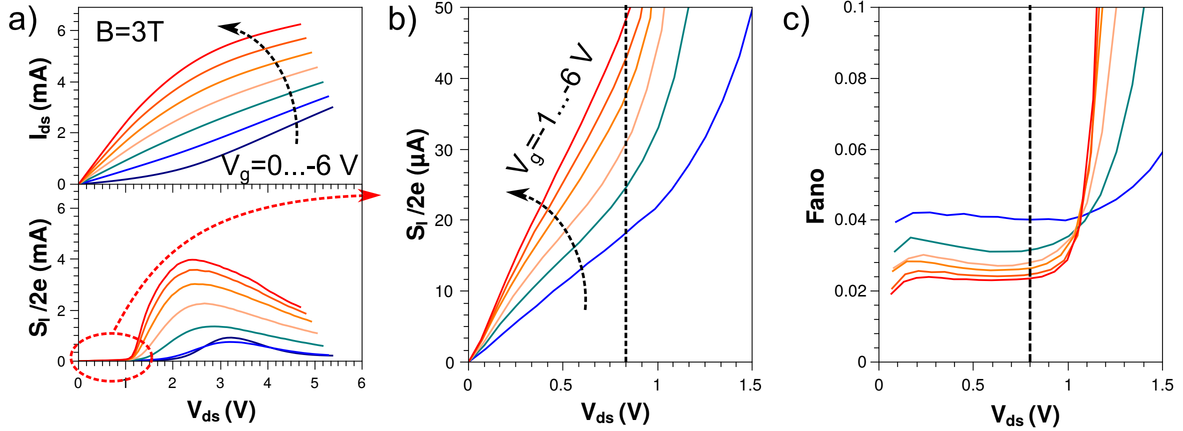

Figure 5.10 – **Noise floor.** a) Source-drain current and noise vs. bias at $B = 3$ T for various densities. b) Zoom on the low bias regime of the noise. c) Fano factor $F = S_I/2eI$ in the same regime. The black dashed line marks the threshold beyond which $S_I(V_{ds})$ deviates from linear behavior.

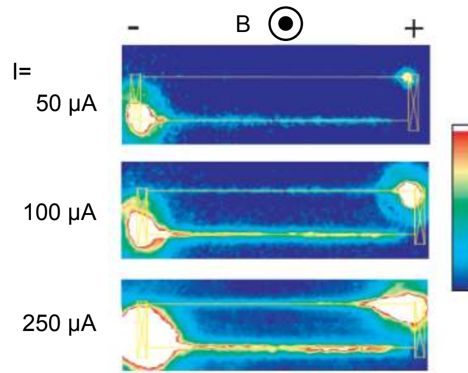

Figure 5.11 – **Contact heating.** THz-emission maps of a GaAs/AlGaAs Hall bar at filling factor $\nu = 2.43$. Figure adapted from ref. [297]

This phenomenon of contact heating was nicely visualized in a semiconductor 2DEG by Ikushima *et al.* [297] who measured the THz emission due to transitions between LLs. Figure 5.11 shows a map of this cyclotron emission, obtained using a THz microscope tuned to the cyclotron resonance frequency. The Hall bar's dimensions are $L \times W = 3 \times 0.5$ mm. One can identify localized hot-spots at the source (left) and the drain (right) electrode. These hot-spots grow significantly with the bias current, whereas the emission from the upper and lower sample edges (where the current flows) stays confined and relatively small.

5.4.4 The Fano factor as a hallmark of a collective breakdown

The Fano factor F is the ratio between the current and its shot noise $S_I = 2eIF$ and contains information about statistical correlations ("bunching") in the tunneling process that generates the noise. For independent single particle tunneling, one would expect Poissonian shot noise with a Fano factor of ≤ 1, depending on the tunneling probability (see section 1.3). For

collective tunneling mechanisms the noise is super-Poissonian ($F > 1$).

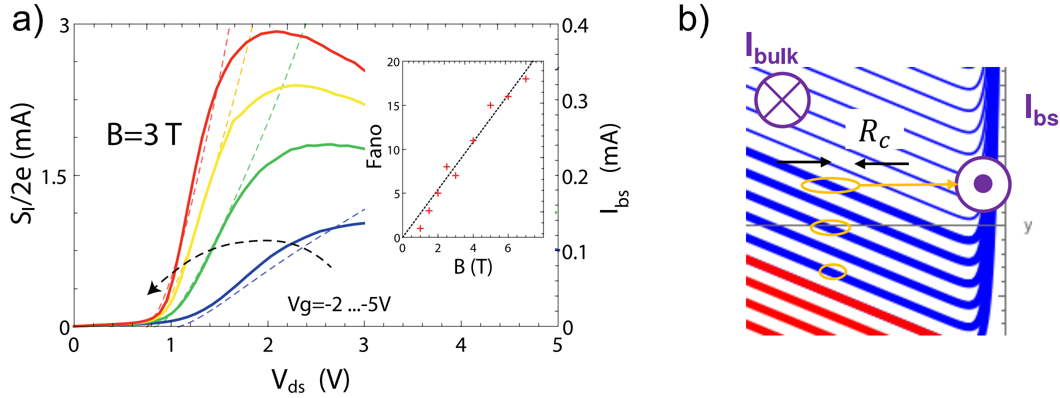

Figure 5.12 – **Superpoissonian noise.** a) Noise (left axis, solid lines) and backscattering current (right axis, dashed lines) vs. source-drain voltage for various gate voltages at $B = 3$ T. The ratio between the two scales corresponds to the Fano factor $F = S_I/2eI_{bs} = 7.5$. Inset: Fano factor vs. B-field. The Fano factor is linear in B with a slope of 2.7 T^{-1}. b) Sketch illustrating the backscattering current I_{bs}.

In figure 5.12a, we compare the noise (in units of current, $S_I/2e$, solid lines, left axis) at constant magnetic field $B = 3$ T to the noise-generating backscattering current $I_{\rm bs}$ (dashed lines, right axis), which we obtain from the deviation between the measured source-drain current and the extrapolated ballistic (i.e. noise-free) Hall current (see also the illustration in fig. 5.12b):

$$I_{\rm bs} = \frac{neV_{\rm ds}}{B} - I_{\rm ds} \tag{5.19}$$

An excellent overlap of current and noise for a large gate voltage range $-2\ \mathrm{V} \geq V_g \geq -5$ V can be obtained by fitting a Fano factor $F = 7.5$ between the two vertical scales. Performing a similar adjustment between current and noise for other magnetic field values shows that $F \propto B$, consistently with the scaling behavior discussed above.

Considering that the Fano factor describes the bunch size $N_{\rm bunch} = F$ in a correlated tunneling event, we can provide a tentative explanation for the proportionality between the Fano factor and the B-field. If the inter-edge charging energy is $\epsilon_c \sim e^2/\epsilon W \approx 2$ meV, then it takes $N_{\rm bunch} \sim \hbar\omega_c/\epsilon_c \approx 2\ \mathrm{T}^{-1} \times B$ carriers to temporarily restore a sub-threshold local electric field. This is in reasonable agreement with the experimental observation $F \approx 2.7\ \mathrm{T}^{-1} \times B$. A more involved theory goes beyond the scope of this thesis.

The fact that Fano factors $\gg 1$ are reached in the breakdown regime rules out a single particle tunneling mechanism, such as QUILLS. From a theoretical point of view, a single particle mechanism is problematic anyway, since the large momentum jump $q = 2k_F$ required for single particle backscattering is only achievable with the help of impurities (which our sample lacks). In the following, we propose a collective breakdown mechanism due to the spontaneous proliferation of magnetoexcitons, where electron-electron interactions help overcome the aforementioned momentum mismatch.

5.5 Magnetoexciton instability

Magnetoexcitons are collective excitations between the Landau levels of the integer quantum Hall effect [110–112]. In section 1.7 and in the appendix 6.5, we discuss how their dispersion arises from the random phase approximation in the case of a generic massive 2DEG.

Here we are dealing with bilayer graphene and not a standard 2DEG. However, it is possible to represent the eigenstates of the bilayer graphene quantum Hall Hamiltonian in terms of the eigenstates $|n, k_y\rangle$ of the non-relativistic Hamiltonian [68, 115]:

$$\psi_{\lambda,n\neq 0,k_y} = \frac{1}{\sqrt{2}} \begin{pmatrix} |n-2, k_y\rangle \\ \lambda\, |n, k_y\rangle \end{pmatrix} \tag{5.20}$$

where λ is the band index and $n > 1$. The calculation of the matrix elements therefore remains unchanged up to a correction on the order of $1/N_F$, where N_F is the highest filled LL. Since we consider the large N_F limit here, we can neglect this correction and use the matrix elements of the standard 2DEG in the following:

$$\psi^{\dagger}_{\lambda,n,k_y} e^{i\mathbf{q}\cdot\mathbf{r}} \psi_{\lambda',n',k'_y} \approx \langle n, k_y|\, e^{i\mathbf{q}\cdot\mathbf{r}}\, |n', k'_y\rangle \tag{5.21}$$

Within this approximation, we can still use the Lindhard function $\chi_{nn}(\mathbf{q}, \omega)$ from eq. 1.66 and the associated RPA susceptibility $\chi_{\mathrm{RPA}}(\mathbf{q}, \omega) = \chi_{nn}(\mathbf{q}, \omega)/\epsilon_{\mathrm{RPA}}(\mathbf{q}, \omega)$. The imaginary part of the latter is plotted once again in figure 5.13. The magnetoexciton modes appear at multiples of the cyclotron frequency ω_c and do not significantly disperse at large wavevectors.

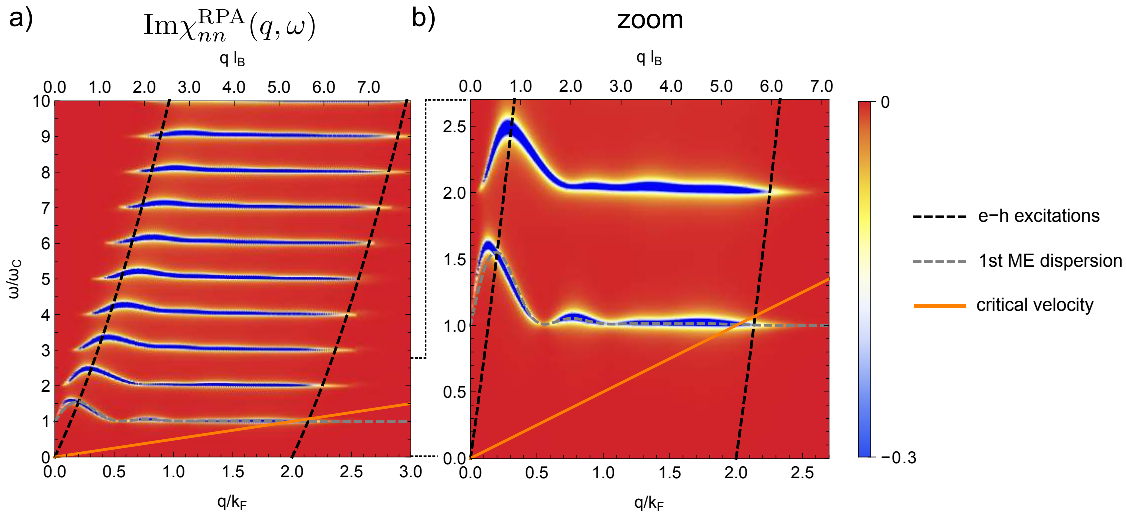

Figure 5.13 – **Magnetoexciton instability.** Color plots of $\mathrm{Im}\chi_{\mathrm{RPA}}(q, \omega)$. Here $N_F = 3$.

If we want to take into account the finite in-plane electric field induced by the drain-source bias, the Hamiltonian in eq. 1.40 has to be amended by a corresponding potential energy term. In appendix 6.5, we show that this modifies the QHE eigenstates by shifting the guiding center of the QH states and that it adds a field-dependent shift to the energy eigenvalues. However, when we re-calculate the Lindhard function $\chi_{nn}(\mathbf{q}, \omega)$, only a global

energy shift $\omega \to \omega - v_d q_y$ remains.[2] The same shift has to be taken into account in the RPA susceptibility $\chi_{\text{RPA}}(\mathbf{q},\omega)$ and the ME dispersion $\omega_{\text{ME}}(\mathbf{q},\omega)$, so that:

$$\chi_{nn}^{E\neq 0}(\mathbf{q},\omega) = \chi_{nn}^{E=0}(\mathbf{q},\omega - v_d q_y) \tag{5.22}$$

$$\chi_{\text{RPA}}^{E\neq 0}(\mathbf{q},\omega) = \chi_{\text{RPA}}^{E=0}(\mathbf{q},\omega - v_d q_y) \tag{5.23}$$

$$\omega_{\text{ME}}^{E\neq 0}(\mathbf{q}) = \omega_{\text{ME}}^{E=0}(\mathbf{q}) - v_d q_y \tag{5.24}$$

where $v_d = E/B$ is the drift velocity. In other words, the system obeys *Galilean invariance*. This means that the magnetoexciton dispersion develops an instability $\omega_{\text{ME}}(q_0) = 0$ when a finite electric field is applied (resulting in a finite drift velocity v_d). However, this instability will only play a significant role, if the spectral weight $\text{Im}\chi_{\text{RPA}}(q_0, 0)$ is non-negligible, which is only the case in the realm intraband excitations $-2qk_F < 2m_b\omega/\hbar - q^2 < 2qk_F$ (black dashed lines in figure). This translates to $0 < |q| < 2k_F$ for small ω.

We can therefore define a critical velocity (orange line in fig. 5.13) as the ratio between the first ME resonance frequency $\omega_{\text{ME}} = \omega_c$ and the maximum wavevector $q = 2k_F$ where the spectral weight is non-negligible:

$$v_c \approx \frac{\omega_c}{2k_F} \sim \frac{\omega_c \ell_B}{\sqrt{N}} \tag{5.25}$$

where we used $k_F \sim \sqrt{N}/\ell_B$ in the last step in order to emphasize the equivalence between the ME critical velocity and the Zener critical velocity from eq. 5.6. Indeed, an intrinsic breakdown due to the magnetoexciton instability occurs roughly at the same field that is predicted by the Zener/QUILLS theories. However, the collective nature of the ME instability also qualitatively explains the large experimentally observed Fano factors.

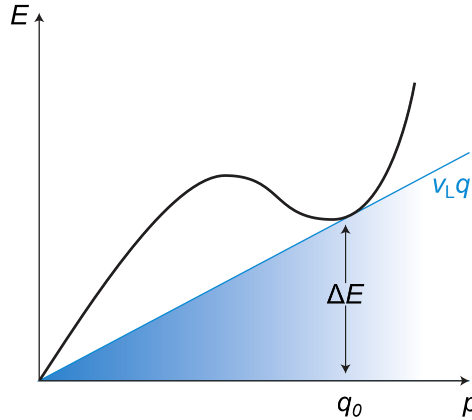

Figure 5.14 – Sketch of the roton dispersion in superfluid helium. Adapted from [298].

A very similar theory for the breakdown mechanism was brought forward by Martin *et al.* in 2003 [299]. Their work takes into account ionized impurities which locally enhance the flow velocity of the quantum Hall fluid until a critical velocity is reached, activating

[2] Note that in this calculation, we consider the scenario just before the breakdown, where, despite the out-of-equilibrium situation, the Fermi level remains stuck between the LLs N_F and $N_F + 1$, where N_F is the highest occupied LL at equilibrium. This enables us to perform the sum over all LLs leading to equations 5.22-5.24, see appendix 6.5.

the magnetoexciton instability. The authors also point out the equivalence between ME instability and QUILLS [260] as far as the critical field is concerned. This impurity-assisted magnetoexciton instability was proposed as an explanation for the experiment in ref. [279], where the QHBD occurred in a series of small, quantized voltage steps. In our clean sample, the breakdown behavior is abrupt, not step-like, indicating a uniform activation of the ME instability.

Furthermore, there is an interesting analogy between the proposed scenario of the QHBD due to a magnetoexciton instability and the breakdown of another macroscopic quantum state, namely the superfluidity of helium. It is limited by the spontaneous proliferation of rotons [300] when a critical flow velocity – called the Landau velocity v_L – is reached. Again, due to Galilean invariance, the roton dispersion of the moving fluid is simply tilted with respect to its dispersion at rest: $\omega(q) \to \omega(q) - vq$, where v denotes the flow velocity. The activation of the roton instability occurs, when the excitation gap ΔE of the minimum of this dispersion disappears: $\Delta E - v_L q_0 = 0$. This is sketched in figure 5.14 where the critical Landau velocity is drawn as a straight line $\omega(q) = v_L q$, touching the roton minimum.

5.6 Conclusion and perspectives

In this chapter, we have investigated the breakdown of the quantum Hall effect in a quasi-intrinsic, two-terminal, locally gated BLG-on-hBN device. The breakdown occurs at unprecedented electric fields $\sim 10^6$ V/m, current densities $\sim 10^3$ A/m and drift velocities $\sim 10^5$ m/s. We have discussed the scaling of the DC current and emphasized the excellent agreement of the onset of the breakdown between scaled DC transport measurements, noise measurements and the theoretical prediction for an intrinsic Zener breakdown. A similar scaling was demonstrated for the noise measurements and a short analysis for the low-bias noise due to contact heating was provided.

Finally, we have seen that the Fano factor of the noise-generating back-scattering current is super-Poissonian, indicating a collective breakdown mechanism. We have then discussed how a magnetoexciton instability could be a new candidate for this mechanism, with a critical velocity comparable to the Zener critical velocity. This implies an analogy with the spontaneous emission of rotons in superfluids moving faster than the critical Landau velocity. In conclusion, we have shed a new light on the old problem of the QHBD by combining an extremely clean and homogeneous sample with GHz shot noise measurements.

From a theoretical point of view, a more quantitative model is required, since the arguments brought forward in this chapter are mostly based on orders of magnitude. In particular, the dependence of the bunching (Fano factor) on the magnetic field should be analyzed theoretically and brought in agreement with the ME instability model.

Recommended future experiments obviously include the investigation of the breakdown in single layer graphene. However, this massless Dirac system does not obey Galilean invariance, which means that the change of reference $\omega_{ME}^{E\neq 0}(q) = \omega_{ME}^{E=0}(q) - v_d q$ is no longer possible. In SLG, a Lorentz boost is required to calculate the ME dispersion in the moving frame of reference. In a Lorentz transformation, energy is not conserved, which could lead to smaller breakdown fields. Figure 5.15 shows a comparison of the conventional 2DEG and SLG in terms of the RPA density-density response function. [301] The SLG susceptibility is dominated by the appearance of linear magnetoplasmons (diagonal lines). However, in order

to define a critical velocity, we need to use the lowest-energy collective excitations at large ($\sim 2k_F$) wave vectors, where the magnetoplasmons are far too high in energy, so that the breakdown should still be mediated by magnetoexcitons, not visible in fig. 5.15b.

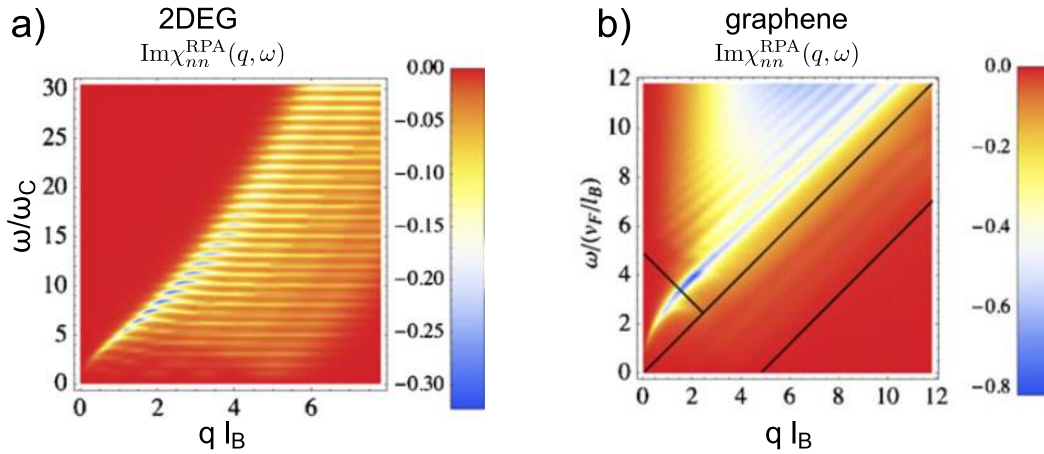

Figure 5.15 – a) Magnetoexciton dispersion in a standard 2DEG compared to b) the magnetoplasmon dispersion in single layer graphene. Figures from [301].

A natural next step would be to study the breakdown of the fractional quantum Hall effect, where inter-LL magnetoexcitons [110–112] are replaced by intra-LL magnetorotons [116]. Unlike magnetoexcitons which have transverse polarization, magnetorotons have a longitudinal one, bringing the analogy with superfluid breakdown even closer. Well-defined fractional quantum Hall states have recently been observed in hBN-encapsulated graphene samples with patterned graphite gates, both in gate-defined Hall bars [79] and in Corbino disks [80]. This was illustrated in fig. 1.10 of the introduction chapter. While the use of graphite gates was not an option for the corner reflectors in chapter 3 or for the plasma resonance capacitors in chapter 4, due to the incompatibility with GHz-operation, it is not excluded for GHz-frequency noise measurements, since the gate electrode is only driven with DC signals in these experiments. A systematic study of the breakdown as a function of the device width and length would also be instructive, e.g. to investigate if the inter-edge charging energy $e^2/\epsilon W$ is really linked to the Fano factor or to check if the critical breakdown current decreases with increasing sample length like in ref. [274]. The effective channel width could also be modulated electrostatically like in a quantum point contact [302].

This chapter has once again shown how the recent availability of extremely clean and highly tunable layer-by-layer assembled heterostructures based on 2D materials has provided a platform to study the intrinsic properties of two-dimensional electron systems. It has been shown that simple modifications in the stacking of these materials can lead to highly surprising phenomena, for example in twisted bilayer graphene, where superconductivity [12], the formation of a Mott-like insulator [13] or the emergence of a network of topological channels [52] have recently been demonstrated. These discoveries imply that our fundamental understanding of these systems is still limited and that the journey is far from being over.

6 Appendix

6.1 Fabrication recipes

In the following, I will provide step-by-step recipes (as seen in previous theses [22–24]) for the fabrication of corner reflectors and plasma resonance capacitors. These recipes should be seen as the "average" fabrication process, meaning that sometimes small deviations from the recipe were required, depending on the individual device. All electron beam lithography (EBL) steps were done on poly(methyl methacrylate) resist (PMMA) with 950k molecular weight. The different thickness values mentioned below were obtained by diluting the mother solution (6% in anisole from Microchem or Allresist). They are nominal values and might vary depending on the substrate and the age of the solution.

6.1.1 Corner reflector devices

Gate nano-patterning.

See also Quentin Wilmart's thesis [23]. He developed the process for tungsten etching.

step	description	tool(s)	parameters
1	substrate preparation	acetone, IPA, sonicator	5 min
2	substrate preparation	Harrick plasma cleaner	5 min O_2 plasma, $\lesssim 20\ \mu$bar, 200 W
3	tungsten or gold deposit	sputtering (at INSP) or Edwards E306A	20~30 nm; for gold: 1 nm Cr, $\sim 10^{-6}$ mbar, ~ 0.1 nm/s, 30 nm Au, $\sim 10^{-5}$ mbar, ~ 0.2 nm/s
4	substrate preparation	acetone, IPA, sonicator	5 min

step	description	tool(s)	parameters
5	spin coating	spin coater & PMMA 50 nm	4000 rpm, 4000 rpm/s, 30 s
6	annealing	heater plate	160°, 10 min
7	EBL 1: fine etch [CPW etch]	Raith e-Line	acceleration: 20 kV aperture: 7.5 [120] μm dose: 900 [300] $\mu C/cm^2$ step: 2 [100] nm
8	development	MIBK:IPA (1:3) & IPA	MIBK:IPA 30 s, IPA 30 s
9	RIE	Corial 200R	for tungsten: SF_6 25 sccm, 6 mTorr, 10 W, ~ 1min30 (laser EPD) for gold: Ar 40 sccm, 50 mTorr, 85 W ~ 2min30 (laser EPD) NB: chamber clean before sample loading and purge before etch is recommended
10	stripping	Corial 200R	O_2 100 sccm, 100 mTorr, 30 W, 10~20 s (laser EPD) NB: purge before etch is recommended
11	spin coating	spin coater & PMMA 50 nm	4000 rpm, 4000 rpm/s, 30 s
12	annealing	heater plate	160°, 10 min
13	EBL 2: rough etch	Raith e-Line	acceleration: 20 kV aperture: 10 μm dose: 240 $\mu C/cm^2$ step: 10 nm
14	development	MIBK:IPA (1:3) & IPA	MIBK:IPA 30 s, IPA 30 s
15	RIE	Corial 200R	c.f. step 9
16	stripping	Corial 200R	c.f. step 10
17	spin coating	spin coater & PMMA 550 nm	4000 rpm, 4000 rpm/s, 30 s
18	annealing	heater plate	160°, 10 min

step	description	tool(s)	parameters
19	EBL 3: CPW deposit	Raith e-Line	acceleration: 20 kV aperture: 120 μm dose: 280 $\mu C/cm^2$ step: 100 nm
20	development	MIBK:IPA (1:3) & IPA	MIBK:IPA 70 s, IPA 30 s
21	stripping	Corial 200R	O_2 100 sccm, 100 mTorr, 30 W, $\sim$ 10 s
22	CPW deposit	Edwards E306A	(Cr 2 nm, $\sim 10^{-6}$ mbar, $\sim$ 0.1 nm/s), Au 200 nm, $\sim 10^{-5}$ mbar, $\sim$ 0.4 nm/s
23	lift-off & rinse	acetone & IPA	acetone over night, IPA $\sim$ 1 min
24	short-circuit tests	Cascade probe station & Keithley source meter	ambient conditions

Stack transfer.

hBN-graphene-hBN stacks for the corner reflector devices were fabricated by Luca Banszerus according to ref. [120]. The procedure is described in section 2.1.3. Homogeneous zones were identified by Raman spectroscopy. These were then aligned with the gate electrodes and the stacks were deposited using a modified “Columbia” method, also described in section 2.1.3.

Stack etching and edge contact.

step	description	tool(s)	parameters
1	spin coating	spin coater & PMMA 150 nm	4000 rpm, 4000 rpm/s, 30 s
2	annealing	heater plate	160°, 10 min
3	EBL 4: etch fine [rough]	Raith e-Line	acceleration: 20 kV aperture: 10 [120] μm dose: 280 $\mu C/cm^2$ step: 10 [100] nm
4	development	MIBK:IPA (1:3) & IPA	MIBK:IPA 70 s, IPA 30 s
5	RIE	Corial 200R	CHF_3 40 sccm, O_2 4 sccm, 60 mTorr, 60 W, 1-2 min
6	cleaning	acetone & IPA	

step	description	tool(s)	parameters
7	spin coating	spin coater & PMMA 300 nm	4000 rpm, 4000 rpm/s, 30 s
8	annealing	heater plate	160°, 10 min
9	EBL 5: edge contact	Raith e-Line	acceleration: 20 kV aperture: 10 μm dose: 300 μC/cm^2 step: 10 nm
10	stripping	RIE Corial 200R	O_2 100 sccm, 100 mTorr, 30 W, 1~2 s
11	evaporation	Edwards E306A	Cr 5 nm, $\sim$ 0.1 nm/s, $\sim 10^{-6}$ mbar, Au 100 nm, $\sim$ 0.3 nm/s, $\sim 10^{-5}$ mbar
12	lift-off & rinse	acetone & IPA	acetone over night, IPA $\sim$ 1 min

6.1.2 Plasma resonance capacitor devices

Preparation of PDMS for top-hBN exfoliation.

Polydimethylsiloxane (Sylgard 184) was prepared in a disposable plastic beaker by mixing 3 g of the curing agent with 30 g of the elastomer. The mix was poured in a ⌀9 cm Petri dish, which was then placed in a desiccator for about 24 hours, in order solidify and to remove bubbles. The PDMS was cut in quarters. A couple of hBN crystals (from NIMS, Japan) were placed between two of these wedges and exfoliated by repeatedly pressing the PDMS wedges together in various orientations.

Preparation of the substrate for bottom-hBN/graphene exfoliation.

The substrate was high-resistivity silicon (> 3000 Ωcm) with a 280 nm SiO_2-layer. Markers (numbered crosses) were fabricated using UV-lithography. Note that the exposure times mentioned below obviously vary with lamp intensity.

step	description	tool(s)	parameters
1	substrate preparation	acetone, IPA, sonicator	5 min
2	substrate preparation	Harrick plasma cleaner	5 min O_2 plasma, $\lesssim 20$ μbar, 200 W
3	spin coating	spin coater & AZ5214E	4000 rpm, 4000 rpm/s, 30 s
4	annealing	heater plate	125°C for 2 min

step	description	tool(s)	parameters
5	UV lithography (alignment crosses)	SUSS MicroTec MJB4	2 s exposure (hard contact 5 s)
6	annealing (image reversal)	heater plate	125°C for 2 min
7	UV flood exposure	SUSS MicroTec MJB4	20 s
8	developing	AZ726MIF & H_2O	35 s MIF, 30 s H_2O
9	stripping	RIE Corial 200R	O_2 100 sccm, 100 mTorr, 30 W, 10∼20 s
10	evaporation	Edwards E306A	Cr 5 nm, ~ 0.1 nm/s, $\sim 10^{-6}$ mbar, Au 50 nm, ~ 0.3 nm/s, $\sim 10^{-5}$ mbar
11	lift-off & rinse	acetone	acetone over night, IPA ~ 1 min
12	cleaning (if required again)	c.f. steps 1-2	

Preparation of the polymer stamps.

The "Aachen type" stamps are prepared on standard glass microscope slides (cut in half).

step	description	tool(s)	parameters
1	cover the slide with scotch tape	Duck HD Clear Tape	
2	spread PVA film	poly vinyl alcohol 13% (in H_2O), pipette	
3	anneal	heater plate	90°C, ~ 10 min
4	spin coat	spin coater & PMMA (50k, 4% in ethyl lactate)	1000 rpm, 30 s
5	anneal	heater plate	110°C, ~ 10 min

Assembly of the stack.

hBN-graphene-hBN stacks were assembled using the "Aachen" method described in section 2.1.3, using either CVD or exfoliated graphene. The exfoliation of graphene and bottom hBN was done on Si/SiO_2 substrates with alignment crosses (see above and section 2.1.1).

Top-hBN was transferred directly to the polymer stamps by pressing them on the PDMS wedges. A suitable flake was identified under the optical microscope, then it was used to pick up the graphene and finally everything was deposited on the bottom hBN.

PRC nano-fabrication.

step	description	tool(s)	parameters
1	Raman	Renishaw inVia	100x objective, 532 nm, power 5%, resolution ~ 1 μm, exposure 1 s
2	AFM	Bruker Dimension Edge	tapping mode
3	spin coating	spin coater & PMMA 300 nm	4000 rpm, 4000 rpm/s, 30 s
4	annealing	heater plate	160°, 10 min
5	EBL 1a (fine alignment markers)	Raith e-Line	acceleration: 20 kV aperture: 10 μm dose: 280 $\mu C/cm^2$ step: 2 nm
6	development	MIBK:IPA (1:3) & IPA	MIBK:IPA 70 s, IPA 30 s
7	EBL 1b (define encapsulated graphene shape)	Raith e-Line	acceleration: 20 kV aperture: 10 μm dose: 280 $\mu C/cm^2$ step: 2 nm
8	Al hard mask deposit	Edwards E306A	Al 50 nm, $\sim 10^{-5}$ mbar, ~ 0.5 nm/s
9	lift-off	acetone & IPA	acetone over night, IPA 3 min
10	RIE	Corial 200R	CHF_3 40 sccm, O_2 4 sccm, 60 mTorr, 60 W, 2-3 min
11	hard mask removal	KOH & H_2O	2 KOH tabs (≈ 0.22 g) + 30 ml H_2O, 1min30, rinse in H_2O
12	spin coating	spin coater & PMMA 550 nm	4000 rpm, 4000 rpm/s, 30 s
13	annealing	heater plate	160°, 10 min
14	EBL 2 (source contact)	Raith e-Line	acceleration: 20 kV aperture: 60 μm dose: 300 $\mu C/cm^2$ step: 8 nm

step	description	tool(s)	parameters
15	development	MIBK:IPA (1:3) & IPA	MIBK:IPA 70 s, IPA 30 s
16	stripping	Corial 200R	O_2 100 sccm, 100 mTorr, 30 W, 2 s
17	source contact deposit	Edwards E306A	Cr 5 nm, $\sim 10^{-6}$ mbar, $\sim$ 0.1 nm/s, Au 200 nm, $\sim 10^{-5}$ mbar, $\sim$ 0.3 nm/s
18	lift-off	acetone & IPA	acetone over night, rinse in IPA
19	Raman (optional)	Renishaw inVia	s.a.
20	AlOx passivation layer deposit	Edwards E306A & Anric AT400 ALD	2 nm of Al in Edwards evaporator with 15 min intermediate O_2 exposure (200 mbar) after each nanometer, ALD 300 mTorr, 100 cycles, 175°C
21	spin coating	spin coater & PMMA 550 nm	4000 rpm, 4000 rpm/s, 30 s
22	annealing	heater plate	160°C, 10 min
23	EBL 3 (oxide layer etching)	Raith e-Line	acceleration: 20 kV aperture: 120 μm dose: 300 μC/cm^2 step: 80 nm
24	development	MIBK:IPA (1:3) & IPA	MIBK:IPA 70 s, IPA 30 s
25	oxide removal	KOH & H_2O	2 KOH tabs ($\approx$ 0.22 g) + 30 ml H_2O, 5 $\sim$ 10 min, rinse in H_2O
26	spin coating	spin coater & PMMA 550 nm	4000 rpm, 4000 rpm/s, 30 s
27	annealing	heater plate	160°, 10 min
28	EBL 4 (coplanar waveguide)	Raith e-Line	acceleration: 20 kV aperture: 60 μm dose: 300 μC/cm^2 step: 10 nm
29	development	MIBK:IPA (1:3) & IPA	MIBK:IPA 70 s, IPA 30 s
30	CPW deposit	Edwards E306A	Cr 5 nm, $\sim 10^{-6}$ mbar, $\sim$ 0.1 nm/s, Au 200 nm, $\sim 10^{-5}$ mbar, $\sim$ 0.3 nm/s

step	description	tool(s)	parameters
31	lift-off	acetone & IPA	acetone over night, rinse in IPA

6.2 Derivation of PRC formulas

The plasma resonance capacitor can be modeled as a two-port network incorporating a transmission line (TL), which is depicted in figure 6.1:

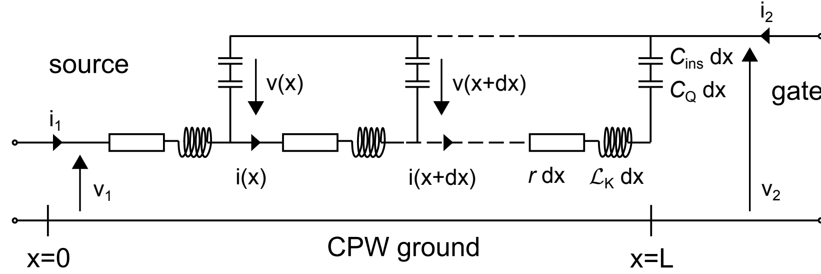

Figure 6.1 – The PRC transmission line model.

Note that in this simplified model, the capacitive coupling to the ground plane of the coplanar waveguide (CPW) is neglected, i.e. we are dealing with an already de-embedded model. We are also neglecting the resistivity of the "gate" metal with respect to that of the graphene sheet. In this distributed element model, the resistance r, the inductance $\mathcal{L}_K$ and the capacitances C_Q and C_{ins} are defined per unit length.

Let us first note some basic properties regarding the admittance of this device. By current conservation, we can state that $i_1 = -i_2$. Since we are neglecting the coupling to the CPW ground plane, we can arbitrarily define *one* of the two terminal potentials, v_1 or v_2. Only the difference $v_1 - v_2 = v_{12}$ matters. $v_{12} = v_1$ if $v_2 = 0$ and $v_{12} = -v_2$ if $v_1 = 0$, so:

$$v_1|_{v_2=0} = -v_2|_{v_1=0} \tag{6.1}$$

The Y parameters are defined as follows:

$$Y_{11} = \left.\frac{i_1}{v_1}\right|_{v_2=0} \qquad Y_{12} = \left.\frac{i_1}{v_2}\right|_{v_1=0}$$

$$Y_{21} = \left.\frac{i_2}{v_1}\right|_{v_2=0} \qquad Y_{22} = \left.\frac{i_2}{v_2}\right|_{v_1=0}$$

With this definition and the above symmetry relations for i and v in mind, we can easily relate the Y parameters to each other in the following way:

$$Y_{11} = Y_{22} = -Y_{12} = -Y_{21} \tag{6.2}$$

Let us now proceed to the calculation of this admittance for the above TL model. By applying Kirchhoff's voltage law between two unit cells of the TL, we easily find:

$$v(x) - v(x + dx) = (r + j\omega\mathcal{L}_K)\ i(x)\ dx \tag{6.3}$$

If we now apply Kirchhoff's current law at one of the nodes, we find:

$$i(x) - i(x + dx) = j\omega C\ v(x)\ dx \tag{6.4}$$

where $C = C_Q C_{\text{ins}}/(C_Q + C_{\text{ins}})$We can rewrite these two equations in the differential form:

$$\frac{dv(x)}{dx} = -(r + j\omega\mathcal{L}_K)\ i(x) \qquad \frac{di(x)}{dx} = -j\omega C\ v(x) \tag{6.5}$$

Combining the two equations yields the following second order differential equation:

$$\frac{d^2v(x)}{dx^2} = j\omega C\ (r + j\omega\mathcal{L}_K)\ v(x) \tag{6.6}$$

The general solution for this equation is:

$$v(x) = A\ \exp(\gamma\ x) + B\ \exp(-\gamma\ x) \tag{6.7}$$

where $\gamma = \sqrt{j\omega C\ (r + j\omega\mathcal{L}_K)}$ is the propagation constant of the left/right-going wave. Thus, we obtain for the current:

$$i(x) = -\frac{\gamma\ A}{r + j\omega\mathcal{L}_K}\ \exp(\gamma\ x) + \frac{\gamma\ B}{r + j\omega\mathcal{L}_K}\ \exp(-\gamma\ x) \tag{6.8}$$

Since we are dealing with a capacitor and the current has to be zero after the right-most unit cell of figure 6.1 ($i(x = L) = 0$)[1], we can use this boundary condition to find the relation between the pre-factors A and B.

$$i(L) = -\frac{\gamma\ A}{r + j\omega\mathcal{L}_K}\ \exp(\gamma\ L) + \frac{\gamma\ B}{r + j\omega\mathcal{L}_K}\ \exp(-\gamma\ L) = 0 \tag{6.9}$$

It is clear that $A = D\exp(-\gamma\ L)$ and $B = D\exp(\gamma\ L)$ solves this equation, which yields:

$$v(x) = 2\ D\ \cosh(\gamma\ (x - L)) \tag{6.10}$$

$$i(x) = -\frac{2\ \gamma\ D}{r + j\omega\mathcal{L}_K}\ \sinh(\gamma\ (x - L)) \tag{6.11}$$

If we want to express this in terms of the voltage applied at the source $v_0 = v(0)$, we find:

$$v(x) = v_0\ \frac{2\ D\ \cosh(\gamma\ (x - L))}{2\ D\ \cosh(\gamma\ (0 - L))} \tag{6.12}$$

$$= v_0\ \frac{\cosh(\gamma\ (x - L))}{\cosh(\gamma L)} \tag{6.13}$$

We can now calculate the admittance, e.g. Y_{11}:

$$Y_{11} = \left.\frac{i_1}{v_1}\right|_{v_2=0} = \frac{i(x = 0)}{v(x = 0)} = \frac{-\gamma \sinh(-\gamma L))}{(r + j\omega\mathcal{L}_K)\cosh(-\gamma L))} \tag{6.14}$$

$$= \frac{\gamma}{(r + j\omega\mathcal{L}_K)}\tanh(\gamma L) \tag{6.15}$$

An important difference between this *capacitor* TL model and a "textbook" version of the TL model is that only one end of the capacitor TL is connected to a port, the other port is actually connected to the conventional "ground" (i.e. in this capacitor model, v_2 is *not* the voltage across the last capacitors; $v_2 \neq v(x = L)$ in general!).

[1]The current i(x=L) is not the current going up to the last capacitor in the drawing (that would be i(x=L-dx)), it is the current going "out of the picture" (which is why it has to be zero).

6.3 Modifying the corner reflector scattering model

The simple formula for the corner reflector transmission derived in section 3.3.1 assumes that any scattering event inside the prism will automatically lead to a transmission of the fermion to the drain side. While the analytical model cannot accommodate more complex scattering models – like a uniform randomization of the direction of propagation – it is easy to implement such random scattering in a ray tracing simulation.

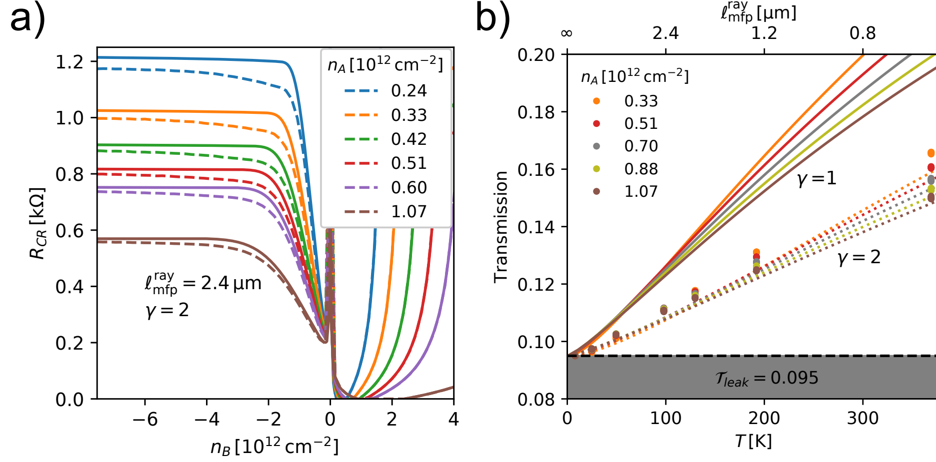

Figure 6.2 – **Uniform scattering.** a) CR resistance from ray tracing simulation (dashed lines) and analytical model (solid lines) with a scaled mean free path $\ell_{\mathrm{mfp}}^{\mathrm{analyt.}} = \gamma \ell_{\mathrm{mfp}}^{\mathrm{ray}}$. b) CR transmission vs. mean free path and temperature from a ray tracing simulation (dots). Solid (dotted) lines are from the analytical model with unscaled (scaled) mean free path.

In order to compare the results of ray tracing and analytical calculations, it is important to keep in mind the "recurrent" nature of the trajectories in the TIR-regime, and the fact that all round-trip trajectories approximately have the same length $\ell_1 = 0.6\ \mu$m. For mean free paths ℓ_{mfp} between multiple integers of ℓ_1, the results of the ray tracing simulations do not change. At the same time it should be avoided to choose ℓ_{mfp} as an exact integer multiple of ℓ_1, since this can lead to numerical "accidents". For good comparability, one should choose $\ell_{\mathrm{mfp}} = N\ell_1 + \epsilon$, where $N \in \mathbb{Z}_0^+$ and $\epsilon \ll \ell_1$. For example, for the ray tracing simulation in fig. 3.11b, $N = 4$ and $\epsilon = 50$ nm, so that $\ell_{\mathrm{mfp}} = 2.45\ \mu$m.

Repeating the ray tracing simulations from fig. 3.11 with a uniform random scattering model produces the results shown in figure 6.2. In panel (a), we compare the results of the ray tracing (dashed lines) to the results of the analytical formula (solid lines) and observe a good agreement if we choose a renormalization prefactor $\gamma = 2$ for the acoustic phonon (AP) mean free path used in the analytical model $\ell_{\mathrm{mfp}}^{\mathrm{analyt.}} = \gamma \ell_{\mathrm{mfp}}^{\mathrm{ray}}$. Similarly, the dots in panel (b) represent results from the ray tracing simulation and are in good agreement with the analytical model with $\gamma = 2$ (dotted lines), whereas the solid lines correspond to $\gamma = 1$. This means that – unsurprisingly – uniform scattering leads to a reduction of the residual transmission by 50% compared to the hypothesis used in section 3.3.1. Without more information on the actual distribution of scattering, we conclude that we cannot use our CR device as a precise *meter* for the AP mean free path, but it nevertheless stays a very sensitive AP *detector*.

6.4 Literature review of graphene plasmonics

From an experimental point of view, plasmons can be probed using a whole range of techniques, e.g. angle resolved photoemission spectroscopy (ARPES), inelastic light scattering, scanning tunneling spectroscopy (STS) or electron energy loss spectroscopy (EELS) [87].

Studying the interaction of plasmons with electromagnetic waves is particularly interesting for applications (e.g. resonant photodetectors) and will be discussed extensively in the following. However, optical measurements are restricted to a small energy range and suffer from the large momentum mismatch between the free-space wave and the confined plasmon.

Due to the extremely low scattering rates $1/\tau$ in high-quality encapsulated graphene at cryogenic temperatures [119], graphene plasmons can be probed down to very low frequencies. In this section, I will omit the GHz-frequency studies, and refer to chapter 4, where these are discussed in detail.

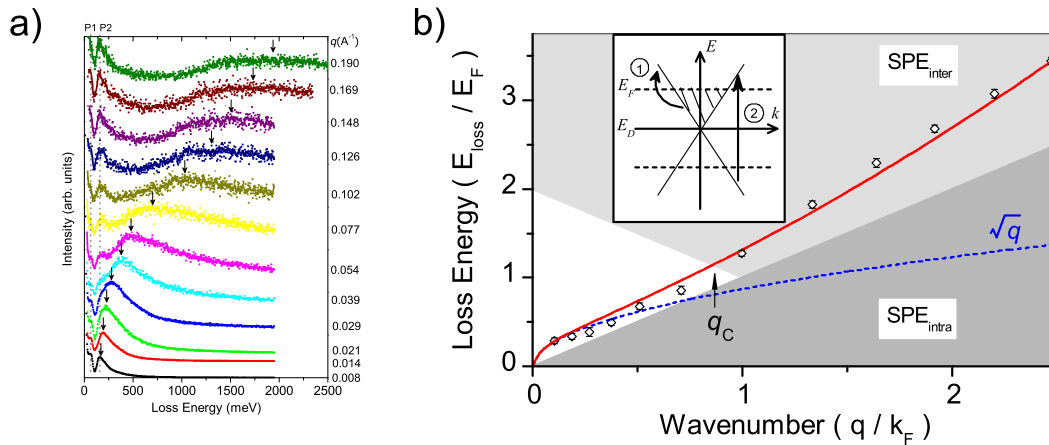

Figure 6.3 – **Electron energy loss spectroscopy.** a) HREELS spectra of graphene on SiC(0001). The 2D-plasmon loss peak disperses with increasing momentum transfer q. b) Comparison of the experimental results with the theoretical $\sqrt{q}$-dispersion. The red line corresponds to a fit taking into account non-local effects. Figure adapted from ref. [101].

High-resolution reflection electron-energy-loss spectroscopy (HREELS) has been used early on to probe graphene plasmons over a large range of energies and wavevectors [101, 228–230]. With this technique, the plasmon can be identified as a peak in the EELS spectrum (see figure 6.3a). Since these studies were carried out in epitaxial graphene grown on a silicon carbide substrate, the plasmon hybridizes with the surface phonon modes of the substrate. Still, as shown in figure 6.3b, the long-wavelength $\sqrt{q}$-behavior is confirmed qualitatively and the overall energy range of the study reaches from this long wavelength limit to far beyond the interband threshold (unlike the optical studies discussed in the following). In ARPES [231] and STS [232] measurements, the plasmon might have been detected indirectly as a many-body correction to the spectral function.

In order to excite/probe plasmons with light, wavevector-matching techniques are required. This can be achieved using prism coupling, grating coupling, highly focused optical beams or near-field excitation [84]. The works mentioned in the following are also summarized at the end of this section in table 6.1, which provides some insights in the experimental conditions (frequency and temperature range) and the sample type (encapsulated or not,

gated or not). The table highlights that most studies were carried out in the THz/infrared range and under ambient conditions.

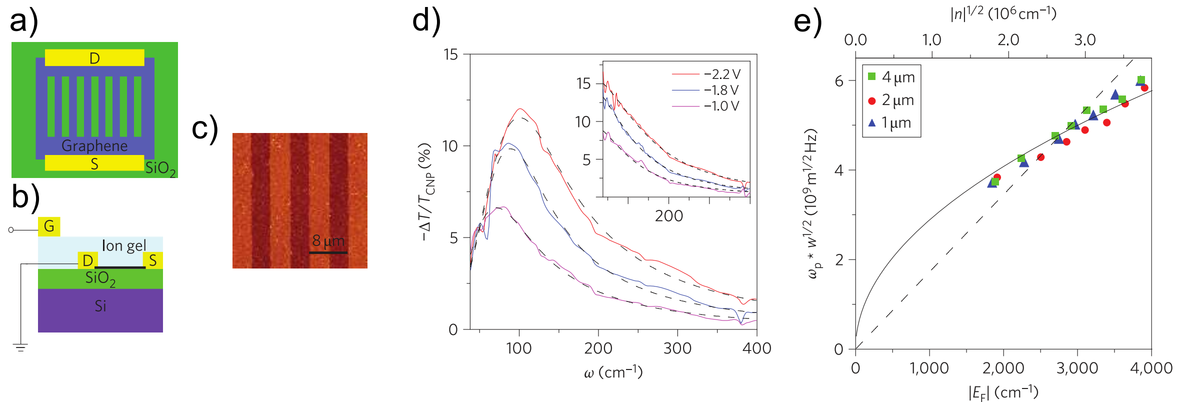

Figure 6.4 – **Grating coupling.** a) and b) top and side view of a graphene micro-ribbon device, gated with an ion gel. c) AFM image of the micro-ribbon array. d) Infrared absorption spectra of the device for different gate voltages. Incident field is polarized perpendicular to the ribbons. Inset: No absorption peaks are observed for parallel polarization. e) Comparison of the absorption peaks for different doping values and grating periodicities, scaled by $1/\sqrt{w}$, where w is the width of the ribbons. The resonance frequency scales with $n^{1/4}$, as expected for graphene. Figure adapted from ref. [102].

The grating coupling method was used by Ju *et al.* in 2011 [102]: A CVD graphene sample was patterned into micro-ribbon arrays of different periodicities ($2-8$ μm, see fig. 6.4a-c). The infrared absorption of the sample was measured using Fourier transform infrared spectroscopy (FTIR) and a plasmon-induced absorption peak (fig. 6.4d) was observed when the incident light was polarized perpendicular to the ribbons. Modulating the charge carrier density using an ion gel gate, a good agreement with the expected $n^{1/4}$-dependence of the plasmon frequency was obtained (fig. 6.4e).

The same experimental technique (FTIR & nano-ribbon array) was combined with a strong magnetic field in 2013 by Poumirol *et al.* [233] In quantizing fields, FTIR-spectroscopy can detect transitions between Landau-levels (see also sections 1.4 and 1.7), but the hybridization of these transitions with the plasmon resonance leads to a shift. By measuring this shift, the plasmon can be detected indirectly.

The near-field coupling method was used by Fei *et al.* [103, 303] and by Chen *et al.* [104] in 2011-2012. Here, the wavevector mismatch was overcome by employing scattering-type scanning near-field optical microscopy (sSNOM) at frequencies ~ 30 THz. In refs. [103, 104], plasmons were launched into tapered graphene ribbons by illuminating a metallized AFM tip close to the graphene surface with infrared light (see fig. 6.5a). The plasmons are reflected by the sample edges, which leads to interference between the incident and the reflected plasmons, so that position-dependent maxima and minima can be detected in the infrared light that is coupled back out of the graphene sample. This way, localized modes could be detected in the tapered ribbons (see fig. 6.5b) and their gate voltage (doping) dependence could be mapped out in accordance with theoretical predictions (panel c).

The same method was later used to study plasmons in hBN-encapsulated graphene samples, where – unsurprisingly – plasmon propagation is enhanced with respect to the exper-

iments on silicon dioxide, since the electronic scattering rates are reduced thanks to the clean, flat and almost lattice-matched substrate [234]. At the same time, the slight lattice mismatch between graphene and hBN can lead to moiré patterns that affect the plasmon dispersion [235].

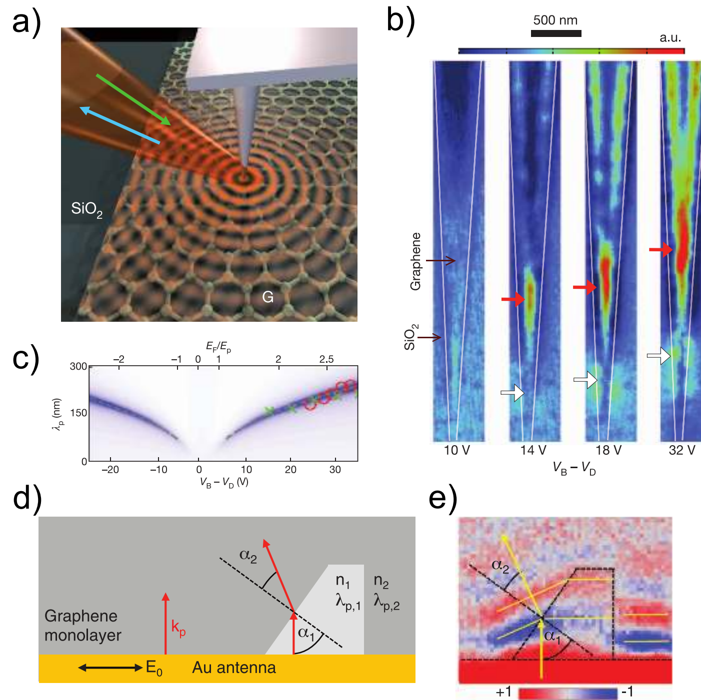

Figure 6.5 – **Near-field coupling.** a) Illustration of the sSNOM experimental setup. A metallized AFM tip close to the graphene surface acts as antenna to couple the incident (green arrow) infrared light to the graphene surface plasmons, which are subsequently reflected from the sample edges. The resulting electric field is encoded in the back-scattered infrared amplitude (blue arrow). Figure from ref. [103]. b) Near-field amplitude images of a tapered graphene ribbon revealing localized modes whose position depends on the applied gate voltage. c) Wavelength of these localized modes (red circles correspond to red arrows in previous panel, green crosses correspond to additional dataset) plotted as a function of gate voltage and Fermi energy, in good agreement with calculated plasmon dispersion. Panels b and c from ref. [104]. d) Sketch of a patterned gold antenna on top of a single layer graphene device with a trapezoidal bilayer region (light gray). At the tilted interface between SLG and BLG one expects plasmon refraction due to the different dispersion in the two regions. d) Near-field image of the sample. Panels d and e from ref. [236].

In these near-field studies, plasmons cannot only be launched from the tip of the imaging apparatus, but also from impurities that can be patterned on top of the graphene sample, see e.g. refs. [236, 237] and figure 6.5d.

The beauty of these imaging techniques lies in the possibility to map out the plasmon propagation in real space, which on one hand gives direct access to the attenuation of the plasmon and on the other hand can reveal interesting propagation phenomena, like the "bending" of the trajectory at a SLG-BLG interface: Since the wavevector component parallel

to the interface has to be conserved, the difference in phase velocities leads to a refraction effect, similarly to what happens at graphene p-n junctions in chapter 3. The experimental observation of this is illustrated in the near-field image in fig. 6.5e [236].

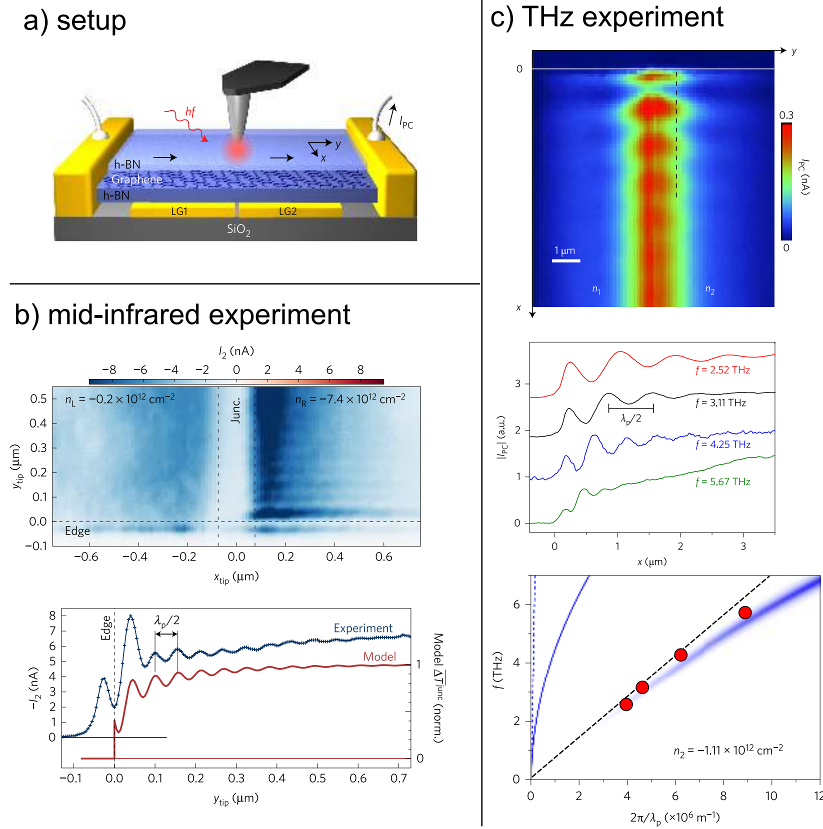

Figure 6.6 – **Photocurrent nanoscopy.** a) The experimental setup in the studies refs. [109, 238] consists of an encapsulated graphene device with two local gate electrodes that induce a p-n junction. An AFM tip is used to couple the incident infrared/THz light to the graphene plasmons. b) Top: The infrared photocurrent map reveals plasmon interferences in the vicinity of the sample edges. Bottom: A vertical average from the data shown in the top panel over the interval 0.2 μm $< x <$ 0.4 μm. c) Top and middle: Equivalent to b, but with data recorded at four different THz frequencies. Bottom: The dispersion of the detected plasmons follows the calculated dispersion for screened plasmons (blue color plot), simplified by the linear approximation (black dashed line) similar to eq. 1.63. The light cone is represented by the dashed blue line and the solid blue line corresponds to the unscreened plasmon dispersion. Figures adapted from refs. [109, 238].

Whereas in the aforementioned works plasmons were detected by measuring the reflected infrared light, it is possible to combine the near-field scanning technique with an electrical readout [105], i.e. measuring the photocurrent. The photothermoelectric detection mechanism is due to variations of the local Seebeck coefficient, which can be maximized by inducing a p-n junction using local gate electrodes (see fig. 6.6a). In 2017, Alonso-González *et al.* [109] and Lundeberg *et al.* [238] have used this technique to create photocurrent images of standing graphene plasmons at $\sim$ 3 THz and $\sim$ 30 THz, respectively. In both studies, interference

patterns near the graphene edges enable to measure the plasmon wavelength, see top and middle panels of fig. 6.6b and c. By performing this experiment at different frequencies, one can map out the dispersion, see bottom of fig. 6.6c. The linear dispersion observed in ref. [109] is in strong contrast with the theoretical prediction for unscreened plasmons and can be explained by the screening effect of the gate electrodes, which slows down the plasmons significantly.

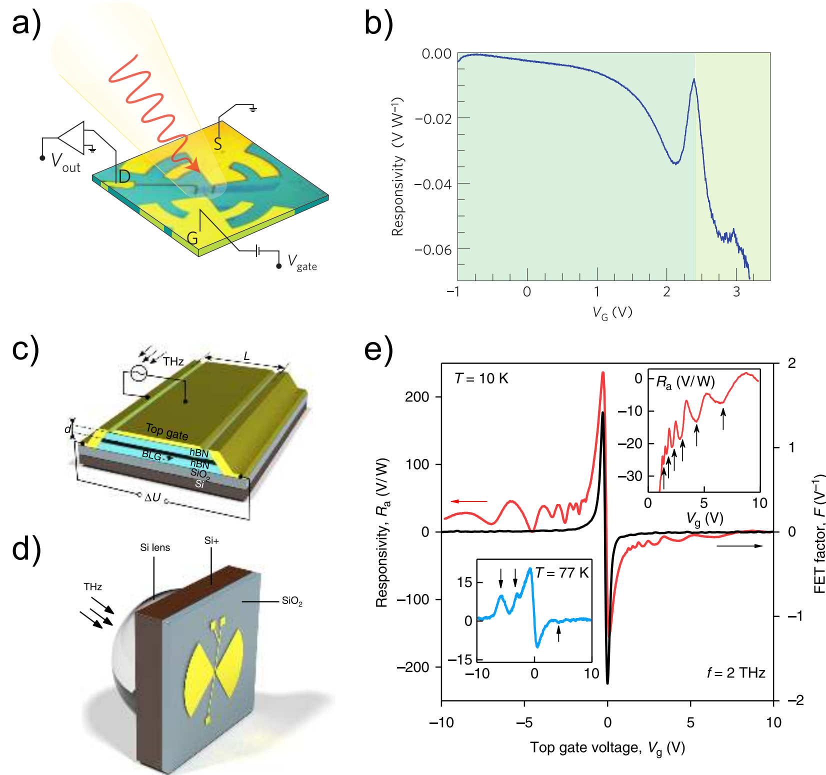

Figure 6.7 – **Photodetectors.** a) Sketch of a graphene-on-SiO_2 device embedded in a log-periodic antenna. b) Its responsivity as a function of gate voltage. Panels a-b from ref. [239] c) Sketch of an encapsulated graphene sample embedded in a d) bow-tie antenna. e) Its responsivity as a function of gate voltage at $T = 10$ K (red line) and at $T = 77$ K (blue line). The upper inset is a zoom on the responsivity for positive gate voltages. The oscillations in the responsivity correspond to plasma resonances in the FET channel. Panels c-e from ref. [106].

Since these imaging techniques provide rather precise information about both the wavelength and the damping of the plasmons, they have culminated in fundamental studies investigating quantum non-local corrections to the plasmon dispersion in the THz range [304] and the intrinsic damping limits of graphene plasmons due to “dielectric [losses], acoustic-phonon scattering and intervalley scattering” [237].

The combination of graphene plasmonics with electronic transport is highly interesting, since it paves the way for the design of novel emitters and detectors in the elusive THz range. An emblematic device for this purpose is the plasma resonance transistor (PRT). Its working principle is based on Dyakonov and Shur’s theory from the early 1990s, which states that

ballistic DC currents in field effect transistors (FETs) may be unstable and lead to plasma oscillations and consequently to the emission of THz radiation [221]. This phenomenon can also be described as an electronic equivalent of the acoustic flute [305]. Dyakonov and Shur further predict that by creating asymmetric boundary conditions, i.e. by applying a bias to a FET, an incident THz field can be rectified and detected as a DC voltage offset [306]. Both in the emission- and in the detection-case, resonances are supposed to occur at frequencies corresponding to the modes of the "plasmonic cavity" formed by the ballistic FET channel.

The emission of THz radiation from such a FET (more specifically, an InGaAs high electron mobility transistor) was demonstrated by Knap *et al.* in 2004 [307]. In GaAS/AlGaAs 2DEGs, a weak resonant detection effect at $f = 600$ GHz was demonstrated at cryogenic temperature (8 K) in 2002 [308] and – in the same type of device – at room temperature in 2005 [309]. A review on this type of THz detection can be found in ref. [310]

In graphene, non-resonant THz detection was achieved at room temperature with an exfoliated graphene sample on an SiO_2 substrate in 2012 [239]. Figure 6.7a and b show a sketch of the device and its responsivity as a function of gate voltage. Due to the relatively low electronic mobility in this kind of device and the room-temperature operation, plasma oscillations were heavily damped, which is why no resonance could be observed. Thanks to the improvements of sample quality (van der Waals stacking) and the strongly enhanced mobilities and mean free paths, resonant detection of THz radiation could be demonstrated in a similar (but hBN-encapsulated) device structure in 2018 [106], see fig. 6.7c and d. At cryogenic temperatures, plasma resonances were observed in the responsivity for various gate voltages, see fig. 6.7e.

This summary of infrared and THz graphene plasmonics clearly shows an evolution from pure optical characterization in 2011 towards device implementation with actual application perspectives in 2018. The interference patterns in figure 6.6 nicely illustrate the order of magnitude of the plasmon wavelength in all these studies: Whereas the mid-infrared experiment ($f \sim 30$ THz) detects plasmons with a wavelength on the order of 100 nm, the THz experiment ($f \sim 3$ THz) yields wavelengths of ~ 1 μm. Extrapolating this tendency linearly to $f \sim 30$ GHz, the frequency range addressed in this work, yields a wavelength on the order of 100 μm. In chapter 4, we investigate resonances of these "ultra-long" wavelength plasmons in hBN-encapsulated graphene devices.

year [ref.]	technique	f	T [K]	enc.	gate
2011 [102]	microribbon array & FTIR	1.2-12 THz	300	no	yes
2012 [239]	*non-resonant* photodetector & THz source	0.3 THz	300	no	yes
2012 [303]	sSNOM	27-38 THz	300	no	yes
2012 [104]	sSNOM	27-33 THz	300	no	yes
2012 [103]	sSNOM	27 THz	300	no	yes
2012 [311]	disk arrays & FTIR	1.2-10 THz	300	no	yes
2013 [89]	microribbon array & FTIR	20-90 THz	300	no	no
2013 [233]	microribbon array, FTIR & B-field	6-21 THz	4.2	no	no
2013 [312]	sSNOM	30-32 THz	300	no	no
2013 [313]	sSNOM	26-31 THz	300	no	no
2013 [252]	time-of-flight in QH states	-	1.5	no	yes
2014 [85]	nanoresonators & FTIR	20-80 THz	300	no	no
2014 [254]	time-of-flight	-	1.5	no	yes
2014 [253]	resonant GHz spectroscopy & time-of-flight in QH states	0-65 GHz	4-80	no	no
2014 [314]	near-field interferometry	28 THz	300	no	no
2014 [226]	*non-resonant* GHz spectroscopy	10-50 GHz	30, 300	yes	yes
2014 [236]	sSNOM & metal antenna on graphene	26-29 THz	300	no	no
2015 [235]	sSNOM	27 THz	300	no	no
2015 [234]	sSNOM	28 THz	300	yes	yes
2016 [105]	"near-field IR nanoscopy with electrical read-out"	28 THz	300	yes	yes
2017 [109]	"nanoscale-resolved THz photocurrent near-field microscopy"	2.5-5.7 THz	300	yes	yes
2017 [238]	sSNOM & transport (p-n junction)	28 THz	300	yes	yes
2017 [304]	s.a.	3.1 THz	300	yes	yes
2017 [315]	s.a.	28 THz	300	yes	yes
2018 [237]	sSNOM & metal launchers	27 THz	60-300	yes	yes
2018 [106]	resonant photodetector & THz source	0.13-2 THz	10, 77, 300	yes	yes
2018 [27]	*resonant* GHz spectroscopy	0-40 GHz	10-300	yes	yes

Table 6.1 – **Graphene plasmonics bibliography.** The column "enc." indicates whether samples were hBN-encapsulated and the column "gate" indicates if a gate electrode was used to modulate the carrier density.

6.5 More on magnetoexcitons

In this section, we will derive the Lindhard function for a massive 2DEG in the integer quantum Hall regime. This is given as an exercise in chapter 10 of Giuliani & Vignale's book [32]. The following calculation roughly corresponds to the one provided in the appendix of ref. [20]. At the end of the section, we will investigate the influence of a uniform electric field on the quantum Hall Hamiltonian, its eigenstates and the Lindhard function. As pointed out in refs. [32, 74], the electric field does not significantly change the eigenfunctions, except for a shift in their center position and a tilt of the associated energy levels.

6.5.1 Matrix element of the density operator

In the following, we will use the eigenfunctions $|n, k_y\rangle$ (see eq. 1.42) of the quantum Hall Hamiltonian (see eq. 1.40) in the Landau gauge. Here we use the notation n instead of N for numbering the eigenstates χ_{n,k_y} of the quantum harmonic oscillator. We want to calculate the matrix element $F_{nn'}^{k_y k_y'}(\mathbf{q}) = \langle n, k_y | e^{-i\mathbf{q}\cdot\mathbf{r}} | n', k_y' \rangle$:

$$F_{nn'}^{k_y k_y'}(\mathbf{q}) = \int dx\; dy\; e^{-iq_x x} e^{-iq_y y} \psi_n^*(x,y)\psi_{n'}(x,y) \tag{6.16}$$

$$= \frac{1}{L_y} \int dy\; e^{-iq_y y} e^{-ik_y y} e^{ik_y' y} \int dx\; e^{-iq_x x} \chi_{n,k_y}^*(x)\chi_{n',k_y'}(x) \tag{6.17}$$

$$= \delta_{k_y'-k_y,q_y} \int dx\; e^{-iq_x x} \chi_{n,k_y}^*(x)\chi_{n',k_y'}(x) \tag{6.18}$$

where $\delta_{k_y'-k_y,q_y}$ denotes the Kronecker delta, meaning that the matrix element is only non-zero if $q_y = k_y' - k_y$. Here the states χ_{n,k_y} and $\chi_{n',k_y'}$ are both eigenstates of the quantum harmonic oscillator, with the same associated energy levels, but different center coordinates $k_y\ell^2$ and $k_y'\ell^2$, where ℓ is the magnetic length. We can re-write this as follows:

$$F_{nn'}^{k_y k_y'}(\mathbf{q}) = \delta_{k_y'-k_y,q_y} \int dx\; e^{-iq_x x} \chi_n^*(x - k_y\ell^2)\chi_{n'}(x - k_y'\ell^2) \tag{6.19}$$

where χ_n are the eigenstates of the quantum harmonic oscillator centered at $x = 0$. Now we perform a change of variables $x \to x + k_y\ell^2$:

$$F_{nn'}^{k_y k_y'}(\mathbf{q}) = \delta_{k_y'-k_y,q_y} \int dx\; e^{-iq_x(x+k_y\ell^2)} \chi_n^*(x)\chi_{n'}(x + (k_y - k_y')\ell^2) \tag{6.20}$$

$$= \delta_{k_y'-k_y,q_y} e^{-iq_x k_y \ell^2} \int dx\; e^{-iq_x x} \chi_n^*(x)\chi_{n'}(x + (k_y - k_y')\ell^2) \tag{6.21}$$

and use the generator of translation $\hat{T}(\mathbf{x}) = \exp(-\frac{i\mathbf{x}\cdot\hat{\mathbf{p}}}{\hbar})$ – where $\hat{T}(\mathbf{x})\,|\mathbf{r}\rangle = |\mathbf{r} + \mathbf{x}\rangle$ – to "shift" $\chi_{n'}$ as follows:

$$F_{nn'}^{k_y k_y'}(\mathbf{q}) = \delta_{k_y'-k_y,q_y} e^{-iq_x k_y \ell^2} \int dx\; e^{-iq_x x} e^{\frac{i\hat{p}_x (k_y - k_y')\ell^2}{\hbar}} \chi_n^*(x)\chi_{n'}(x) \tag{6.22}$$

$$= \delta_{k_y'-k_y,q_y} e^{-iq_x k_y \ell^2} \,\langle n | e^{-iq_x x} e^{\frac{-i\hat{p}_x q_y \ell^2}{\hbar}} | n' \rangle \tag{6.23}$$

where we used $q_y = k'_y - k_y$ in the last step. We can re-express the matrix element in terms of the ladder operators for the quantum harmonic oscillator:

$$\hat{x} = \frac{\ell}{\sqrt{2}}\left(\hat{a} + \hat{a}^\dagger\right) \tag{6.24}$$

$$\hat{p}_x = \frac{\hbar}{i\sqrt{2}\ell}\left(\hat{a} - \hat{a}^\dagger\right) \tag{6.25}$$

which leads to:

$$F_{nn'}^{k_y k'_y}(\mathbf{q}) = \delta_{k'_y - k_y, q_y} e^{-iq_x k_y \ell^2} \langle n| e^{-iq_x \frac{\ell}{\sqrt{2}}\left(\hat{a}+\hat{a}^\dagger\right)} e^{-q_y \frac{\ell}{\sqrt{2}}\left(\hat{a}-\hat{a}^\dagger\right)} |n'\rangle \tag{6.26}$$

Since $[\hat{x}, \hat{p}_x] = i\hbar$ which commutes with both $\hat{x}$ and $\hat{p}_x$, we can use the Baker-Campbell-Hausdorff formula $e^{\hat{A}} e^{\hat{B}} = e^{\hat{A}+\hat{B}} e^{\frac{1}{2}[\hat{A},\hat{B}]}$ for the above matrix element, where

$$\frac{1}{2}\left[\hat{A}, \hat{B}\right] = \frac{1}{2}\left[-iq_x \frac{\ell}{\sqrt{2}}\left(\hat{a} + \hat{a}^\dagger\right), -q_y \frac{\ell}{\sqrt{2}}\left(\hat{a} - \hat{a}^\dagger\right)\right] \tag{6.27}$$

$$= \frac{i\ell^2}{4} q_x q_y \left[\hat{a} + \hat{a}^\dagger, \hat{a} - \hat{a}^\dagger\right] \tag{6.28}$$

$$= -\frac{i\ell^2}{2} q_x q_y \tag{6.29}$$

which leads to:

$$F_{nn'}^{k_y k'_y}(\mathbf{q}) = \delta_{k'_y - k_y, q_y} e^{-iq_x k_y \ell^2} e^{-\frac{i\ell^2}{2} q_x q_y} \langle n| e^{-iq_x \frac{\ell}{\sqrt{2}}\left(\hat{a}+\hat{a}^\dagger\right) - q_y \frac{\ell}{\sqrt{2}}\left(\hat{a}-\hat{a}^\dagger\right)} |n'\rangle \tag{6.30}$$

$$= \delta_{k'_y - k_y, q_y} e^{-\frac{iq_x \ell^2}{2}(k_y + k'_y)} \langle n| e^{\alpha \hat{a}^\dagger - \alpha^* \hat{a}} |n'\rangle \tag{6.31}$$

where $\alpha = \ell(q_y - iq_x)/\sqrt{2}$ and α^* is its complex conjugate. Since $[\hat{a}, \hat{a}^\dagger] = 1$ which commutes with both $\hat{a}$ and $\hat{a}^\dagger$, we can use the Baker-Campbell-Hausdorff formula from above (this time the other way round) and obtain:

$$F_{nn'}^{k_y k'_y}(\mathbf{q}) = \delta_{k'_y - k_y, q_y} e^{-\frac{iq_x \ell^2}{2}(k_y + k'_y)} \langle n| e^{\alpha \hat{a}^\dagger} e^{-\alpha^* \hat{a}} e^{-\frac{1}{2}[\alpha \hat{a}^\dagger, -\alpha^* \hat{a}]} |n'\rangle \tag{6.32}$$

$$= \delta_{k'_y - k_y, q_y} e^{\frac{-iq_x \ell^2}{2}(k_y + k'_y)} e^{-\frac{1}{2}|\alpha|^2} \langle n| e^{\alpha \hat{a}^\dagger} e^{-\alpha^* \hat{a}} |n'\rangle \tag{6.33}$$

$$= \delta_{k'_y - k_y, q_y} e^{\frac{-iq_x \ell^2}{2}(k_y + k'_y)} e^{-\frac{1}{2}|\alpha|^2} \sum_{m=0}^{\infty} \langle n| e^{\alpha \hat{a}^\dagger} |m\rangle \langle m| e^{-\alpha^* \hat{a}} |n'\rangle \tag{6.34}$$

where we inserted the identity in the last line. Let us Taylor-expand the exponential function in the matrix element $\langle n| e^{\alpha \hat{a}^\dagger} |m\rangle$:

$$\langle n| e^{\alpha \hat{a}^\dagger} |m\rangle = \sum_{\mu=0}^{\infty} \frac{\alpha^\mu}{\mu!} \langle n| (\hat{a}^\dagger)^\mu |m\rangle \tag{6.35}$$

The only non-zero term of this sum is for $\mu = n - m$ (where $m \leq n$), so that:

$$\langle n| e^{\alpha \hat{a}^\dagger} |m\rangle = \frac{\alpha^{n-m}}{(n-m)!}\left(\sqrt{m+1}\sqrt{m+2}\ldots\sqrt{n}\right) \tag{6.36}$$

$$= \frac{\alpha^{n-m}}{(n-m)!}\sqrt{\frac{n!}{m!}} \tag{6.37}$$

Similarly, when we Taylor expand the second matrix element $\langle m|e^{-\alpha^*\hat{a}}|n'\rangle$, the only non-zero term is for $\mu' = n' - m$ where $m \leq n'$:

$$\langle m|e^{-\alpha^*\hat{a}}|n'\rangle = \frac{(-\alpha^*)^{n'-m}}{(n'-m)!}\left(\sqrt{n'}\sqrt{n'-1}\dots\sqrt{m+1}\right) \tag{6.38}$$

$$= \frac{(-\alpha^*)^{n'-m}}{(n'-m)!}\sqrt{\frac{n'!}{m!}} \tag{6.39}$$

We obtain:

$$F_{nn'}^{k_y k_y'}(\mathbf{q}) = \delta_{k_y'-k_y,q_y} e^{\frac{-iq_x\ell^2}{2}(k_y+k_y')} e^{-\frac{1}{2}|\alpha|^2} \sum_{m=0}^{n_{\min}} \frac{\alpha^{n-m}}{(n-m)!}\frac{(-\alpha^*)^{n'-m}}{(n'-m)!}\sqrt{\frac{n!}{m!}}\sqrt{\frac{n'!}{m!}} \tag{6.40}$$

$$= \delta_{k_y'-k_y,q_y} e^{\frac{-iq_x\ell^2}{2}(k_y+k_y')} e^{-\frac{1}{2}|\alpha|^2}\sqrt{n!n'!} \sum_{m=0}^{n_{\min}} \frac{(-1)^{n'-m}\alpha^{n-m}}{(n-m)!}\frac{(\alpha^*)^{n'-m}}{(n'-m)!}\frac{1}{m!} \tag{6.41}$$

where the sum now goes from zero to $n_{\min} = \min(n, n')$. Let us now assume that $n' \leq n$ and "invert" the sum by introducing the new index $\lambda = n' - m$:

$$F_{nn'}^{k_y k_y'}(\mathbf{q}) = \delta_{k_y'-k_y,q_y} e^{\frac{-iq_x\ell^2}{2}(k_y+k_y')} e^{-\frac{1}{2}|\alpha|^2}\sqrt{n!n'!} \times \sum_{\lambda=0}^{n'} \frac{(-1)^{\lambda}\alpha^{n-n'+\lambda}}{(n-n'+\lambda)!}\frac{(\alpha^*)^{\lambda}}{\lambda!}\frac{1}{(n'-\lambda)!} \tag{6.42}$$

$$= \delta_{k_y'-k_y,q_y} e^{\frac{-iq_x\ell^2}{2}(k_y+k_y')} e^{-\frac{1}{2}|\alpha|^2}\sqrt{n!n'!}\ \alpha^{n-n'} \times \sum_{\lambda=0}^{n'} \frac{(-1)^{\lambda}|\alpha|^{2\lambda}}{\lambda!}\frac{1}{(n-n'+\lambda)!}\frac{1}{(n'-\lambda)!} \tag{6.43}$$

$$= \delta_{k_y'-k_y,q_y} e^{\frac{-iq_x\ell^2}{2}(k_y+k_y')} e^{-\frac{1}{2}|\alpha|^2}\sqrt{n!n'!}\ \alpha^{n-n'}\frac{1}{n!}\sum_{\lambda=0}^{n'} \frac{(-1)^{\lambda}|\alpha|^{2\lambda}}{\lambda!}\binom{n}{n'-\lambda} \tag{6.44}$$

$$= \delta_{k_y'-k_y,q_y} e^{\frac{-iq_x\ell^2}{2}(k_y+k_y')} e^{-\frac{1}{2}|\alpha|^2}\alpha^{n-n'}\sqrt{\frac{n'!}{n!}}L_{n'}^{n-n'}(|\alpha|^2) \tag{6.45}$$

where $L_{n'}^{n-n'}(x)$ denotes the associated Laguerre polynomial. The modulus squared of α is:

$$|\alpha|^2 = \left|\frac{\ell(q_y - iq_x)}{\sqrt{2}}\right|^2 = \frac{\ell^2 q^2}{2} \tag{6.46}$$

where $q = |\mathbf{q}|$. This leads to the following expression for the matrix element if $n \geq n'$:

$$F_{nn'}^{k_y k_y'}(\mathbf{q}) = \delta_{k_y'-k_y,q_y} e^{\frac{-iq_x\ell^2}{2}(k_y+k_y')} e^{-\frac{\ell^2q^2}{4}}\left[\frac{\ell(q_y - iq_x)}{\sqrt{2}}\right]^{n-n'}\sqrt{\frac{n'!}{n!}}L_{n'}^{n-n'}\left(\frac{\ell^2q^2}{2}\right) \tag{6.47}$$

In the case $n' > n$, we introduce the index $\lambda' = n - m$, do the same analysis as demonstrated above and obtain:

$$F_{nn'}^{k_y k_y'}(\mathbf{q}) = \delta_{k_y'-k_y,q_y} e^{\frac{-iq_x\ell^2}{2}(k_y+k_y')} e^{-\frac{1}{2}|\alpha|^2} (-\alpha^*)^{n'-n} \sqrt{\frac{n!}{n'!}} L_n^{n'-n}(|\alpha|^2) \tag{6.48}$$

where the only change with respect to equation 6.47 is that the indices n and n' are swapped and that we replace a α by $-\alpha^*$.

6.5.2 Lindhard function

We now insert this matrix element into the Lindhard function (equation 1.52), the imaginary part of which will provide us with the particle-hole excitation spectrum:

$$\chi_{nn}(\mathbf{q},\omega) = \frac{1}{\hbar L_x L_y} \sum_{n,n'} \sum_{k_y,k_y'} \frac{P_{n'} - P_n}{\omega - \omega_{nn'} + i\eta} \left|\langle n, k_y|\hat{n}(\mathbf{q})|n', k_y'\rangle\right|^2 \tag{6.49}$$

where the energy difference between the states $\omega_{nn'} = (n - n')\omega_c$ obviously does not depend on the wavevectors k_y or k_y'. Note that we did not take into account spin degeneracy here. In the zero temperature limit, and assuming that we are dealing with completely filled or empty LLs, the population factors P_n do not depend on the wavevector either and can be replaced by Heaviside step functions $P_n = \Theta(N_F - n)$, where N_F is the highest filled LL and we use the convention $\Theta(0) = 1$.

Since the modulus square of the matrix element does not explicitly depend on k_y (in eq. 6.47, k_y and k_y' only affect the complex phase) and the Kronecker delta forces $k_y' = k_y + q_y$, the sum over k_y and k_y' reduces to a multiplication by the LL degeneracy from eq. 1.45:

$$\chi_{nn}(\mathbf{q},\omega) = \frac{1}{2\pi\hbar\ell^2} \sum_{n,n'} \frac{\Theta(N_F - n') - \Theta(N_F - n)}{\omega - \omega_{nn'} + i\eta} \left|\langle n, k_y|\hat{n}(\mathbf{q})|n', k_y'\rangle\right|^2 \tag{6.50}$$

The only non-zero terms in this sum are for transitions between full and empty LLs, i.e. either $n \leq N_F$ and $n' > N_F$ or vice versa. This means we can re-write the sum as follows:

$$\begin{aligned}\chi_{nn}(\mathbf{q},\omega) =& \frac{1}{2\pi\hbar\ell^2} \\ &\times \sum_{k=1}^{\infty}\sum_{j} \left[\frac{|\langle j+k, k_y|\hat{n}(\mathbf{q})|j, k_y+q_y\rangle|^2}{\omega - k\omega_c + i\eta} - \frac{|\langle j, k_y|\hat{n}(\mathbf{q})|j+k, k_y+q_y\rangle|^2}{\omega + k\omega_c + i\eta}\right]\end{aligned} \tag{6.51}$$

where k is now the distance between two LLs $|n' - n|$ and the sum over j goes from the lowest reachable filled LL $\max(0, N_F - k + 1)$ to the highest filled LL N_F. Using eq. 6.47 for the first term ($n > n'$) and 6.48 for the second term ($n' > n$) in the square brackets leads to:

$$\begin{aligned}\chi_{nn}(\mathbf{q},\omega) =& \frac{1}{2\pi\hbar\ell^2} \sum_{k=1}^{\infty}\sum_{j} e^{-\frac{\ell^2q^2}{2}} \left(\frac{\ell^2q^2}{2}\right)^k \frac{j!}{(j+k)!} \left[L_j^k\left(\frac{\ell^2q^2}{2}\right)\right]^2 \\ &\times \left[\frac{1}{\omega - k\omega_c + i\eta} - \frac{1}{\omega + k\omega_c + i\eta}\right]\end{aligned} \tag{6.52}$$

6.5.3 Effect of the electric field

Let us now consider what happens if an in-plane electric field is applied to the 2DEG. This case is also investigated in chapter 10 of Giuliani and Vignale's book [32]. The time independent Schrödinger equation 1.40 (TISE) has to be adapted as follows:

$$\frac{1}{2m_b}\left[\hat{\mathbf{p}} - e\mathbf{A}(\mathbf{r})\right]^2 \psi(\mathbf{r}) - eV(\mathbf{r})\psi(\mathbf{r}) = \epsilon\psi(\mathbf{r}) \tag{6.53}$$

where $\mathbf{A}$ is the vector potential such that $\nabla\times\mathbf{A} = \mathbf{B}$ and V is the electric potential. Choosing the Landau gauge $\mathbf{A}(\mathbf{r}) = Bx\mathbf{e_y}$ and aligning the electric field with the x direction so that $V = -Ex$, one finds:

$$\left[-\frac{\hbar^2}{2m_b}\frac{\partial^2}{\partial x^2} + \frac{1}{2m_b}\left(-i\hbar\frac{\partial}{\partial y} - eBx\right)^2 + eEx\right]\psi(x,y) = \epsilon\psi(x,y) \tag{6.54}$$

As mentioned in section 1.4.1, we can insert plane-wave solutions for the y-direction $\psi_n(x,y) = e^{ik_y y}\chi_{n,k_y}(x)/\sqrt{L_y}$, so that the problem reduces to a one dimensional TISE:

$$\left[-\frac{\hbar^2}{2m_b}\frac{\partial^2}{\partial x^2} + \frac{m_b\omega_c^2}{2}\left(x - k_y\ell^2\right)^2 + eEx\right]\chi_{n,k_y}(x) = \epsilon\chi_{n,k_y}(x) \tag{6.55}$$

which we can re-write as follows [32]:

$$\left[-\frac{\hbar^2}{2m_b}\frac{\partial^2}{\partial x^2} + \frac{m_b\omega_c^2}{2}\left(x - X_{k_y}\right)^2 + eEk_y\ell^2 - \frac{m_b v_d^2}{2}\right]\chi_{n,k_y}(x) = \epsilon\chi_{n,k_y}(x) \tag{6.56}$$

where $X_{k_y} = k_y\ell^2 - v_d/\omega_c$. Similarly to the zero-$E$-field case, this is the TISE for the one-dimensional quantum harmonic oscillator (QHO). The solution is given by the QHO eigenfunctions centered around X_{k_y} (i.e. shifted by $-v_d/\omega_c$ with respect to the zero-E-field case) and the energy eigenvalues are given by:

$$\epsilon_{n,k_y} = \left(n + \frac{1}{2}\right)\hbar\omega_c + eEX_{k_y} + \frac{m_b v_d^2}{2} \tag{6.57}$$

For the calculation of the matrix element $\langle n, k_y|\, e^{i\mathbf{q}\cdot\mathbf{r}}\, |n', k_y'\rangle$, the shift of the QHO center only results in a complex phase prefactor that cancels out once we take the modulus squared (c.f. the change of variables between eq. 6.19 and eq. 6.21). As far as the Lindhard function is concerned, it therefore only enters as an energy shift depending on q_y:

$$\omega_{nn'} = \frac{1}{\hbar}\left(\epsilon_{n,k_y} - \epsilon_{n',k_y'}\right) = (n-n')\omega_c + \frac{eE}{\hbar}\left(X_{k_y} - X_{k_y'}\right) \tag{6.58}$$

$$= (n-n')\omega_c + \frac{eE\ell^2}{\hbar}\left(k_y - k_y'\right) \tag{6.59}$$

$$= (n-n')\omega_c - v_d q_y \tag{6.60}$$

which leads to the following expression for the Lindhard function:

$$\chi_{nn}(\mathbf{q},\omega) = \frac{e^{\frac{-q^2\ell^2}{2}}}{2\pi\hbar\ell^2}\sum_{k=1}^{\infty}\sum_{j}\frac{j!}{(j+k)!}\left(\frac{q^2\ell^2}{2}\right)^k\left[L_j^k\left(\frac{q^2\ell^2}{2}\right)\right]^2 \times\left[\frac{1}{\omega - k\omega_c - v_d q_y + i\eta} - \frac{1}{\omega + k\omega_c - v_d q_y + i\eta}\right] \tag{6.61}$$

This finally leads to the conclusion that our system obeys Galilean invariance:

$$\chi_{nn}^{E\neq 0}(\mathbf{q},\omega) = \chi_{nn}^{E=0}(\mathbf{q},\omega - v_d q_y) \tag{6.62}$$
$$\chi_{\text{RPA}}^{E\neq 0}(\mathbf{q},\omega) = \chi_{\text{RPA}}^{E=0}(\mathbf{q},\omega - v_d q_y) \tag{6.63}$$
$$\omega_{\text{ME}}^{E\neq 0}(\mathbf{q}) = \omega_{\text{ME}}^{E=0}(\mathbf{q}) - v_d q_y \tag{6.64}$$

6.6 Dielectric characterization of hBN

For the design and fabrication of hBN-encapsulated graphene devices with local gate electrodes it is important to know the hBN permittivity ϵ_r (in order to calculate the charge carrier density) and its breakdown voltage V_{bd} (in order to estimate the operation limits of the device). Since it is a hyperbolic material, hBN's permittivity is anisotropic [316], but due to the structure of our devices, we are only interested in the out-of-plane permittivity. In the literature, one can find values ranging from 2.9 to 4.9 [316, 317], depending on material thickness and frequency.

In the framework of the GoBN (graphene on boron nitride) ANR (French National Research Agency) project, two different hBN sources were characterized in terms of ϵ_r (at radio frequency $\lesssim$ 10 GHz) and V_{bd}. The first source was used for all the devices of this thesis and is widely used throughout the research community. This hBN was synthesized by Takashi Taniguchi and Kenji Watanabe at the National Institute for Materials Science (NIMS) in Japan, by a High-Pressure-High-Temperature (HPHT) method at $\sim$ 6 GPa and $\sim$ 2000°C. [128] The second sample was synthesized by Yangdi Li, Catherine Journet and Bérangère Toury at Laboratoire des Multimatériaux et Interfaces (LMI) in Lyon, France, using a polymer-derived ceramics process. [318]

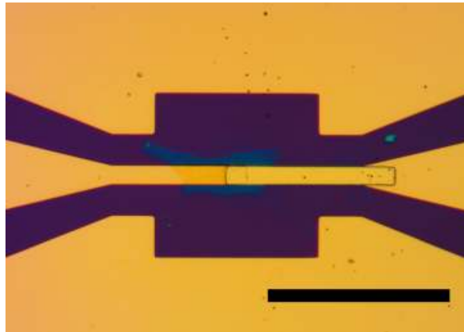

Figure 6.8 – Microscope image of device 01 of the series NIMS-MIMS-3. Scale bar is 100 μm.

The crystals were exfoliated (see section 2.1.1) in order to obtain flakes with a thickness on the order of tens of nanometers. Each flake was then transferred (see section 2.1.3) onto a gold electrode embedded in a co-planar waveguide. Finally, a second gold electrode was patterned on top of the flake by electron beam or optical lithography, so that the two electrodes form a parallel plate capacitor with a hBN dielectric. An example is shown in figure 6.8. In the following, we define d as the thickness of the hBN flake, measured using atomic force microscopy, and S as the surface of the capacitor, measured using scanning

electron microscopy. The sample fabrication was done by Aurélie Pierret, José Palomo, Michael Rosticher and Mohamed Boukhicha.

6.6.1 Permittivity measurements

The capacitance was obtained by measuring the complex admittance $Y = j\omega C$ of the device, either using a lock-in amplifier or (mostly) using a vector network analyzer (VNA), c.f. section 2.2. This characterization was done by David Mele, Aurélie Pierret, Andreas Inhofer, Mohamed Boukhicha and myself.

Supposing that the total capacitance C is a series addition of the hBN-capacitance and the spurious capacitance of air gaps or polymer residues (induced by the fabrication process and considered to be independent of d), we can write:

$$\frac{1}{C} = \frac{d}{\epsilon_0 \epsilon_r S} + \frac{1}{C_\mathrm{p}} \tag{6.65}$$

where ϵ_r is the permittivity of hBN that we want to measure. This can be re-written as follows:

$$d = \epsilon_r \frac{\epsilon_0 S}{C} - \frac{\epsilon_0 \epsilon_r S}{C_\mathrm{p}} \tag{6.66}$$

By plotting the hBN thickness d as a function of $\epsilon_0 S/C$, where C is the measured capacitance, we obtain the permittivity ϵ_r as the slope and any parasitic, thickness-independent capacitance encoded as the offset of the data. Figure 6.9 shows the results obtained on six series of devices, mostly characterized by VNA at room temperature. The data points for hBN from LMI are red, those for hBN from NIMS are green and black. The black and the red data points are fitted with a linear function to extract the permittivity and the aforementioned offset.

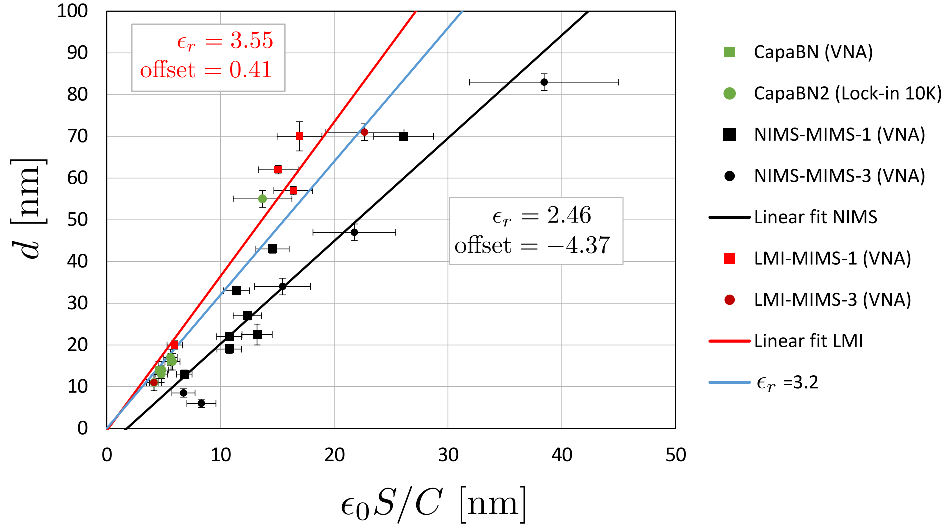

Figure 6.9 – Determining the out-of-plane permittivity of hBN from capacitance measurements.

The blue line corresponds to the value $\epsilon_r = 3.2$ used throughout this thesis and measured in ref. [144] by calibration against quantum Hall plateaus. Preliminary (CapaBN and Ca-

paBN2) capacitance measurements on thin (< 20 nm) hBN flakes were in accordance with this value.

Our linear fits suggest that the hBN from LMI has a significantly higher permittivity $\epsilon_r \approx 3.6$ than the one from NIMS where we find $\epsilon_r \approx 2.5$. However, the data obtained for the NIMS samples is scattered around the fit beyond the reach of the error bars and the fit exhibits a significant offset, indicating that spurious series capacitances due to sample imperfections still play a role. A new sample generation with graphene/graphite contacts might solve this issue, since air gaps and polymer residues can be avoided this way.

In conclusion, the permittivity of hBN is still the least precisely known quantity in our devices. For the corner reflectors discussed in chapter 3, this might result in a systematic error $\sim 20\%$ for the calculation of the carrier densities n, but also for the transmission of the device, which is calculated by taking into account the number of transverse modes $k_F W/\pi$, where $k_F = \sqrt{\pi n}$. For the plasma resonance capacitors discussed in chapter 4 and the BLG FET in chapter 5, this uncertainty is less of a problem, because the gate capacitance was measured in both cases.

6.6.2 Breakdown measurements

The breakdown was measured in the same samples by repeatedly sweeping the applied DC voltage and increasing the range after every sweep. The breakdown was identified as a sharp increase in the leak current. This is illustrated in figure 6.10. The hysteresis between forward and backward sweep (arrows) is due to the finite charging time of the capacitor and can be reduced by increasing the measurement delay. The breakdown voltages for the positive ($V+$) and negative ($V-$) sweep are highlighted by vertical black lines (two each, in order to indicate the measurement uncertainty).

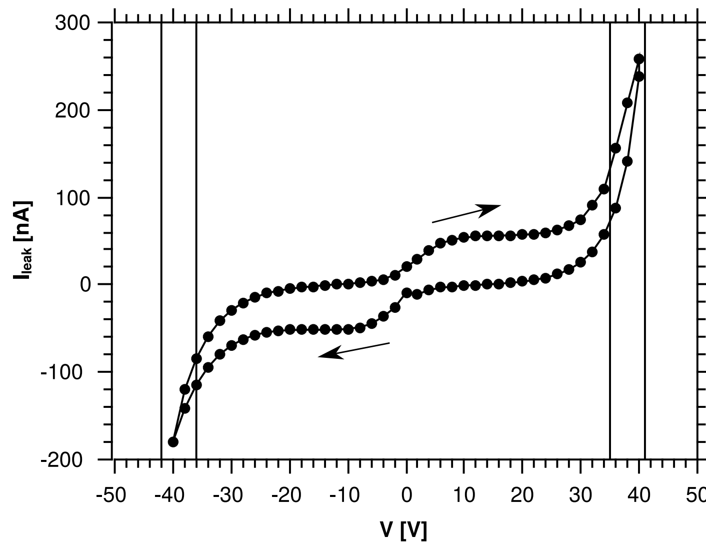

Figure 6.10 – Leak current as a function of applied voltage for device 32 of series NIMS-MIMS-3.

Figure 6.11 shows the collected results of the breakdown measurements on samples made with LMI (red) and NIMS (black) hBN. The positive and negative breakdown voltages over-

lap, indicating a reproducible measurement. From the present dataset, no evident difference between the two hBN types can be established. The blue line is a guide for the eye and corresponds to $V_{bd} = 0.8$ V/nm, which is close to the 0.7 V/nm quoted in ref. [14]. Within the thickness range used in this thesis (10nm $\lesssim d < 50$ nm), there is a good agreement between the data and this line. For samples exceeding this range (thinner or thicker), smaller breakdown fields were measured, indicating that the breakdown field might depend on the sample thickness.

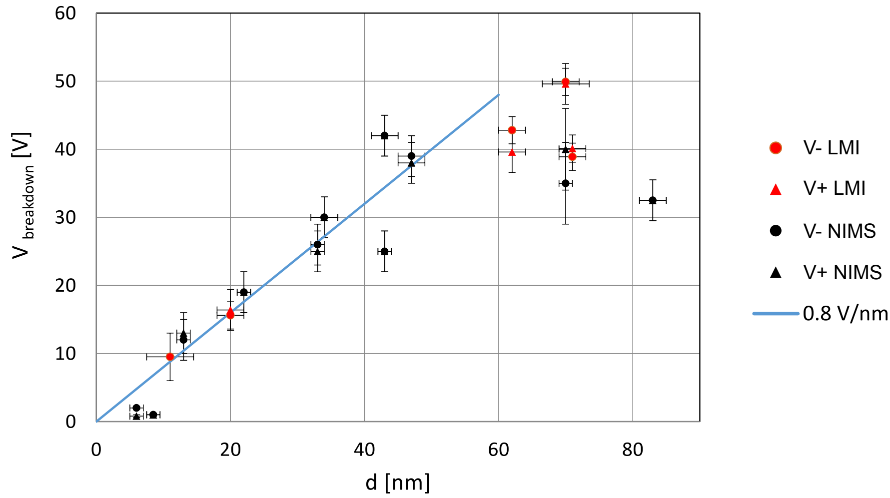

Figure 6.11 – Breakdown voltage as a function of hBN thickness for positive ($V+$) and negative ($V-$) applied voltages.

Bibliography

[1] K. S. Novoselov, A. K. Geim, S. V. Morozov, D. Jiang, Y. Zhang, S. V. Dubonos, I. V. Grigorieva, and A. A. Firsov, "Electric Field Effect in Atomically Thin Carbon Films," *Science*, vol. 306, pp. 666–669, oct 2004.

[2] J. N. Fuchs and M. O. Goerbig, *Introduction to the Physical Properties of Graphene (Lecture Notes).* Université Paris-Sud/UPMC, 2008.

[3] C. Lee, X. Wei, J. W. Kysar, and J. Hone, "Measurement of the Elastic Properties and Intrinsic Strength of Monolayer Graphene," *Science*, vol. 321, pp. 385–388, jul 2008.

[4] F. H. L. Koppens, T. Mueller, P. Avouris, A. C. Ferrari, M. S. Vitiello, and M. Polini, "Photodetectors based on graphene, other two-dimensional materials and hybrid systems," *Nature Publishing Group*, vol. 9, no. 10, pp. 780–793, 2014.

[5] A. Geim and K. Novolesov, "Rise of graphene," *Nature Materials*, vol. 6, pp. 183–191, 2007.

[6] P. Wallace, "The Band Theory of Graphite," *Physical Review*, vol. 71, no. 9, 1947.

[7] S. Das Sarma, S. Adam, E. H. Hwang, and E. Rossi, "Electronic transport in two-dimensional graphene," *Reviews of Modern Physics*, vol. 83, no. 2, pp. 407–470, 2011.

[8] M. Konig, S. Wiedmann, C. Brune, A. Roth, H. Buhmann, L. W. Molenkamp, X.-L. Qi, and S.-C. Zhang, "Quantum Spin Hall Insulator State in HgTe Quantum Wells," *Science*, vol. 318, pp. 766–770, nov 2007.

[9] D. Hsieh, D. Qian, L. Wray, Y. Xia, Y. S. Hor, R. J. Cava, and M. Z. Hasan, "A topological Dirac insulator in a quantum spin Hall phase," *Nature*, vol. 452, no. 7190, pp. 970–974, 2008.

[10] S.-Y. Xu, I. Belopolski, N. Alidoust, M. Neupane, G. Bian, C. Zhang, R. Sankar, G. Chang, Z. Yuan, C.-C. Lee, S.-M. Huang, H. Zheng, J. Ma, D. S. Sanchez, B. Wang, A. Bansil, F. Chou, P. P. Shibayev, H. Lin, S. Jia, and M. Z. Hasan, "Discovery of a Weyl fermion semimetal and topological Fermi arcs," *Science*, vol. 349, pp. 613–617, aug 2015.

[11] M. Yankowitz, S. Chen, H. Polshyn, Y. Zhang, K. Watanabe, T. Taniguchi, D. Graf, A. F. Young, and C. R. Dean, "Tuning superconductivity in twisted bilayer graphene," *Science*, vol. 363, pp. 1059–1064, mar 2019.

[12] Y. Cao, V. Fatemi, S. Fang, K. Watanabe, T. Taniguchi, E. Kaxiras, and P. Jarillo-Herrero, "Magic-angle graphene superlattices: a new platform for unconventional superconductivity," *Nature Publishing Group*, vol. 556, no. 7699, pp. 43–50, 2018.

[13] Y. Cao, V. Fatemi, A. Demir, S. Fang, S. L. Tomarken, J. Y. Luo, J. D. Sanchez-Yamagishi, K. Watanabe, T. Taniguchi, E. Kaxiras, R. C. Ashoori, and P. Jarillo-Herrero, "Correlated Insulator Behaviour at Half-Filling in Magic Angle Graphene Superlattices," *Nature Publishing Group*, vol. 556, no. 7699, pp. 80–84, 2018.

[14] C. R. Dean, A. F. Young, I. Meric, C. Lee, L. Wang, S. Sorgenfrei, K. Watanabe, T. Taniguchi, P. Kim, K. L. Shepard, and J. Hone, "Boron nitride substrates for high-quality graphene electronics.," *Nature Nanotechnology*, vol. 5, no. 10, pp. 722–726, 2010.

[15] R. Y. Tay, M. H. Griep, G. Mallick, S. H. Tsang, R. S. Singh, T. Tumlin, E. H. T. Teo, and S. P. Karna, "Growth of large single-crystalline two-dimensional boron nitride hexagons on electropolished copper," *Nano Letters*, vol. 14, no. 2, pp. 839–846, 2014.

[16] O. Cometto, B. Sun, S. H. Tsang, X. Huang, Y. K. Koh, and E. H. T. Teo, "Vertically self-ordered orientation of nanocrystalline hexagonal boron nitride thin films for enhanced thermal characteristics," *Nanoscale*, vol. 7, no. 45, pp. 18984–18991, 2015.

[17] M. Loeblein, R. Y. Tay, S. H. Tsang, W. B. Ng, and E. H. T. Teo, "Configurable three-dimensional boron nitride-carbon architecture and its tunable electronic behavior with stable thermal performances," *Small*, vol. 10, no. 15, pp. 2992–2999, 2014.

[18] M. Loeblein, S. H. Tsang, M. Pawlik, E. J. R. Phua, H. Yong, X. W. Zhang, C. L. Gan, and E. H. T. Teo, "High-Density 3D-Boron Nitride and 3D-Graphene for High-Performance Nano-Thermal Interface Material," *ACS Nano*, vol. 11, no. 2, pp. 2033–2044, 2017.

[19] A. H. Castro Neto, F. Guinea, N. M. R. Peres, K. S. Novoselov, and A. K. Geim, "The electronic properties of graphene," *Reviews of Modern Physics*, vol. 81, pp. 109–162, jan 2009.

[20] M. O. Goerbig, "Electronic properties of graphene in a strong magnetic field," *Reviews of Modern Physics*, vol. 83, pp. 1193–1243, nov 2011.

[21] R. Roldán, L. Chirolli, E. Prada, J. A. Silva-Guillén, P. San-Jose, and F. Guinea, "Theory of 2D crystals: Graphene and beyond," *Chemical Society Reviews*, vol. 46, no. 15, pp. 4387–4399, 2017.

[22] A. Betz, *Elastic and inelastic scattering in graphene studied by microwave transport and noise*. PhD thesis, École Normale Supérieure, 2012.

[23] Q. Wilmart, *Engineering doping profiles in graphene: from Dirac fermion optics to high frequency electronics*. PhD thesis, Ecole Normale Superieure, 2016.

[24] A. Inhofer, *Probing AC electronic compressibility of 3D HgTe and Bi2Se3 topological insulators at high electric fields: Evidence for excited massive surface states*. PhD thesis, École Normale Supérieure, 2017.

[25] S. Berthou, *Étude opto-électronique des mécanismes de relaxation des électrons de haute énergie dans les hétérostructures en graphène.* Phd thesis, Université Sorbonne Paris Cité, 2017.

[26] H. Graef, Q. Wilmart, M. Rosticher, D. Mele, L. Banszerus, C. Stampfer, T. Taniguchi, K. Watanabe, J.-M. Berroir, E. Bocquillon, G. Fève, E. H. T. Teo, and B. Plaçais, "A corner reflector of graphene Dirac fermions as a phonon-scattering sensor," *Nature Communications*, vol. 10, p. 2428, dec 2019.

[27] H. Graef, D. Mele, M. Rosticher, L. Banszerus, C. Stampfer, T. Taniguchi, K. Watanabe, E. Bocquillon, G. Fève, J.-M. Berroir, E. H. T. Teo, and B. Plaçais, "Ultra-long wavelength Dirac plasmons in graphene capacitors," *Journal of Physics: Materials*, vol. 1, p. 01LT02, sep 2018.

[28] W. Yang, H. Graef, X. Lu, G. Zhang, T. Taniguchi, K. Watanabe, A. Bachtold, E. H. T. Teo, E. Baudin, E. Bocquillon, G. Fève, J.-M. Berroir, D. Carpentier, M. O. Goerbig, and B. Plaçais, "Landau Velocity for Collective Quantum Hall Breakdown in Bilayer Graphene," *Physical Review Letters*, vol. 121, p. 136804, sep 2018.

[29] O. Klein, "Die Reflexion von Elektronen an einem Potentialsprung nach der relativistischen Dynamik von Dirac," *Zeitschrift für Physik*, vol. 53, no. 3, p. 157, 1929.

[30] M. I. Katsnelson, K. S. Novoselov, and A. K. Geim, "Chiral tunnelling and the Klein paradox in graphene," *Nature Physics*, vol. 2, pp. 620–625, sep 2006.

[31] J. P. Hobson and W. A. Nierenberg, "The statistics of a two-dimensional, hexagonal net," *Physical Review*, vol. 89, no. 3, p. 662, 1953.

[32] G. Giuliani and G. Vignale, *Quantum Theory of the Electron Liquid.* Cambridge University Press, 2005.

[33] D. L. John, L. C. Castro, and D. L. Pulfrey, "Quantum capacitance in nanoscale device modeling," *Journal of Applied Physics*, vol. 96, no. 9, pp. 5180–5184, 2004.

[34] T. Fang, A. Konar, H. Xing, and D. Jena, "Carrier statistics and quantum capacitance of graphene sheets and ribbons," *Applied Physics Letters*, vol. 91, no. 9, 2007.

[35] E. McCann and V. I. Fal'ko, "Landau-level degeneracy and quantum hall effect in a graphite bilayer," *Physical Review Letters*, vol. 96, no. 8, pp. 1–4, 2006.

[36] L. M. Malard, J. Nilsson, D. C. Elias, J. C. Brant, F. Plentz, E. S. Alves, A. H. Castro Neto, and M. A. Pimenta, "Probing the electronic structure of bilayer graphene by Raman scattering," *Physical Review B - Condensed Matter and Materials Physics*, vol. 76, no. 20, pp. 1–4, 2007.

[37] N. Ashcroft and N. Mermin, *Solid State Physics.* Harcourt, Inc., 1976.

[38] E. Pallecchi, A. C. Betz, J. Chaste, G. Fève, B. Huard, T. Kontos, J. M. Berroir, and B. Plaçais, "Transport scattering time probed through rf admittance of a graphene capacitor," *Physical Review B - Condensed Matter and Materials Physics*, vol. 83, no. 12, pp. 1–6, 2011.

[39] E. H. Hwang and S. Das Sarma, "Acoustic phonon scattering limited carrier mobility in two-dimensional extrinsic graphene," *Physical Review B - Condensed Matter and Materials Physics*, vol. 77, no. 11, pp. 1–6, 2008.

[40] N. H. Shon and T. Ando, "Quantum Transport in Two-Dimensional Graphite System," *Journal of the Physical Society of Japan*, vol. 67, no. 7, pp. 2421–2429, 1998.

[41] I. L. Aleiner and K. B. Efetov, "Effect of disorder on transport in graphene," *Physical Review Letters*, vol. 97, no. 23, pp. 1–4, 2006.

[42] K. Ziegler, "Robust transport properties in graphene," *Physical Review Letters*, vol. 97, no. 26, pp. 2–5, 2006.

[43] K. Nomura and A. H. MacDonald, "Quantum transport of massless dirac fermions," *Physical Review Letters*, vol. 98, no. 7, pp. 1–4, 2007.

[44] P. M. Ostrovsky, I. V. Gornyi, and A. D. Mirlin, "Electron transport in disordered graphene," *Physical Review B - Condensed Matter and Materials Physics*, vol. 74, no. 23, pp. 1–20, 2006.

[45] M. I. Katsnelson and A. K. Geim, "Electron scattering on microscopic corrugations in graphene," *Philosophical Transactions of the Royal Society A: Mathematical, Physical and Engineering Sciences*, vol. 366, no. 1863, pp. 195–204, 2008.

[46] A. Lucas and K. C. Fong, "Hydrodynamics of electrons in graphene," *Journal of Physics: Condensed Matter*, vol. 30, p. 053001, feb 2018.

[47] D. K. Efetov and P. Kim, "Controlling Electron-Phonon Interactions in Graphene at Ultrahigh Carrier Densities," *Physical Review Letters*, vol. 105, p. 256805, 2010.

[48] S. Datta, *Electronic transport in mesoscopic systems.* Cambridge University Press, 1997.

[49] S. Feng and P. A. Lee, "Mesoscopic Conductors and Correlations in Laser Speckle Patterns," *Science*, vol. 251, no. 4994, pp. 633–639, 1991.

[50] A. F. Young and P. Kim, "Quantum interference and Klein tunneling in graphene heterojunctions," *Nature Physics*, vol. 5, no. 3, pp. 222–226, 2009.

[51] P. Rickhaus, R. Maurand, M. H. Liu, M. Weiss, K. Richter, and C. Schönenberger, "Ballistic interferences in suspended graphene," *Nature Communications*, vol. 4, pp. 1–6, 2013.

[52] P. Rickhaus, J. Wallbank, S. Slizovskiy, R. Pisoni, H. Overweg, Y. Lee, M. Eich, M. H. Liu, K. Watanabe, T. Taniguchi, T. Ihn, and K. Ensslin, "Transport Through a Network of Topological Channels in Twisted Bilayer Graphene," *Nano Letters*, vol. 18, no. 11, pp. 6725–6730, 2018.

[53] A. Yacoby, U. Sivan, C. P. Umbach, and J. M. Hong, "Interference and dephasing by electron-electron interaction on length scales shorter than the elastic mean free path," *Physical Review Letters*, vol. 66, pp. 1938–1941, apr 1991.

[54] S. Kogan, *Electronic Noise and Fluctuations in Solids.* Cambridge University Press, 1996.

[55] Y. M. Blanter and M. Büttiker, "Shot noise in mesoscopic conductors," *Physics Reports*, vol. 336, pp. 1–166, oct 2000.

[56] H. Nyquist, "Thermal agitation of electric charge in conductors," *Phys. Rev.*, vol. 32, p. 110, 1928.

[57] J. Johnson, "Thermal agitation of electricity in conductors," *Phys. Rev.*, vol. 32, p. 97, 1928.

[58] W. Schottky, "Über spontane Stromschwankungen in verschiedenen Elektrizitätsleitern," *Annalen der Physik*, vol. 362, no. 23, pp. 541–567, 1918.

[59] U. Fano, "Ionization Yield of Radiations. II. The Fluctuations of the Number of Ions," *Physical Review*, vol. 72, pp. 26–29, jul 1947.

[60] C. W. Beenakker and M. Büttiker, "Suppression of shot noise in metallic diffusive conductors," *Physical Review B*, vol. 46, no. 3, pp. 1889–1892, 1992.

[61] A. H. Steinbach, J. M. Martinis, and M. H. Devoret, "Observation of hot-electron shot noise in a metallic resistor," *Physical Review Letters*, vol. 76, no. 20, pp. 3806–3809, 1996.

[62] K. E. Nagaev, "Influence of electron-electron scattering on shot noise in diffusive contacts," *Physical Review B*, vol. 52, pp. 4740–4743, aug 1995.

[63] W. Belzig, "Full counting statistics of super-Poissonian shot noise in multilevel quantum dots," *Physical Review B - Condensed Matter and Materials Physics*, vol. 71, no. 16, pp. 1–4, 2005.

[64] F. N. Hooge, "1/f noise is no surface effect," *Physics Letters A*, vol. 29, no. 3, pp. 139–140, 1969.

[65] A. C. Betz, F. Vialla, D. Brunel, C. Voisin, M. Picher, A. Cavanna, A. Madouri, G. Fève, J. M. Berroir, B. Plaçais, and E. Pallecchi, "Hot electron cooling by acoustic phonons in graphene," *Physical Review Letters*, vol. 109, no. 5, 2012.

[66] G. Liu, W. Stillman, S. Rumyantsev, Q. Shao, M. Shur, and A. A. Balandin, "Low-frequency electronic noise in the double-gate single-layer graphene transistors," *Applied Physics Letters*, vol. 95, no. 3, pp. 1–4, 2009.

[67] G. Liu, S. Rumyantsev, M. Shur, and A. A. Balandin, "Graphene thickness-graded transistors with reduced electronic noise," *Applied Physics Letters*, vol. 100, no. 3, 2012.

[68] M. O. Goerbig, "Quantum Hall effects," *arXiv preprint 0909.1998*, 2009.

[69] K. V. Klitzing, G. Dorda, and M. Pepper, "New method for high-accuracy determination of the fine-structure constant based on quantized hall resistance," *Physical Review Letters*, vol. 45, no. 6, pp. 494–497, 1980.

[70] K. von Klitzing, "Essay: Quantum Hall Effect and the New International System of Units," *Physical Review Letters*, vol. 122, no. 20, p. 200001, 2019.

[71] *Le Système international d'unités (SI).* Bureau international des poids et Mesures, 2019.

[72] D. C. Tsui, H. L. Stormer, and A. C. Gossard, "Two-dimensional magnetotransport in the extreme quantum limit," *Physical Review Letters*, vol. 48, no. 22, pp. 1559–1562, 1982.

[73] R. B. Laughlin, "Anomalous Quantum Hall Effect: An Incompressible Quantum Fluid with Fractionally Charged Excitations," *Physical Review Letters*, vol. 50, pp. 1395–1398, may 1983.

[74] D. Yoshioka, *The Quantum Hall Effect.* Springer-Verlag Berlin Heidelberg GmbH, 2002.

[75] R. Willett, J. P. Eisenstein, H. L. Störmer, D. C. Tsui, A. C. Gossard, and J. H. English, "Observation of an even-denominator quantum number in the fractional quantum Hall effect," *Physical Review Letters*, vol. 59, no. 15, pp. 1776–1779, 1987.

[76] Y. Zheng and T. Ando, "Hall conductivity of a two-dimensional graphite system," *Physical Review B - Condensed Matter and Materials Physics*, vol. 65, no. 24, pp. 2454201–24542011, 2002.

[77] Y. Zhang, Y. W. Tan, H. L. Stormer, and P. Kim, "Experimental observation of the quantum Hall effect and Berry's phase in graphene," *Nature*, vol. 438, no. 7065, pp. 201–204, 2005.

[78] K. S. Novoselov, E. McCann, S. V. Morozov, V. I. Fal'ko, M. I. Katsnelson, U. Zeitler, D. Jiang, F. Schedin, and A. K. Geim, "Unconventional quantum Hall effect and Berry's phase of 2π in bilayer graphene," *Nature Physics*, vol. 2, no. 3, pp. 177–180, 2006.

[79] R. Ribeiro-Palau, S. Chen, Y. Zeng, K. Watanabe, T. Taniguchi, J. Hone, and C. R. Dean, "High-Quality Electrostatically Defined Hall Bars in Monolayer Graphene," *Nano Letters*, p. acs.nanolett.9b00351, mar 2019.

[80] Y. Zeng, J. I. Li, S. A. Dietrich, O. M. Ghosh, K. Watanabe, T. Taniguchi, J. Hone, and C. R. Dean, "High-Quality Magnetotransport in Graphene Using the Edge-Free Corbino Geometry," *Physical Review Letters*, vol. 122, no. 13, pp. 3–8, 2019.

[81] P. Coleman, *Introduction to Many-Body Physics.* Cambridge University Press, 2015.

[82] J. Lindhard, "On the properties of a gas of charged particles," *Dan. Mat. Fys. Medd*, vol. 28, no. 8, 1954.

[83] Q. Fontaine, *Étude de la propagation d'un plasmon dans le graphène au passage d'une jonction p-n.* Master thesis, Universite Paris-Sud, 2016.

[84] S. A. Maier, *Plasmonics - Fundamentals and Applications.* Springer, 2007.

[85] V. W. Brar, M. S. Jang, M. Sherrott, S. Kim, J. J. Lopez, L. B. Kim, M. Choi, and H. Atwater, "Hybrid surface-phonon-plasmon polariton modes in graphene/monolayer h-BN heterostructures," *Nano Letters*, vol. 14, no. 7, pp. 3876–3880, 2014.

[86] T. Low and P. Avouris, "Graphene plasmonics for terahertz to mid-infrared applications," *ACS Nano*, vol. 8, pp. 1086–1101, 2014.

[87] A. N. Grigorenko, M. Polini, and K. S. Novoselov, "Graphene plasmonics," *Nature Photonics*, vol. 6, pp. 749–758, nov 2012.

[88] S. Huang, C. Song, G. Zhang, and H. Yan, "Graphene plasmonics: Physics and potential applications," *Nanophotonics*, vol. 6, no. 6, pp. 1191–1204, 2017.

[89] H. Yan, T. Low, W. Zhu, Y. Wu, M. Freitag, X. Li, F. Guinea, P. Avouris, and F. Xia, "Damping pathways of mid-infrared plasmons in graphene nanostructures," *Nature Photonics*, vol. 7, no. 5, pp. 394–399, 2013.

[90] Y. Jia, H. Zhao, Q. Guo, X. Wang, H. Wang, and F. Xia, "Tunable Plasmon–Phonon Polaritons in Layered Graphene–Hexagonal Boron Nitride Heterostructures," *ACS Photonics*, vol. 2, no. 7, pp. 907–912, 2015.

[91] A. Tomadin and M. Polini, "Theory of the plasma-wave photoresponse of a gated graphene sheet," *Physical Review B - Condensed Matter and Materials Physics*, vol. 88, no. 20, pp. 1–10, 2013.

[92] R. Roldán, J. N. Fuchs, and M. O. Goerbig, "Collisionless hydrodynamics of doped graphene in a magnetic field," *Solid State Communications*, vol. 175-176, pp. 114–118, 2013.

[93] A. Principi, D. Bandurin, H. Rostami, and M. Polini, "Pseudo-Euler equations from nonlinear optics: Plasmon-assisted photodetection beyond hydrodynamics," *Physical Review B*, vol. 99, p. 075410, feb 2019.

[94] M. Polini, R. Asgari, G. Borghi, Y. Barlas, T. Pereg-Barnea, and A. H. MacDonald, "Plasmons and the spectral function of graphene," *Physical Review B*, vol. 77, p. 081411, feb 2008.

[95] M. Jablan, H. Buljan, and M. Soljačić, "Plasmonics in graphene at infrared frequencies," *Physical Review B*, vol. 80, p. 245435, dec 2009.

[96] A. Principi, R. Asgari, and M. Polini, "Acoustic plasmons and composite hole-acoustic plasmon satellite bands in graphene on a metal gate," *Solid State Communications*, vol. 151, no. 21, pp. 1627–1630, 2011.

[97] P. J. Burke, I. B. Spielman, J. P. Eisenstein, L. N. Pfeiffer, and K. W. West, "High frequency conductivity of the high-mobility two-dimensional electron gas," *Applied Physics Letters*, vol. 76, no. 6, p. 745, 2000.

[98] P. Burke, "An RF circuit model for carbon nanotubes," *IEEE Trans. Nanotechnol.*, vol. 2, pp. 55–58, 2003.

[99] F. Rana, "Graphene Terahertz Plasmon Oscillators," *IEEE Transactions on Nanotechnology*, vol. 7, no. 1, pp. 91–99, 2008.

[100] H. Yoon, K. Y. M. Yeung, P. Kim, D. Ham, and D. Ham, "Plasmonics with two-dimensional conductors Subject Areas : Author for correspondence :," *Phil. Trans. R. Soc. A*, vol. 372, 2014.

[101] Y. Liu, R. F. Willis, K. V. Emtsev, and T. Seyller, "Plasmon dispersion and damping in electrically isolated two-dimensional charge sheets," *Physical Review B*, vol. 78, p. 201403, nov 2008.

[102] L. Ju, B. Geng, J. Horng, C. Girit, M. Martin, Z. Hao, H. a. Bechtel, X. Liang, A. Zettl, Y. R. Shen, and F. Wang, "Graphene plasmonics for tunable terahertz metamaterials," *Nature Nanotechnology*, vol. 6, no. 10, pp. 630–634, 2011.

[103] Z. Fei, A. S. Rodin, G. O. Andreev, W. Bao, A. S. McLeod, M. Wagner, L. M. Zhang, Z. Zhao, M. Thiemens, G. Dominguez, M. M. Fogler, A. H. C. Neto, C. N. Lau, F. Keilmann, and D. N. Basov, "Gate-tuning of graphene plasmons revealed by infrared nano-imaging," *Nature*, vol. 487, pp. 82–85, jul 2012.

[104] J. Chen, M. Badioli, P. Alonso-González, S. Thongrattanasiri, F. Huth, J. Osmond, M. Spasenović, A. Centeno, A. Pesquera, P. Godignon, A. Zurutuza Elorza, N. Camara, F. J. G. de Abajo, R. Hillenbrand, and F. H. L. Koppens, "Optical nano-imaging of gate-tunable graphene plasmons," *Nature*, pp. 1–5, 2012.

[105] A. Woessner, P. Alonso-González, M. B. Lundeberg, Y. Gao, J. E. Barrios-Vargas, G. Navickaite, Q. Ma, D. Janner, K. Watanabe, A. W. Cummings, T. Taniguchi, V. Pruneri, S. Roche, P. Jarillo-Herrero, J. Hone, R. Hillenbrand, and F. H. L. Koppens, "Near-field photocurrent nanoscopy on bare and encapsulated graphene," *Nature Communications*, vol. 7, p. 10783, dec 2016.

[106] D. A. Bandurin, D. Svintsov, I. Gayduchenko, S. G. Xu, A. Principi, M. Moskotin, I. Tretyakov, D. Yagodkin, S. Zhukov, T. Taniguchi, K. Watanabe, I. V. Grigorieva, M. Polini, G. N. Goltsman, A. K. Geim, and G. Fedorov, "Resonant terahertz detection using graphene plasmons," *Nature Communications*, vol. 9, p. 5392, dec 2018.

[107] B. Wunsch, T. Stauber, F. Sols, and F. Guinea, "Dynamical polarization of graphene at finite doping," *New Journal of Physics*, vol. 8, 2006.

[108] E. H. Hwang and S. D. Sarma, "Dielectric function, screening, and plasmons in two-dimensional graphene," *Physical Review B*, no. October 2006, pp. 1–6, 2007.

[109] P. Alonso-González, A. Y. Nikitin, Y. Gao, A. Woessner, M. B. Lundeberg, A. Principi, N. Forcellini, W. Yan, S. Vélez, A. J. Huber, K. Watanabe, T. Taniguchi, F. Casanova, L. E. Hueso, M. Polini, J. Hone, F. H. L. Koppens, and R. Hillenbrand, "Acoustic terahertz graphene plasmons revealed by photocurrent nanoscopy," *Nature Nanotechnology*, vol. 12, no. 1, pp. 31–35, 2017.

[110] C. Kallin and B. I. Halperin, "Excitations from a filled Landau level in the two-dimensional electron gas," *Physical Review B*, vol. 30, pp. 5655–5668, nov 1984.

[111] C. Kallin and B. I. Halperin, "Many-body effects on the cyclotron resonance in a two-dimensional electron gas," *Physical Review B*, vol. 31, pp. 3635–3647, mar 1985.

[112] A. H. Macdonald, "Hartree-Fock approximation for response functions and collective excitations in a two-dimensional electron gas with filled Landau levels," *Journal of Physics C: Solid State Physics*, vol. 18, pp. 1003–1016, 1985.

[113] A. H. MacDonald, H. C. A. Oji, and S. M. Girvin, "Magnetoplasmon Excitations from Partially Filled Landau Levels in Two Dimensions," *Physical Review Letters*, vol. 55, pp. 2208–2211, nov 1985.

[114] R. Roldán, J. N. Fuchs, and M. O. Goerbig, "Collective modes of doped graphene and a standard two-dimensional electron gas in a strong magnetic field: Linear magnetoplasmons versus magnetoexcitons," *Physical Review B - Condensed Matter and Materials Physics*, vol. 80, no. 8, pp. 1–6, 2009.

[115] J. Sári and C. Tőke, "Theory of inter-Landau-level magnetoexcitons in bilayer graphene," *Physical Review B*, vol. 87, p. 085432, feb 2013.

[116] S. M. Girvin, A. H. MacDonald, and P. M. Platzman, "Magneto-roton theory of collective excitations in the fractional quantum Hall effect," *Physical Review B*, vol. 33, no. 4, pp. 2481–2494, 1986.

[117] K. Watanabe, T. Taniguchi, and H. Kanda, "Direct-bandgap properties and evidence for ultraviolet lasing of hexagonal boron nitride single crystal," *Nature Materials*, vol. 3, no. 6, pp. 404–409, 2004.

[118] L. Wang, I. Meric, P. Y. Huang, Q. Gao, Y. Gao, H. Tran, T. Taniguchi, K. Watanabe, L. M. Campos, D. a. Muller, J. Guo, P. Kim, J. Hone, K. L. Shepard, and C. R. Dean, "One-dimensional electrical contact to a two-dimensional material.," *Science*, vol. 342, pp. 614–617, 2013.

[119] L. Banszerus, M. Schmitz, S. Engels, M. Goldsche, K. Watanabe, T. Taniguchi, B. Beschoten, and C. Stampfer, "Ballistic Transport Exceeding 28 um in CVD Grown Graphene," *Nano Letters*, vol. 16, no. 2, pp. 1387–1391, 2016.

[120] L. Banszerus, M. Schmitz, S. Engels, J. Dauber, M. Oellers, F. Haupt, K. Watanabe, T. Taniguchi, B. Beschoten, and C. Stampfer, "Ultrahigh-mobility graphene devices from chemical vapor deposition on reusable copper," *Science Advances*, vol. 1, no. 6, pp. 1–6, 2015.

[121] R. Y. Tay, H. J. Park, G. H. Ryu, D. Tan, S. H. Tsang, H. Li, W. Liu, E. H. T. Teo, Z. Lee, Y. Lifshitz, and R. S. Ruoff, "Synthesis of aligned symmetrical multifaceted monolayer hexagonal boron nitride single crystals on resolidified copper," *Nanoscale*, vol. 8, no. 4, pp. 2434–2444, 2016.

[122] R. Y. Tay, S. H. Tsang, M. Loeblein, W. L. Chow, G. C. Loh, J. W. Toh, S. L. Ang, and E. H. T. Teo, "Direct growth of nanocrystalline hexagonal boron nitride films on dielectric substrates," *Applied Physics Letters*, vol. 106, no. 10, 2015.

[123] D. G. Purdie, N. M. Pugno, T. Taniguchi, K. Watanabe, A. C. Ferrari, and A. Lombardo, "Cleaning Interfaces in Layered Materials Heterostructures," *Nature Communications*, no. 2018, pp. 1–12, 2018.

[124] S. Chen, Z. Han, M. M. Elahi, K. M. M. Habib, L. Wang, B. Wen, Y. Gao, T. Taniguchi, K. Watanabe, J. Hone, A. W. Ghosh, and C. R. Dean, "Electron optics with p-n junctions in ballistic graphene," *Science*, vol. 353, pp. 1522–1525, sep 2016.

[125] T. Uwanno, T. Taniguchi, K. Watanabe, and K. Nagashio, "Electrically Inert h-BN/Bilayer Graphene Interface in All-Two-Dimensional Heterostructure Field Effect Transistors," *ACS Applied Materials and Interfaces*, vol. 10, no. 34, pp. 28780–28788, 2018.

[126] L. Banszerus, B. Frohn, A. Epping, D. Neumaier, K. Watanabe, T. Taniguchi, and C. Stampfer, "Gate-Defined Electron-Hole Double Dots in Bilayer Graphene," *Nano Letters*, vol. 18, no. 8, pp. 4785–4790, 2018.

[127] X. Zhou, A. Kerelsky, M. M. Elahi, D. Wang, K. M. M. Habib, R. N. Sajjad, P. Agnihotri, J. U. Lee, A. W. Ghosh, F. M. Ross, and A. N. Pasupathy, "Atomic-Scale Characterization of Graphene p–n Junctions for Electron-Optical Applications," *ACS Nano*, p. acsnano.8b09575, jan 2019.

[128] K. Watanabe, T. Taniguchi, and H. Kanda, "Ultraviolet luminescence spectra of boron nitride single crystals grown under high pressure and high temperature," *Physica Status Solidi (A) Applied Research*, vol. 201, no. 11, pp. 2561–2565, 2004.

[129] Q. Wilmart, A. Inhofer, M. Boukhicha, W. Yang, M. Rosticher, P. Morfin, N. Garroum, G. Fève, J.-M. Berroir, and B. Plaçais, "Contact gating at GHz frequency in graphene," *Scientific Reports*, vol. 6, p. 21085, 2016.

[130] S. Morikawa, Q. Wilmart, S. Masubuchi, K. Watanabe, T. Taniguchi, B. Plaçais, and T. Machida, "Dirac fermion reflector by ballistic graphene sawtooth-shaped npn junctions," *Semiconductor Science and Technology*, vol. 32, no. 4, p. 045010, 2017.

[131] F. T. Aldridge, "High Speed Anisotropic Reactive Ion Etching of Gold Films," *Journal of The Electrochemical Society*, vol. 142, no. 5, p. 1563, 1995.

[132] J. Cayssol, B. Huard, and D. Goldhaber-Gordon, "Contact resistance and shot noise in graphene transistors," *Physical Review B*, vol. 79, no. 7, pp. 1–6, 2009.

[133] L. M. Zhang and M. M. Fogler, "Nonlinear screening and ballistic transport in a graphene p-n junction," *Physical Review Letters*, vol. 100, no. 11, pp. 1–4, 2008.

[134] F. Pizzocchero, L. Gammelgaard, B. S. Jessen, J. M. Caridad, L. Wang, J. Hone, P. Bøggild, and T. J. Booth, "The hot pick-up technique for batch assembly of van der Waals heterostructures," *Nature Communications*, vol. 7, no. May, p. 11894, 2016.

[135] K. Kang, K.-H. Lee, Y. Han, H. Gao, S. Xie, D. A. Muller, and J. Park, "Layer-by-layer assembly of two-dimensional materials into wafer-scale heterostructures," *Nature*, pp. 3–7, 2017.

[136] S. Masubuchi, M. Morimoto, S. Morikawa, M. Onodera, Y. Asakawa, K. Watanabe, T. Taniguchi, and T. Machida, “Autonomous robotic searching and assembly of two-dimensional crystals to build van der Waals superlattices,” *Nature Communications*, vol. 9, no. 1, pp. 4–6, 2018.

[137] A. C. Ferrari, J. C. Meyer, V. Scardaci, C. Casiraghi, M. Lazzeri, F. Mauri, S. Piscanec, D. Jiang, K. S. Novoselov, S. Roth, and A. K. Geim, “Raman spectrum of graphene and graphene layers,” *Physical Review Letters*, vol. 97, no. 18, pp. 1–4, 2006.

[138] A. C. Ferrari and D. M. Basko, “Raman spectroscopy as a versatile tool for studying the properties of graphene,” *Nature Nanotechnology*, vol. 8, no. 4, pp. 235–246, 2013.

[139] R. Geick, C. H. Perry, and G. Rupprecht, “Normal Modes in Hexagonal Boron Nitride,” *Physical Review*, vol. 146, pp. 543–547, jun 1966.

[140] L. Schué, I. Stenger, F. Fossard, A. Loiseau, and J. Barjon, “Characterization methods dedicated to nanometer-thick hBN layers,” *2D Materials*, vol. 4, no. 1, 2017.

[141] L. Banszerus, H. Janssen, M. Otto, A. Epping, T. Taniguchi, K. Watanabe, B. Beschoten, D. Neumaier, and C. Stampfer, “Identifying suitable substrates for high-quality graphene-based heterostructures,” *2D Materials*, pp. 1–6, 2016.

[142] B. Cheng, P. Wang, C. Pan, T. Miao, Y. Wu, T. Taniguchi, K. Watanabe, C. N. Lau, and M. Bockrath, “Raman spectroscopy measurement of bilayer graphene’s twist angle to boron nitride,” *Applied Physics Letters*, vol. 107, no. 3, 2015.

[143] R. Ribeiro-Palau, C. Zhang, K. Watanabe, T. Taniguchi, J. Hone, and C. R. Dean, “Twistable electronics with dynamically rotatable heterostructures,” *Science*, vol. 361, pp. 690–693, aug 2018.

[144] W. Yang, S. Berthou, X. Lu, Q. Wilmart, A. Denis, M. Rosticher, T. Taniguchi, K. Watanabe, G. Fève, J. M. Berroir, G. Zhang, C. Voisin, E. Baudin, and B. Plaçais, “A graphene Zener-Klein transistor cooled by a hyperbolic substrate,” *Nature Nanotechnology*, vol. 13, no. 1, pp. 47–52, 2018.

[145] J. Son, J. Kwon, S. P. Kim, Y. Lv, J. Yu, J. Y. Lee, H. Ryu, K. Watanabe, T. Taniguchi, R. Garrido-Menacho, N. Mason, E. Ertekin, P. Y. Huang, G. H. Lee, and A. M. van der Zande, “Atomically precise graphene etch stops for three dimensional integrated systems from two dimensional material heterostructures,” *Nature Communications*, vol. 9, no. 1, pp. 1–9, 2018.

[146] R. Du, M.-H. Liu, J. Mohrmann, F. Wu, R. Krupke, H. von Löhneysen, K. Richter, and R. Danneau, “Tuning Anti-Klein to Klein Tunneling in Bilayer Graphene,” *Physical Review Letters*, vol. 121, p. 127706, sep 2018.

[147] Anritsu, *The Essentials of Vector Analysis.* 2009.

[148] D. M. Pozar, *Microwave Engineering.* John Wiley & Sons, 3rd ed., 2005.

[149] F. Schwierz, H. Wong, and J. J. Liou, *Nanometer CMOS.* Pan Stanford, 2010.

[150] F. Schwierz, "Graphene transistors," *Nature Nanotechnology*, vol. 5, no. 7, pp. 487–496, 2010.

[151] J. Chaste, E. Pallecchi, P. Morfin, G. Fève, T. Kontos, J. M. Berroir, P. Hakonen, and B. Plaçais, "Thermal shot noise in top-gated single carbon nanotube field effect transistors," *Applied Physics Letters*, vol. 96, no. 19, 2010.

[152] A. C. Betz, S. H. Jhang, E. Pallecchi, R. Ferreira, G. Fève, J. M. Berroir, and B. Plaçais, "Supercollision cooling in undoped graphene," *Nature Physics*, vol. 9, no. 2, pp. 109–112, 2013.

[153] M. von Ardenne, "Das Elektronen-Rastermikroskop. Praktische Ausführung (The scanning electron microscope— practical construction)," *Z tech Phys*, vol. 19, pp. 407–416, 1938.

[154] O. Donati, G. P. Missiroli, and G. Pozzi, "An Experiment on Electron Interference," *American Journal of Physics*, vol. 41, no. 5, pp. 639–644, 1973.

[155] D. Dragoman and M. Dragoman, "Optical analogue structures to mesoscopic devices," *Progress in Quantum Electronics*, vol. 23, no. 4, pp. 131–188, 1999.

[156] D. Dragoman and M. Dragoman, *Quantum-Classical Analogies.* Springer, 2013.

[157] J. Spector, H. L. Stormer, K. W. Baldwin, L. N. Pfeiffer, and K. W. West, "Refractive switch for two-dimensional electrons," *Applied Physics Letters*, vol. 56, no. 24, pp. 2433–2435, 1990.

[158] J. Spector, H. L. Stormer, K. W. Baldwin, L. N. Pfeiffer, and K. W. West, "Electron focusing in two-dimensional systems by means of an electrostatic lens," *Applied Physics Letters*, vol. 56, no. 13, pp. 1290–1292, 1990.

[159] U. Sivan, M. Heiblum, C. P. Umbach, and H. Shtrikman, "Electrostatic electron lens in the ballistic regime," *Physical Review B*, vol. 41, no. 11, pp. 7937–7940, 1990.

[160] V. V. Cheianov, V. Fal'ko, and B. L. Altshuler, "The Focusing of Electron Flow and a Veselago Lens in Graphene p-n Junctions," *Science*, vol. 315, pp. 1252–1255, mar 2007.

[161] V. V. Cheianov and V. I. Fal'ko, "Selective transmission of Dirac electrons and ballistic magnetoresistance of n-p junctions in graphene," *Physical Review B - Condensed Matter and Materials Physics*, vol. 74, no. 4, pp. 1–4, 2006.

[162] B. Huard, J. A. Sulpizio, N. Stander, K. Todd, B. Yang, and D. Goldhaber-Gordon, "Transport measurements across a tunable potential barrier in graphene," *Physical Review Letters*, vol. 98, no. 23, p. 236803, 2007.

[163] P. E. Allain and J. N. Fuchs, "Klein tunneling in graphene: Optics with massless electrons," *European Physical Journal B*, vol. 83, pp. 301–317, 2011.

[164] R. N. Sajjad, S. Sutar, J. U. Lee, and A. W. Ghosh, "Manifestation of chiral tunneling at a tilted graphene p-n junction," *Physical Review B - Condensed Matter and Materials Physics*, vol. 86, no. 15, pp. 1–5, 2012.

[165] A. V. Shytov, M. S. Rudner, and L. S. Levitov, “Klein Backscattering and Fabry-Pérot Interference in Graphene Heterojunctions,” *Physical Review Letters*, vol. 101, p. 156804, oct 2008.

[166] J. R. Williams, T. Low, M. S. Lundstrom, and C. M. Marcus, “Gate-controlled guiding of electrons in graphene,” *Nature Nanotechnology*, vol. 6, no. 4, pp. 222–225, 2011.

[167] G. H. Lee, G. H. Park, and H. J. Lee, “Observation of negative refraction of Dirac fermions in graphene,” *Nature Physics*, vol. 11, no. 11, pp. 925–929, 2015.

[168] S. Chen, Z. Han, M. M. Elahi, K. M. M. Habib, L. Wang, B. Wen, Y. Gao, T. Taniguchi, K. Watanabe, J. Hone, A. W. Ghosh, and C. R. Dean, “Electron optics with ballistic graphene junctions,” *Science*, vol. 353, no. 6307, 2016.

[169] R. V. Gorbachev, A. S. Mayorov, A. K. Savchenko, D. W. Horsell, and F. Guinea, “Conductance of p-n-p Graphene Structures with ”Air-Bridge” Top Gates,” *Nano Letters*, vol. 8, no. 7, pp. 1995–1999, 2008.

[170] N. Stander, B. Huard, and D. Goldhaber-Gordon, “Evidence for Klein tunneling in graphene p-n junctions,” *Physical Review Letters*, vol. 102, no. 2, p. 026807, 2009.

[171] P. Rickhaus, M. H. Liu, P. Makk, R. Maurand, S. Hess, S. Zihlmann, M. Weiss, K. Richter, and C. Schönenberger, “Guiding of Electrons in a Few-Mode Ballistic Graphene Channel,” *Nano Letters*, vol. 15, no. 9, pp. 5819–5825, 2015.

[172] A. L. Grushina, D. K. Ki, and A. F. Morpurgo, “A ballistic pn junction in suspended graphene with split bottom gates,” *Applied Physics Letters*, vol. 102, no. 22, 2013.

[173] M. Oksanen, A. Uppstu, A. Laitinen, D. J. Cox, M. F. Craciun, S. Russo, A. Harju, and P. Hakonen, “Single-mode and multimode Fabry-Pérot interference in suspended graphene,” *Physical Review B - Condensed Matter and Materials Physics*, vol. 89, no. 12, pp. 1–5, 2014.

[174] P. Rickhaus, P. Makk, M. H. Liu, E. Tóvári, M. Weiss, R. Maurand, K. Richter, and C. Schönenberger, “Snake trajectories in ultraclean graphene p-n junctions,” *Nature Communications*, vol. 6, pp. 1–6, 2015.

[175] A. Rahman, J. W. Guikema, N. M. Hassan, and N. Marković, “Angle-dependent transmission in graphene heterojunctions,” *Applied Physics Letters*, vol. 106, no. 1, 2015.

[176] H. van Houten, C. W. J. Beenakker, J. G. Willianson, M. E. I. Broekaart, P. H. M. VanLoosdrecht, B. J. van Wees, J. E. Mooji, C. T. Foxon, and J. J. Harris, “Coherent electron focusing with quantum point contacts in a 2DEG,” *Phys. Rev. B*, vol. 39, no. 12, p. 8556, 1989.

[177] T. Taychatanapat, K. Watanabe, T. Taniguchi, and P. Jarillo-Herrero, “Electrically tunable transverse magnetic focusing in graphene,” *Nature Physics*, vol. 9, no. 4, pp. 225–229, 2013.

[178] V. Tsoi, J. Bass, and P. Wyder, “Studying conduction-electron/interface interactions using tranverse electron focusing,” *Reviews of Modern Physics-file:///home/hgraef/Downloads/e_021_03_0655.pdf*, vol. 71, no. 5, pp. 1641–1693, 1999.

[179] S. Bhandari, G. H. Lee, A. Klales, K. Watanabe, T. Taniguchi, E. Heller, P. Kim, and R. M. Westervelt, “Imaging Cyclotron Orbits of Electrons in Graphene,” *Nano Letters*, vol. 16, no. 3, pp. 1690–1694, 2016.

[180] M. Lee, J. R. Wallbank, P. Gallagher, K. Watanabe, T. Taniguchi, V. I. Falko, and D. Goldhaber-Gordon, “Ballistic miniband conduction in a graphene superlattice,” *Science*, vol. 353, pp. 1526–1529, sep 2016.

[181] A. W. Barnard, A. Hughes, A. L. Sharpe, K. Watanabe, T. Taniguchi, and D. Goldhaber-Gordon, “Absorptive pinhole collimators for ballistic Dirac fermions in graphene,” *Nature Communications*, vol. 8, p. 15418, may 2017.

[182] E. V. Castro, K. S. Novoselov, S. V. Morozov, N. M. R. Peres, J. M. B. L. dos Santos, J. Nilsson, F. Guinea, A. K. Geim, and A. H. C. Neto, “Biased bilayer graphene: Semiconductor with a gap tunable by the electric field effect,” *Physical Review Letters*, vol. 99, pp. 8–11, nov 2007.

[183] Y. Zhang, T. T. Tang, C. Girit, Z. Hao, M. C. Martin, A. Zettl, M. F. Crommie, Y. R. Shen, and F. Wang, “Direct observation of a widely tunable bandgap in bilayer graphene,” *Nature*, vol. 459, no. 7248, pp. 820–823, 2009.

[184] A. F. Young and L. S. Levitov, “Capacitance of graphene bilayer as a probe of layer-specific properties,” *Physical Review B - Condensed Matter and Materials Physics*, vol. 84, no. 8, pp. 1–7, 2011.

[185] A. F. Young, C. R. Dean, I. Meric, S. Sorgenfrei, H. Ren, K. Watanabe, T. Taniguchi, J. Hone, K. L. Shepard, and P. Kim, “Electronic compressibility of layer-polarized bilayer graphene,” *Physical Review B - Condensed Matter and Materials Physics*, vol. 85, no. 23, pp. 1–5, 2012.

[186] M. Eich, R. Pisoni, A. Pally, H. Overweg, A. Kurzmann, Y. Lee, P. Rickhaus, K. Watanabe, T. Taniguchi, K. Ensslin, and T. Ihn, “Coupled Quantum Dots in Bilayer Graphene,” *Nano Letters*, vol. 18, no. 8, pp. 5042–5048, 2018.

[187] R. N. Sajjad and A. W. Ghosh, “High efficiency switching using graphene based electron ”optics”,” *Applied Physics Letters*, vol. 99, no. 12, pp. 1–4, 2011.

[188] R. N. Sajjad and A. W. Ghosh, “Manipulating chiral transmission by gate geometry: Switching in graphene with transmission gaps,” *ACS Nano*, vol. 7, no. 11, pp. 9808–9813, 2013.

[189] M. S. Jang, H. Kim, Y.-W. Son, H. A. Atwater, and W. A. Goddard, “Graphene field effect transistor without an energy gap,” *Proceedings of the National Academy of Sciences*, vol. 110, no. 22, pp. 8786–8789, 2013.

[190] Q. Wilmart, S. Berrada, D. Torrin, V. Hung Nguyen, G. Fève, J.-M. Berroir, P. Dollfus, and B. Plaçais, "A Klein-tunneling transistor with ballistic graphene," *2D Materials*, vol. 1, 2014.

[191] M. M. Elahi, K. M. Masum Habib, K. Wang, G.-H. Lee, P. Kim, and A. W. Ghosh, "Impact of geometry and non-idealities on electron "optics" based graphene p-n junction devices," *Applied Physics Letters*, vol. 114, p. 013507, jan 2019.

[192] C. Stampfer, J. Güttinger, S. Hellmüller, F. Molitor, K. Ensslin, and T. Ihn, "Energy gaps in etched graphene nanoribbons," *Physical Review Letters*, vol. 102, no. 5, pp. 1–4, 2009.

[193] D. Mele, S. Mehdhbi, D. Fadil, W. Wei, A. Ouerghi, S. Lepilliet, H. Happy, and E. Pallecchi, "Graphene FETs based on high resolution nanoribbons for HF low power applications," *Electronic Materials Letters*, vol. 14, no. 2, pp. 133–138, 2018.

[194] S. Sutar, E. S. Comfort, J. Liu, T. Taniguchi, K. Watanabe, and J. U. Lee, "Angle-dependent carrier transmission in graphene p-n junctions," *Nano Letters*, vol. 12, no. 9, pp. 4460–4464, 2012.

[195] Y. Tan, M. M. Elahi, H. Y. Tsao, K. M. Habib, N. S. Barker, and A. W. Ghosh, "Graphene Klein tunnel transistors for high speed analog RF applications," *Scientific Reports*, vol. 7, no. 1, pp. 1–9, 2017.

[196] P. Rickhaus, P. Makk, M. H. Liu, K. Richter, and C. Schönenberger, "Gate tuneable beamsplitter in ballistic graphene," *Applied Physics Letters*, vol. 107, no. 25, 2015.

[197] K. Wang, G.-H. Lee, M. M. Elahi, K. M. M. Habib, A. W. Ghosh, and P. Kim, "Graphene transistor based on tunable Dirac-Fermion-optics," *Manuscript in preparation*, 2018.

[198] E. Bocquillon, V. Freulon, F. D. Parmentier, J. M. Berroir, B. Plaçais, C. Wahl, J. Rech, T. Jonckheere, T. Martin, C. Grenier, D. Ferraro, P. Degiovanni, and G. Fève, "Electron quantum optics in ballistic chiral conductors," *Annalen der Physik*, vol. 526, no. 1-2, pp. 1–30, 2014.

[199] N. Kumada, F. D. Parmentier, H. Hibino, D. C. Glattli, and P. Roulleau, "Shot noise generated by graphene p-n junctions in the quantum Hall effect regime," *Nature Communications*, vol. 6, pp. 1–5, 2015.

[200] D. S. Wei, T. Van Der Sar, J. D. Sanchez-Yamagishi, K. Watanabe, T. Taniguchi, P. Jarillo-Herrero, B. I. Halperin, and A. Yacoby, "Mach-Zehnder interferometry using spin- and valley-polarized quantum Hall edge states in graphene," *Science Advances*, vol. 3, no. 8, pp. 1–8, 2017.

[201] K. Zimmermann, A. Jordan, F. Gay, K. Watanabe, T. Taniguchi, Z. Han, V. Bouchiat, H. Sellier, and B. Sacépé, "Tunable transmission of quantum Hall edge channels with full degeneracy lifting in split-gated graphene devices," *Nature Communications*, vol. 8, pp. 1–7, 2017.

[202] P. Bøggild, J. M. Caridad, C. Stampfer, G. Calogero, N. R. Papior, and M. Brandbyge, “A two-dimensional Dirac fermion microscope,” *Nature Communications*, vol. 8, p. 15783, 2017.

[203] H. Y. Xu, G. L. Wang, L. Huang, and Y. C. Lai, “Chaos in Dirac Electron Optics: Emergence of a Relativistic Quantum Chimera,” *Physical Review Letters*, vol. 120, no. 12, p. 124101, 2018.

[204] J. M. Caridad, S. Connaughton, C. Ott, H. B. Weber, and V. Krstić, “An electrical analogy to Mie scattering,” *Nature Communications*, vol. 7, p. 12894, 2016.

[205] B. Brun, N. Moreau, S. Somanchi, V.-H. Nguyen, K. Watanabe, T. Taniguchi, J.-C. Charlier, C. Stampfer, and B. Hackens, “Imaging Dirac fermions flow though a circular Veselago lens,” *arXiv preprint 1811.02929*, nov 2018.

[206] D. A. Bandurin, I. Torre, R. K. Kumar, M. Ben Shalom, A. Tomadin, A. Principi, G. H. Auton, E. Khestanova, K. S. Novoselov, I. V. Grigorieva, L. A. Ponomarenko, A. K. Geim, and M. Polini, “Negative local resistance caused by viscous electron backflow in graphene,” *Science*, vol. 351, no. 6277, pp. 1055–1058, 2016.

[207] R. Krishna Kumar, D. A. Bandurin, F. M. Pellegrino, Y. Cao, A. Principi, H. Guo, G. H. Auton, M. Ben Shalom, L. A. Ponomarenko, G. Falkovich, K. Watanabe, T. Taniguchi, I. V. Grigorieva, L. S. Levitov, M. Polini, and A. K. Geim, “Superballistic flow of viscous electron fluid through graphene constrictions,” *Nature Physics*, vol. 13, no. 12, pp. 1182–1185, 2017.

[208] D. Pandey, M. Villani, E. Colomés, Z. Zhan, and X. Oriols, “Implications of the Klein tunneling times on high frequency graphene devices using Bohmian trajectories,” *Semiconductor Science and Technology*, vol. 34, p. 034002, mar 2019.

[209] T. I. Andersen, B. L. Dwyer, J. D. Sanchez-Yamagishi, J. F. Rodriguez-Nieva, K. Agarwal, K. Watanabe, T. Taniguchi, E. A. Demler, P. Kim, H. Park, and M. D. Lukin, “Electron-phonon instability in graphene revealed by global and local noise probes.,” *Science (New York, N.Y.)*, vol. 364, no. 6436, pp. 154–157, 2019.

[210] S. Morikawa, Z. Dou, S. W. Wang, C. G. Smith, K. Watanabe, T. Taniguchi, S. Masubuchi, T. Machida, and M. R. Connolly, “Imaging ballistic carrier trajectories in graphene using scanning gate microscopy,” *Applied Physics Letters*, vol. 107, no. 24, 2015.

[211] B. Brun, F. Martins, S. Faniel, A. Cavanna, C. Ulysse, A. Ouerghi, U. Gennser, D. Mailly, P. Simon, S. Huant, M. Sanquer, H. Sellier, V. Bayot, and B. Hackens, “Thermoelectric Scanning-Gate Interferometry on a Quantum Point Contact,” *Physical Review Applied*, vol. 11, no. 3, p. 1, 2019.

[212] L. Ella, A. Rozen, J. Birkbeck, M. Ben-Shalom, D. Perello, J. Zultak, T. Taniguchi, K. Watanabe, A. K. Geim, S. Ilani, and J. A. Sulpizio, “Simultaneous imaging of voltage and current density of flowing electrons in two dimensions,” *Nature Nanotechnology*, 2018.

[213] J.-P. Tetienne, N. Dontschuk, D. A. Broadway, A. Stacey, D. A. Simpson, and L. C. L. Hollenberg, "Quantum imaging of current flow in graphene," *Science Advances*, vol. 3, p. e1602429, apr 2017.

[214] Y. Betancur-Ocampo and V. Gupta, "Perfect transmission of 3D massive Kane fermions in HgCdTe Veselago lenses," *Journal of Physics Condensed Matter*, vol. 30, no. 3, 2018.

[215] V. Hung Nguyen and J.-C. Charlier, "Klein tunneling and electron optics in Dirac-Weyl fermion systems with tilted energy dispersion," *Physical Review B*, vol. 97, p. 235113, jun 2018.

[216] I. Meric, M. Y. Han, A. F. Young, B. Ozyilmaz, P. Kim, and K. L. Shepard, "Current saturation in zero-bandgap, top-gated graphene field-effect transistors," *Nature Nanotechnology*, vol. 3, no. 11, pp. 654–659, 2008.

[217] G. Fiori, F. Bonaccorso, G. Iannaccone, T. Palacios, D. Neumaier, A. Seabaugh, S. K. Banerjee, and L. Colombo, "Electronics based on two-dimensional materials," *Nature Nanotechnology*, vol. 9, no. 10, pp. 768–779, 2014.

[218] E. Pallecchi, C. Benz, A. C. Betz, H. V. Lhneysen, B. Plaais, and R. Danneau, "Graphene microwave transistors on sapphire substrates," *Applied Physics Letters*, vol. 99, no. 11, pp. 199–201, 2011.

[219] M. Bonmann, M. Asad, X. Yang, A. Generalov, A. Vorobiev, L. Banszerus, C. Stampfer, M. Otto, D. Neumaier, and J. Stake, "Graphene field-effect transistors with high extrinsic fT and fmax," *IEEE Electron Device Letters*, vol. 40, no. 1, pp. 131–134, 2019.

[220] Y.-M. Lin, C. Dimitrakopoulos, K. A. Jenkins, D. B. Farmer, H.-Y. Chiu, A. Grill, and P. Avouris, "100-GHz Transistors from Wafer-Scale Epitaxial Graphene," *Science*, vol. 327, no. 5966, pp. 662–662, 2010.

[221] M. Dyakonov and M. Shur, "Shallow water analogy for a ballistic field effect transistor: New mechanism of plasma wave generation by dc current," *Physical Review Letters*, vol. 71, no. 15, pp. 2465–2468, 1993.

[222] M. I. Dyakonov and M. S. Shur, "Plasma wave electronics: Novel terahertz devices using two dimensional electron fluid," *IEEE Transactions on Electron Devices*, vol. 43, no. 10, pp. 1640–1645, 1996.

[223] M. Staffaroni, J. Conway, S. Vedantam, J. Tang, and E. Yablonovitch, "Circuit analysis in metal-optics," *Photonics and Nanostructures - Fundamentals and Applications*, vol. 10, no. 1, pp. 166–176, 2012.

[224] G. R. Aizin and G. C. Dyer, "Transmission line theory of collective plasma excitations in periodic two-dimensional electron systems: Finite plasmonic crystals and Tamm states," *Physical Review B - Condensed Matter and Materials Physics*, vol. 86, no. 23, pp. 1–11, 2012.

[225] J. S. Gomez-Diaz and J. Perruisseau-Carrier, “A transmission line model for plasmon propagation on a graphene strip,” *IEEE MTT-S International Microwave Symposium Digest*, no. 1, pp. 13–15, 2013.

[226] H. Yoon, C. Forsythe, L. Wang, N. Tombros, K. Watanabe, T. Taniguchi, J. Hone, P. Kim, and D. Ham, “Measurement of collective dynamical mass of Dirac fermions in graphene,” *Nature Nanotechnology*, vol. 9, no. 8, pp. 594–599, 2014.

[227] M. H. Devoret, A. Wallraff, and J. M. Martinis, “Superconducting Qubits: A Short Review,” *arXiv preprint 041174*, 2004.

[228] Y. Liu and R. F. Willis, “Plasmon-phonon strongly coupled mode in epitaxial graphene,” *Physical Review B - Condensed Matter and Materials Physics*, vol. 81, no. 8, pp. 1–4, 2010.

[229] R. J. Koch, T. Seyller, and J. A. Schaefer, “Strong phonon-plasmon coupled modes in the graphene/silicon carbide heterosystem,” *Physical Review B - Condensed Matter and Materials Physics*, vol. 82, no. 20, pp. 1–4, 2010.

[230] C. Tegenkamp, H. Pfnür, T. Langer, J. Baringhaus, and H. W. Schumacher, “Plasmon electron-hole resonance in epitaxial graphene,” *Journal of Physics Condensed Matter*, vol. 23, no. 1, 2011.

[231] A. Bostwick, T. Ohta, T. Seyller, K. Horn, and E. Rotenberg, “Quasiparticle dynamics in graphene,” *Nature Physics*, vol. 3, no. 1, pp. 36–40, 2007.

[232] V. W. Brar, S. Wickenburg, M. Panlasigui, C. H. Park, T. O. Wehling, Y. Zhang, R. Decker, Ç. Girit, A. V. Balatsky, S. G. Louie, A. Zettl, and M. F. Crommie, “Observation of Carrier-Density-Dependent Many-Body Effects in Graphene via Tunneling Spectroscopy,” *Physical Review Letters*, vol. 104, no. 3, pp. 1–4, 2010.

[233] J. M. Poumirol, W. Yu, X. Chen, C. Berger, W. A. de Heer, M. L. Smith, T. Ohta, W. Pan, M. O. Goerbig, D. Smirnov, and Z. Jiang, “Magnetoplasmons in Quasineutral Epitaxial Graphene Nanoribbons,” *Physical Review Letters*, vol. 110, p. 246803, jun 2013.

[234] A. Woessner, M. B. Lundeberg, Y. Gao, A. Principi, P. Alonso-González, M. Carrega, K. Watanabe, T. Taniguchi, G. Vignale, M. Polini, J. Hone, R. Hillenbrand, and F. H. Koppens, “Highly confined low-loss plasmons in graphene-boron nitride heterostructures,” *Nature Materials*, vol. 14, no. 4, pp. 421–425, 2015.

[235] G. X. Ni, H. Wang, J. S. Wu, Z. Fei, M. D. Goldflam, F. Keilmann, B. Özyilmaz, A. H. Castro Neto, X. M. Xie, M. M. Fogler, and D. N. Basov, “Plasmons in graphene moiré superlattices,” *Nature Materials*, vol. 14, pp. 1217–1222, dec 2015.

[236] P. Alonso-Gonzalez, A. Y. Nikitin, F. Golmar, A. Centeno, A. Pesquera, S. Velez, J. Chen, G. Navickaite, F. Koppens, A. Zurutuza, F. Casanova, L. E. Hueso, and R. Hillenbrand, “Controlling graphene plasmons with resonant metal antennas and spatial conductivity patterns,” *Science*, vol. 344, pp. 1369–1373, jun 2014.

[237] G. X. Ni, A. S. Mcleod, Z. Sun, L. Wang, L. Xiong, K. W. Post, S. S. Sunku, B.-Y. Jiang, J. Hone, C. R. Dean, M. M. Fogler, and D. N. Basov, "Fundamental limits to graphene plasmonics," *Nature*, vol. 557, p. 530, 2018.

[238] M. B. Lundeberg, Y. Gao, A. Woessner, C. Tan, P. Alonso-González, K. Watanabe, T. Taniguchi, J. Hone, R. Hillenbrand, and F. H. L. Koppens, "Thermoelectric detection and imaging of propagating graphene plasmons," *Nature Materials*, vol. 16, pp. 204–207, feb 2017.

[239] L. Vicarelli, M. S. Vitiello, D. Coquillat, A. Lombardo, A. C. Ferrari, W. Knap, M. Polini, V. Pellegrini, and A. Tredicucci, "Graphene field-effect transistors as room-temperature terahertz detectors," *Nature Materials*, vol. 11, no. 10, pp. 865–871, 2012.

[240] A. Inhofer, S. Tchoumakov, B. A. Assaf, G. Fève, J. M. Berroir, V. Jouffrey, D. Carpentier, M. O. Goerbig, B. Plaçais, K. Bendias, D. M. Mahler, E. Bocquillon, R. Schlereth, C. Brüne, H. Buhmann, and L. W. Molenkamp, "Observation of Volkov-Pankratov states in topological HgTe heterojunctions using high-frequency compressibility," *Physical Review B*, vol. 96, no. 19, pp. 1–13, 2017.

[241] A. Inhofer, J. Duffy, M. Boukhicha, E. Bocquillon, J. Palomo, K. Watanabe, T. Taniguchi, I. Estève, J. M. Berroir, G. Fève, B. Plaçais, and B. A. Assaf, "rf Quantum Capacitance of the Topological Insulator Bi2Se3 in the Bulk Depleted Regime for Field-Effect Transistors," *Physical Review Applied*, vol. 9, no. 2, p. 024022, 2018.

[242] M. C. Dartiailh, S. Hartinger, A. Gourmelon, K. Bendias, H. Bartolomei, J.-M. Berroir, G. Fève, B. Plaçais, L. Lunczer, R. Schlereth, H. Buhmann, L. W. Molenkamp, and E. Bocquillon, "Dressed topological edge states in HgTe-based 2D topological insulators," *arXiv preprint 1903.12391*, pp. 1–11, 2019.

[243] S. J. Allen, D. C. Tsui, and R. A. Logan, "Observation of the two-dimensional plasmon in silicon inversion layers," *Physical Review Letters*, vol. 38, no. 17, pp. 980–983, 1977.

[244] R. Tarkiainen, M. Ahlskog, J. Penttilä, L. Roschier, P. Hakonen, M. Paalanen, and E. Sonin, "Multiwalled carbon nanotube: Luttinger versus Fermi liquid," *Physical Review B*, vol. 64, p. 195412, oct 2001.

[245] P. J. Burke, "Lüttinger liquid theory as a model of the gigahertz electrical properties of carbon nanotubes," *IEEE Transactions on Nanotechnology*, vol. 1, no. 3, pp. 129–144, 2002.

[246] P. J. Burke, "AC performance of nanoelectronics: Towards a ballistic THz nanotube transistor," *Solid-State Electronics*, vol. 48, no. 10-11 SPEC. ISS., pp. 1981–1986, 2004.

[247] G. C. Dyer, G. R. Aizin, S. Preu, N. Q. Vinh, S. J. Allen, J. L. Reno, and E. A. Shaner, "Inducing an incipient terahertz finite plasmonic crystal in coupled two dimensional plasmonic cavities," *Physical Review Letters*, vol. 109, no. 12, pp. 1–5, 2012.

[248] G. C. Dyer, G. R. Aizin, S. J. Allen, A. D. Grine, D. Bethke, J. L. Reno, and E. A. Shaner, "Induced transparency by coupling of Tamm and defect states in tunable terahertz plasmonic crystals," *Nature Photonics*, vol. 7, no. 11, pp. 925–930, 2013.

[249] W. F. Andress, H. Yoon, K. Y. M. Yeung, L. Qin, K. West, L. Pfeiffer, and D. Ham, "Ultra-subwavelength two-dimensional plasmonic circuits," *Nano Letters*, vol. 12, no. 5, pp. 2272–2277, 2012.

[250] H. J. Lee, E. Kim, J. G. Yook, and J. Jung, "Intrinsic characteristics of transmission line of graphenes at microwave frequencies," *Applied Physics Letters*, vol. 100, no. 22, pp. 1–4, 2012.

[251] H. S. Skulason, H. V. Nguyen, A. Guermoune, V. Sridharan, M. Siaj, C. Caloz, and T. Szkopek, "110 GHz measurement of large-area graphene integrated in low-loss microwave structures," *Applied Physics Letters*, vol. 99, no. 15, pp. 10–13, 2011.

[252] N. Kumada, S. Tanabe, H. Hibino, H. Kamata, M. Hashisaka, K. Muraki, and T. Fujisawa, "Plasmon transport in graphene investigated by time-resolved electrical measurements," *Nature Communications*, vol. 4, p. 1363, dec 2013.

[253] N. Kumada, P. Roulleau, B. Roche, M. Hashisaka, H. Hibino, I. Petković, and D. C. Glattli, "Resonant edge magnetoplasmons and their decay in graphene," *Physical Review Letters*, vol. 113, no. 26, pp. 1–5, 2014.

[254] N. Kumada, R. Dubourget, K. Sasaki, S. Tanabe, H. Hibino, H. Kamata, M. Hashisaka, K. Muraki, and T. Fujisawa, "Plasmon transport and its guiding in graphene," *New Journal of Physics*, vol. 16, no. 6, p. 063055, 2014.

[255] V. M. Muravev, A. A. Fortunatov, I. V. Kukushkin, J. H. Smet, W. Dietsche, and K. Von Klitzing, "Tunable plasmonic crystals for edge magnetoplasmons of a two-dimensional electron system," *Physical Review Letters*, vol. 101, no. 21, pp. 1–4, 2008.

[256] V. Ryzhii, M. Ryzhii, M. S. Shur, V. Mitin, A. Satou, and T. Otsuji, "Resonant plasmonic terahertz detection in graphene split-gate field-effect transistors with lateral p–n junctions," *Journal of Physics D: Applied Physics*, vol. 49, no. 31, p. 315103, 2016.

[257] J. Hofmann, "Quantum oscillations in Dirac magnetoplasmons," *arXiv preprint 1904.01583*, pp. 1–6, apr 2019.

[258] D. O. Oriekhov and L. S. Levitov, "Plasmon Resonances and Tachyon Ghost Modes in Highly Conducting Sheets," *arXiv preprint 1903.10648*, no. 2, pp. 1–5, 2019.

[259] Y. V. Sharvin, "A possible method for studying Fermi surfaces," *Zh. Eksp. Teor. Fiz.*, vol. 48, p. 984, 1965.

[260] L. Eaves and F. W. Sheard, "Size-dependent quantised breakdown of the dissipationless quantum Hall effect in narrow channels," *Semiconductor Science and Technology*, vol. 1, no. 6, pp. 346–349, 1986.

[261] Y. Kawano, Y. Hisanaga, and S. Komiyama, "Cyclotron emission from quantized Hall devices: Injection of nonequilibrium electrons from contacts," *Physical Review B*, vol. 59, no. 19, pp. 12537–12546, 1999.

[262] G. Nachtwei, "Breakdown of the quantum Hall effect," *Physica E*, vol. 4, pp. 79–101, 1999.

[263] G. Ebert, K. von Klitzing, K. Ploog, and G. Weinmann, “Two-dimensional magneto-quantum transport on GaAs-Al x Ga 1-x As heterostructures under non-ohmic conditions,” *Journal of Physics C: Solid State Physics*, vol. 16, pp. 5441–5448, oct 1983.

[264] M. E. Cage, R. F. Dziuba, B. F. Field, E. R. Williams, S. M. Girvin, A. C. Gossard, D. C. Tsui, and R. J. Wagner, “Dissipation and Dynamic Nonlinear Behavior in the Quantum Hall Regime,” *Physical Review Letters*, vol. 51, pp. 1374–1377, oct 1983.

[265] D. Tsui, G. Dolan, and A. Gossard, “?,” *Bull. Am. Phys. Soc.*, vol. 28, p. 365, 1983.

[266] P. Streda and K. von Klitzing, “Critical non-dissipative current of quantum Hall regime,” *Journal of Physics C: Solid State Physics*, vol. 17, pp. L483–L486, 1984.

[267] V. Tsemekhman, K. Tsemekhman, C. Wexler, J. H. Han, and D. J. Thouless, “Theory of the breakdown of the quantum Hall effect,” *Physical Review B*, vol. 55, no. 16, pp. R10201–R10204, 1997.

[268] O. Heinonen, P. L. Taylor, and S. M. Girvin, “Electron-phonon interactions and the breakdown of the dissipationless quantum Hall effect,” *Physical Review B*, vol. 30, pp. 3016–3019, sep 1984.

[269] S. Komiyama, T. Takamasu, S. Hiyamizu, and S. Sasa, “Breakdown of the quantum Hall effect due to electron heating,” *Solid State Communications*, vol. 54, no. 6, pp. 479–484, 1985.

[270] S. Komiyama and Y. Kawaguchi, “Heat instability of quantum Hall conductors,” *Physical Review B*, vol. 61, pp. 2014–2027, jan 2000.

[271] J. A. Alexander-Webber, A. M. R. Baker, T. J. B. M. Janssen, A. Tzalenchuk, S. Lara-Avila, S. Kubatkin, R. Yakimova, B. A. Piot, D. K. Maude, and R. J. Nicholas, “Phase Space for the Breakdown of the Quantum Hall Effect in Epitaxial Graphene,” *Physical Review Letters*, vol. 111, p. 096601, aug 2013.

[272] G. Nachtwei, Z. Liu, G. Lütjering, R. Gerhardts, D. Weiss, K. v. Klitzing, and K. Eberl, “Critical currents in quantum Hall conductors with antidot arrays,” *Physical Review B - Condensed Matter and Materials Physics*, vol. 57, no. 16, pp. 9937–9944, 1998.

[273] Y. Kawaguchi, F. Hayashi, S. Komiyama, T. Osada, Y. Shiraki, and R. Atoh, “Disappearance of the breakdown of quantum hall effects in short devices,” *Japanese Journal of Applied Physics*, vol. 34, no. 8, pp. 4309–4312, 1995.

[274] S. Komiyama, Y. Kawaguchi, T. Osada, and Y. Shiraki, “Evidence of nonlocal breakdown of the integer quantum hall effect,” *Physical Review Letters*, vol. 77, no. 3, pp. 558–561, 1996.

[275] L. Bliek, E. Braun, G. Hein, V. Kose, J. Niemeyer, G. Weimann, and W. Schlapp, “Critical current density for the dissipationless quantum Hall effect,” *Semiconductor Science and Technology*, vol. 1, pp. 110–112, aug 1986.

[276] S. Kawaji, K. Hirakawa, and M. Nagata, “Device-width dependence of plateau width in quantum Hall states,” *Physica B: Physics of Condensed Matter*, vol. 184, no. 1-4, pp. 17–20, 1993.

[277] A. Boisen, P. Boggild, A. Kristensen, and P. E. Lindelof, “Nonlinear current-voltage characteristics at quantum Hall resistance minima,” *Physical Review B*, vol. 50, no. 3, pp. 1957–1960, 1994.

[278] N. Q. Balaban, U. Meirav, H. Shtrikman, and Y. Levinson, “Scaling of the critical current in the quantum Hall effect: A probe of current distribution,” *Physical Review Letters*, vol. 71, pp. 1443–1446, aug 1993.

[279] C. Lavine, M. Cage, and R. Elmquist, “Spectroscopic study of quantized breakdown voltage states of the quantum Hall effect,” *Journal of Research of the National Institute of Standards and Technology*, vol. 99, p. 757, nov 1994.

[280] K. Chida, T. Hata, T. Arakawa, S. Matsuo, Y. Nishihara, T. Tanaka, T. Ono, and K. Kobayashi, “Avalanche electron bunching in a Corbino disk in the quantum Hall effect breakdown regime,” *Physical Review B*, vol. 89, p. 235318, jun 2014.

[281] R. Ribeiro-Palau, F. Lafont, J. Brun-Picard, D. Kazazis, A. Michon, F. Cheynis, O. Couturaud, C. Consejo, B. Jouault, W. Poirier, and F. Schopfer, “Quantum Hall resistance standard in graphene devices under relaxed experimental conditions,” *Nature Nanotechnology*, vol. 10, no. 11, pp. 965–971, 2015.

[282] A. M. R. Baker, J. A. Alexander-Webber, T. Altebaeumer, and R. J. Nicholas, “Energy relaxation for hot Dirac fermions in graphene and breakdown of the quantum Hall effect,” *Physical Review B*, vol. 85, p. 115403, mar 2012.

[283] K. Panos, R. R. Gerhardts, J. Weis, and K. V. Klitzing, “Current distribution and Hall potential landscape towards breakdown of the quantum Hall effect: a scanning force microscopy investigation,” *New Journal of Physics*, vol. 16, p. 113071, nov 2014.

[284] T. Hata, T. Arakawa, K. Chida, S. Matsuo, and K. Kobayashi, “Giant Fano factor and bistability in a Corbino disk in the quantum Hall effect breakdown regime,” *Journal of Physics: Condensed Matter*, vol. 28, p. 055801, feb 2016.

[285] J. Guignard, D. Leprat, D. C. Glattli, F. Schopfer, and W. Poirier, “Quantum Hall effect in exfoliated graphene affected by charged impurities: Metrological measurements,” *Physical Review B - Condensed Matter and Materials Physics*, vol. 85, no. 16, pp. 1–14, 2012.

[286] V. Singh and M. M. Deshmukh, “Nonequilibrium breakdown of quantum Hall state in graphene,” *Physical Review B - Condensed Matter and Materials Physics*, vol. 80, no. 8, pp. 6–9, 2009.

[287] A. Tzalenchuk, S. Lara-Avila, A. Kalaboukhov, S. Paolillo, M. Syväjärvi, R. Yakimova, O. Kazakova, T. J. Janssen, V. Fal'Ko, and S. Kubatkin, “Towards a quantum resistance standard based on epitaxial graphene,” *Nature Nanotechnology*, vol. 5, no. 3, pp. 186–189, 2010.

[288] A. Laitinen, M. Kumar, P. Hakonen, and E. Sonin, “Gyrotropic Zener tunneling and nonlinear IV curves in the zero-energy Landau level of graphene in a strong magnetic field,” *Scientific Reports*, vol. 8, p. 594, dec 2018.

[289] A. Laitinen, M. Kumar, T. Elo, Y. Liu, T. S. Abhilash, and P. J. Hakonen, “Breakdown of Zero-Energy Quantum Hall State in Graphene in the Light of Current Fluctuations and Shot Noise,” *Journal of Low Temperature Physics*, vol. 191, pp. 272–287, jun 2018.

[290] S. Tian, P. Wang, X. Liu, J. Zhu, H. Fu, T. Taniguchi, K. Watanabe, J. H. Chen, and X. Lin, “Nonlinear transport of graphene in the quantum Hall regime,” *2D Materials*, vol. 4, no. 1, 2017.

[291] H. Tanaka, H. Kawashima, H. Iizuka, H. Fukuda, and S. Kawajiy, “Temperature dependence of collapse of quantized hall resistance,” *Journal of the Physical Society of Japan*, vol. 75, no. 1, pp. 1–6, 2006.

[292] D. R. Leadley, R. J. Nicholas, J. J. Harris, and C. T. Foxon, “Cyclotron phonon emission and electron energy loss rates in GaAsGaAlAs heterojunctions,” *Solid State Electronics*, vol. 32, no. 12, pp. 1473–1477, 1989.

[293] J. A. Alexander-Webber, A. M. R. Baker, P. D. Buckle, T. Ashley, and R. J. Nicholas, “High-current breakdown of the quantum Hall effect and electron heating in InSb/AlInSb,” *Physical Review B*, vol. 86, p. 045404, jul 2012.

[294] A. M. Baker, J. A. Alexander-Webber, T. Altebaeumer, S. D. McMullan, T. J. Janssen, A. Tzalenchuk, S. Lara-Avila, S. Kubatkin, R. Yakimova, C. T. Lin, L. J. Li, and R. J. Nicholas, “Energy loss rates of hot Dirac fermions in epitaxial, exfoliated, and CVD graphene,” *Physical Review B - Condensed Matter and Materials Physics*, vol. 87, no. 4, pp. 3–8, 2013.

[295] J. Huang, J. A. Alexander-Webber, T. J. Janssen, A. Tzalenchuk, T. Yager, S. Lara-Avila, S. Kubatkin, R. L. Myers-Ward, V. D. Wheeler, D. K. Gaskill, and R. J. Nicholas, “Hot carrier relaxation of Dirac fermions in bilayer epitaxial graphene,” *Journal of Physics Condensed Matter*, vol. 27, no. 16, 2015.

[296] K. Chida, T. Arakawa, S. Matsuo, Y. Nishihara, T. Tanaka, D. Chiba, T. Ono, T. Hata, K. Kobayashi, and T. Machida, “Observation of finite excess noise in the voltage-biased quantum Hall regime as a precursor for breakdown,” *Physical Review B*, vol. 87, p. 155313, apr 2013.

[297] K. Ikushima, H. Sakuma, S. Komiyama, and K. Hirakawa, “Visualization of quantum Hall edge channels through imaging of terahertz emission,” *Physical Review B - Condensed Matter and Materials Physics*, vol. 76, no. 16, pp. 1–6, 2007.

[298] W. P. Halperin, “Caught speeding,” *Nature Physics*, vol. 12, p. 993, 2016.

[299] A. M. Martin, K. A. Benedict, F. W. Sheard, and L. Eaves, “Model for the voltage steps in the breakdown of the integer quantum hall effect,” *Physical Review Letters*, vol. 91, no. 12, pp. 3–6, 2003.

[300] L. Landau, "Theory of the superfluidity of helium II," *Physical Review*, vol. 60, no. 4, pp. 356–358, 1941.

[301] R. Roldán, M. O. Goerbig, and J. N. Fuchs, "The magnetic field particle-hole excitation spectrum in doped graphene and in a standard two-dimensional electron gas," *Semiconductor Science and Technology*, vol. 25, no. 3, 2010.

[302] C. Dillard, X. Lin, M. A. Kastner, L. N. Pfeiffer, and K. W. West, "Breakdown of the integer and fractional quantum Hall states in a quantum point contact," *Physica E: Low-Dimensional Systems and Nanostructures*, vol. 47, pp. 290–296, 2013.

[303] Z. Fei, G. O. Andreev, W. Bao, L. M. Zhang, A. S. McLeod, C. Wang, M. K. Stewart, Z. Zhao, G. Dominguez, M. Thiemens, M. M. Fogler, M. J. Tauber, A. H. Castro-Neto, C. N. Lau, F. Keilmann, and D. N. Basov, "Infrared Nanoscopy of Dirac Plasmons at the Graphene–SiO 2 Interface," *Nano Letters*, vol. 11, pp. 4701–4705, nov 2011.

[304] M. B. Lundeberg, Y. Gao, R. Asgari, C. Tan, B. Van Duppen, M. Autore, P. Alonso-González, A. Woessner, K. Watanabe, T. Taniguchi, R. Hillenbrand, J. Hone, M. Polini, and F. H. L. Koppens, "Tuning quantum nonlocal effects in graphene plasmonics," *Science*, vol. 357, pp. 187–191, jul 2017.

[305] M. I. Dyakonov and M. S. Shur, "Two dimensional electronic flute," *Applied Physics Letters*, vol. 67, pp. 1137–1139, aug 1995.

[306] M. Dyakonov and M. Shur, "Detection, mixing, and frequency multiplication of terahertz radiation by two-dimensional electronic fluid," *IEEE Transactions on Electron Devices*, vol. 43, no. 3, pp. 380–387, 1996.

[307] W. Knap, J. Lusakowski, T. Parenty, S. Bollaert, A. Cappy, V. V. Popov, and M. S. Shur, "Terahertz emission by plasma waves in 60 nm gate high electron mobility transistors," *Applied Physics Letters*, vol. 84, no. 13, pp. 2331–2333, 2004.

[308] W. Knap, Y. Deng, S. Rumyantsev, J.-Q. Lü, M. S. Shur, C. a. Saylor, and L. C. Brunel, "Resonant detection of subterahertz radiation by plasma waves in a submicron field-effect transistor," *Applied Physics Letters*, vol. 80, no. 18, p. 3433, 2002.

[309] F. Teppe, W. Knap, D. Veksler, M. S. Shur, A. P. Dmitriev, V. Y. Kachorovskii, and S. Rumyantsev, "Room-temperature plasma waves resonant detection of subterahertz radiation by nanometer field-effect transistor," *Applied Physics Letters*, vol. 87, p. 052107, aug 2005.

[310] W. Knap, M. Dyakonov, D. Coquillat, F. Teppe, N. Dyakonova, J. Łusakowski, K. Karpierz, M. Sakowicz, G. Valusis, D. Seliuta, I. Kasalynas, A. El Fatimy, Y. M. Meziani, and T. Otsuji, "Field effect transistors for terahertz detection: Physics and first imaging applications," *Journal of Infrared, Millimeter, and Terahertz Waves*, vol. 30, no. 12, pp. 1319–1337, 2009.

[311] H. Yan, X. Li, B. Chandra, G. Tulevski, Y. Wu, M. Freitag, W. Zhu, P. Avouris, and F. Xia, "Tunable infrared plasmonic devices using graphene/insulator stacks," *Nature Nanotechnology*, vol. 7, pp. 330–334, may 2012.

[312] J. Chen, M. L. Nesterov, A. Y. Nikitin, S. Thongrattanasiri, P. Alonso-González, T. M. Slipchenko, F. Speck, M. Ostler, T. Seyller, I. Crassee, F. H. L. Koppens, L. Martin-Moreno, F. J. García de Abajo, A. B. Kuzmenko, and R. Hillenbrand, "Strong Plasmon Reflection at Nanometer-Size Gaps in Monolayer Graphene on SiC," *Nano Letters*, vol. 13, pp. 6210–6215, dec 2013.

[313] Z. Fei, A. S. Rodin, W. Gannett, S. Dai, W. Regan, M. Wagner, M. K. Liu, A. S. McLeod, G. Dominguez, M. Thiemens, A. H. Castro Neto, F. Keilmann, A. Zettl, R. Hillenbrand, M. M. Fogler, and D. N. Basov, "Electronic and plasmonic phenomena at graphene grain boundaries," *Nature Nanotechnology*, vol. 8, pp. 821–825, nov 2013.

[314] J. A. Gerber, S. Berweger, B. T. O'Callahan, and M. B. Raschke, "Phase-resolved surface plasmon interferometry of graphene," *Physical Review Letters*, vol. 113, no. 5, pp. 1–5, 2014.

[315] A. Woessner, Y. Gao, I. Torre, M. B. Lundeberg, C. Tan, K. Watanabe, T. Taniguchi, R. Hillenbrand, J. Hone, M. Polini, and F. H. L. Koppens, "Electrical 2π phase control of infrared light in a 350-nm footprint using graphene plasmons," *Nature Photonics*, vol. 11, pp. 421–424, jul 2017.

[316] A. Kumar, T. Low, K. H. Fung, P. Avouris, and N. X. Fang, "Tunable light-matter interaction and the role of hyperbolicity in graphene-hbn system," *Nano Letters*, vol. 15, no. 5, pp. 3172–3180, 2015.

[317] A. Laturia, M. L. Van de Put, and W. G. Vandenberghe, "Dielectric properties of hexagonal boron nitride and transition metal dichalcogenides: from monolayer to bulk," *npj 2D Materials and Applications*, vol. 2, no. 1, pp. 1–7, 2018.

[318] Y. Li, V. Garnier, C. Journet, J. Barjon, A. Loiseau, I. Stenger, A. Plaud, B. Toury, and P. Steyer, "Advanced synthesis of highly crystallized hexagonal boron nitride by coupling polymer-derived ceramics and spark plasma sintering processes - Influence of the crystallization promoter and sintering temperature," *Nanotechnology*, vol. 30, no. 3, 2019.